Coordinate Transformation Based Electromagnetic Design and Applications.

Tang, Wenxuan

Coordinate Transformation Based Electromagnetic Design and Applications

by

Wenxuan Tang

A thesis submitted to the University of London in partial fulfilment of the requirements for the degree of

Doctor of Philosophy

School of Electronic Engineering and Computer Science
Queen Mary, University of London
United Kingdom

October 2012

To my family

Abstract

The main objective of this thesis is to take one step forward to practical and realisable devices for antenna and microwave engineering, using the technique of discrete coordinate transformation (DCT), which is a practical implementation of the coordinate transformation method. During this thesis, the DCT technique was demonstrated and analysed from the theory, and was proved to provide an all-dielectric approach to design devices under certain conditions. Two schemes were proposed on how to use this technique in a practical design. The first one is to transform an existing device into a flattened profile, meanwhile maintaining its electromagnetic performance. As examples, a flat reflector and a flat lens were created from a parabolic reflector and a convex lens, respectively. The second scheme is to project the propagating paths of an electromagnetic wave, and then generate a distorted space according to the paths by engineering the electromagnetic properties of the media. In this scheme, two examples of application were presented: an undetectable antenna composed of a carpet cloak and a conducting cavity, and a broadband device which can extraordinarily enhance the transmission through a sub-wavelength aperture.

Numerical simulations based on the Finite-Difference Time-Domain (FDTD) method were implemented to verify all the designs. Several specific configurations were employed in the modelling in order to simulate the DCT based devices more efficiently and precisely. Performance of these devices was validated and analysed, and the advantages and disadvantages of this technique were investigated. Realisation and fabrication methods

were also studied, and a prototype was designed, fabricated and measured. At the end, as an extension, a multiple discrete coordinate transformation method was proposed and presented. This multiple transformation was proved to effectively relax the limitation of the one-step transformation, and was used to design an all-dielectric thin absorber from a conventional pyramidal one for demonstration.

Acknowledgements

My sincere gratitude goes first and foremost to Prof. Yang Hao, my supervisor, for his consistent support, patient guidance and professional supervision. I deeply appreciate all his contributions of time and work to make my PhD experience productive and stimulating. His knowledge and enthusiasm towards research have inspired me, and encouraged me all the time during my study. My heartfelt thanks also go to Prof. Clive Parini and Dr. Robert Donnan for their positive and helpful comments.

I am extremely grateful to my colleagues in Queen Mary. The group has been a source of friendship, good advice and collaboration. Many appreciations to Dr. Christos Argyropoulos, Dr. Efthymios Kallos, Dr. Rui Yang, Dr. Oscar Quevedo-Teruel, Dr. Khalid Rajab, Ms. Di Bao and Dr. Rhiannon Mitchell-Thomas for their great help and fruitful collaboration. Many thanks also to Dr. Anestis Katsounaros, Dr. Qammer Abbasi, Dr. Lianhong Zhang, Dr. Robert Foster, Dr. Atiqur Rahman, Dr. George Palikaras, Mr. Jiefu Zhang, Mr. Yifeng Fan, Mr. Saul Wiggin, Mr. Paolo Turati, Ms. Tuba Yilmaz, Dr. Alice Pellegrini, Mr. Ke Yang, Mr. Max Munoz and all the rest for their encouragement and willingness to help. Deep thanks are also due to the China Scholarship Council for the financial support during my study.

Finally, I would like to thank my beloved family. For my parents who raised me, love me and support me for years. And for my dear husband, Mr. Jian Hua, whose patience and faithful support are so appreciated.

List of Publications

Journal Publications

1. **Wenxuan Tang**, Yang Hao, and Francisco Medina, "Broadband Extraordinary Transmission in a Single Sub-wavelength Aperture," Optics Express, Vol. 18, No. 16, pp. 16946-16954, 2010.

2. Di Bao, Khalid Z. Rajab, **Wenxuan Tang**, and Yang Hao, "Experimental Demonstration of Broadband Transmission Through Subwavelength Aperture," Applied Physics Letters, Vol. 97, No. 13, pp. 134105, 2010.

3. **Wenxuan Tang**, Christos Argyropoulos, Efthymios Kallos, Wei Song, and Yang Hao, "Discrete Coordinate Transformation for Designing All-dielectric Flat Antennas," IEEE Transaction on Antennas and Propagation, Vol. 58, No. 12, pp. 3795-3804, 2010.

4. Di Bao, Efthymios Kallos, **Wenxuan Tang**, Christos Argyropoulos, Yang Hao, and Tiejun Cui, "A broadband Simplified Free Space Cloak Realized by Nonmagnetic Dielectric Cylinders," Frontiers of Physics in China, Vol. 5, No. 3, pp. 319-323, 2010.

5. Rui Yang, **Wenxuan Tang**, and Yang Hao, "A Broadband Zone Plate Lens from Transformation Optics," Optics Express, Vol. 19, No. 13, pp. 12348-12355, 2011.

6. Rui Yang, **Wenxuan Tang**, Yang Hao, and Ian Youngs, "A Coordinate Trans-

formation Based Broadband Flat Lens via Microstrip Array," IEEE Antennas and Wireless Propagation Letters, Vol. 10, pp. 99-102, 2011.

7. Di Bao, Khalid Z Rajab, Yang Hao, Efthymios Kallos, **Wenxuan Tang**, Christos Argyropoulos, Yongzhe Piao, and Shoufeng Yang, "All-dielectric Invisibility Cloaks Made of BaTiO3-loaded Polyurethane Foam," New Journal of Physics, Vol. 13, pp. 103023, 2011.

8. Rui Yang, **Wenxuan Tang**, and Yang Hao, "Wideband Beam-Steerable Flat Reflectors via Transformation Optics," IEEE Antennas and Wireless Propagation Letters, Vol. 10, pp. 1290-1294, 2011.

9. **Wenxuan Tang**, Yang Hao, and Raj Mittra, "Design of a Carpet Cloak to Conceal an Antenna Located Underneath," IEEE Transaction on Antennas and Propagation, Vol. 60, No. 9, pp. 4444-4449, 2012.

Conference Papers

1. **Wenxuan Tang**, Christos Argyropoulos, Efthymios Kallos, and Yang Hao, "Discrete Transformation Electromagnetics and Its Applications in Antenna Design," 2010 International Workshop on Antenna Technology, March, 2010, Lisbon, Portugal.

2. **Wenxuan Tang**, Christos Argyropoulos, Efthymios Kallos, Di Bao, Wei Song, and Yang Hao, "Flat Devices Design for Antenna Systems Using Coordinate Transformation," IEEE Antennas and Propagation Society International Symposium (APS 2010), July, 2010, Toronto, Canada.

3. **Wenxuan Tang**, Francisco Medina, and Yang Hao, "Coordinate Transformation Based Device for Extraordinary Transmission Through a Sub-wavelength Aperture," the Fourth International Congress on Advanced Electromagnetic Materials in Microwaves and Optics, September, 2010, Karlsruhe, Germany.

4. **Wenxuan Tang**, Yang Hao, and Raj Mittra, "Cloaking a Reflector Using Coordinate Transformation Approach," the 5th European Conference on Antennas and Propagation (EuCAP 2011), April, 2011, Rome, Italy.

5. Di Bao, Khalid Z. Rajab, **Wenxuan Tang**, and Yang Hao, "Broadband Extraordinary Transmission Device Realized with Dielectrics", the 5th European Conference on Antennas and Propagation (EuCAP 2011), April, 2011, Rome, Italy.

6. Rui Yang, **Wenxuan Tang**, and Yang Hao, "Broadband Dielectric Zone Plate Antenna from Transformation Electromagnetics", the 5th European Conference on Antennas and Propagation (EuCAP 2011), April, 2011, Rome, Italy.

7. **Wenxuan Tang**, and Yang Hao, "Cloak an Underground Antenna Using Transformation Electromagnetics," IEEE Antennas and Propagation Society International Symposium (APS 2011), July, 2011, Spokane, Washington, USA.

8. Di Bao, **Wenxuan Tang**, Christos Argyropoulos, Efthymios Kallos, and Yang Hao, "Experimental Verification of Carpet Cloak Realized with Dielectric Cylinders," IEEE Antennas and Propagation Society International Symposium (APS 2011), July, 2011, Spokane, Washington, USA.

9. **Wenxuan Tang**, Christos Argyropoulos, Efthymios Kallos, and Yang Hao, "Investigation of Broadband Flat Antennas Using Transformation Electromagnetics," Progress In Electromagnetics Research Symposium (PIERS 2011), September, 2011, Suzhou, China.

10. Qi Wu, Jeremiah P. Turpin, Douglas H. Werner, Pingjuan L. Werner, **Wenxuan Tang**, and Yang Hao, "Flat Collimating Lenses Based on Quasi-conformal Transformation Electromagnetics," the 6th European Conference on Antennas and Propagation (EUCAP 2012), March, 2012, Prague, Czech Republic.

Table of Contents

List of Abbreviations

2D	Two-dimensional
3D	Three-dimensional
ACT	Analytical coordinate transformation
CT	Coordinate transformation
DCT	Discrete coordinate transformation
EOT	Extraordinary (optical) transmission
FDTD	Finite-difference time-domain
FEM	Finite element method
FSSs	Frequency selective surfaces
FWHM	Full width at half maximum
GRIN	Gradient-index
LHMs	Left-handed materials
MTMs	Metamaterials
NTFF	Near-to-far-field
NIMs	Negative (refractive) index materials
PBC	Periodic boundary condition

PCB	Printed circuit board
PDE	Partial differential equation
PEC	Perfect electric conductor
PML	Perfectly matched layer
RCS	Radar cross section
SRR	Split-ring resonator
TF/SF	Total-field/scattered-field

List of Figures

List of Tables

Chapter 1

Introduction

1.1 Introduction

Metamaterials (MTMs), first known as the left-handed materials (LHMs) or negative (refractive) index materials (NIMs), have been a new frontier for both the scientific and the engineering community in recent years. The LHMs (or MTMs) possess both negative permittivity and negative permeability, and exhibit extraordinary physical properties such as negative refraction. The concept of negative refraction was first presented in 1968 in a pioneering theoretical work by Veselago [1]. A recent study suggested that the concept may be originated by another Russian scientist back in 1940s [2]. It was over 50 years until Sir Pendry and others proposed several schemes to realise materials with negative permittivity and permeability [3–5], along with some potential applications of LHMs [6–8]. These contributions, accompanied with a successful experimental demonstration of negative refraction at microwave frequencies in 2001 [9], have brought about great expectation for this new kind of artificial material. However, most realised LHMs rely upon resonant structures and, therefore, have the distinct disadvantages of being high-loss and narrow-band [10]. Further development on LHMs was focussed on practical applications [11–13] until 2005. Ever since, the concept of MTMs has been

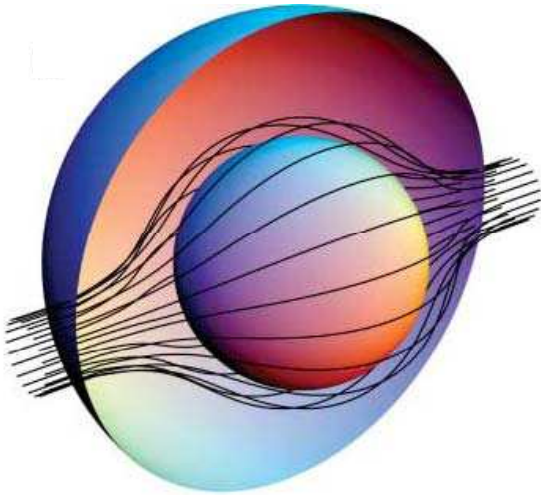

Figure 1.1: The incident waves are diverted within the cloak and emerge on the far side un-deviated from their original course. The cloaking region is contained between the two spheres. [15]

extended and it is no longer restricted to the material with negative permittivity and/or permeability, but can also be referred to as other materials with extreme properties such as near-zero, or extremely high refractive indices.

Along with metamaterials, a new concept of the "cloak of invisibility" was proposed in 2006 [14, 15]. Electromagnetic waves are controlled by the media of the cloak, and objects surrounded by the cloak are undisturbed (See Fig. 1.1). To achieve a perfect cloak, metamaterials are essential, with their properties changing spatially. A two-dimensional (2D) cloak was experimentally verified at microwave frequencies (see Fig. 1.2) by Smith *et al.* in 2006 [16], followed by more explorations at different frequencies [17–21].

The undergoing theory behind the invisibility is a method called "coordinate transformation", also termed as "optical transformation". It is based on the special characteristics of Maxwell's equations in different coordinate systems. Maxwell's equations have a form-invariant nature under coordinate transformation, where the only change is a normalization of the electromagnetic parameters (refractive index n, or permittivity ε and permeability μ) of the background media of the space [22]. This means that a space filled with engineered spatially-dispersive background media can exactly mimic

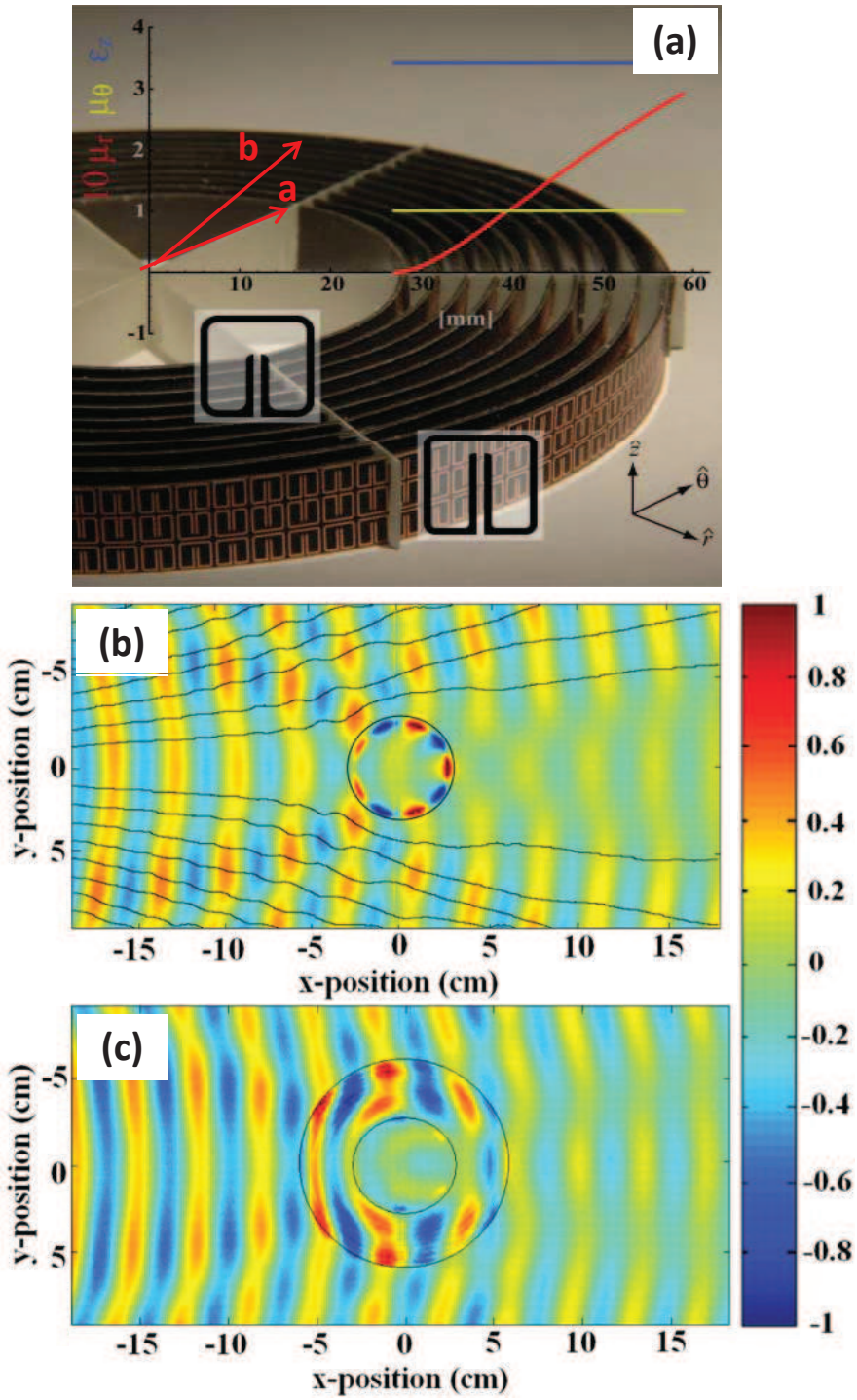

Figure 1.2: Experimental verification of the first 2D cloak at microwave frequencies. (a) The cloak with a plot of the material parameters that are implemented. The fields shown are (b) the experimental measurement of a bare conducting cylinder and (c) the experimental measurement of the cloaked conducting cylinder. [16]

the electromagnetic behaviour of another space. Thanks to the ability of controlling electromagnetic fields, different devices with novel functionalities have been constructed aside from cloaks, such as the EM rotators [23, 24], EM concentrators [25–27], sensor cloaks [28], optical black holes [29, 30], antenna devices [31, 32], etc. Metamaterials with/without negative index are commonly employed as the realising material. In 2008, another important device of invisibility, the "carpet cloak", was proposed by Li *et al.* [33]. The carpet cloak enables the use of non-resonant elements (such as conventional dielectric materials), and offers the possibility to achieve low-loss and broadband performance. This contribution led to some successful demonstrations of all-dielectric cloaks at different frequencies [34–36].

To investigate all devices designed with the coordinate transformation, and to predict their performance, numerical modelling is widely implemented. In this work, the Finite-Difference Time-Domain (FDTD) method based in-house codes have been used to characterise the performance of devices. The FDTD method is one of the most popular numerical methods for solving electromagnetic problems [37, 38]. It provides a simple and elegant way to discretise the differential form of Maxwell's equations, and a direct solution to complex electromagnetic problems. This method was firstly proposed by Yee [39], and has recently been employed to simulate metamaterials [38, 40–42]. Dispersive FDTD modelling has also been developed to deal with the spatially dispersive property of metamaterials and cloaks [43, 44]. This time-domain method is especially suitable for modelling transformation devices designed in this work, since it can easily deal with their dispersive characteristics in a given space as well as over a wide frequency band.

1.2 Research Objective

Although the coordinate transformation method has demonstrated its power to control the electromagnetic wave, there are still problems to overcome. One of them is that in practice transformation devices often require extreme values of permittivity and/or

permeability (e.g., near zero or extremely high). Even though metamaterials are proved capable of providing a wide range of permittivity and permeability, to achieve extreme values, they always require resonant structures which severely limit the operating bandwidth. In addition, many transformation devices require anisotropic permittivity and permeability simultaneously, which makes the practical realisation even more difficult.

Therefore, the focus of this work is to take one step forward to practical devices for microwave engineering and antenna systems, by using the discrete coordinate transformation technique. Based on the theoretical analysis presented in Chapter 2, some broadband novel devices are proposed in Chapter 3 and Chapter 4. All designed devices are achievable by using conventional isotropic dielectrics or non-resonant metamaterials, and, therefore, demonstrate broadband performance. FDTD method based numerical simulations are primarily employed to validate the design, meanwhile a prototype of the transformation device is fabricated and measured. Two designing approaches are developed and clarified, and an extension of multiple coordinate transformation is proposed.

The major contributions presented during this work can be summarised as follows:

1. The discrete coordinate transformation has been developed as a general approach for antenna and microwave engineering. Validity and limitation of this technique have been demonstrated through theoretical analyses, numerical simulations and experiments. A detailed designing procedure of all dielectric devices has been presented and studied.

2. Two important schemes of creating devices using the discrete coordinate transformation have been proposed and clarified. The first one is to change the geometry of an existing device while maintain its electromagnetic performance. The second one is to project the propagating paths in a distorted space, and then generate this distorted physical space using transformation media.

3. A broadband flat reflector has been proposed, designed and numerically demonstrated. It is flattened from a parabolic reflector using the discrete coordinate transformation, and is only composed of conventional dielectrics. A new scheme to steer the

radiating beam of the dielectric reflector has also been proposed.

4. A broadband flat lens has been proposed, designed and numerically demonstrated. It is flattened from a convex lens and is only composed of seven dielectric blocks.

5. An undetectable antenna combined with a carpet cloak and a conducting cavity has been proposed, designed and numerically demonstrated. This is a new kind of stealth radome. A new technique called the "virtual boundary" has been proposed to replace the conducting bump on the bottom of the carpet cloak, and so as to allow the antenna element under the carpet cloak to transmit and receive signals. A new function of the carpet cloak, that to create highly directive beam as a specific lens, has also been proposed and demonstrated.

6. A novel broadband device which can extraordinarily enhance the transmission through a sub-wavelength aperture has been proposed, designed and demonstrated through both simulations and measurements. This device serves to smoothly guide an incidence from a large aperture to a small one, hence can be viewed as a new kind of impedance matching device.

7. Key features of applying the discrete coordinate transformation, including the size of the transformation region, the orthogonality of the local coordinate systems, and the impact of the boundary have been researched and analysed. Sampling of the permittivity map of a transformation device has been proposed and studied. This kind of simplification significantly reduces the difficulty of fabrication, and therefore leads to easily realisable devices. Theoretical analyses and numerical simulations have demonstrated its validity.

8. The analytical coordinate transformation (in global coordinate systems) and the discrete coordinate transformation (in local coordinate systems) have been compared in terms of the properties of transformation media and the performance of transformation device. Example designs for comparison have been presented.

9. A multiple discrete coordinate transformation has been proposed and demonstrated. This multiple technique can effectively relax the limitation of the one-step transformation, and is able to steer the propagation of a wave with more flexibility.

10. An isotropic dielectric absorber has been created from a pyramidal absorber using the multiple discrete coordinate transformation. This broadband absorber has been demonstrated numerically. It requires no magnetic or anisotropic materials, and is able to reduce the thickness of the pyramidal absorber by 2/3.

1.3 Structure of the Thesis

In *Chapter Two*, fundamentals of the coordinate transformation is introduced and physics behind the theory is explained. The "cloak of invisibility", accompanied with some other designs, are briefly studied as example applications of the method. After that, the technique of discrete coordinate transformation is developed to design all-dielectric devices. Applying condition and designing procedure are presented in detail.

In *Chapter Three*, the discrete coordinate transformation is applied to change the profile of an existing device, so as to achieve a flat device. Two examples, a flat reflector and a flat focusing lens, are designed from a parabolic reflector and a convex lens respectively. The FDTD based simulation is used to demonstrate their performance.

In *Chapter Four*, the discrete coordinate transformation is applied to design novel functional devices by distorting the physical space with pre-designed propagating paths. A carpet cloak, combined with a so-called "virtual boundary", is designed as a new type of stealth radome to protect antennas. Besides, a dielectric device for extraordinarily enhanced transmission through a sub-wavelength aperture is also proposed. Numerical and experimental verifications are presented.

In *Chapter Five*, performance of the DCT based devices is analysed, meanwhile limitations and conditions of this technique are investigated. In addition, the discrete coordi-

nate transformation is compared with the analytical coordinate transformation, in terms of the composing material and the operating bandwidth of transformation devices.

In *Chapter Six*, a multiple discrete coordinate transformation is proposed to manipulate wave propagation through the highly distorted space and isotropic dielectric materials. A broadband flat absorber is created from the conventional pyramidal absorber to validate the concept through numerical simulations.

In *Chapter Seven*, conclusions are drawn and future work after this thesis is suggested and discussed.

References

[1] V. G. Veselago, "The electrodynamics of substances with simultaneously negative values of ε and μ," *Sov. Phys. Usp.*, vol. 10, pp. 509–514, 1968.

[2] S. Tretyakov, "Research on negative refraction and backward-wave media: A historical perspective," in *Negative Refraction: Revisiting Electromagnetics from Microwave to Optics, EPFL Latsis Symposium, Lausanne, Switzerland*, 2005, pp. 30–35.

[3] J. B. Pendry, A. J. Holden, W. J. Stewart, and I. Youngs, "Extremely low frequency plasmons in metallic mesostructures," *Phys. Rev. Lett.*, vol. 76, no. 25, pp. 4773–4776, 1996.

[4] J. Pendry, A. Holden, D. Robbins, and W. Stewart, "Magnetism from conductors and enhanced nonlinear phenomena," *IEEE Trans. Micr. Theory Techn.*, vol. 47, no. 11, pp. 2075–2084, 1999.

[5] D. Smith, W. Padilla, D. Vier, S. Nemat-Nasser, and S. Schultz, "Composite medium with simultaneously negative permeability and permittivity," *Phys. Rev. Lett.*, vol. 84, no. 18, pp. 4184–4187, 2000.

[6] J. Pendry, "Negative refraction makes a perfect lens," *Phys. Rev. Lett.*, vol. 85, no. 18, pp. 3966–3969, 2000.

[7] R. W. Ziolkowski, "Superluminal transmission of information through an electro-

magnetic metamaterial," *Phys. Rev. E*, vol. 63, no. 4, p. 046604, 2001.

[8] D. R. Smith, J. B. Pendry, and M. C. K. Wiltshire, "Metamaterials and negative refractive index," *Science*, vol. 305, pp. 788–792, 2004.

[9] R. A. Shelby, D. R. Smith, and S. Schultz, "Experimental verification of a negative index of refraction," *Science*, vol. 292, p. 7779, 2001.

[10] R. Greegor, C. Parazzoli, K. Li, and M. Tanielian, "Origin of dissipative losses in negative index of refraction materials," *Appl. Phys. Lett.*, vol. 82, no. 14, p. 2356, 2003.

[11] J. Pendry and S. Ramakrishna, "Focusing light using negative refraction," *J. Phys. Cond. Matter*, vol. 15, p. 6345, 2003.

[12] A. Grbic and G. Eleftheriades, "Overcoming the diffraction limit with a planar left-handed transmission-line lens," *Phys. Rev. Lett.*, vol. 92, no. 11, p. 117403, 2004.

[13] J. Baena, L. Jelinek, R. Marqués, and F. Medina, "Near-perfect tunneling and amplification of evanescent electromagnetic waves in a waveguide filled by a metamaterial: Theory and experiments," *Phys. Rev. B*, vol. 72, no. 7, p. 075116, 2005.

[14] U. Leonhardt, "Optical conformal mapping," *Science*, vol. 312, pp. 1777–1780, 2006.

[15] J. B. Pendry, D. Schurig, and D. R. Smith, "Controlling electromagnetic fields," *Science*, vol. 312, pp. 1780–1782, 2006.

[16] D. Schurig, J. J. Mock, B. J. Justice, S. A. Cummer, J. B. Pendry, A. F. Starr, and D. R. Smith, "Metamaterial electromagnetic cloak at microwave frequencies," *Science*, vol. 314, p. 977980, 2006.

[17] D. Schurig, J. B. Pendry, and D. R. Smith, "Calculation of material properties and ray tracing in transformation media," *Opt. Express*, vol. 14, no. 21, pp. 9794–9804, 2006.

[18] W. Jiang, J. Chin, Z. Li, Q. Cheng, R. Liu, and T. Cui, "Analytical design of conformally invisible cloaks for arbitrarily shaped objects," *Phys. Rev. E*, vol. 77, no. 6, p. 66607, 2008.

[19] W. Cai, U. Chettiar, A. Kildishev, and V. Shalaev, "Optical cloaking with meta-

materials," *Nature Photon.*, vol. 1, no. 4, pp. 224–227, 2007.

[20] A. Alù and N. Engheta, "Multifrequency optical invisibility cloak with layered plasmonic shells," *Phys. Rev. Lett.*, vol. 100, no. 11, p. 113901, 2008.

[21] D. Gaillot, C. Croënne, D. Lippens, *et al.*, "An all-dielectric route for terahertz cloaking," *Opt. Express*, vol. 16, no. 6, pp. 3986–3992, 2008.

[22] A. J. Ward and J. B. Pendry, "Refraction and geometry in Maxwell's equations," *J. Mod. Opt*, vol. 43, no. 4, pp. 773–793, 1996.

[23] H. Chen, B. Hou, S. Chen, X. Ao, W. Wen, and C. Chan, "Design and experimental realization of a broadband transformation media field rotator at microwave frequencies," *Phys. Rev. Lett.*, vol. 102, no. 18, p. 183903, 2009.

[24] Y. Luo, H. Chen, J. Zhang, L. Ran, and J. Kong, "Design and analytical full-wave validation of the invisibility cloaks, concentrators, and field rotators created with a general class of transformations," *Phys. Rev. B*, vol. 77, no. 12, p. 125127, 2008.

[25] M. Rahm, D. Schurig, D. Roberts, S. Cummer, D. Smith, and J. Pendry, "Design of electromagnetic cloaks and concentrators using form-invariant coordinate transformations of Maxwell's equations," *Photon. Nanostruct. Fundam. Appl.*, vol. 6, no. 1, pp. 87–95, 2008.

[26] A. Yaghjian and S. Maci, "Alternative derivation of electromagnetic cloaks and concentrators," *New J. of Phys.*, vol. 10, p. 115022, 2008.

[27] W. Jiang, T. Cui, Q. Cheng, J. Chin, X. Yang, R. Liu, and D. Smith, "Design of arbitrarily shaped concentrators based on conformally optical transformation of nonuniform rational B-spline surfaces," *Appl. Phys. Lett.*, vol. 92, p. 264101, 2008.

[28] A. Alù and N. Engheta, "Cloaking a sensor," *Phys. Rev. Lett.*, vol. 102, no. 23, p. 233901, 2009.

[29] E. Narimanov and A. Kildishev, "Optical black hole: Broadband omnidirectional light absorber," *Appl. Phys. Lett.*, vol. 95, no. 4, p. 041106, 2009.

[30] Q. Cheng, T. Cui, W. Jiang, and B. Cai, "An omnidirectional electromagnetic absorber made of metamaterials," *New J. of Phys.*, vol. 12, p. 063006, 2010.

[31] F. Kong, B. Wu, J. Kong, J. Huangfu, S. Xi, and H. Chen, "Planar focusing antenna design by using coordinate transformation technology," *Appl. Phys. Lett*, vol. 91,

p. 253509, 2007.

[32] N. Kundtz and D. Smith, "Extreme-angle broadband metamaterial lens," *Nat. Mater.*, vol. 9, pp. 129–132, 2010.

[33] J. Li and J. Pendry, "Hiding under the carpet: A new strategy for cloaking," *Phys. Rev. Lett.*, vol. 101, no. 20, p. 203901, 2008.

[34] R. Liu, C. Ji, J. J. Mock, J. Y. Chin, T. J. Cui, and D. R. Smith, "Broadband ground-plane cloak," *Science*, vol. 323, no. 5912, pp. 366–369, 2009.

[35] H. Ma, W. Jiang, X. Yang, X. Zhou, and T. Cui, "Compact-sized and broadband carpet cloak and free-space cloak," *Opt. Express*, vol. 17, no. 22, pp. 19 947–19 959, 2009.

[36] J. Valentine, J. Li, T. Zentgraf, G. Bartal, and X. Zhang, "An optical cloak made of dielectrics," *Nat. Mater.*, vol. 8, no. 7, pp. 568–571, 2009.

[37] A. Taflove and S. C. Hagness, *Computational electrodynamics : the finite-difference time-domain method, 3rd Edition*. Artech House, 2005.

[38] Y. Hao and R. Mittra, *FDTD Modelling of Metamaterials: Theory and Applications*. Artech House, MA, 2009.

[39] K. Yee, "Numerical solution of initial boundary value problems involving Maxwell's equations in isotropic media," *IEEE Trans. Ant. Propag.*, vol. 14, no. 3, pp. 302–307, 1966.

[40] M. Feise, J. Schneider, and P. Bevelacqua, "Finite-difference and pseudospectral time-domain methods applied to backward-wave metamaterials," *IEEE Trans. Antennas Propagat.*, vol. 52, no. 11, pp. 2955–2962, 2004.

[41] N. Panoiu and R. Osgood Jr, "Influence of the dispersive properties of metals on the transmission characteristics of left-handed materials," *Phys. Rev. E*, vol. 68, no. 1, p. 016611, 2003.

[42] J. Lee, J. Lee, H. Kim, N. Kang, and H. Jung, "Effective medium approach of left-handed material using a dispersive FDTD method," *IEEE Trans. Magnetics*, vol. 41, no. 5, pp. 1484–1487, 2005.

[43] Y. Zhao, C. Argyropoulos, and Y. Hao, "Full-wave finite-difference time-domain simulation of electromagnetic cloaking structures," *Opt. Express*, vol. 16, no. 9, pp.

6717–6730, 2008.

[44] C. Argyropoulos, Y. Zhao, and Y. Hao, "A radially-dependent dispersive finite-difference time-domain method for the evaluation of electromagnetic cloaks," *IEEE Trans. Ant. Propag.*, vol. 57, no. 5, pp. 1432–1441, 2009.

Chapter 2

The Coordinate Transformation Technique

2.1 Introduction

The technique of the coordinate transformation (CT) is the pivotal tool to design novel functional devices in this thesis. Each device can be viewed as a specific space which manipulates the propagation of electromagnetic waves as required. Such a distorted space can be constructed with custom-engineered media. One question may arise, that how one can theoretically predict the electromagnetic parameters of the media? The answer is to use the coordinate transformation technique. This technique serves to derive the relationship between the electromagnetic properties of the distorted space and the constitutive parameters of the filling media.

In this chapter, first, the theory of coordinate transformation will be studied, and the method of calculating the parameters of transformation media will be explained. Then, an important application based on the theory of the coordinate transformation, the "cloak of invisibility ", will be presented. Some other devices, including a planar reflector, a compressed convex lens and a compressed pyramidal absorber will also be

designed as proof of the concept. Along the way, the technique of discrete coordinate transformation (DCT) will be proposed, aiming for isotropic and broadband solutions. Some key formulations will be presented to describe the theory, and to illustrate the restrictions and limitations of the technique when applied in practice. At the end, potential applications of the discrete coordinate transformation will be discussed.

2.2 Theory of the Coordinate Transformation

The technique of coordinate transformation, also termed as "optical transformation" when referred to the behaviour of rays, had been proposed in the last century when researchers studied Maxwell's equations in complex geometries [1–7]. This technique is essentially based on the foundation that Maxwell's equations have a form invariant nature in different coordinate systems, where the only change is a normalization of electromagnetic parameters (e.g., the permittivity ε and the permeability μ) of the background media. Derivation of the form invariant property in Maxwell's equations can be found in Appendix A. To clearly describe the coordinate transformation technique, two spaces characterised by two different coordinate systems are plotted in Fig. 2.1. Figure (a) presents a so-called "virtual space". It is a space where the coordinates can be "pulled"

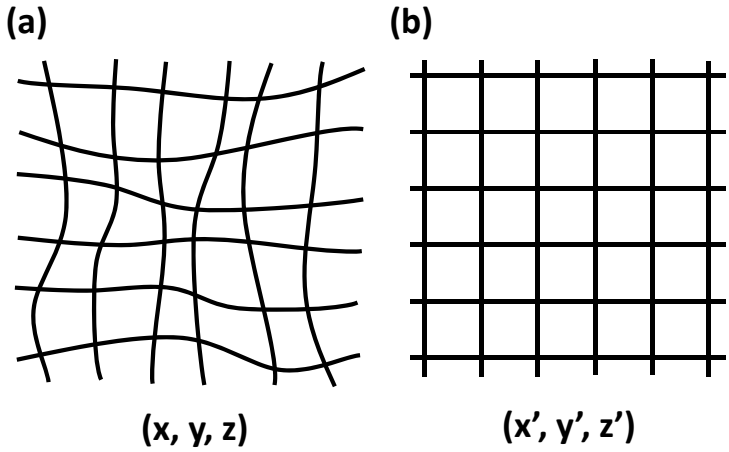

Figure 2.1: (a) The virtual space described in (x, y, z) coordinate system. (b) The physical space described in (x', y', z') coordinate system. The grid in (a) is distorted.

or "stretched", according to the paths which an electromagnetic wave travels along. Figure (b) can be viewed as a "physical space", which is described in the Cartesian coordinates. We start from Maxwell's equations in the virtual space:

$$\bigtriangledown \times \mathbf{E} + \bar{\bar{\mu}} \partial \mathbf{H}/\partial t = 0, \;\; \bigtriangledown \times \mathbf{H} - \bar{\bar{\varepsilon}} \partial \mathbf{E}/\partial t = 0. \tag{2.1}$$

Both the permittivity ε and the permeability μ may vary spatially. Because of its invariant nature, Maxwell's equations have exactly the same form in the physical space, as

$$\bigtriangledown' \times \mathbf{E}' + \bar{\bar{\mu}}' \partial \mathbf{H}'/\partial t = 0, \;\; \bigtriangledown' \times \mathbf{H}' - \bar{\bar{\varepsilon}}' \partial \mathbf{E}'/\partial t = 0. \tag{2.2}$$

However, the refractive index, or more specifically the permittivity and the permeability, are scaled by a factor. This factor is decided by the relationship between the two coordinate systems. Suppose the two coordinate systems are related as

$$x' = x'(x, y, z), \;\; y' = y'(x, y, z), \;\; z' = z'(x, y, z), \tag{2.3}$$

then the parameters in Eq. (2.2) can be calculated by [6, 8]

$$\bar{\bar{\varepsilon}}' = \frac{\mathbf{J} \bar{\bar{\varepsilon}} \mathbf{J}^T}{det(\mathbf{J})}, \;\; \bar{\bar{\mu}}' = \frac{\mathbf{J} \bar{\bar{\mu}} \mathbf{J}^T}{det(\mathbf{J})}. \tag{2.4}$$

Solutions of the electromagnetic fields in the physical space are presented as

$$\mathbf{E}' = (\mathbf{J}^T)^{-1} \mathbf{E}, \;\; \mathbf{H}' = (\mathbf{J}^T)^{-1} \mathbf{H}. \tag{2.5}$$

In Eqs. (2.4) and (2.5), J is the Jacobian transformation matrix between the two

coordinate systems, defined as

$$J = \begin{pmatrix} \frac{\partial x'}{\partial x} & \frac{\partial x'}{\partial y} & \frac{\partial x'}{\partial z} \\ \frac{\partial y'}{\partial x} & \frac{\partial y'}{\partial y} & \frac{\partial y'}{\partial z} \\ \frac{\partial z'}{\partial x} & \frac{\partial z'}{\partial y} & \frac{\partial z'}{\partial z} \end{pmatrix}. \tag{2.6}$$

Obviously, the Jacobian matrix represents the distortion between the two coordinate systems. Eqs. (2.4) and (2.5) indicate that the distortion of electromagnetic fields can be maintained with the distortion of permittivity and permeability. In other words, if the physical space is filled with transformation media satisfying Eq. (2.4), an incident electromagnetic wave is "pulled" or "stretched" in the same way as in the virtual space. It should be pointed out that permittivity and permeability in Eq. (2.4) are spatially dependent in the physical space. Usually they are tensors if the transformation media are anisotropic.

The technique of coordinate transformation provides us with a method to connect the propagation of the wave to the property of the media. Eq. (2.4) is the primary tool for constructing a physical space which mimics the electromagnetic environment of a wanted virtual space. This technique opened up a new way of controlling the propagation of electromagnetic waves and creating novel functional devices. It became dramatically appealing when the "cloak of invisibility" was proposed by Sir Pendry and Leonhardt respectively in the year of 2006 [5, 6].

2.3 Transformation Devices

2.3.1 "Cloaks of invisibility"

The most well-known application using the technique of coordinate transformation is the cloaking device, which can render an object inside the cloaking area "invisible" to

external detections. A cloak of invisibility is essentially a physical space that filled with inhomogeneous media. It wraps an object to be concealed, and mimics a virtual space - the empty free space. Inside the cloak, an incident wave is controlled to travel around the object without any disturbance, and then recomposes into its original manner at the other side of the cloak. Therefore, the incident wave will see the whole cloaked area as the free space.

The first cloak was proposed in [6] (see Fig. 2.2). The scheme is to cloak the secure region $r < R_1$ with the cloaking region $R_1 < r < R_2$. The cloaking region functions to deflect incidences that would have struck the secure region, guide them around the secure region, and return them to their original trajectory. An outside observer concludes that the secure region is empty, so an arbitrary object could be hidden inside it. A simple coordinate transformation that achieves the desired result can be found by taking all fields in the region of $r < R_2$ and compressing them into the region of $R_1 < r < R_2$. In other words, the coordinate transformation is operated between two spaces: the virtual space inside the sphere of $r = R_2$, filled with the air; and the physical space inside the annulus of $R_1 < r' < R_2$, filled with transformation media. A relation between them is found as

$$r' = R_1 + r(R_2 - R_1)/R_2,\ \theta' = \theta,\ \phi' = \phi. \tag{2.7}$$

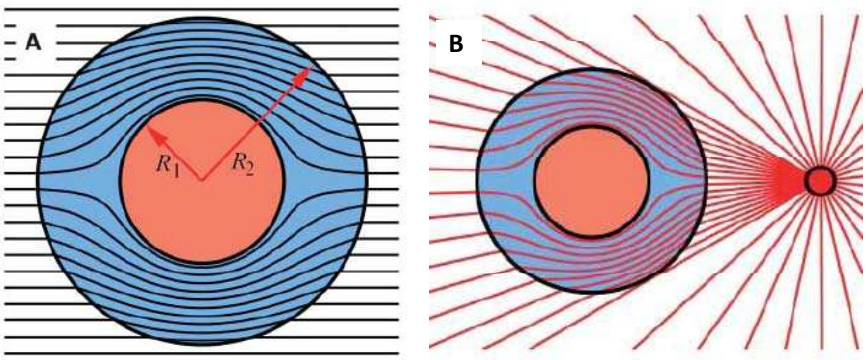

Figure 2.2: A two-dimensional (2D) cross section of the spherical cloak with (a) plane wave incidence and (b) a point source located near the cloaked sphere. The lines illustrate the rays.[6]

Eq. (2.7) indicates two interesting properties of the cloak. First, the center $r = 0$ in the virtual space becomes a sphere $r' = R_1$ in the physical space. This property explains the "invisibility" from another point of view. Apparently, a singular point in the virtual space causes no disturbance of an incident electromagnetic wave. Since the physical space has the same electromagnetic propagation environment as the virtual space, as stated in the theory of coordinate transformation, the projection of the singular point in the physical space (which is the spherical region $r' < R_1$) should behave in the same way as the singular point. Therefore, the spherical region $r' < R_1$ causes no disturbance, and anything inside is undetectable. Second, we have found that the two spaces are equivalent at the outer boundary (when $r = R_2$, $r' = R_2$ as well). This is an important property of the coordinate transformation. If the two spaces have different outer boundaries, the physical space will cause reflections to the surroundings.

Eqs. (2.4) and (2.7) are used to calculate the permittivity ε' and the permeability μ' in the physical space. In the concealed area where $r' < R_1$, ε' and μ' are free to take any value without restriction and do not contribute to electromagnetic scattering; for $R_1 < r' < R_2$

$$\varepsilon'_{r'} = \mu'_{r'} = \frac{R_2}{R_2 - R_1}\frac{(r' - R_1)^2}{r'},\ \varepsilon'_{\theta'} = \mu'_{\theta'} = \frac{R_2}{R_2 - R_1},\ \varepsilon'_{\phi'} = \mu'_{\phi'} = \frac{R_2}{R_2 - R_1}; \quad (2.8)$$

for $r' > R_2$

$$\varepsilon'_{r'} = \mu'_{r'} = \varepsilon'_{\theta'} = \mu'_{\theta'} = \varepsilon'_{\phi'} = \mu'_{\phi'} = 1, \quad (2.9)$$

which is the free space environment. At the outer boundary of the cloak ($r' = R_2$), we observe that

$$\varepsilon'_{\theta'} = \varepsilon'_{\phi'} = 1/\varepsilon'_{r'},\ \mu'_{\theta'} = \mu'_{\phi'} = 1/\mu'_{r'}, \quad (2.10)$$

which are the conditions for a perfectly matched layer (PML). So theoretically the cloak is reflectionless to the surroundings and the electromagnetic fields are continuous.

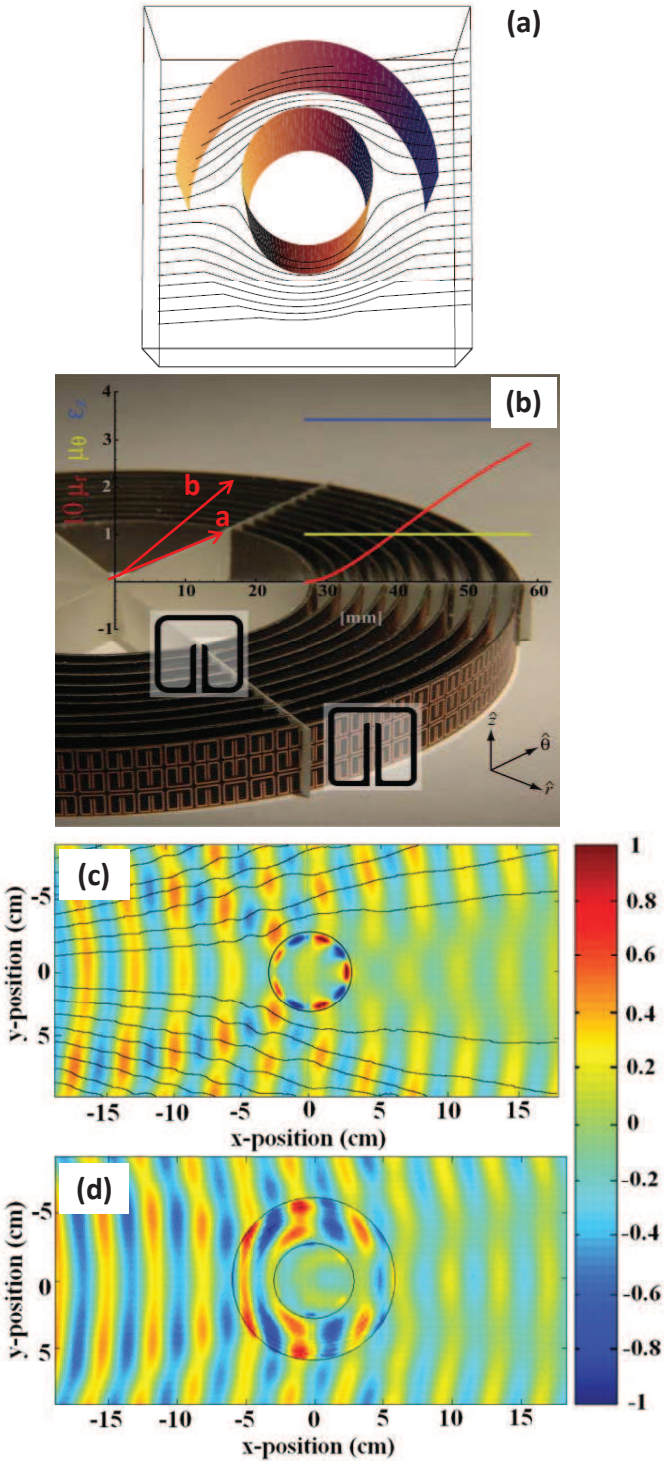

Figure 2.3: Experimental demonstration of the first 2D cloak at microwave frequencies. (a) Top view of waves traversing a cylindrical cloak. Waves are guided to avoid touching the inner cylinder [9]. (b) The cloak with a plot of the material parameters that are implemented. The fields shown are (c) the experimental measurement of a bare conducting cylinder and (d) the experimental measurement of the cloaked conducting cylinder. [10]

A few months after the theoretical proposals, the first cloaking device was experimentally demonstrated at microwave frequencies by Schurig *et al.* [10]. They practically realised the concealing function from a cylindrical cloak, which is easier for fabrication and measurement than a spherical one. Using a similar analytical procedure, permittivity and permeability of the cylindrical cloak can be computed in cylindrical coordinates (r', θ', z') as

$$\varepsilon'_{z'} = (\frac{b}{b-a})^2,\ \mu'_{r'} = (\frac{r'-a}{r'})^2,\ \mu'_{\theta'} = 1. \tag{2.11}$$

a and b are defined in Fig. 2.3(b) and transformation media fill in the cloaking region where $a < r' < b$. The cylindrical cloak is a two-dimensional (2D) device in nature, and it works when the electric field is polarized along the cylinder axis. The cloak was constructed with an artificially structured split-ring resonator (SRR) array, as plotted in Fig. 2.3(b), and was measured in a parallel-plate waveguide at the X-band (8 to 12 GHz) [11]. The fields in Fig. 2.3(c) and (d) have proved that the cloak decreases scattering from the hidden object while at the same time reducing its shadow, so that the cloak and object combined begin to resemble empty space.

In the early stage, cloaking devices were devoted to cylindrical or spherical cloaks because they were relatively easy to analyse and realise [6, 10, 12, 13]. However, they are not always efficient at concealing arbitrarily shaped objects. As a consequence, cloaking devices with different shapes have been invented afterwards [14–18]. Furthermore, the invisibility of cloak has been developed for other region of the electromagnetic spectrum, such as the optical frequency and the terahertz frequency [13, 19, 20].

2.3.2 Other transformation devices

Aside from cloaking devices, the coordinate transformation also serves for creating novel functional devices by engineering the electromagnetic propagation environments. A plenty of devices have been proposed and designed for practical applications [17, 21–

27]. Here, we discuss the design of three devices for demonstrating purpose: a planar reflector [28], a flattened convex lens [29], and a flattened absorber. These devices will be re-designed in Chapters 3 and 6 using a technique called the "discrete coordinate transformation", which will be introduced in the next section. To distinguish the two coordinate transformation (CT) techniques, the above studied CT is termed as the "analytical coordinate transformation (ACT)" onwards because it is an analytical method based on Maxwell's equations; and the CT to be studied in Section 2.4 is termed as the "discrete coordinate transformation (DCT)". Devices designed using these two techniques will be compared for their properties in Chapter 5.

2.3.2.1 A planar reflector [28]

A low-profile planar focusing antenna can be achieved based on the transformation of a parabolic reflector antenna in [28]. The red curve in Fig. 2.4(a) illustrates the parabolic shape of a metallic surface which works as a reflector antenna. The equation describing the shape in the $x-y$ plane is

$$y^2 = 2p(x+a). \tag{2.12}$$

Fig. 2.4(b) shows the planar reflector in the physical space. The curved profile in (a) is transformed into a planar area between the red line and the y' axis. This area is filled with transformation media, and is expected to maintain the same electromagnetic properties as the parabolic reflector. The relation between the parabolic shape and the planar shape is

$$x' = \frac{2pdx}{2pa - y^2},\ y' = y,\ z' = z. \tag{2.13}$$

The Jacobian transformation matrix between the two coordinate systems can be

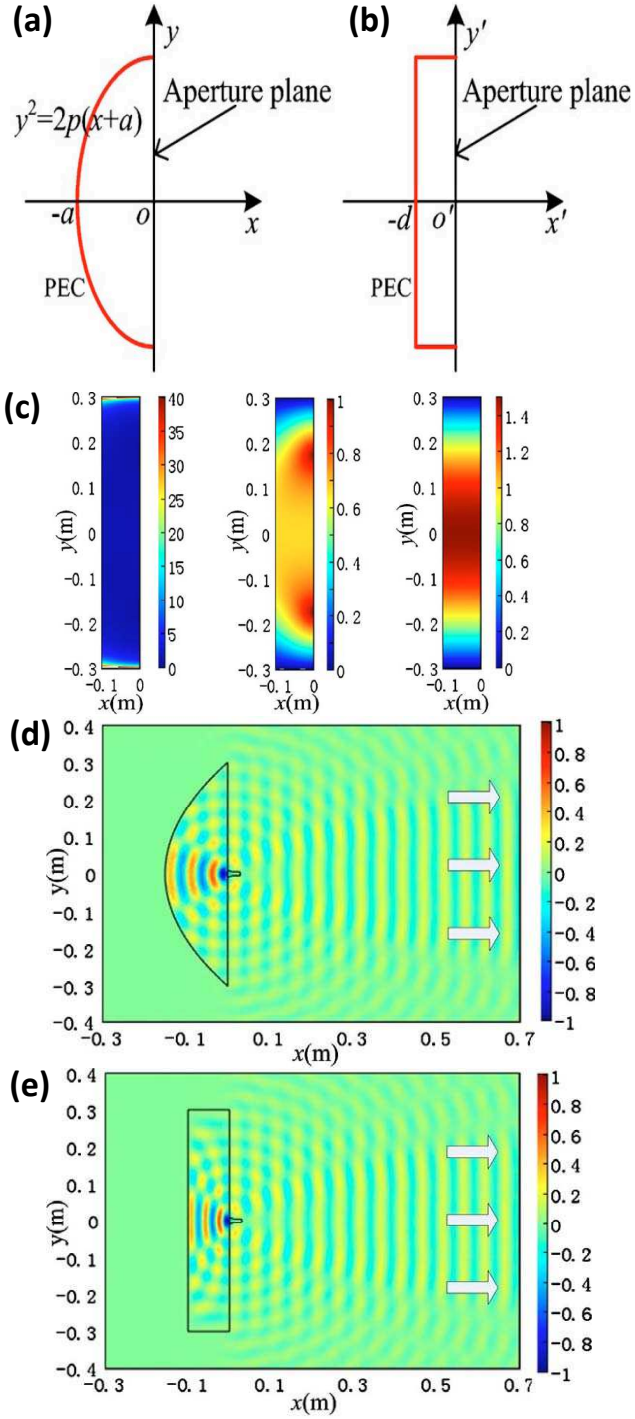

Figure 2.4: Transformation from a parabolic reflector to a planar one [28]. (a) The parabolic reflector in the virtual space (section view). (b) The planar reflector in the physical space. (c) The parameter maps of the planar reflector for z-polarized TE wave. They are μ'_u, μ'_v and ε'_z from left to right. (d) E_z distribution when the parabolic reflector is fed by a horn antenna. (e) E_z distribution when the planar reflector is fed by a horn antenna. The arrows indicate the propagating direction of TE waves.

presented according to Eq. (2.6) as

$$\bar{\bar{J}} = \begin{pmatrix} \frac{2pd}{2pa-y^2} & \frac{4pdxy}{(2pa-y^2)^2} & 0 \\ 0 & 1 & 0 \\ 0 & 0 & 1 \end{pmatrix}. \tag{2.14}$$

The relative permittivity and the relative permeability tensors of the transformation media in the planar area can be calculated by using Eq. (2.4) as

$$\bar{\bar{\varepsilon}}' = \bar{\bar{\mu}}' = \begin{pmatrix} \frac{2(p^2d^2+x'^2y'^2)}{pd(2pa-y'^2)} & \frac{x'y'}{pd} & 0 \\ \frac{x'y'}{pd} & \frac{2pa-y'^2}{2pd} & 0 \\ 0 & 0 & \frac{2pa-y'^2}{2pd} \end{pmatrix}. \tag{2.15}$$

It is noted that the permittivity and permeability tensors in Eq. (2.15) are non-diagonal. However, due to the symmetry of the tensors, there always exists a coordinate transformation that can transform the permittivity and permeability tensors into diagonal ones. This diagonalization corresponds physically to a rotation of the coordinate system. In this case a rotation in the $x' - y'$ plane with respect to the z axis is applicable, and in the new principle coordinate system (u, v, z), the relative permittivity and the relative permeability tensors can be expressed using the eigenvalues of the tensors as

$$\bar{\bar{\varepsilon}}' = diag\left(\varepsilon'_u, \varepsilon'_v, \varepsilon'_z\right), \tag{2.16}$$

$$\bar{\bar{\mu}}' = diag\left(\mu'_u, \mu'_v, \mu'_z\right). \tag{2.17}$$

The rotation between the coordinate systems (x', y') and (u, v) is defined by

$$\begin{pmatrix} cos\theta & -sin\theta \\ sin\theta & cos\theta \end{pmatrix} \begin{pmatrix} \varepsilon'_u & 0 \\ 0 & \varepsilon'_v \end{pmatrix} \begin{pmatrix} cos\theta & sin\theta \\ -sin\theta & cos\theta \end{pmatrix} = \tag{2.18}$$

$$\begin{pmatrix} \frac{2(p^2d^2+x'^2y'^2)}{pd(2pa-y'^2)} & \frac{x'y'}{pd} \\ \frac{x'y'}{pd} & \frac{2pa-y'^2}{2pd} \end{pmatrix} \equiv \begin{pmatrix} \varepsilon'_{xx} & \varepsilon'_{xy} \\ \varepsilon'_{yx} & \varepsilon'_{yy} \end{pmatrix}, \tag{2.19}$$

where θ is the rotation angle. Therefore,

$$\varepsilon'_{yy} - \varepsilon'_{xx} = (\varepsilon'_v - \varepsilon'_u)\cos 2\theta, \tag{2.20}$$

and

$$\varepsilon'_{xy} = \varepsilon'_{yx} = \frac{1}{2}(\varepsilon'_u - \varepsilon'_v)\sin 2\theta. \tag{2.21}$$

Combining Eq. (2.20) and Eq. (2.21), the rotation angle can be defined as

$$\theta = \frac{1}{2}\arctan(\frac{2\varepsilon'_{xy}}{\varepsilon'_{xx} - \varepsilon'_{yy}}). \tag{2.22}$$

After the diagonalization, the relative permittivity and the relative permeability tensors are in the form of

$$\bar{\bar{\varepsilon}}' = \bar{\bar{\mu}}' = diag\left(\frac{A + \sqrt{A^2 - (4dpB)^2}}{4pdB},\ \frac{A - \sqrt{A^2 - (4dpB)^2}}{4pdB},\ \frac{B}{2pd}\right) \tag{2.23}$$

in the (u, v, z) coordinate system, where

$$A = (2pa - y'^2)^2 + 4(p^2d^2 + x'^2y'^2),\ B = 2pa - y'^2. \tag{2.24}$$

Fig. 2.4(c) plots the relative permittivity and the relative permeability maps of the

planar reflector for the z-polarized TE wave (with H_u, H_v and E_z components). The dimensions defined in Fig. 2.4(a) are chosen as $d = 0.1\ m$, $p = 0.3\ m$ and $a = 0.15\ m$. Fig. 2.4(c) shows that the values of μ'_v and ε'_z range from 0 to 1 and from 0 to 1.5 respectively. However, μ'_u has an infinite value at the two corners. In other area except the special corners, μ'_u has a value below 40. Figure (c) indicates one property of the planar reflector, that the transformation media are anisotropic and inhomogeneous, requiring spatially dispersive permittivity and permeability simultaneously. Although carefully designed metamaterials are capable of achieving the required parameters, the fabrication is always challenging and complicated.

Fig. 2.4(d) and (e) are the simulated results when the reflectors are fed by a horn antenna at the focal point. The real part of the electric field is plotted and similar plane waves are observed applying both two reflectors. Therefore, qualitively, the planar reflector is proved to be as functional as a parabolic reflector to transform a cylindrical wave from a horn antenna to a plane wave in 2D circumstances. In Chapter 3, another planar reflector will be designed using the DCT technique. It has similar performance as this one, but is constructed of dielectrics.

Additionally, in Section 2.3.1, we mentioned that the coordinate transformation of cloaking devices has an important property, which is, the physical space and the virtual space should have the same boundaries. Under this condition, the physical space can exactly mimic the virtual space. However, in the above reflector design, the physical space does not maintain the boundaries of the virtual space. For example, the PEC boundaries in Fig. 2.4(a) and Fig. 2.4(b) are different. However, the planar reflector does work very well. This is due to the fact that the PEC boundaries in both the virtual space and the physical space are non-transparent, where no electromagnetic wave can propagate through. As a result, no impedance mismatching happens on the boundaries between the physical/virtual space and the surroundings. In other words, though with different shapes, the PEC boundary in the physical space and the one in the virtual space nevertheless perform in the same manner.

2.3.2.2 Lens compression

Here we discuss another scheme to compress devices [29], and design a flattened convex lens as an example. Instead of merely transforming the profile of a device, the coordinate transformation can compress a region of space, and consequently results in an overall decrease in the thickness of the device. Fig. 2.5(a) plots the two-dimensional view of a free space in (x, y) coordinate system. A convex lens is embedded in the grey region with its optical axis in the x direction. To achieve lens flattening, we consider a transformation that compress the space in the x direction (see Fig. 2.5(b)). A simple form for the element of the Jacobian matrix between the two spaces before and after transformation is [29]

$$\frac{dx'}{dx} = \begin{cases} a, & l_1 < x < l_2 \\ 1, & x \leq l_1 \ \cup \ x \geq l_2, \end{cases} \tag{2.25}$$

where l_1 and l_2 are the bounds of the grey region noted in Fig. 2.5(a), and a is the compression factor. This expression can be integrated to determine the relation between

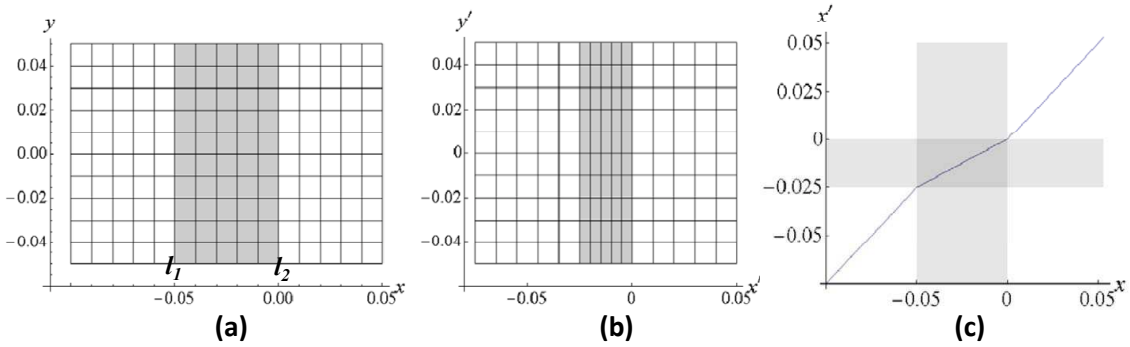

Figure 2.5: Plots of the spaces (a) before and (b) after the coordinate transformation. The grey region in (a) is compressed in (b) by a factor a. (c) Plot of x' versus x when $a = 0.5$. [29]

two coordinate systems as [29]

$$x'(x) = \begin{cases} ax + c, & l_1 < x < l_2 \\ l'_1 + (x - l_1), & x \leq l_1 \\ l'_2 + (x - l_2), & x \geq l_2. \end{cases} \tag{2.26}$$

Because the space is only compressed in x direction, $y'(y) = y$ and $z'(z) = z$ always exist. For the convenience of calculation, l_2 is chosen to be 0, so that $x = 0$ maps to $x' = 0$. Eq. (2.4) is used again to find the relative permittivity and the relative permeability tensors as [29]

$$\bar{\bar{\varepsilon}}' = \begin{pmatrix} a & 0 & 0 \\ 0 & 1/a & 0 \\ 0 & 0 & 1/a \end{pmatrix} n(x,y)^2, \quad \bar{\bar{\mu}}' = \begin{pmatrix} a & 0 & 0 \\ 0 & 1/a & 0 \\ 0 & 0 & 1/a \end{pmatrix}. \tag{2.27}$$

Transformation media filled in the compressed space is decided by the above equations. Here we assume the index of refraction $n(x, y)$ occurs via an electric response, with $n = \varepsilon^{1/2}$. This assumption is applicable for dielectric devices such as a convex lens. It is also observed that the permittivity value in Eq. (2.27) is dependent on position. In the grey region, the compression factor a is less than unity, and the dielectric property of the original device must be transformed in addition to the air surrounding it. Outside the grey region, $a = 1$ and $n(x, y) = 1$ always exist.

Next, a dielectric convex lens is compressed using this transformation scheme. Fig. 2.6(a) plots the dimensions of the original lens. It is made of isotropic homogeneous dielectric with $\varepsilon_r = 3$. The aperture L is 160 mm, and the radius of the two arcs are 300 mm. The maximum thickness D is 45.6 mm and the minimum thickness T is 23.8 mm. This convex lens is exactly the same as the one that we will re-design in Chapter 3 for the sake of fair comparison.

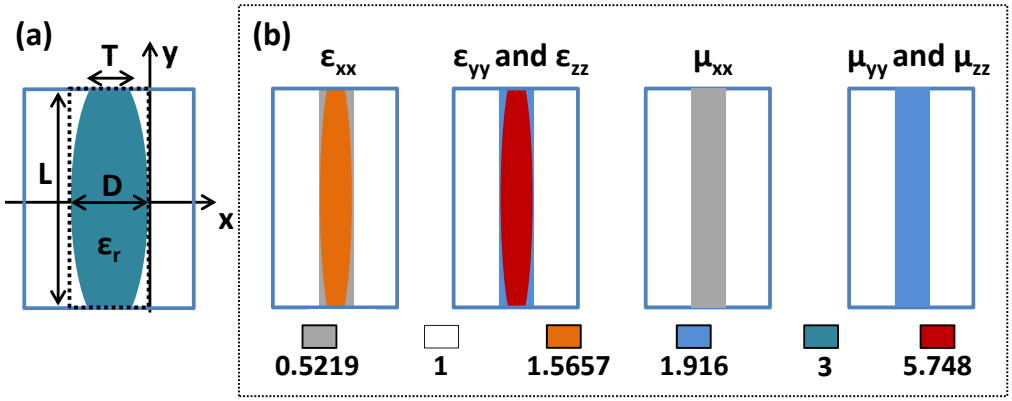

Figure 2.6: (a) Dimensions of the convex lens. (b) The relative permittivity and the relative permeability maps of the transformation lens. The colored blocks represent relative permittivity/permeability values.

To compress the maximum thickness from 45.6 mm to 23.8 mm, the compression factor a is chosen to be 0.5219 (= 23.8/45.6). Accordingly the relative permittivity and the relative permeability tensors in the compressed region become

$$\bar{\bar{\varepsilon}}' = 3 \times \begin{pmatrix} 0.5219 & 0 & 0 \\ 0 & 1.9160 & 0 \\ 0 & 0 & 1.9160 \end{pmatrix}, \quad \bar{\bar{\mu}}' = \begin{pmatrix} 0.5219 & 0 & 0 \\ 0 & 1.9160 & 0 \\ 0 & 0 & 1.9160 \end{pmatrix} \tag{2.28}$$

within the area of the lens; and

$$\bar{\bar{\varepsilon}}' = \begin{pmatrix} 0.5219 & 0 & 0 \\ 0 & 1.9160 & 0 \\ 0 & 0 & 1.9160 \end{pmatrix}, \quad \bar{\bar{\mu}}' = \begin{pmatrix} 0.5219 & 0 & 0 \\ 0 & 1.9160 & 0 \\ 0 & 0 & 1.9160 \end{pmatrix} \tag{2.29}$$

in the area surrounding the lens. Outside the compressed region, it's the free space as before. Fig. 2.6(b) shows the relative permittivity and the relative permeability maps of the compressed lens. Clearly, the total thickness of the lens is reduced to about half the original value.

It is noticed that the transformation media required by Eqs. (2.23), (2.28) and (2.29)

are anisotropic, and have relative permittivity and relative permeability with less-than-unity values. This is a feature property of the ACT based devices. In view of this fact, metamaterials composed of resonators are widely used in transformation devices because they can flexibly provide anisotropic parameters and less-than-unity values. We will discuss the adoption of resonator arrays in Chapters 4 and 5. However, they are usually narrow-band because of their resonant nature, hence are not suitable for broadband devices. Since achieving realisable transformation devices is the main target in this PhD work, we will show in Chapter 3 that by using the DCT technique, this convex lens can be efficiently flattened to half the thickness, while is only constructed of dielectrics.

2.3.2.3 Absorber compression

In this sub-section, another device, the pyramidal absorber, is compressed using a similar procedure as described above.

The electromagnetic absorbing materials have been successfully applied in anechoic chambers to eliminate backwall reflections, and therefore ensure the accuracy of indoor measurements. Below 1 GHz, ferrite tile absorbers have proven to show good performance with only a few millimeters thickness [30]. For microwave measurements, the pyramidal absorbers can provide good absorption over a broad bandwidth. The pyrami-

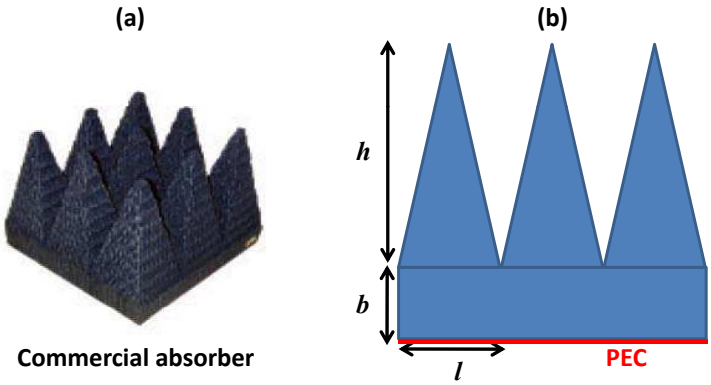

Figure 2.7: Model of a pyramidal absorber. (a) Geometry of a 3 ×3 microwave pyramidal absorber unit from TDK corporation [32]. (b) Dimensions of the pyramidal absorber (section view).

dal absorbers are commonly composed of dielectric materials like carbon-embedded urethane or polystyrol foam. In the literature, magnetic materials have been also employed to reduce the thickness of the pyramidal absorber [30, 31].

Fig. 2.7(a) is the model of a microwave pyramidal absorber provided by the TDK Corporation [32]. Figure (b) marks three dimensions: the height of the pyramid h, the thickness of the base b, and the size of one unit pyramid l. The perfect electric conductor (PEC) surface represents the chamber's wall. The height h is the key dimension because it decides the operating frequency of the pyramidal absorber. It should be no less than one-fourth a wavelength at the lowest operating frequency so as to guarantee low reflectivity [33]. A problem arises accordingly: the absorbers can be very high and heavy, restricting its use to small chambers and causing problems in implementation along vertical walls.

To reduce the height of a pyramidal absorber, the ACT again serves to compress the space where the absorber is embedded. Fig. 2.8 describes how the compression is carried out. Taking a similar procedure as that in Section 2.3.2.2, the height of the pyramidal absorber (h) is divided by a factor k. The permittivity and the permeability tensors in

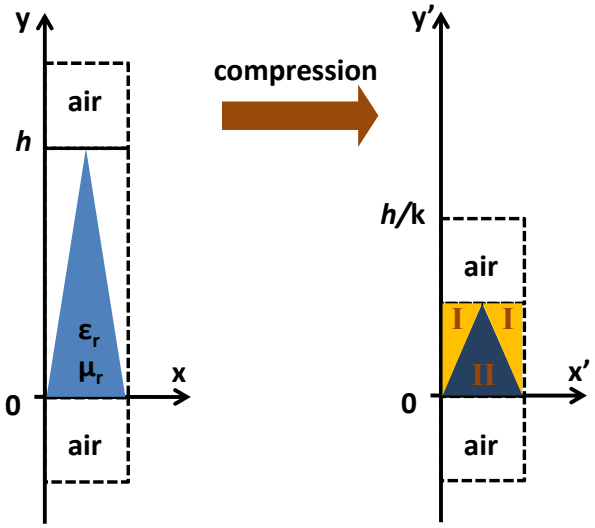

Figure 2.8: The pyramidal absorber before and after the coordinate transformation.

the compressed region can be written as

$$\bar{\bar{\varepsilon}}' = \begin{pmatrix} 1/k & 0 & 0 \\ 0 & k & 0 \\ 0 & 0 & k \end{pmatrix} \varepsilon(x,y), \quad \bar{\bar{\mu}}' = \begin{pmatrix} 1/k & 0 & 0 \\ 0 & k & 0 \\ 0 & 0 & k \end{pmatrix} \mu(x,y). \tag{2.30}$$

It is noted that in Region **I** (defined in Fig. 2.8) the permittivity $\varepsilon(x,y)$ and the permeability $\mu(x,y)$ in Eq. (2.30) are ε_0 and μ_0 respectively, whilst in Region **II** they are ε_r and μ_r. If the pyramidal absorber is made of non-magnetic materials, $\mu_r = \mu_0$. If the absorber material is lossy, ε_r and μ_r have complex values. In contrast, in Chapter 6 we will apply an all dielectric approach to compress the pyramidal absorber by using the DCT technique.

2.4 Discrete Coordinate Transformation

2.4.1 The carpet cloak

The fundamental theory of the coordinate transformation and the "cloak of invisibility" have been discussed in previous sections. However, the theoretically fantastic cloak can never be perfect in practice. One big challenge is, usually there are some singular points in the physical space. For example, in the spherical cloak shown in Fig. 2.2, when the virtual space $r < R_2$ is transformed to the physical space $R_1 < r' < R_2$, the center point is mapped to a sphere on the inner boundary. This means the parameters of transformation media can achieve infinite values (0 in this case) on the sphere of $r' = R_1$. This property is extremely difficult to be realised by existing materials or even artificial materials. Although carefully designed metamaterials are able to approach infinite values, in practice they exhibit extremely narrow band and potentially large reflections. In addition, the transformation media usually have isotropic and inhomogeneous permittivity

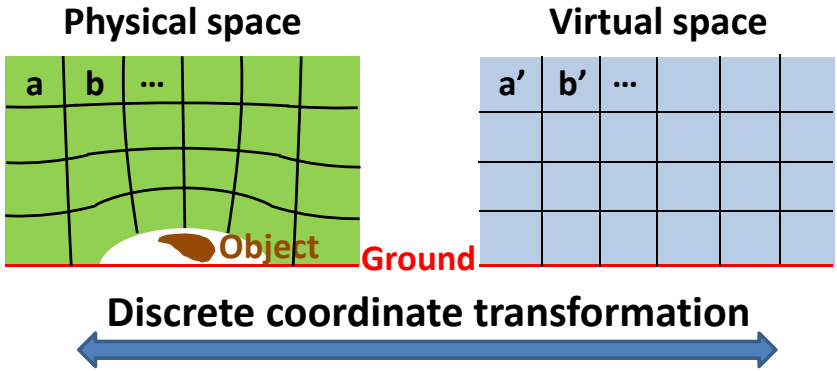

Figure 2.9: Carpet cloak design using the discrete coordinate transformation. The transformation is operated between each pair of the local coordinate system in the physical space and the virtual space (e.g., a and a', b and b').

and permeability, as indicated in Eqs. (2.23), (2.27) and (2.30).

The discrete coordinate transformation (DCT) is therefore proposed to circumvent these problems [34]. Instead of using the analytical coordinate transformation (ACT) as discussed before, both the virtual space and the physical space are discretised and described with local coordinates. Fig. 2.9 shows the design of a carpet cloak. The DCT technique is applied to map the physical space including an object on the ground plane (see the left figure) to a virtual space without any object (see the right figure). Instead of using global coordinates, the two spaces are described with orthogonal local coordinates. The transformation is then carried out between one local coordinate system in the virtual space and its corresponding peer in the physical space. Because the ground-plane carpet cloak requires significantly less bending and distortion of the incident waves, due to the presence of the ground plane, a proper grid can be generated in the physical space containing near-orthogonal local coordinates. As demonstrated in [34], the carpet cloak can be constructed with conventional isotropic dielectrics instead of resonant metamaterials, and consequently overcomes the disadvantage of its narrow-band performance. Experimental validations of the carpet cloak have been done using low-loss and non-resonant metamaterials at microwave frequencies [35] (see Fig. 2.10) and at optical frequencies [36, 37].

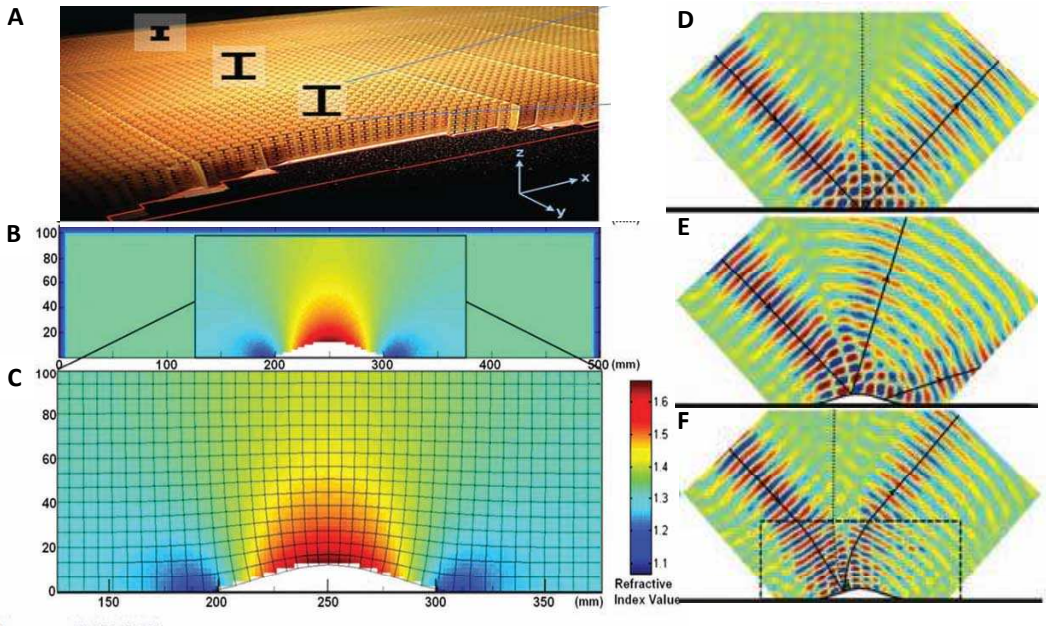

Figure 2.10: The experimental verification of the carpet cloak. (a) The fabricated metamaterial sample. (b) Refractive index distribution. (c) Expanded view of the transformation region. (d) Collimated beam incident on the ground plane at 14 GHz. (e) Collimated beam incident on the bare perturbation on the ground plane at 14 GHz. (f) Collimated beam incident on the cloaked perturbation at 14 GHz. [35]

2.4.2 Discrete coordinate transformation for device design

For the reason that the coordinate transformation is inversible, there are many underlying applications other than the carpet cloak. Instead of using a physical space with distorted coordinate systems to mimic a virtual space with orthogonal coordinate systems, we use a physical space with orthogonal coordinate systems to mimic a virtual space with distorted coordinate systems, so as to obtain specific functions. For example, in antenna systems, many widely used devices have curved surfaces, such as parabolic reflectors and convex lenses. Using the discrete coordinate transformation, we can design equivalent devices that operate in the same manner but have flexible profiles. In the virtual space perceived by the electromagnetic waves, those devices have curved surfaces, contain homogeneous and isotropic materials, and can be described with distorted coordinate systems. By using appropriate transformations, these distorted coordinate systems are mapped to the physical space, where the devices possess flat surfaces, contain spatially dispersive but isotropic materials, and are represented in new coordinate systems, for example, the

Cartesian coordinate system.

Next we will demonstrate that generating nearly isotropic transformation media in the physical space is possible in general whenever the physical space and the virtual space have no strongly-curved boundaries. For illustrative purpose we show here an example of designing a flat reflector. In the virtual space, a metallic parabolic reflector is placed in the free space, represented as the PEC surface in Fig. 2.11(a). In the physical space shown in Fig. 2.11(b), there is a flat PEC surface covered by transformation media instead. The two spaces have the same boundaries to the air. Their "South" boundaries (defined in Fig. 2.11) are different because the PEC surfaces are different.

The geometry of the parabolic surface is given in Fig. 2.12, where

$$R = \frac{2F}{1+\cos\theta}. \tag{2.31}$$

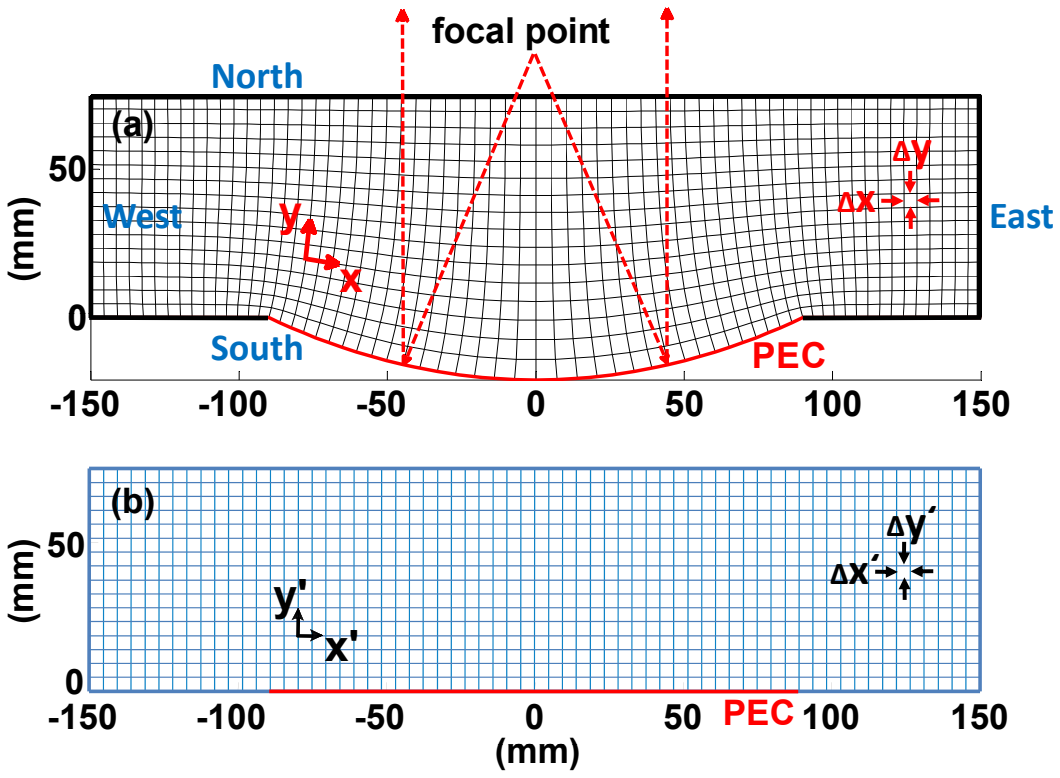

Figure 2.11: (Section view) (a) The virtual space with distorted coordinates. A parabolic reflector is placed in the free space, as illustrated by the red curve. (b) The physical space with orthogonal coordinates. The parabolic reflector is replaced with a flat PEC surface.

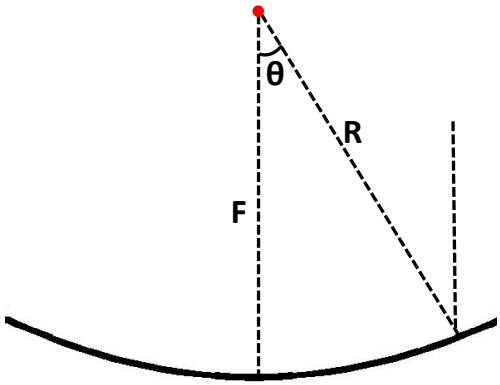

Figure 2.12: The geometry of the parabolic surface.

The focal length F is set to be 108.6 mm and the angle θ ranges from -45^o to 45^o. Accordingly, the aperture of the parabolic surface is 180 mm. It is noted that in Fig. 2.11 the focal point is outside of the transformation region, hence, in the physical space, a source at the focal point is not embedded in the transformation media.

Both spaces are discretised into small cells, and in each cell there is a set of local coordinates to be applied in the discrete coordinate transformation. According to the Nyquist - Shannon Sampling Theorem [38], when converting a signal from a continuous space into a discrete space, to fully reconstruct the signal, the sampling rate should be no less than twice the maximum operating frequency. In other words, in the discretised space, the dimension of each cell should be less than half the wavelength inside the media. This statement will be examined in detail in Section 5.3. In this case, the reflector is designed to operate at the X-Band (8-12 GHz), and, therefore, the size of a cell ought to be less than 12.5 mm. In addition, since the local coordinates are chosen to be orthogonal in the distorted space, the parabolic boundary in Fig. 2.11(a) should be divided into small segments to ensure a smooth transition of each cell. In the spaces illustrated in Fig. 2.11, the size of each cell is set to be about 5 mm, which is approximately 1/5 wavelength at 12 GHz.

A software called "GenGrid" [39] is utilised to generate a near-orthogonal grid consisting of quadrilateral cells in the distorted space. The procedure of generating the grid

is described here briefly. In Fig. 2.11, points are evenly located on the "North", "West" and "East" boundaries in both the virtual space and the physical space. However, on the "South" boundary of the virtual space, points on the parabolic curve are distributed following a "Hyperbolic Sine" stretching function. The software provides partial differential equation (PDE) methods for generating a structured grid under the guidelines of smoothness, clustering and orthogonality [40]. A hyperbolic PDE method is chosen to initially create a structured grid. The "Laplace control function" is then employed to provide control over the quality of all cells. The "Laplace control function" is especially suitable to achieve a smooth transition of the size of each cell, which consequently leads to low reflections throughout the physical space. Iterative solution procedure is repeated until certain criteria are met. In this reflector design, for example, the error limit is set to be $1e^{-5}$, and the maximum number of iteration is 2000. Once the error limit is met, the iterative solution procedure stops and a smooth near-orthogonal grid is generated. Fig. 2.14 shows later that the orthogonal property of the grid is indeed obtained, indicating the transformation of coordinates is conformal [5].

Suppose that the coordinate transformation between the virtual space and the physical space is $x' = x'(x, y, z),\ y' = y'(x, y, z),\ z' = z'(x, y, z)$, where (x, y, z) are local coordinates in the virtual space and (x', y', z') are local coordinates in the physical space, as described in the grids in Fig. 2.11. For the convenience of reading, we re-write Eq. (2.4) here as

$$\bar{\bar{\varepsilon}}' = \frac{J\bar{\bar{\varepsilon}}J^T}{det(J)},\ \bar{\bar{\mu}}' = \frac{J\bar{\bar{\mu}}J^T}{det(J)}, \tag{2.32}$$

where

$$J = \begin{pmatrix} \frac{\partial x'}{\partial x} & \frac{\partial x'}{\partial y} & \frac{\partial x'}{\partial z} \\ \frac{\partial y'}{\partial x} & \frac{\partial y'}{\partial y} & \frac{\partial y'}{\partial z} \\ \frac{\partial z'}{\partial x} & \frac{\partial z'}{\partial y} & \frac{\partial z'}{\partial z} \end{pmatrix}. \tag{2.33}$$

Since the reflector is placed in the free space, the original permittivity and permeability tensors are

$$\begin{aligned} \bar{\bar{\epsilon}} &= \varepsilon_0 \mathbf{I}, \\ \bar{\bar{\mu}} &= \mu_0 \mathbf{I}, \end{aligned} \tag{2.34}$$

where $\mathbf{I}$ is the unitary matrix.

To simplify the problem, we now assume that the transformation is two-dimensional (2D), and thus the device is infinite in the z direction normal to the $x-y$ plane defined in Fig. 2.11. The bold reduction from three-dimension to two-dimension makes the design process much simpler. In practice, because many devices are symmetric, or work at a specified polarization, three-dimensional (3D) transformation devices can be obtained by rotating or extending 2D models to an axis. Examples will be presented in Section 5.3.

In the 2D case, the Jacobian matrix has a simpler form:

$$J = \begin{pmatrix} \frac{\partial x'}{\partial x} & \frac{\partial x'}{\partial y} & 0 \\ \frac{\partial y'}{\partial x} & \frac{\partial y'}{\partial y} & 0 \\ 0 & 0 & 1 \end{pmatrix}, \tag{2.35}$$

and Eq. (2.32) is explicitly written as

$$\bar{\bar{\varepsilon}}' = \frac{\varepsilon_0}{det(J)} \begin{pmatrix} (\frac{\partial x'}{\partial x})^2 + (\frac{\partial x'}{\partial y})^2 & \frac{\partial x'}{\partial x}\frac{\partial y'}{\partial x} + \frac{\partial x'}{\partial y}\frac{\partial y'}{\partial y} & 0 \\ \frac{\partial y'}{\partial x}\frac{\partial x'}{\partial x} + \frac{\partial x'}{\partial y}\frac{\partial y'}{\partial y} & (\frac{\partial y'}{\partial x})^2 + (\frac{\partial y'}{\partial y})^2 & 0 \\ 0 & 0 & 1 \end{pmatrix}, \tag{2.36}$$

$$\bar{\bar{\mu}}' = \frac{\mu_0}{det(J)} \begin{pmatrix} (\frac{\partial x'}{\partial x})^2 + (\frac{\partial x'}{\partial y})^2 & \frac{\partial x'}{\partial x}\frac{\partial y'}{\partial x} + \frac{\partial x'}{\partial y}\frac{\partial y'}{\partial y} & 0 \\ \frac{\partial y'}{\partial x}\frac{\partial x'}{\partial x} + \frac{\partial x'}{\partial y}\frac{\partial y'}{\partial y} & (\frac{\partial y'}{\partial x})^2 + (\frac{\partial y'}{\partial y})^2 & 0 \\ 0 & 0 & 1 \end{pmatrix}. \tag{2.37}$$

For an E-polarized incident wave (electric field along the z direction), only the components of μ_{xx}, μ_{xy}, μ_{yy}, μ_{yx} and ε_{zz} contribute, and the permittivity and the permeability become

$$\varepsilon'_z \equiv \varepsilon'_{zz} = \varepsilon_0 det(J)^{-1}, \tag{2.38}$$

$$\bar{\bar{\mu}}' = \frac{\mu_0}{det(J)} \begin{pmatrix} (\frac{\partial x'}{\partial x})^2 + (\frac{\partial x'}{\partial y})^2 & \frac{\partial x'}{\partial x}\frac{\partial y'}{\partial x} + \frac{\partial x'}{\partial y}\frac{\partial y'}{\partial y} \\ \frac{\partial y'}{\partial x}\frac{\partial x'}{\partial x} + \frac{\partial x'}{\partial y}\frac{\partial y'}{\partial y} & (\frac{\partial y'}{\partial x})^2 + (\frac{\partial y'}{\partial y})^2 \end{pmatrix}. \tag{2.39}$$

Instead of using the permittivity ε' and the permeability μ' to describe the transformation media in the physical space, we now use the anisotropy factor α and the averaged refractive index n', which have geometrical meanings in terms of the metric. The anisotropy factor is represented by the cell aspect ratio in the grids shown in Fig. 2.11. Since the grids in both the virtual space and the physical space are near-orthogonal ones consisting of quadrilateral cells, the anisotropy factor α can be approximately considered as 1.

On the other hand, the averaged refractive index n' is defined by [34]

$$n' = \sqrt{n'_L n'_T}, \tag{2.40}$$

where n'_L and n'_T are the principal values of the refractive index tensor of the transfor-

mation media, which can be defined from Eqs. (2.38) and (2.39) as

$$n'_L = n'_{xx} = \sqrt{\mu'_{yy}\varepsilon'_{zz}}/\sqrt{\varepsilon_0\mu_0} \tag{2.41}$$

and

$$n'_T = n'_{yy} = \sqrt{\mu'_{xx}\varepsilon'_{zz}}/\sqrt{\varepsilon_0\mu_0}. \tag{2.42}$$

Consequently, the averaged refractive index becomes

$$n'^2 = \sqrt{\mu'_{yy}\mu'_{xx}}\varepsilon'_z/(\varepsilon_0\mu_0). \tag{2.43}$$

Eq. (2.43) indicates that if $\mu'_{xx}\mu'_{yy} = \mu_0^2$, i.e. if there is no magnetic dependence, then the refractive index n', which determines the trace of the wave, can be realised by the permittivity alone, leading to an all-dielectric device. Next, we shall show that this condition is approximately satisfied if a certain grid is properly chosen in the coordinate transformation.

The explicit value of $\mu'_{xx}\mu'_{yy}$ from Eq. (2.39) is

$$\mu'_{xx}\mu'_{yy} = \mu_0^2 \frac{[(\frac{\partial x'}{\partial x})^2(\frac{\partial y'}{\partial x})^2 + (\frac{\partial x'}{\partial x})^2(\frac{\partial y'}{\partial y})^2 + (\frac{\partial x'}{\partial y})^2(\frac{\partial y'}{\partial x})^2 + (\frac{\partial x'}{\partial y})^2(\frac{\partial y'}{\partial y})^2]}{[(\frac{\partial x'}{\partial x})^2(\frac{\partial y'}{\partial y})^2 - 2\frac{\partial x'}{\partial x}\frac{\partial y'}{\partial y}\frac{\partial x'}{\partial y}\frac{\partial y'}{\partial x} + (\frac{\partial x'}{\partial y})^2(\frac{\partial y'}{\partial x})^2]}. \tag{2.44}$$

According to Eq. (2.44), the approximate condition $\mu'_{xx}\mu'_{yy} \simeq \mu_0^2$ is satisfied when at the same time

$$\frac{\partial x'}{\partial y} \simeq 0, \tag{2.45}$$

$$\frac{\partial y'}{\partial x} \simeq 0 \tag{2.46}$$

Since x' and y' are functions of both x and y, Eqs. (2.45) and (2.46) can be also written

using the chain rule as

$$\frac{\partial x'}{\partial y} = \frac{\partial x'}{\partial x}\frac{\partial x}{\partial y} \simeq 0, \tag{2.47}$$

$$\frac{\partial y'}{\partial x} = \frac{\partial y'}{\partial y}\frac{\partial y}{\partial x} \simeq 0. \tag{2.48}$$

However, the above condition can indeed be satisfied because we can generate a grid in the virtual space with near-orthogonal cells such that

$$\frac{\partial x}{\partial y} \simeq 0, \tag{2.49}$$

$$\frac{\partial y}{\partial x} \simeq 0. \tag{2.50}$$

To illustrate how this orthogonality restriction can be approximately satisfied, see for example the virtual space shown in Fig. 2.11(a). A sample distorted cell is drawn in Fig. 2.13, and the 2×2 covariant metric g is re-defined to characterise the distortion as [41–43]:

$$g = \begin{pmatrix} g_{11} & g_{12} \\ g_{21} & g_{22} \end{pmatrix}, \tag{2.51}$$

$$g_{i,j} = \vec{a}_i \cdot \vec{a}_j \quad (i, j = 1, 2). \tag{2.52}$$

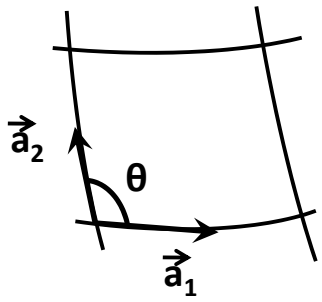

Figure 2.13: The covariant base vectors in a 2D distorted cell.

$\vec{a}_1$ and $\vec{a}_2$ are the covariant base vectors defined in Fig. 2.13, and θ is the angle between them. We quantify the orthogonality of the grid using the parameter θ for each cell, defined through

$$\cos\theta = \sqrt{\frac{g_{12}g_{21}}{g_{11}g_{22}}}. \tag{2.53}$$

The distribution of the angle parameter θ is plotted in Fig. 2.14 for the grid shown in Fig. 2.11(a). We observe that in most cells, θ is distributed around the 90^o point, with a much smaller exception further away from 90^o. We also measure from this plot a full width at half maximum (FWHM) index of the distribution, which is only 1^o, indicating that most of the local coordinates are near-orthogonal. Thus, for a perfectly orthogonal grid, g is a unit matrix, $\cos\theta = 0$, FWHM $= 0$, and ultimately $\mu'_{xx}\mu'_{yy} = \mu_0^2$. And even for a near-orthogonal grid such as the one in Fig. 2.11(a), these conditions can be approximately satisfied, yielding an all-dielectric device with very minor sacrifice in

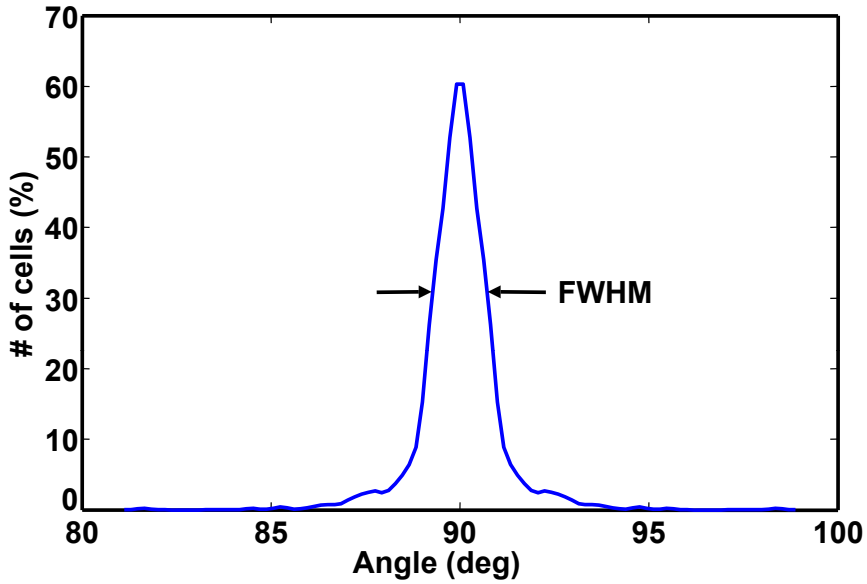

Figure 2.14: Distribution of the angle between two local coordinates in every cell of the virtual space. The orthogonal property is quantified by the full width at half maximum (FWHM) index. When the FWHM index is approaching zero, the local coordinates are near-orthogonal. In this case the index is only 1^o, indicating that most of the local coordinates are near-orthogonal.

performance.

Furthermore, the near-orthogonal property ensures an approximation of Eq. (2.39) that

$$\bar{\bar{\mu}}' = \frac{\mu_0}{det(J)} \begin{pmatrix} (\frac{\partial x'}{\partial x})^2 & 0 \\ 0 & (\frac{\partial y'}{\partial y})^2 \end{pmatrix}. \tag{2.54}$$

Because all cells are generated to be approximately square-shaped, μ'_{xx} and μ'_{yy} have very similar values which are close to the unity. Accordingly, the relative permeability of the device can be assumed to be isotropic and unity, and the effective relative refractive index in Eq. (2.43) is only dependent on ε'_z as

$$n'^2 \simeq \varepsilon'_z/\varepsilon_0 = \frac{1}{det(J)}. \tag{2.55}$$

Note that under the orthogonal condition of Eqs. (2.45) and (2.46), the refractive index profile of the device can be directly retrieved from each cell within the grid, using Eq. (2.35):

$$n'^2 \simeq \frac{1}{\frac{\partial x'}{\partial x}\frac{\partial y'}{\partial y}} \simeq \frac{\Delta x \Delta y}{\Delta x' \Delta y'}, \tag{2.56}$$

where $\Delta x, \Delta y, \Delta x', \Delta y'$ are the dimensions of cells in two spaces, as marked in Fig. 2.11.

For the case of H polarization, similar results are obtained. Now the contributing components of the permittivity and the permeability are ε_{xx}, ε_{xy}, ε_{yy}, ε_{yx} and μ_{zz} in Eqs. (2.36) and (2.37). Under the orthogonality criteria of Eqs. (2.45) and (2.46), the permittivity and the permeability tensors become

$$\bar{\bar{\varepsilon}}' = \frac{\varepsilon_0}{det(J)} \begin{pmatrix} (\frac{\partial x'}{\partial x})^2 & 0 \\ 0 & (\frac{\partial y'}{\partial y})^2 \end{pmatrix}, \mu'_z = \mu_0 det(J)^{-1}, \tag{2.57}$$

while $det(J) = \frac{\partial x'}{\partial x} \cdot \frac{\partial y'}{\partial y}$. The effective refractive index is now

$$n'^2 = n'_{xx} n'_{yy}/(\varepsilon_0 \mu_0) = \sqrt{\varepsilon'_{yy} \varepsilon'_{xx}} \mu'_z/(\varepsilon_0 \mu_0). \tag{2.58}$$

It can be easily checked that in this case $\varepsilon'_{xx} \varepsilon'_{yy} \simeq \varepsilon_0^2$, and thus the effective relative refractive index in this case is dependent on μ'_z only, similar to Eq. (2.55) as:

$$n'^2 \simeq \mu'_z/\mu_0 = \frac{1}{det(J)}. \tag{2.59}$$

The above analysis indicates that a properly selected magnetic material can control the H-polarized wave, similar to how a dielectric material can control the E-polarized wave. Thus the designer can generate a grid under the assumptions specified in this section, calculate the refractive index distribution from Eq. (2.56), and choose to tune either ε or μ to operate using E-polarization or H-polarization respectively.

2.5 Summary

The technique of coordinate transformation was studied in this chapter. It is used to transform one space into another, while retaining electromagnetic properties, thanks to the form invariance of Maxwell's equations. An important application of this technique is to design specific transformation media so as to control the propagation characteristics of electromagnetic waves. A notable example is the "cloak of invisibility", which makes an object undetectable. The properties of transformation media are usually exotic, possessing anisotropic parameters (permittivity or permeability) with less-than-unit values, and therefore, resonant metamaterials are commonly required. However, the discrete coordinate transformation offers the possibility to create all dielectric transformation media, and consequently leads to devices with several important advantages such as the broadband performance. The transformation is applied to local coordinates in discretised spaces, and each element cell is mapped from one space to the other. Whenever the

local coordinates are near-orthogonal, the physical space can be realised with isotropic dielectrics. The discrete coordinate transformation is inversible between a general Cartesian space and a distorted space, leading to more potential applications in addition to the carpet cloaks.

Based on the study in this chapter, differences between the analytical coordinate transformation (ACT) and the discrete coordinate transformation (DCT) can be summarised here: Firstly, the ACT method essentially relies on the mathematical expression for the geometry of the transformation space, therefore is competent for coordinate transformations including only standard-shaped boundaries. In contrast, the DCT method is applicable for coordinate transformations including arbitrarily-shaped boundaries, as no mathematical expressions are needed. Secondly, the ACT method is applied in global coordinate systems, whilst the DCT method is applied in local coordinate systems. As a result, the ACT method usually leads to a more complicated Jacobian transformation matrix compared to the DCT method. Thirdly, transformation media decided by the ACT method usually have anisotropic permittivities and permeabilities, and sometimes require extreme values which approach the infinity. These properties may cause problems in practical realisation. The DCT technique also produces transformation media with anisotropic permittivities and permeabilities, but under certain orthogonal conditions which are pretty achievable in a structured grid, the transformation media can be approximately isotropic. In addition, no extreme values of permittivities or permeabilities are required. Due to these properties, the DCT based designs are much easier to realise than the ACT based ones.

Two schemes of applying the discrete coordinate transformation will be discussed in the following chapters. First, the transformation is carried out between a distorted virtual space and a Cartesian physical space, an alternative approach to the design of a carpet cloak. Devices with curved boundaries, such as parabolic reflectors and convex lenses, are placed in the distorted virtual space. Their transformed peers in the physical space will obtain flat profiles. Designs of flat reflectors and flat lenses will be

presented in Chapter 3. The second scheme is to create a non-existing space which has novel electromagnetic performance. The distorted space is generated based on the propagating paths of the wave, and serves as a device with designed electromagnetic functions. An undetectable antenna incooperating the carpet cloak, and a broadband extraordinary transmission device will be proposed and tested in Chapter 4 as examples. In addition, in Chapter 6, a multiple discrete coordinate transformation will be proposed and demonstrated as an extension to the one-step discrete coordinate transformation.

References

[1] L. S. Dolin, "On a possibility of comparing three-dimensional electromagnetic systems with inhomogeneous filling," *Izv. Vyssh. Uchebn. Zaved. Radiofiz*, vol. 4, pp. 964–7, 1961.

[2] E. G. Post, *Formal Structure of Electromagnetics; General Covariance and Electromagnetics*. New York: Interscience, 1962.

[3] M. Lax and D. F. Nelson, "Maxwell equations in material form," *Phys. Rev. B*, vol. 13, p. 1777, 1976.

[4] A. J. Ward and J. B. Pendry, "Refraction and geometry in Maxwell's equations," *J. Mod. Opt*, vol. 43, no. 4, pp. 773–793, 1996.

[5] U. Leonhardt, "Optical conformal mapping," *Science*, vol. 312, pp. 1777–1780, 2006.

[6] J. B. Pendry, D. Schurig, and D. R. Smith, "Controlling electromagnetic fields," *Science*, vol. 312, pp. 1780–1782, 2006.

[7] A. V. Kildishev, W. Cai, U. K. Chettiar, and V. M. Shalaev, "Transformation optics: approaching broadband electromagnetic cloaking," *New J. of Phys.*, vol. 10, p. 115029, 2008.

[8] W. X. Jiang and T. J. Cui, "Optical transformation theory," in *Metamaterials: Theory, Design, and Applications*, T. J. Cui, R. P. Liu, and D. R. Smith, Eds. Springer, 2010, ch. 2, pp. 21–48.

[9] D. Schurig, J. B. Pendry, and D. R. Smith, "Calculation of material properties and ray tracing in transformation media," *Opt. Express*, vol. 14, no. 21, pp. 9794–9804, 2006.

[10] D. Schurig, J. J. Mock, B. J. Justice, S. A. Cummer, J. B. Pendry, A. F. Starr, and D. R. Smith, "Metamaterial electromagnetic cloak at microwave frequencies," *Science*, vol. 314, p. 977980, 2006.

[11] B. Justice, J. Mock, L. Guo, A. Degiron, D. Schurig, and D. Smith, "Spatial mapping of the internal and external electromagnetic fields of negative index metamaterials," *Opt. Express*, vol. 14, no. 19, pp. 8694–8705, 2006.

[12] S. A. Cummer, B.-I. Popa, D. Schurig, D. R. Smith, and J. B. Pendry, "Full-wave simulations of electromagnetic cloaking structures," *Phys. Rev. E*, vol. 74, p. 036621, 2006.

[13] W. Cai, U. Chettiar, A. Kildishev, and V. Shalaev, "Optical cloaking with metamaterials," *Nature Photon.*, vol. 1, no. 4, pp. 224–227, 2007.

[14] D.-H. Kwon and D. H. Werner, "Two-dimensional eccentric elliptic electromagnetic cloaks," *Appl. Phys. Lett.*, vol. 92, p. 013505, 2008.

[15] W. Jiang, T. Cui, G. Yu, X. Lin, Q. Cheng, and J. Chin, "Arbitrarily elliptical–cylindrical invisible cloaking," *J. Phys. D: Appl. Phys.*, vol. 41, p. 199801, 2008.

[16] W. Jiang, J. Chin, Z. Li, Q. Cheng, R. Liu, and T. Cui, "Analytical design of conformally invisible cloaks for arbitrarily shaped objects," *Phys. Rev. E*, vol. 77, no. 6, p. 66607, 2008.

[17] M. Rahm, D. Schurig, D. Roberts, S. Cummer, D. Smith, and J. Pendry, "Design of electromagnetic cloaks and concentrators using form-invariant coordinate transformations of Maxwell's equations," *Photon. Nanostruct. Fundam. Appl.*, vol. 6, no. 1, pp. 87–95, 2008.

[18] S. Maci, "A cloaking metamaterial based on an inhomogeneous linear field transformation," *IEEE Trans. Ant. Propag.*, vol. 58, no. 4, pp. 1136–1143, 2010.

[19] A. Alù and N. Engheta, "Multifrequency optical invisibility cloak with layered plasmonic shells," *Phys. Rev. Lett.*, vol. 100, no. 11, p. 113901, 2008.

[20] D. Gaillot, C. Croënne, D. Lippens, *et al.*, "An all-dielectric route for terahertz

cloaking," *Opt. Express*, vol. 16, no. 6, pp. 3986–3992, 2008.

[21] H. Chen, B. Hou, S. Chen, X. Ao, W. Wen, and C. Chan, "Design and experimental realization of a broadband transformation media field rotator at microwave frequencies," *Phys. Rev. Lett.*, vol. 102, no. 18, p. 183903, 2009.

[22] Y. Luo, H. Chen, J. Zhang, L. Ran, and J. Kong, "Design and analytical full-wave validation of the invisibility cloaks, concentrators, and field rotators created with a general class of transformations," *Phys. Rev. B*, vol. 77, no. 12, p. 125127, 2008.

[23] W. Jiang, T. Cui, Q. Cheng, J. Chin, X. Yang, R. Liu, and D. Smith, "Design of arbitrarily shaped concentrators based on conformally optical transformation of nonuniform rational B-spline surfaces," *Appl. Phys. Lett.*, vol. 92, p. 264101, 2008.

[24] A. Alù and N. Engheta, "Cloaking a sensor," *Phys. Rev. Lett.*, vol. 102, no. 23, p. 233901, 2009.

[25] E. Narimanov and A. Kildishev, "Optical black hole: Broadband omnidirectional light absorber," *Appl. Phys. Lett.*, vol. 95, no. 4, p. 041106, 2009.

[26] Q. Cheng, T. Cui, W. Jiang, and B. Cai, "An omnidirectional electromagnetic absorber made of metamaterials," *New J. of Phys.*, vol. 12, p. 063006, 2010.

[27] N. Kundtz and D. Smith, "Extreme-angle broadband metamaterial lens," *Nat. Mater.*, vol. 9, pp. 129–132, 2010.

[28] F. Kong, B. Wu, J. Kong, J. Huangfu, S. Xi, and H. Chen, "Planar focusing antenna design by using coordinate transformation technology," *Appl. Phys. Lett*, vol. 91, p. 253509, 2007.

[29] D. Roberts, N. Kundtz, and D. Smith, "Optical lens compression via transformation optics," *Opt. Express*, vol. 17, no. 19, pp. 16 535–16 542, 2009.

[30] H. Musal Jr and H. Hahn, "Thin-layer electromagnetic absorber design," *IEEE Trans. Magnetics*, vol. 25, no. 5, pp. 3851–3853, 1989.

[31] M. Park, J. Choi, and S. Kim, "Wide bandwidth pyramidal absorbers of granular ferrite and carbonyl iron powders," *IEEE Trans. Magnetics*, vol. 36, no. 5, pp. 3272–3274, 2000.

[32] "TDK corporation," http://www.tdk.com/.

[33] B. Chung and H. Chuah, "Modeling of rf absorber for application in the design of

anechoic chamber," *Prog. Electromagn. Res.*, vol. 43, pp. 273–285, 2003.

[34] J. Li and J. Pendry, "Hiding under the carpet: A new strategy for cloaking," *Phys. Rev. Lett.*, vol. 101, no. 20, p. 203901, 2008.

[35] R. Liu, C. Ji, J. J. Mock, J. Y. Chin, T. J. Cui, and D. R. Smith, "Broadband ground-plane cloak," *Science*, vol. 323, no. 5912, pp. 366–369, 2009.

[36] J. Valentine, J. Li, T. Zentgraf, G. Bartal, and X. Zhang, "An optical cloak made of dielectrics," *Nat. Mater.*, vol. 8, no. 7, pp. 568–571, 2009.

[37] L. Gabrielli, J. Cardenas, C. Poitras, and M. Lipson, "Silicon nanostructure cloak operating at optical frequencies," *Nature Photon.*, vol. 3, no. 8, pp. 461–463, 2009.

[38] C. E. Shannon, "Communication in the Presence of Noise," *Proc. IRE*, vol. 37, pp. 10–21, 1949.

[39] K. Computer Applied Fluid Laboratory at Yeungnam Univ., "CFD simulation software for educational purposes," http://caflab.yeungnam.ac.kr.

[40] J. Steinbrenner and J. Chawner, "Gridgen's Implementation of Partial Differential Equation Based Structured Grid Generation Methods," in *Proceedings, 8th International Meshing Roundtable*, California, USA, October 1999.

[41] J. Thompson, B. Soni, and N. Weatherill, *Handbook of grid generation.* CRC, 1999.

[42] R. Holland, "Finite-Difference Solution of Maxwell's Equations in Generalized Nonorthogonal Coordinates," *IEEE Trans. Nucl. Sci.*, vol. 30, pp. 4589–4591, 1983.

[43] Y. Hao and C. Railton, "Analyzing electromagnetic structures with curved boundaries on Cartesian FDTD meshes," *IEEE Trans. Microwave Theory Tech.*, vol. 46, pp. 82–88, 1998.

Chapter 3

Discrete Coordinate Transformation Based Flat Device Design and Its FDTD Modelling

3.1 Introduction

The technique of coordinate transformation provides us with a practical approach to control electromagnetic fields. The underlying theory has been studied in Chapter 2. Moreover, the technique of discrete coordinate transformation (DCT), a more practical case of the coordinate transformation technique, has been developed to further simplify the requirement for transformation media, and consequently grant the transformation based device a broadband performance and an easy fabricating process.

In this chapter, we will apply the discrete coordinate transformation to design flat devices in antenna systems. Many antenna devices have curved profiles, and their volume can be efficiently reduced by flattening their profiles. According to the theory of coordinate transformation [1, 2], the flattened devices shall have the same electromagnetic

performance as the conventional ones. In this chapter, two flat devices will be proposed and designed by using the DCT technique for demonstration. The first example is a flat reflector designed from a conventional parabolic reflector. The flat device contains dielectric blocks with permittivity values greater than the unity, so it is achievable from conventional materials. Because the parabolic surface is replaced with a flat surface, this new device is much easier to be located or integrated on other platforms. Furthermore, instead of rotating or displacing the parabolic reflector and/or the feeding antenna to steer the radiating direction, we will propose an alternative way to manipulate the reflected emission by tuning the dielectric blocks. This technique has the advantage of keeping the same flat profile and the same feeding position. The second example is a flat all-dielectric lens. A convex lens is flattened to half the thickness, while its focusing function is preserved. This flattened lens is only composed of a few dielectric blocks, hence is easy to fabricate. The Finite-Difference Time-Domain (FDTD) method [3–6] will be used to demonstrate their performance over a broad frequency band.

3.2 FDTD Modelling of Transformation Devices

Numerical modelling is an important and efficient tool to verify the performance of new designs. Commercial software packages, such as CST Microwave Studio [7], Ansoft's HFSS [8] and COMSOL Multiphysics [9], are commonly used for microwave problems. However, there are some concerns when those numerical techniques are applied to transformation devices. First of all, many devices designed using the coordinate transformation often require materials which are spectrally and spatially dispersive, and sometimes they are also anisotropic [10]. In these cases, the CST Microwave Studio or Ansoft's HFSS are no longer suitable to model those physical structures, because they require huge effort to construct models and large computing resource to ensure valid solutions. In contrast, COMSOL Multiphysics can provide position-dependent permittivity and permeability input module, therefore it has been commonly used to simulate devices based

on the coordinate transformation and/or metamaterials. Secondly, for transformation devices which operate over a broad frequency band, COMSOL Multiphysics becomes inefficient as its core solver based on the finite element method (FEM) is a frequency-domain approach, and, sufficient frequency sweep is needed to ensure the convergence of the solution. Based on these two considerations, we conclude that each commercial software can be employed depending on specific problems under investigation.

In addition to available commercial softwares, a Finite-Difference Time-Domain (FDTD) method based in-house coding [4] is another favored option for modelling transformation devices due to its flexibility. The basic FDTD method can be extended to simulate both spatially and spectrally dispersive media. Besides, this time-domain method is appropriate for modelling broadband electromagnetic responses. Furthermore, the in-house code is extremely suitable for modelling discrete structures based on the DCT technique, as the profile of permittivity and permeability can be directly mapped onto the FDTD grid. In addition, for an isotropic dielectric device, one can simulate the problem in two-dimensional (2D) circumstance using the FDTD code. A three-dimensional (3D) device can be achieved by rotating/extending the 2D model to an axis. In this thesis, the 2D FDTD method based in-house code is the primary tool employed for modelling the transformation devices. For some devices composed of very few dielectric blocks, Ansoft's HFSS is also utilised for comparison and validation.

The foundation of the FDTD method is briefly introduced in Appendix B. In this section, we discuss some targeted techniques which are applied to the basic FDTD method in order to precisely simulate the electromagnetic environments including transformation devices and/or metamaterials [3–6].

3.2.1 Source conditions

Electromagnetic wave excitation is essential in the FDTD modelling. Three source configurations have been employed in this thesis based on [3, 4]. They are: (1) hard-sourced

$\vec{E}$ and $\vec{H}$ fields in a two-dimensional grid, (2) the total-field/scatterred-field formulation for plane-wave excitation, and (3) the source to mimic the excitation from a horn antenna.

A *hard source* is set up simply by assigning a desired time function to specific components of $\vec{E}$ or $\vec{H}$ in the FDTD domain. This time function is independent of anything in the FDTD model. For example, in a one-dimensional, x-directive Yee grid [11], an E_z hard source could be established at the grid-point i_s to generate a continuous sinusoidal wave of frequency f_0 that is switched on at $n = 0$:

$$E_z|_{i_s}^n = E_0 sin(2\pi f_0 n \Delta t). \tag{3.1}$$

Another applied pointwise hard source provides a bandpass Gaussian pulse with zero DC content. The Fourier spectrum of this pulse has even symmetry around f_0. The pulse is centered at the time-step n_0 and has a $1/e$ characteristic decay of n_{decay} time-steps:

$$E_z|_{i_s}^n = E_0 e^{-[(n-n_0)/n_{decay}]^2} sin(2\pi f_0 (n - n_0)\Delta t). \tag{3.2}$$

This source is very important and has been used in this thesis to test the broadband performance of our designs. Received signals at observation positions are recorded at each time step, and their Fourier spectra are compared to that of the input signal in order to calculate the scattering parameters (S11 and S21) over frequencies.

The hard source at one point can be regarded as a point source in a 3D problem, or as a line source in a 2D case. Hard sources along a line can approximately represent a plane wave incidence with suitable boundary conditions.

The *total-field/scattered-field (TF/SF)* technique succeeds to permit FDTD modelling of long-duration pulse or sinusoidal illuminations for arbitrary plane-wave propagation directions [3]. The TF/SF formulation is based on the linearity of Maxwell's equations. It assumes that the physical total electric and magnetic fields $\vec{E}_{total}$ or $\vec{H}_{total}$ can be

decomposed in the following manner:

$$\vec{E}_{total} = \vec{E}_{inc} + \vec{E}_{scat},\ \vec{H}_{total} = \vec{H}_{inc} + \vec{H}_{scat}, \tag{3.3}$$

where $\vec{E}_{inc}$ and $\vec{H}_{inc}$ are the fields of the incident wave, which would exist in vacuum when there are no materials of any sort in the modelling space. $\vec{E}_{scat}$ and $\vec{H}_{scat}$ are the fields of the scattered wave, which are initially unknown. They result from the interaction of the incident wave with any materials in the space.

Fig. 3.1 (a) illustrates the the TF/SF technique in a general way. Because the finite-difference operations of the FDTD algorithm can be applied with equal validity to the incident field, the scattered filed and the total field, the modelling space can be separated into two distinct regions: Region 1 where total fields (the propagating fields of both the

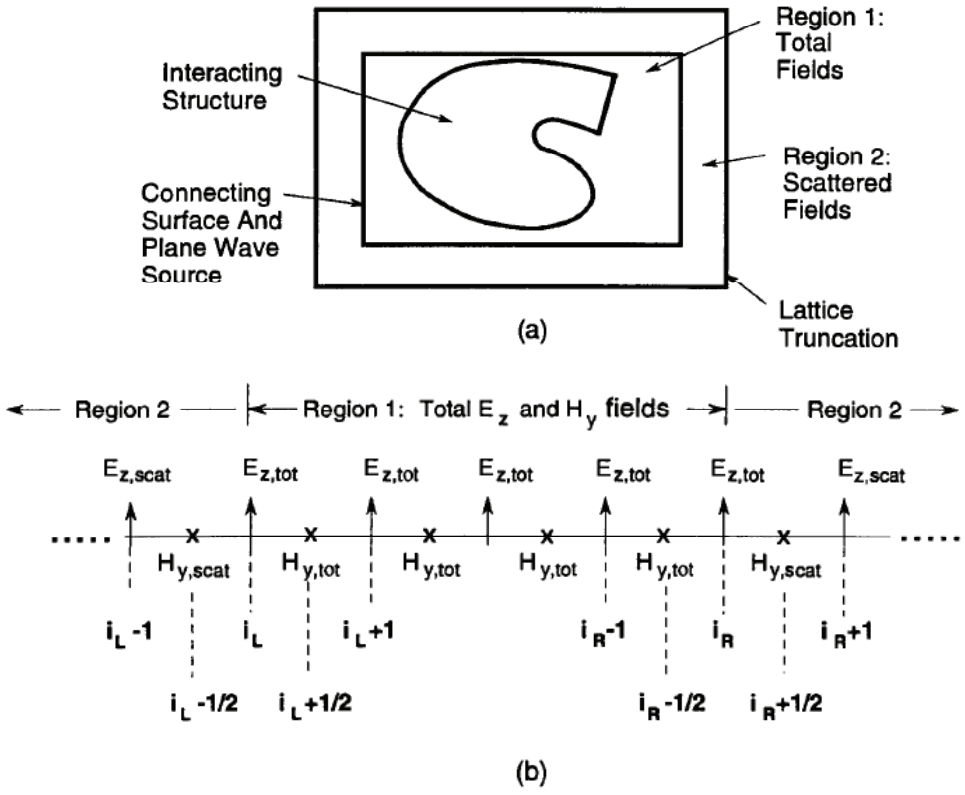

Figure 3.1: (a) Total-field and scattered-field regions; (b) Detail of field component locations in a one-dimensional x-directed cut through the space lattice of (a). [3]

incident wave and the scattered wave) are assumed to be stored in the computer memory; and Region 2 where scattered fields are assumed stored in the computer memory. Region 1 and 2 are separated by a nonphysical virtual surface that serves to connect the fields in each region, and thereby generates the incident wave. Fig. 3.1 (b) shows the detail of field component locations in a one-dimensional view. Assume that all points in the one-dimensional grid are in free space, then the FDTD algorithm to time-step the E-field is given at any grid-point by

$$E_z\,|_i^{n+1} = E_z\,|_i^n + \frac{\Delta t}{\varepsilon_0 \Delta x}(H_y\,|_{i+\frac{1}{2}}^{n+\frac{1}{2}} - H_y\,|_{i-\frac{1}{2}}^{n+\frac{1}{2}}). \tag{3.4}$$

Eq. (3.4) is consistent and valid when all three field components on the right-hand side are contained within a single region in Fig. 3.1 (a), whether Region 1 or Region 2. For example, if points $i-1/2$, i and $i+1/2$ are in Region 1, Eq. (3.4) can be written in an equivalent manner as

$$E_{z,total}\,|_i^{n+1} = E_{z,total}\,|_i^n + \frac{\Delta t}{\varepsilon_0 \Delta x}(H_{y,total}\,|_{i+\frac{1}{2}}^{n+\frac{1}{2}} - H_{y,total}\,|_{i-\frac{1}{2}}^{n+\frac{1}{2}}), \tag{3.5}$$

and if points $i-1/2$, i and $i+1/2$ are in Region 2, it can be written as

$$E_{z,scat}\,|_i^{n+1} = E_{z,scat}\,|_i^n + \frac{\Delta t}{\varepsilon_0 \Delta x}(H_{y,scat}\,|_{i+\frac{1}{2}}^{n+\frac{1}{2}} - H_{y,scat}\,|_{i-\frac{1}{2}}^{n+\frac{1}{2}}). \tag{3.6}$$

However, at the interface between Region 1 and Region 2, for example, at the grid point i_L in Fig. 3.1 (b), direct application of Eq. (3.4) yields

$$E_{z,total}\,|_{i_L}^{n+1} = E_{z,total}\,|_{i_L}^n + \frac{\Delta t}{\varepsilon_0 \Delta x}(H_{y,total}\,|_{i_L+\frac{1}{2}}^{n+\frac{1}{2}} - H_{y,scat}\,|_{i_L-\frac{1}{2}}^{n+\frac{1}{2}}), \tag{3.7}$$

which is inconsistent and incorrect because H_y component at $i_L - 1/2$ is supposed to be a scattered field whilst H_y component at $i_L + 1/2$ is a total field. To solve this problem

of consistency, another term is added to Eq. (3.7):

$$E_{z,total}\,|_{i_L}^{n+1} = E_{z,total}\,|_{i_L}^{n} + \frac{\Delta t}{\varepsilon_0 \Delta x}(H_{y,total}\,|_{i_L+\frac{1}{2}}^{n+\frac{1}{2}} - H_{y,scat}\,|_{i_L-\frac{1}{2}}^{n+\frac{1}{2}}) - \frac{\Delta t}{\varepsilon_0 \Delta x} H_{y,inc}\,|_{i_L-\frac{1}{2}}^{n+\frac{1}{2}}, \tag{3.8}$$

where

$$-H_{y,scat}\,|_{i_L-\frac{1}{2}}^{n+\frac{1}{2}} - H_{y,inc}\,|_{i_L-\frac{1}{2}}^{n+\frac{1}{2}} = -H_{y,total}\,|_{i_L-\frac{1}{2}}^{n+\frac{1}{2}}, \tag{3.9}$$

and the incident field $H_{y,inc}$ is already known from the source. This correction fixes the points on the interface where inconsistency arises, and avoids needlessly breaking up the E_z stepping loop. Similarly, the H_y field can be achieved by

$$H_{y,scat}\,|_{i_L-\frac{1}{2}}^{n+\frac{1}{2}} = H_{y,scat}\,|_{i_L-\frac{1}{2}}^{n-\frac{1}{2}} + \frac{\Delta t}{\mu_0 \Delta x}(E_{z,total}\,|_{i_L}^{n} - E_{z,scat}\,|_{i_L-1}^{n}) - \frac{\Delta t}{\mu_0 \Delta x} E_{z,inc}\,|_{i_L}^{n}\,. \tag{3.10}$$

In addition, to test the directive property of a reflector, a *horn* is usually located at the focal point to illuminate the reflector. Materials with high electric conductivity are employed to simulate the wall of a horn so as to bound energy inside. A point source is placed inside the horn $\lambda/4$ away from the back wall in the stimulation. In Section 3.3, a horn antenna will be carefully designed to feed reflectors.

3.2.2 Boundary conditions

To terminate the outer boundary of the simulation domain, a highly effective absorbing-material: the *perfectly matched layer* (PML) is applied [12]. The innovation of PML is that plane waves of arbitrary incidence, polarization and frequency are matched at the boundary. In the PML, each component of the electromagnetic field is split into two parts. In the Cartesian coordinates, the six field components yields 12 subcomponents.

Each of the 12 resulting components is then expressed as satisfying a coupled set of first-order partial differential equations. With carefully designed electric and magnetic conductivities in the PML, propagating waves are transmitted into and in between the PMLs with no reflection.

A *periodic boundary condition* (PBC) is another useful configuration in the modelling [3, 13]. An infinite periodic structure can be studied by using the unit cell approach, in which only elements in one unit cell are modelled. For example, consider a configuration which is periodic in the x-direction as shown in Fig. 3.2. Because of the periodicity inherent in the geometry, only the fields in one unit cell are unique and need to be determined. When the FDTD algorithm is applied, the field components that cannot be directly updated can instead be determined using periodic boundary conditions that relate the field on one side of the unit cell to those on the other side. Therefore, in the case depicted in Fig. 3.2, the update equations for electric fields at the periodic boundary

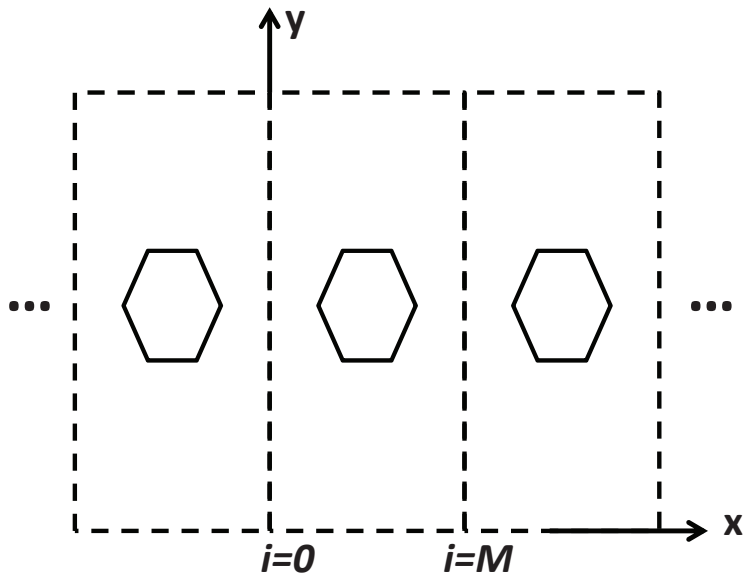

Figure 3.2: An infinite geometry that is periodic in the x direction.

($i = 0$ and $i = M$) can be expressed as [14]

$$E_y\mid_{M,j,k}^{n+1} = E_y\mid_{M,j,k}^{n} + \frac{\Delta t}{\varepsilon_0 \Delta z}(H_x\mid_{M,j,k+1}^{n+\frac{1}{2}} - H_x\mid_{M,j,k}^{n+\frac{1}{2}}) - \frac{\Delta t}{\varepsilon_0 \Delta x}(H_z\mid_{1,j,k}^{n+\frac{1}{2}} - H_z\mid_{M,j,k}^{n+\frac{1}{2}}), \tag{3.11}$$

$$E_z\mid_{M,j,k}^{n+1} = E_z\mid_{M,j,k}^{n} + \frac{\Delta t}{\varepsilon_0 \Delta x}(H_y\mid_{1,j,k}^{n+\frac{1}{2}} - H_y\mid_{M,j,k}^{n+\frac{1}{2}}) - \frac{\Delta t}{\varepsilon_0 \Delta y}(H_x\mid_{M,j+1,k}^{n+\frac{1}{2}} - H_x\mid_{M,j,k}^{n+\frac{1}{2}}), \tag{3.12}$$

$$E_z\mid_{0,j,k}^{n+1} = E_z\mid_{M,j,k}^{n+1}, \tag{3.13}$$

and

$$E_y\mid_{0,j,k}^{n+1} = E_y\mid_{M,j,k}^{n+1}, \tag{3.14}$$

where superscript n is the time step index and subscripts i, j and k are the spatial indices corresponding to the x, y and z axes.

PBC is a very important boundary condition in metamaterial modelling because it provides an efficient numerical approach for analysing 3D infinite periodic structures. When electromagnetic fields in the FDTD computational domain are updated, one can utilise the PBC to express the field components outside the computational domain. Update equations for 3D geometries with arbitrary incidences are more complicated than Eqs. (3.11)-(3.14), and have been studied thoroughly in [3]. Besides, PBC is also used to launch an infinite plane wave.

3.2.3 Near-to-far-field transformation

The FDTD method can efficiently calculate the electromagnetic responses of a structure to its surrounding environment. However, to test the radiating property of an antenna, for example the radiation pattern of a reflector, the electromagnetic field in the far-field region is required. Therefore, the *near-to-far-field (NTFF)* transformation is needed to obtain the far-field parameters. Using the Green's theorem, $\vec{E}$ field and $\vec{H}$ field that are tangential to a virtual surface which completely surrounds the antenna of interest can be integrated to provide the desired far-field response [3]. This virtual surface is independent of the shape or the composition of the structure being modelled, and therefore can have a fixed rectangular shape which conforms with the Cartesian FDTD grid. Thanks to this technique, we can enormously save computing time and memory because we no longer need to extend the FDTD computational domain to the far-field region.

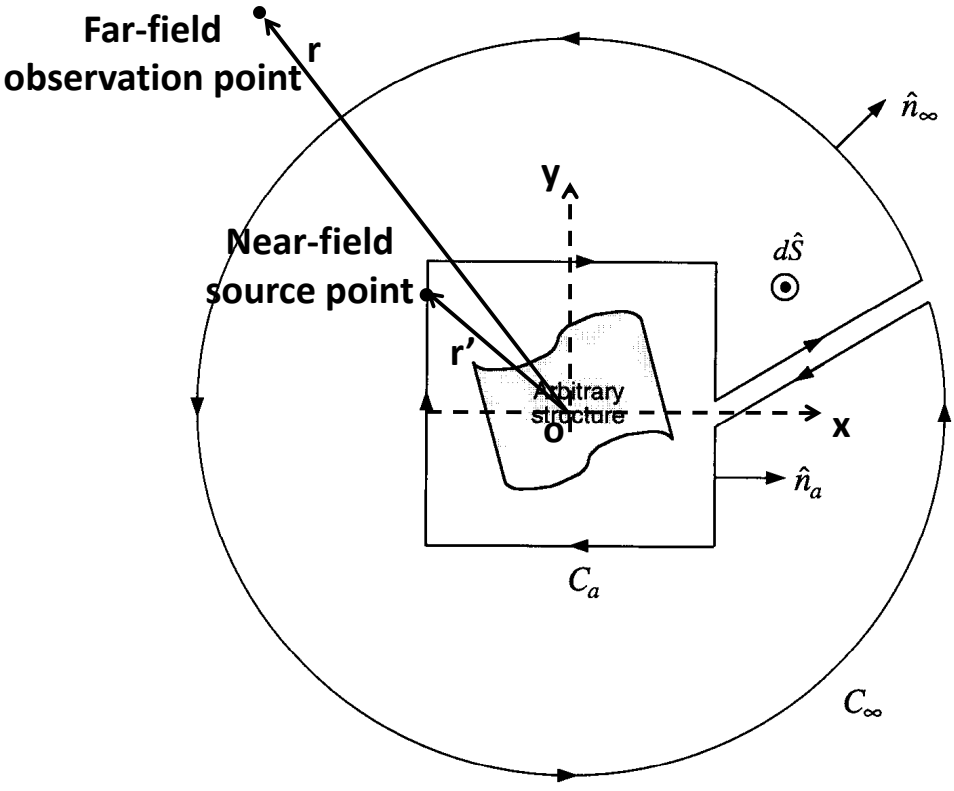

Figure 3.3: Two-dimensional scattering or radiation geometry showing the integration contours used in the derivation of the near-to-far-field transformation. [3]

Here we present the 2D solution with components of E_z, H_x and H_y. This circumstance is applicable to most designs in this thesis. In Fig. 3.3 we assume that an arbitrary structure of interest is enclosed by an arbitrary contour C_a, which has the unit outward normal vector $\vec{n}_a$. We further assume an infinite circular contour C_∞ centered at the coordinate system origin having the unit outward normal vector $\vec{n}_\infty = \hat{r}$. Furthermore, we assume that C_a and C_∞ are connected by an infinitely thin path to form a single continuous, closed contour that encloses the surface S. Note that $\vec{n}_\infty$ and $\vec{n}_a$ have opposite orientations relative to S.

The Green's theorem is applied as [3]:

$$\begin{aligned}
&\int_S [E_z(\vec{r}')(\nabla^2)' G(\vec{r}|\vec{r}') - G(\vec{r}|\vec{r}')(\nabla^2)' E_z(\vec{r}')] dS' \\
&= \oint_{C_\infty} [E_z(\vec{r}') \frac{\partial G(\vec{r}|\vec{r}')}{\partial r\prime} - G(\vec{r}|\vec{r}\prime) \frac{\partial E_z(\vec{r}')}{\partial r'}] dC' \\
&- \oint_{C_a} [E_z(\vec{r}') \frac{\partial G(\vec{r}|\vec{r}')}{\partial n'_a} - G(\vec{r}|\vec{r}') \frac{\partial E_z(\vec{r}')}{\partial n'_a}] dC',
\end{aligned} \tag{3.15}$$

where $\vec{r}$ is a far-field observation point, $\vec{r}'$ is a near-field source point, and dC' is a differential path element along the combined C_a and C_∞ contour as shown in Fig. 3.3. For the C_∞ integral term, both $E_z(\vec{r}')$ and $G(\vec{r}|\vec{r}')$ decay as $1/\sqrt{r'}$ in two dimensions as $r' \to \infty$. Thus the estimated order of this integral is obtained as [3]:

$$\begin{aligned}
\int_{C_\infty} &\approx \lim_{r'\to\infty} [2\pi r' \cdot \frac{1}{\sqrt{r'}} \cdot \frac{\partial(1/\sqrt{r'})}{\partial r'}] \\
&\approx r' \cdot \frac{1}{r'^{1/2}} \cdot \frac{1}{r'^{3/2}} \approx \frac{r'}{r'^2} \to 0.
\end{aligned} \tag{3.16}$$

Clearly, the contribution of this integral term is zero in the limit as $r' \to \infty$.

Now consider the S integral term evaluated at an observation point $\vec{r}$ in Fig. 3.3. From the definition of the Green's function for time-harmonic systems, we have

$$(\nabla^2)' G(\vec{r}|\vec{r}') = \delta(\vec{r} - \vec{r}') - k^2 G(\vec{r}|\vec{r}'), \tag{3.17}$$

where δ is the Dirac delta function and k is the wave number. Further, from the Helmholtz equation, we have

$$(\nabla^2)' E_z(\vec{r}') = -k^2 E_z(\vec{r}'). \tag{3.18}$$

Substituting Eq. (3.17) and Eq. (3.18) into the S integral term, we have [3]

$$\begin{aligned}\int_S \{E_z(\vec{r}') \cdot [\delta(\vec{r}-\vec{r}') - k^2 G(\vec{r}|\vec{r}')] - G(\vec{r}|\vec{r}') \cdot [-k^2 E_z(\vec{r}')]\} dS' \\ = \int_S E_z(\vec{r}')\delta(\vec{r}-\vec{r}')ds' = E_z(\vec{r}).\end{aligned} \tag{3.19}$$

Thus, Eq. (3.15) simplifies to [3]

$$\begin{aligned}E_z(\vec{r}) = \oint_{C_a} [G(\vec{r}|\vec{r}')\frac{\partial E_z(\vec{r}')}{\partial n_a'} - E_z(\vec{r}')\frac{\partial G(\vec{r}|\vec{r}')}{\partial n_a'}] dC' \\ = \oint_{C_a} [G(\vec{r}|\vec{r}')\hat{n_a}' \cdot \nabla' E_z(\vec{r}') - E_z(\vec{r}')\hat{n_a}' \cdot \nabla' G(\vec{r}|\vec{r}')] dC'.\end{aligned} \tag{3.20}$$

The Green's function is given by the Hankel function and could be reduced to the expression in terms of $\vec{r}$ and $\vec{r}'$ when the observation point is far enough from the point source. Eq. (3.20) indicates that the far-field components are achievable using near-field information. This derivation can be further reduced to a standard form that is convenient for the FDTD grid [3].

3.2.4 Dispersive FDTD modelling for metamaterials

A plenty of transformation devices have less-than-unity permittivity and/or permeability. From a straightforward point of view, the squeezing of a space leads to higher permittivity whilst the expanding of a space results in lower permittivity than that of the air. To simulate this special kind of problem, dispersive FDTD techniques have been developed in [5, 6] and applied in this thesis.

The material parameters are mapped with a well-known and widely-used Drude dis-

persive material model, in which, the frequency-dependent permittivity can be written as:

$$\varepsilon_r(\omega) = 1 - \frac{\omega_p^2}{\omega^2 - j\omega\gamma}, \tag{3.21}$$

where ω_p is the plasma frequency and γ is the collision frequency, which characterises the losses of the dispersive material. Here we present the calculation of E_z component as an example. Eq. (3.21) is substituted into the constitutive equation of

$$D_z = \varepsilon E_z. \tag{3.22}$$

Using the following rules of

$$j\omega \to \frac{\partial}{\partial t}, \quad \omega^2 \to -\frac{\partial^2}{\partial t^2}, \tag{3.23}$$

Eq. (3.22) can be written in the time domain as

$$(\frac{\partial^2}{\partial t^2} + \frac{\partial}{\partial t}\gamma)D = (\frac{\partial^2}{\partial t^2} + \frac{\partial}{\partial t}\gamma + \omega_p^2)\varepsilon_0 E_z. \tag{3.24}$$

The FDTD simulation domain is represented by a grid whose periods are $\triangle x$, $\triangle y$ and $\triangle z$ in three directions. To discretise Eq. (3.24), a second-order discretisation procedure is applied as [15]

$$\frac{\partial^2}{\partial t^2} \to \frac{\delta_t^2}{(\triangle t)^2}, \ \frac{\partial}{\partial t} \to \frac{\delta_t}{\triangle t}\mu_t, \ \omega_p^2 \to \omega_p^2\mu_t^2, \tag{3.25}$$

where the central finite difference operators in time (δ_t and δ_t^2) and the central average

operators with respect to time (μ_t and μ_t^2) are explained in [16] as

$$\begin{aligned}
\delta_t F\,|^n_{m_x,m_y,m_z} &\equiv F\,|^{n+\frac{1}{2}}_{m_x,m_y,m_z} - F\,|^{n-\frac{1}{2}}_{m_x,m_y,m_z},\\
\delta_t^2 F\,|^n_{m_x,m_y,m_z} &\equiv F\,|^{n+1}_{m_x,m_y,m_z} - 2F\,|^{n}_{m_x,m_y,m_z} + F\,|^{n-1}_{m_x,m_y,m_z},\\
\mu_t F\,|^n_{m_x,m_y,m_z} &\equiv \frac{F\,|^{n+\frac{1}{2}}_{m_x,m_y,m_z} + F\,|^{n-\frac{1}{2}}_{m_x,m_y,m_z}}{2},\\
\mu_t^2 F\,|^n_{m_x,m_y,m_z} &\equiv \frac{F\,|^{n+1}_{m_x,m_y,m_z} + 2F\,|^{n}_{m_x,m_y,m_z} + F\,|^{n-1}_{m_x,m_y,m_z}}{4}.
\end{aligned} \tag{3.26}$$

Here F represents any of the field components, and m_x, m_y, m_z are the indices corresponding to a certain discretisation point in the FDTD domain.

Substituting Eqs. (3.25) and (3.26) into Eq. (3.24), the updating equation for E_z can be obtained as [6]:

$$\begin{aligned}
E_z^{n+1} = \{&[\frac{1}{\varepsilon_0\triangle t^2} + \frac{\gamma}{2\varepsilon_0\triangle t}]D_z^{n+1} - \frac{2}{\varepsilon_0\triangle t^2}D_z^n + [\frac{1}{\varepsilon_0\triangle t^2} - \frac{\gamma}{2\varepsilon_0\triangle t}]D_z^{n-1}\\
&+[\frac{2}{\triangle t^2} - \frac{\omega_p^2}{2}]E_z^n - [\frac{1}{\triangle t^2} - \frac{\gamma}{2\triangle t} + \frac{\omega_p^2}{4}]E_z^{n-1}\}/[\frac{1}{\triangle t^2} + \frac{\gamma}{2\triangle t} + \frac{\omega_p^2}{4}].
\end{aligned} \tag{3.27}$$

The plasma frequency ω_p and the collision frequency γ can be presented based on Eq. (3.21) as [6]

$$\omega_p^2 = (1-\varepsilon_r)\omega^2 + \varepsilon_r\omega\gamma\tan\delta, \tag{3.28}$$

$$\gamma = \frac{\varepsilon_r\omega\tan\delta}{1-\varepsilon_r}. \tag{3.29}$$

Here ε_r is decided according to the required permittivity distribution, ω is the operating frequency, and $\tan\delta$ is the loss tangent of the lossy material. Moreover, other components of $\vec{\mathbf{E}}$ and $\vec{\mathbf{H}}$ can be calculated in the same way.

3.3 Design of a Flat Reflector

The parabolic reflector antenna is one of the most commonly used antennas from radio to optical frequencies [17]. A planar reflector design was presented in Section 2.3.2.1 using the analytical coordinate transformation (ACT). That planar device requires spatially dispersive permittivity and permeability simultaneously, which poses a great challenge to the practical design. In Section 2.4.2, we theoretically analysed that the discrete coordinate transformation (DCT) is able to provide us with an all-dielectric approach of device design. And here, in this section, we use this technique to design an all-dielectric flat reflector that works at the C-band (4 to 8 GHz) and the X-band (8 to 12 GHz). The FDTD Method is employed to verify its electromagnetic performance in terms of the directivity and the bandwidth. An alternative approach of beam steering using tunable gradient-index (GRIN) materials is also presented.

3.3.1 Dimensions and parameters

To begin with, a horn antenna is designed to feed a parabolic reflector. Its dimensions are illustrated in Fig. 3.4. Since the study in Section 2.4.2 was aimed to create all-dielectric devices in 2D scenario with E-polarization, the electric field is assumed to be normal to the paper surface in Fig. 3.4. So the plot is the H-plane view of a pyramidal horn, or a section view of a conical horn. Its dimensions are selected to support TE modes above 4 GHz [17], as listed in the caption. To reduce reflections from its structure, the horn is made short in length and its aperture is electrically small.

The equivalent phase center of the horn antenna is tested in order to feed the reflector accurately from the focal point. To decide the position, a 2D FDTD method is applied to simulate the horn model alone, and the phase distribution of the electric field is plotted in Fig. 3.5. The equivalent phase center is an apparent center of the curvature in the far field, and for this small horn, the boundary between near-field and far-field is $0.5\lambda_0$ [18]. The phase center is then decided following the next steps. First, we assume the

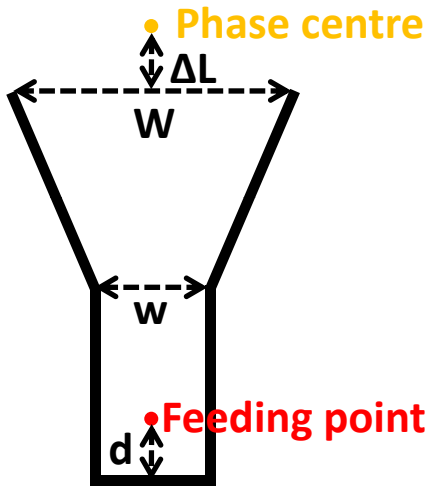

Figure 3.4: The horn antenna to feed the parabolic reflector. It is designed to work above 4 GHz. The dimensions are: at 8 GHz, $W = 0.5\lambda_0$, $w = 0.3\lambda_0$, $d = 0.25\lambda_0$. The dimension ΔL is the displacement from the equivalent phase centre to the aperture surface.

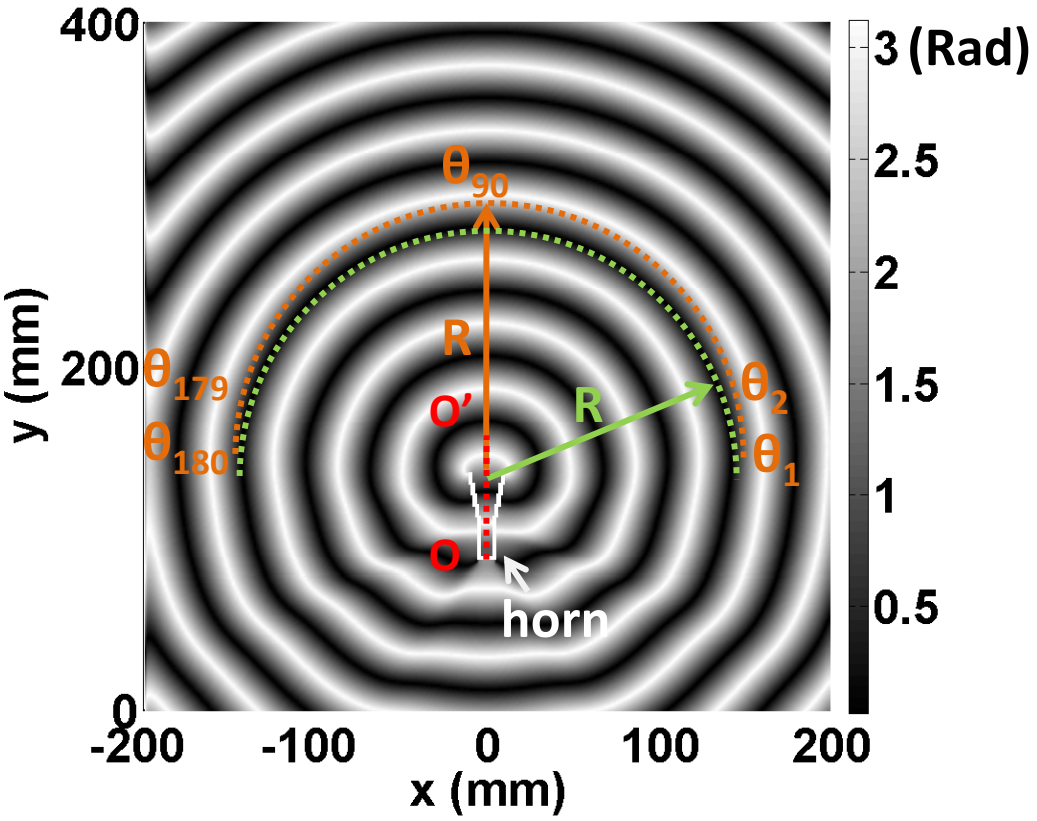

Figure 3.5: Equivalent phase center of the horn antenna. The horn is portrayed with the white lines.

phase center is on the line $OO^{'}$ (defined in Fig. 3.5). O is the center of the bottom wall inside the horn, and $O^{'}$ is $0.5\lambda_0$ away from the aperture surface. We draw a series of semi-circles with $R = 3\lambda_0$ centered at each point along $OO^{'}$. The dashed yellow arc and green arc are two examples of these semi-circles. The spacing between neighboring points on $OO^{'}$ is $\lambda_0/30$, which is the resolution of the FDTD grid. Then, their phase differences are integrated on every semi-circle, calculated as

$$\Delta_{phase} = \sum_{i=1}^{180} (\theta_i - \theta_{90})^2, \tag{3.30}$$

where θ_i represents the phase (in radian) along the semi-circle. The minimum phase difference is found out to be 0.85 and its center point is $\lambda_0/30$ outside the horn aperture ($\Delta L = \lambda_0/30$ in Fig. 3.4). Therefore this point is considered as the equivalent phase center, from which the wave spreads outward spherically (or cylindrically in the 2D scenario).

A parabolic reflector is designed based on the feeding horn. The geometry was illustrated in Fig. 2.12 and here again we plot it in Fig. 3.6(a). Using numerical simulations in Ansoft's HFSS, we find its -3 dB beamwidth is around $\pm 50^o$. Apparently, the directive property of the horn is not good, due to the small aperture size. The flare angle of θ is therefore chosen to be $\pm 45^o$. Another concern is the horn antenna should be excluded from the transformation region, otherwise the incidence itself will be distorted. As a result, the focal length F should be long enough and we set it to be 109 mm, which is about $3\lambda_0$ at 8 GHz. The aperture of the reflector is consequently decided to be 180 mm, according to Eq. (2.31). Fig. 3.6(b) shows the virtual space including the parabolic reflector (the same figure as Fig. 2.11(a)). It is noted that the coordinate transformation is applied in a region sized 300 mm $\times$ 75 mm, leaving two spare areas of 60 mm $\times$ 75 mm on the both sides of the reflector. This feature is to maintain the continuity on the boundary, so as to reduce the reflection between the flat device and the surroundings. In Chapter 5 we will further discuss the relationship between the size of the transformation region and the property of the transformation device.

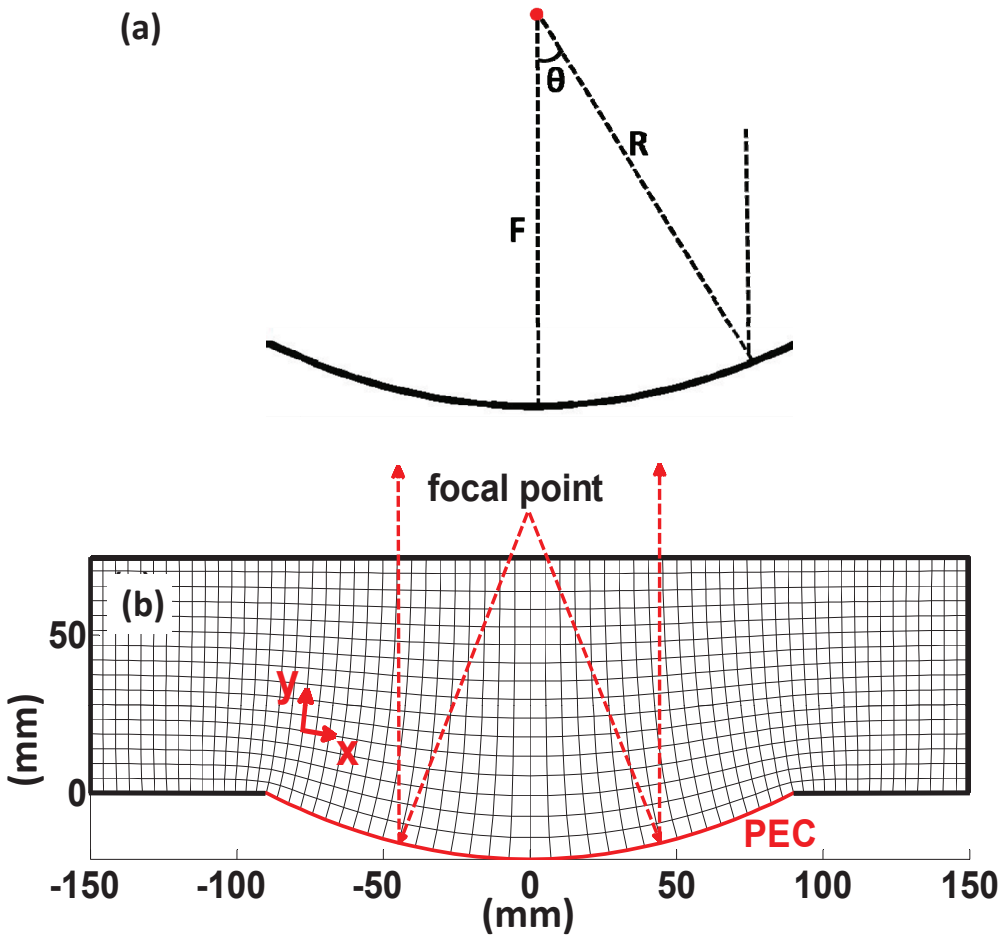

Figure 3.6: (a) Geometry of the parabolic reflector. (b) The virtual space including the parabolic reflector.

A near-orthogonal grid is generated using the scheme described in Section 2.4. The FWHM (full width at half maximum) index of the angle distribution shown in Fig. 2.14 is minimised to be 1^{o}, which represents good orthogonal properties of all local coordinate systems. The permittivity distribution of the transformation based flat reflector is calculated according to Eqs. (2.55) and (2.56). The complete permittivity map is shown in Fig. 3.7(a), consisting of 64×16 square blocks.

To reduce the complexity of the flat reflector and to make it more realisable, some simplifications are adopted. First, materials with relative permittivity of less-than-unity value are neglected and replaced with those of $\varepsilon_r = 1$ as the air in the free space. In

this design, materials with less-than-unity permittivities are found close to the bottom around $x = 80$ mm and $x = -80$ mm (see Fig. 3.7(a)). Since these areas are electrically small at operating frequencies, and those permittivity values are often very close to one, the simplification is considered to be safe. This fact has been demonstrated in [19–21], and will be shown later by simulation results in this chapter. The permittivity map without less-than-unity values is shown in Fig. 3.7(b). It should be pointed out that materials with less-than-unity parameters are termed as "dispersive materials" in this thesis, as they are strongly dispersive in frequency. Strictly speaking, all materials are essentially dispersive in frequency. However, conventional dielectrics can be nearly non-dispersive at the X-band and the C-band [19]. A second step to approximate and simplify the transformation device is based on the concept which has been developed to design

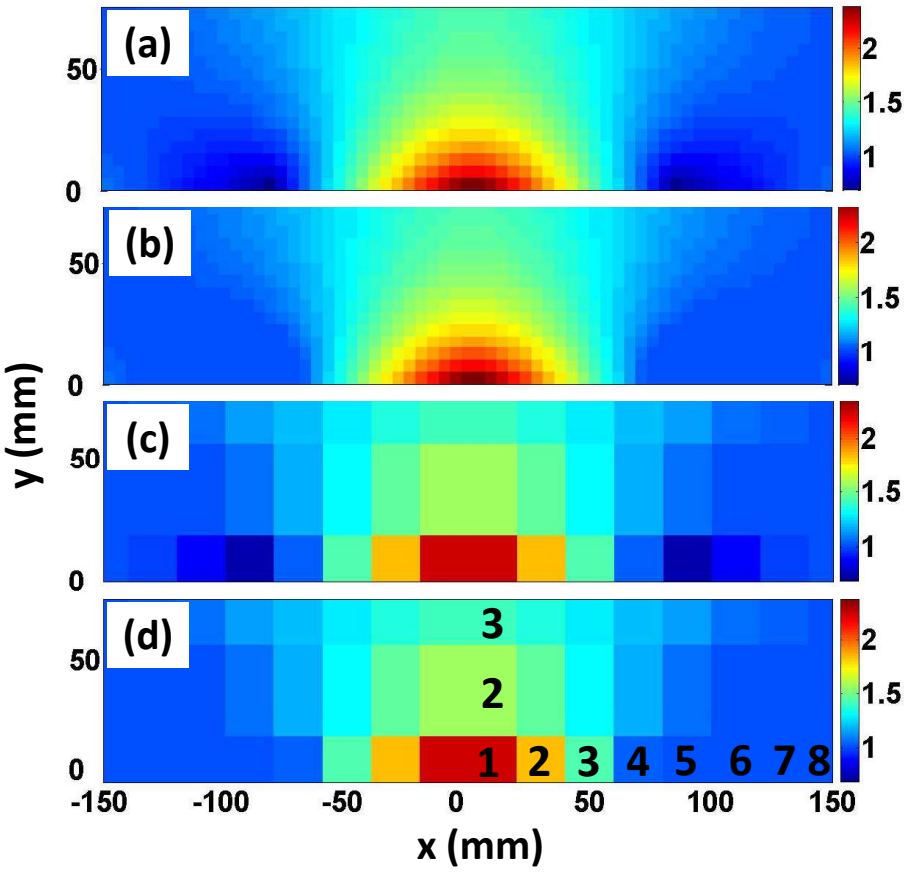

Figure 3.7: (a) Relative permittivity map consisting of 64 × 16 blocks. (b) Relative permittivity map consisting of 64 × 16 blocks, without less-than-unity values. (c) Relative permittivity map consisting of 16 × 3 blocks. (d)Relative permittivity map consisting of 16 × 3 blocks, without less-than-unity values.

a simplified carpet cloak made of only a few blocks of isotropic all-dielectric materials [19, 22]. According to the Nyquist-Shannon sampling theorem [23], an incident wave cannot resolve properties of media when their sizes are similar to or smaller than half a wavelength. As a result, two devices with different resolutions are possible to possess similar performances, providing that both resolutions are sufficient. This statement will be proved in this chapter through simulation results, and a detailed analysis will be given to quantify the effect of resolution on the performance of a transformation device in Chapter 5. Such a concept has made significant advances for the transformation device to be able to be realised in practice. When applied to the present work, the high resolution permittivity map shown in Fig. 3.7(a) thus can be approximated using a relatively low resolution sampling map of 16 × 3 blocks as shown in Fig. 3.7(c). The size of each block is 18.75 mm, which is half a wavelength in free space at 8 GHz. This is a guaranteed resolution by our simulation results, and in Chapter 5 we will explain in detail the impact of resolution and the tradeoff between resolution and performance. To execute the simplification, the position of a block in Fig. 3.7(a)-(d) is defined as the position of its center point. Each low-resolution block in figure (c)/(d) can find a high-resolution one in figure (a)/(b) which has the closest position to it. Once the pair is decided, the permittivity in the high-resolution block is filled into the low-resolution block uniformly. Fig. 3.7(d) shows the simplified map without values less than unity (we call it a "non-dispersive map" in the following text). Table 3-A presents the explicit values of the relative permittivity map depicted in Fig. 3.7(c). Because the map is symmetric, only the right half of the values are shown in the table.

Table 3-A: Relative permittivity values of the 16 × 3 dielectric blocks (right half)

		Column							
		1	2	3	4	5	6	7	8
Row	3	1.34	1.28	1.21	1.14	1.07	1.01	0.97	0.94
	2	1.49	1.39	1.24	1.10	1.00	0.96	0.96	0.96
	1	2.11	1.74	1.37	0.98	0.69	0.84	0.92	1.00

3.3.2 Numerical verification

The FDTD method discussed in Section 3.2 is used to compare the performances of the parabolic reflector and the flat reflector. For simplicity, we use 2D modelling with H_x, H_y and E_z components (E polarization). A 3D reflector is easily realisable by rotating the permittivity map in Fig. 3.7 to the y axis. For the reflector in design, the simulation domain is relatively small and a conventional Cartesian grid is fine enough to accurately model the device. A spatial resolution of $\lambda/30$ is chosen. The total-field/scattered-field technique is applied to implement an incident plane wave. PML absorbing boundary conditions are added surrounding the devices in order to terminate the simulation domain. The full-mapped flat reflector with less-than-unity values in Fig. 3.7(a) is also simulated using the dispersive modelling.

First, a plane wave with E polarization comes along $+y$ direction at 8 GHz, in order

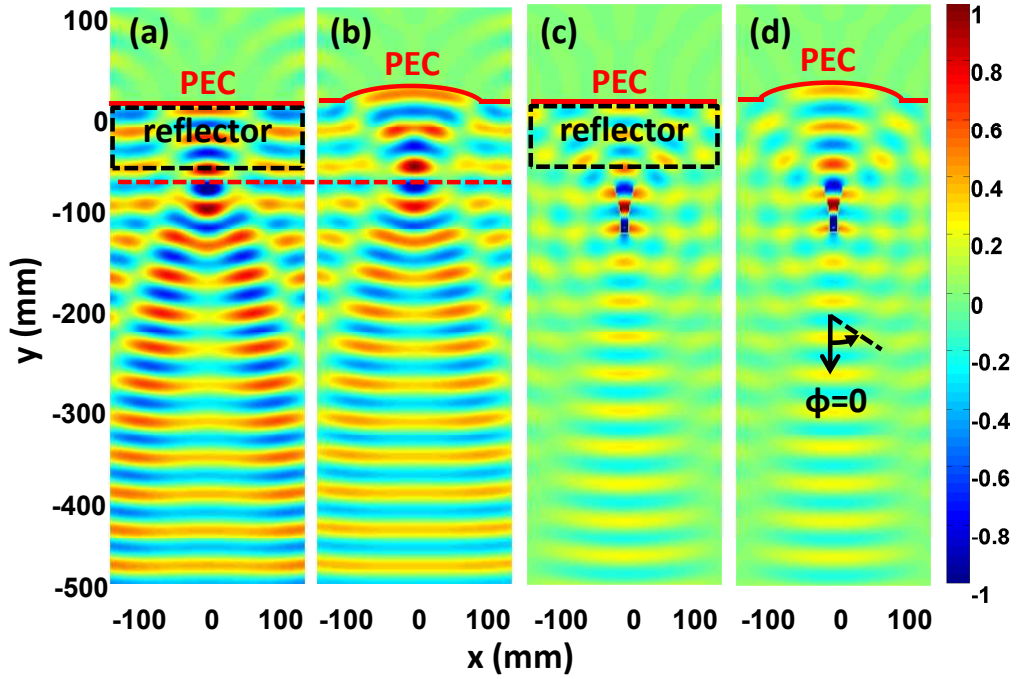

Figure 3.8: Real part of the Ez field at 8 GHz. (a) A plane wave along the y direction illuminates a low-resolution flat reflector. The focal length (measured from the dashed red line to the center of the PEC) is 102.6 mm. (b) The same plane wave illuminates the conventional reflector. The focal length is 102.7 mm. (c) A small horn antenna is applied at the focal point to feed the flat reflector. (d) A small horn antenna is applied at the focal point to feed the conventional reflector.

to compare the low-resolution non-dispersive flat reflector shown in Fig. 3.7(d) with the parabolic reflector in term of the focal length. Fig. 3.8(a) and Fig. 3.8(b) illustrate the real part of the E_z field from the transformed flat reflector and the conventional parabolic reflector, respectively, after steady-state is reached. Their focal lengths are measured as the distances from the center of the perfect electric conductor (PEC) surface to the narrowest envelope marked with the dashed red line in (a) and (b). The focal lengths in (a) and (b) are 102.6 mm and 102.7 mm respectively, very close to each other. In addition, we observe slightly different reflections on two sides of the reflectors. These reflections are due to the neglecting of less-than-unity permittivities, and the discontinuity between the flat reflector and the air.

In Fig. 3.8(c) and (d) we also compare the performance of these two reflectors when fed by a small horn with its phase center located at the focal point. The field distributions illustrated are indeed similar, which indicates that the flat reflector maintains the function of transforming an incident cylindrical wave to a plane wave and consequently obtains highly directive beams.

To investigate the directive property of the devices, in Fig. 3.9 radiation patterns

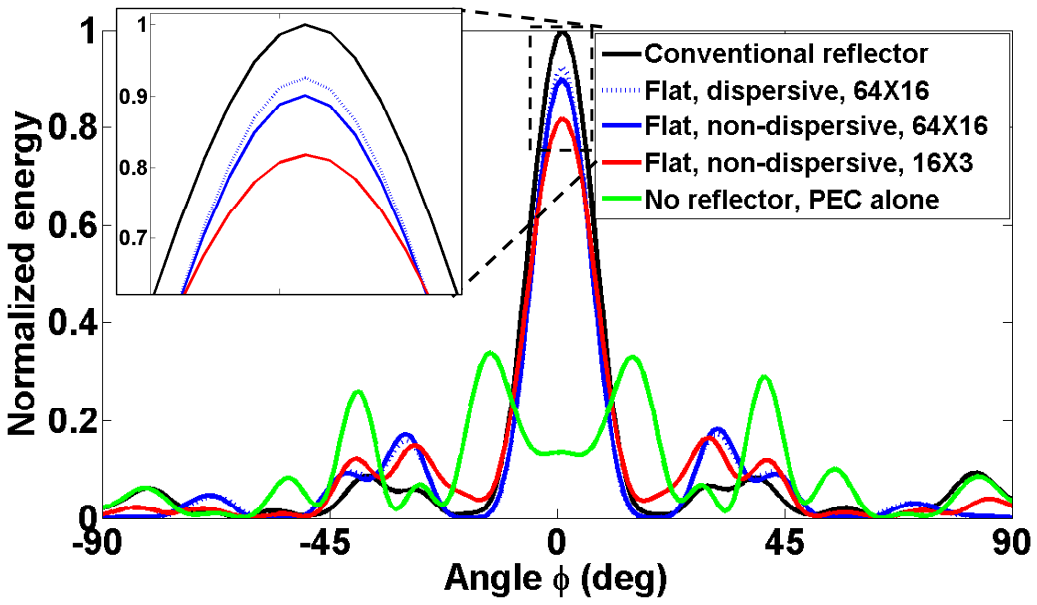

Figure 3.9: The comparison of the radiation patterns at 8 GHz. The definition of Φ is shown in Fig. 3.8(d).

of the conventional reflector, flat reflectors with different resolutions, and the radiation pattern of a flat PEC surface alone, are compared. The near-to-far-field (NTFF) transformation is applied to observe the far-field characteristics. Using the data obtained from the near-field simulation, the NTFF transformation calculates the forward radiation patterns of the reflectors. The energy is calculated as $|E_z|^2$, and normalised to the peak energy of the conventional reflector. It is shown in Fig. 3.9 that the conventional reflector and all the three flat reflectors produce highly directive beams around $\phi = 0$ (ϕ defined in Fig. 3.8(d)), which verifies the excellent cylindrical-to-plane wave transformation. The high-resolution flat reflectors, dispersive (with less-than-unity permittivities) or non-dispersive (without less-than-unity permittivities), seem to have energy loss around the radiating direction when compared to the conventional parabolic reflector. When the less-than-unity values are neglected from the high-resolution map, the performance deteriorates only slightly, in term of the energy reduction around $\phi = 0$. To apply the low-resolution map further, the reflector suffers more energy loss in radiating direction, but the directive property is still comparable to that of the conventional reflector. When all reflectors are removed, the PEC surface cannot hold the directive property.

Furthermore, the bandwidths of the dispersive and non-dispersive flat reflectors are tested at different frequencies. Both the flat reflectors are composed of 16×3 large blocks, and the testing frequencies are 4 GHz, 6 GHz, 10 GHz and 12 GHz respectively. Fig. 3.10 shows that at the frequencies higher than 8 GHz, the two reflectors have extremely similar radiation patterns. When the working frequency goes lower, the dispersive reflector has higher radiation around the angle of $\phi = 0$, but slightly larger side-lobes than the non-dispersive one. It is because when the operating frequency decreases, the less-than-unity values change more and more rapidly according to the Drude model. In conclusion, a non-dispersive reflector has a comparable radiating performance and a wider bandwidth than the dispersive one, and is much easier to realise.

From the point of view of practical applications, reflection at the feed is also tested to measure the backscattering of the reflectors. A reflector is stimulated by launching

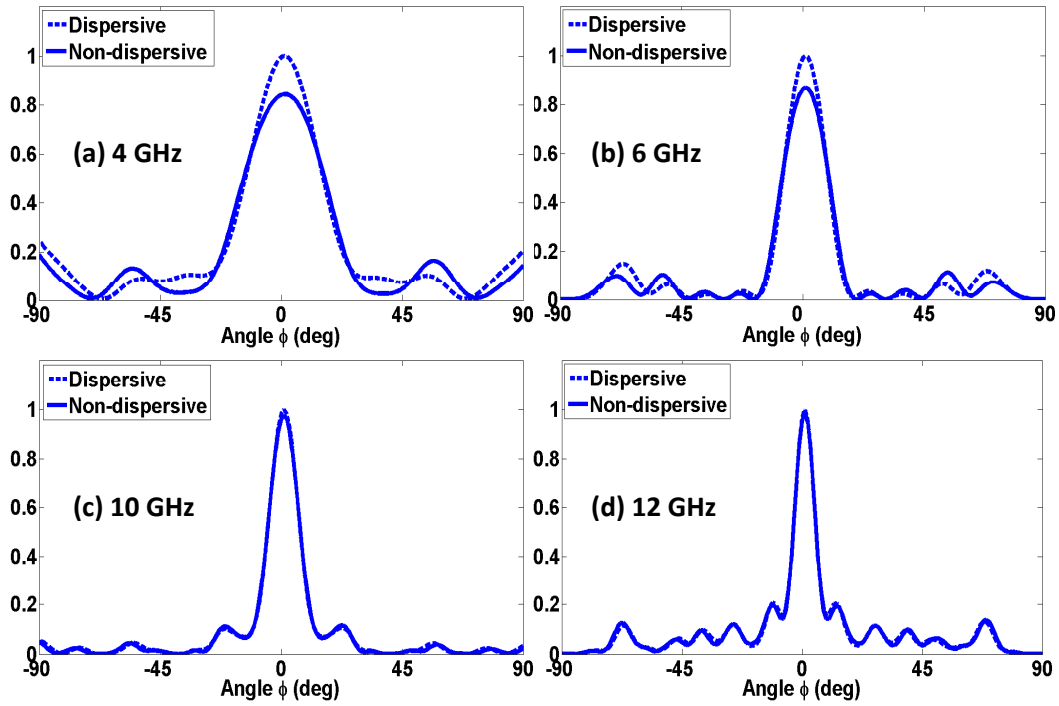

Figure 3.10: Comparison of the radiation patterns between dispersive and non-dispersive flat reflectors at 4 GHz, 6 GHz, 10 GHz and 12 GHz. Both the flat reflectors are composed of 16 × 3 blocks.

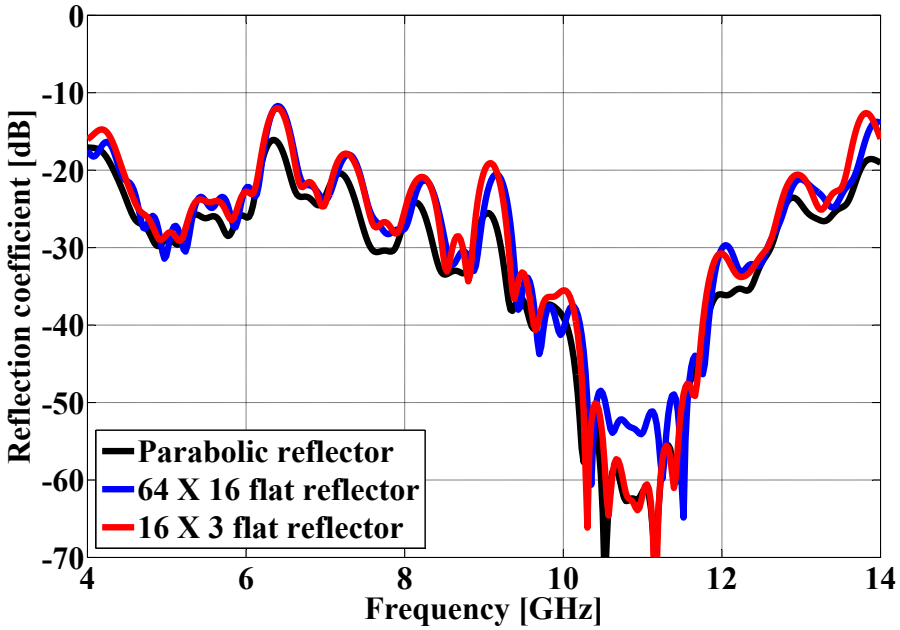

Figure 3.11: Comparison of the reflections between the conventional parabolic reflector and the two flat reflectors over 4-14 GHz. The reflectors are stimulated by a wideband Gaussian pulse.

a wideband Gaussian pulse with a fixed bandwidth between 4 to 14 GHz inside the small feed horn. The electric field E_z is recorded at the feeding point, and the input signal is isolated from the reflected signal. The reflection coefficient, which is the ratio of the reflected signal over the input signal, is then calculated and plotted in Fig. 3.11. The reflection curves have similar shapes when the parabolic reflector, the 64×16-block flat reflector and the 16×3-block flat reflector are applied. Nevertheless, the reflections from the designed flat reflectors are slightly higher than that from the parabolic reflector. This is reasonable due to the impedance mismatching at interfaces between the dielectric blocks and the air. However, the two flat reflectors with different resolutions still have similarly low reflection coefficients over the frequency range.

3.3.3 Extension: a beam steerable flat reflector

Achieving highly directive beams from reflectors has been studied above. Meanwhile, a wide angular scanning with sharp beams is practically required to various applications. Fig. 3.12 describes two common ways to steer beams: by simply moving or tilting the feed as shown in (a) and (c). Alternatively, we can achieve the same beam control by moving or tilting the reflector inversely while maintaining the feed on the original focal point, as shown in (b) and (d). Such schemes utilise the linear/angular displacements within the reflector system to achieve the desired electromagnetic beams, which reveals the essential links between the geometry of the reflector and the corresponding optical ray-trace [24].

An all-dielectric flat reflector has been proposed in this section, and here, we extend this technique to design beam steerable flat reflectors [25]. Instead of moving or tilting the feed/reflctor, we employ an alternative way to manipulate the reflected emission by tuning the permittivity of dielectrics derived from the DCT technique. This method has a merit of maintaining the profile of the feed-reflector combined system, therefore is potentially applicable for mounting reflectors on the platform such as the surface of an aircraft.

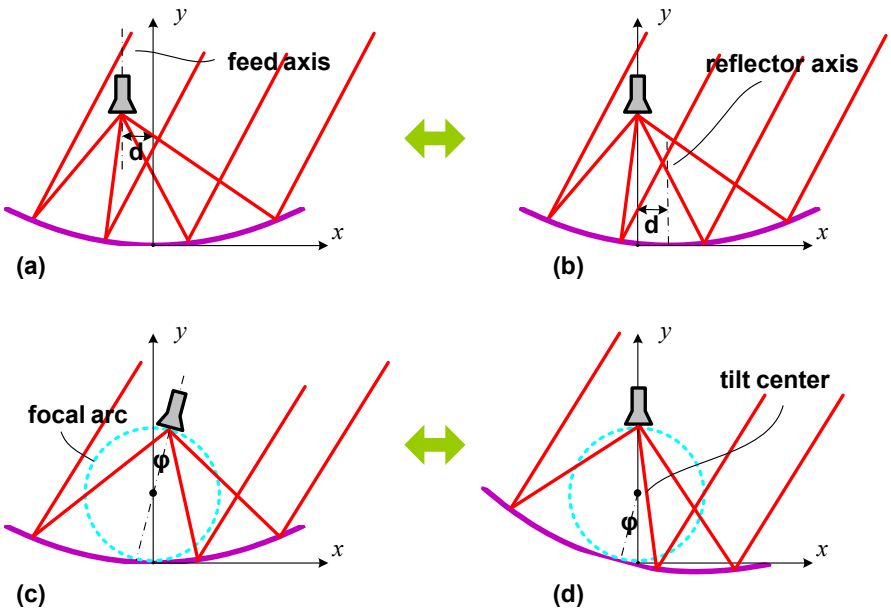

Figure 3.12: Scenarios to steer the beam of a parabolic reflector. (a) Moving the feed. (b)Moving the reflector. d refers to the displacement between the feed axis and the reflector axis. (c) Tilting the feed. (d) Tilting the reflector. φ refers to the rotating degree of the feed and the reflector around the tilting center. The dashed cyan circle refers to the focal arc when the feed/reflector rotates.

A new parabolic reflector is designed at 15 GHz, among the Ku-band that aims for satellite communications. The dimensions of the parabolic reflector and the transformation region (shown in Fig. 3.13) are chosen based on similar concerns discussed in Section 3.3.1. The parabolic surface (the purple lines) has an aperture of 200 mm (10 λ_0), a focal length of 100 mm (5 λ_0) and the flare angle about 53^o. Instead of the small horn, a short waveguide is located on the focal point to feed the reflector. The waveguide has an aperture of 15.2 mm (0.76 λ_0) $\times$ 6.8 mm (0.34 λ_0), with its equivalent phase center 3 mm inside of the aperture. The permittivity map is again calculated using the DCT technique. Three steps of simplification are applied. Firstly, the less-than-unity permittivity values are neglected and replaced with ε_0. Secondly, the high-resolution permittivity map is approximately reduced to a low-resolution map. The dimensions of the low-resolution blocks are given in the caption of Fig. 3.13. Thirdly, the blocks outside the parabolic aperture (outside the two red lines in Fig. 3.13) are deleted in order to achieve the same aperture as the conventional parabolic reflector. The third step is reasonable based on the fact: it is observed in Fig. 3.13 that the relative permittivity

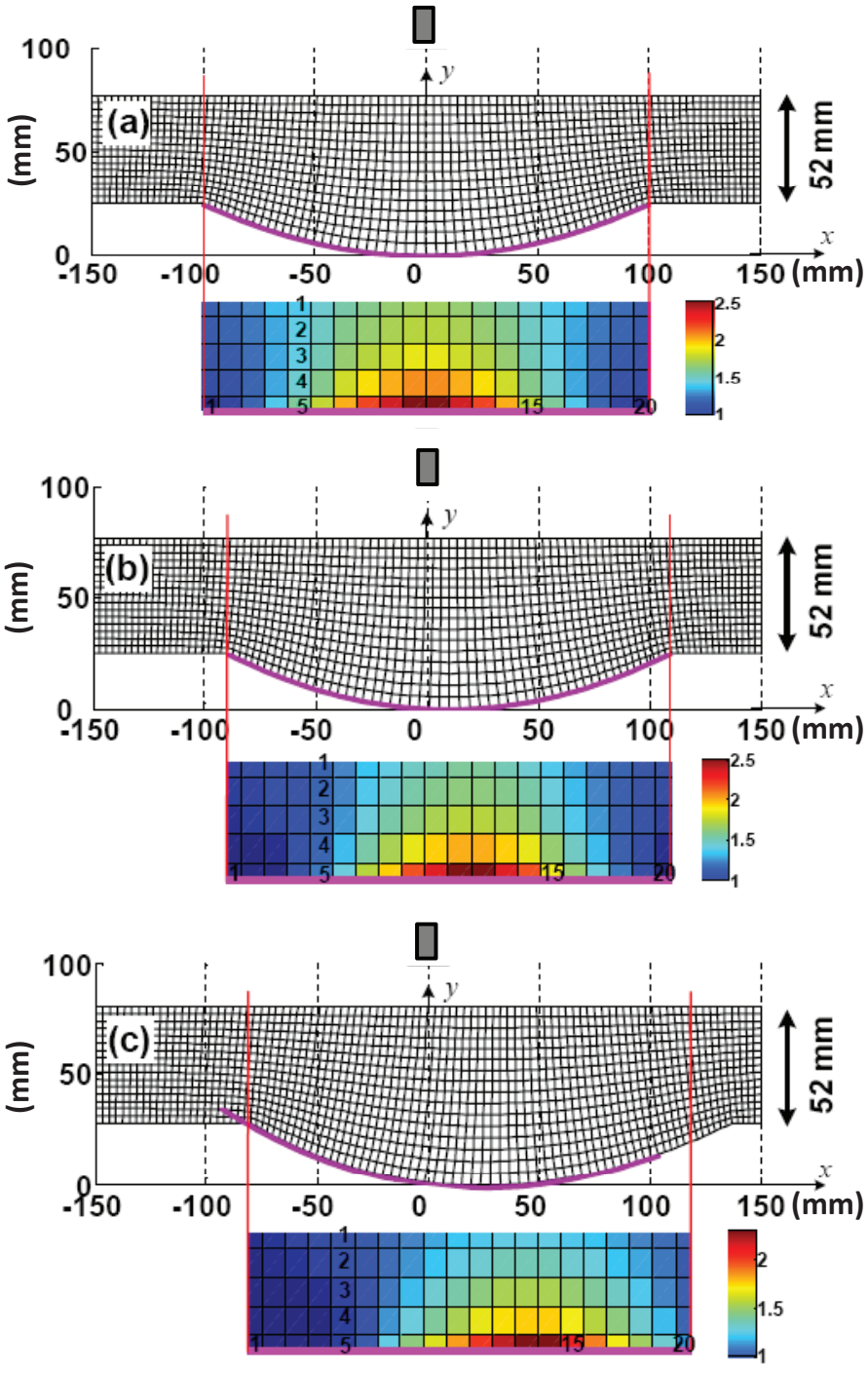

Figure 3.13: The near-orthogonal grid in the virtual space with a parabolic reflector embedded in the air, and the 20×5-block flat reflector. The five layers of the flat reflector have heights of 6.5 mm, 13 mm, 13 mm, 13 mm and 6.5 mm respectively. The 1st and 20th columns have a width of 6.94 mm and the rest have a width of 10.34 mm. (a) The symmetric grid and the symmetric transformation flat reflector with the permittivity value from 1 to 2.541. (b) The asymmetric grid regarding the 10 mm moving of the reflector and the asymmetric transformation flat reflector with the permittivity value from 1 to 2.537. (c) The asymmetric grid regarding the 9° tilting of the reflector and the asymmetric transformation flat reflector with the permittivity value from 1 to 2.317.

value is close to 1 outside the two red lines, hence materials outside them have similar electromagnetic properties as the air. In Chapter 5 we will prove this simplification is reasonable. Fig. 3.13(b) and (c) describe the scheme to control the reflected emission by tuning the permittivity map. When the parabolic surface is moved or tilted, the shape of the virtual space is changed accordingly. A new grid is generated and the corresponding asymmetric permittivity map is calculated through the discrete coordinate transformation. Therefore, the linear or the angular displacement between the feed and reflector is now represented by the variation of the permittivities of the dielectric blocks.

A full-wave finite-element simulation using Ansoft's HFSS is then performed to verify the proposed design. The far field performance of these reflectors is demonstrated in Fig. 3.14 at 15 GHz. As is observed, the reflectors can generate steerable beams as expected. On the one hand, we can observe that the off-axis feeding will lead to a shift of the main beam for the conventional parabolic reflector, and approximately every 5 mm displacement results in 2.5^o shift. As a result, 10 mm off-axis feed as well as the corresponding asymmetric flat reflector in Fig. 3.13(b) creates a 5^o scanning angle. On the other hand, tilted feed will redirect the beam from the reflector, and approximately every 3^o tilt leads to 4^o shift of the reflected emission, among which 3^o is from the rotation while another 1^o is from the off-axis feeding, because the parabolic surface is moved to right a little before being tilted. As a result, the 9^o feed tilt as well as the corresponding asymmetric flat reflector in Fig. 3.13(c) has a 12^o scanning angle. There are slight differences between the radiation patterns, due to the simplifications to the permittivity map, as discussed before. However, the overall performance of the transformation flat reflector is considerably promising.

In this sub-section, we have initially tested the idea of creating a flat dielectric "matrix" with a fixed feed and a constant profile, meanwhile producing different radiation patterns. An underlying application is that the coordinate transformation can be applied to more kinds of reflectors (eg. the corner reflector and the Cassegrain reflector), and permittivity maps are generated accordingly. Without changing the feed or the sur-

roundings, the "matrix" works as different antennas when the permittivity map inside is changed. In some scenarios, the position of the metallic plane may vary as well.

A big challenge to put this idea into practice is to find out a competent technique for controlling the permittivity values of the dielectric blocks individually. At microwaves, metamaterials composed of lumped unit structures may be one option. By tuning the

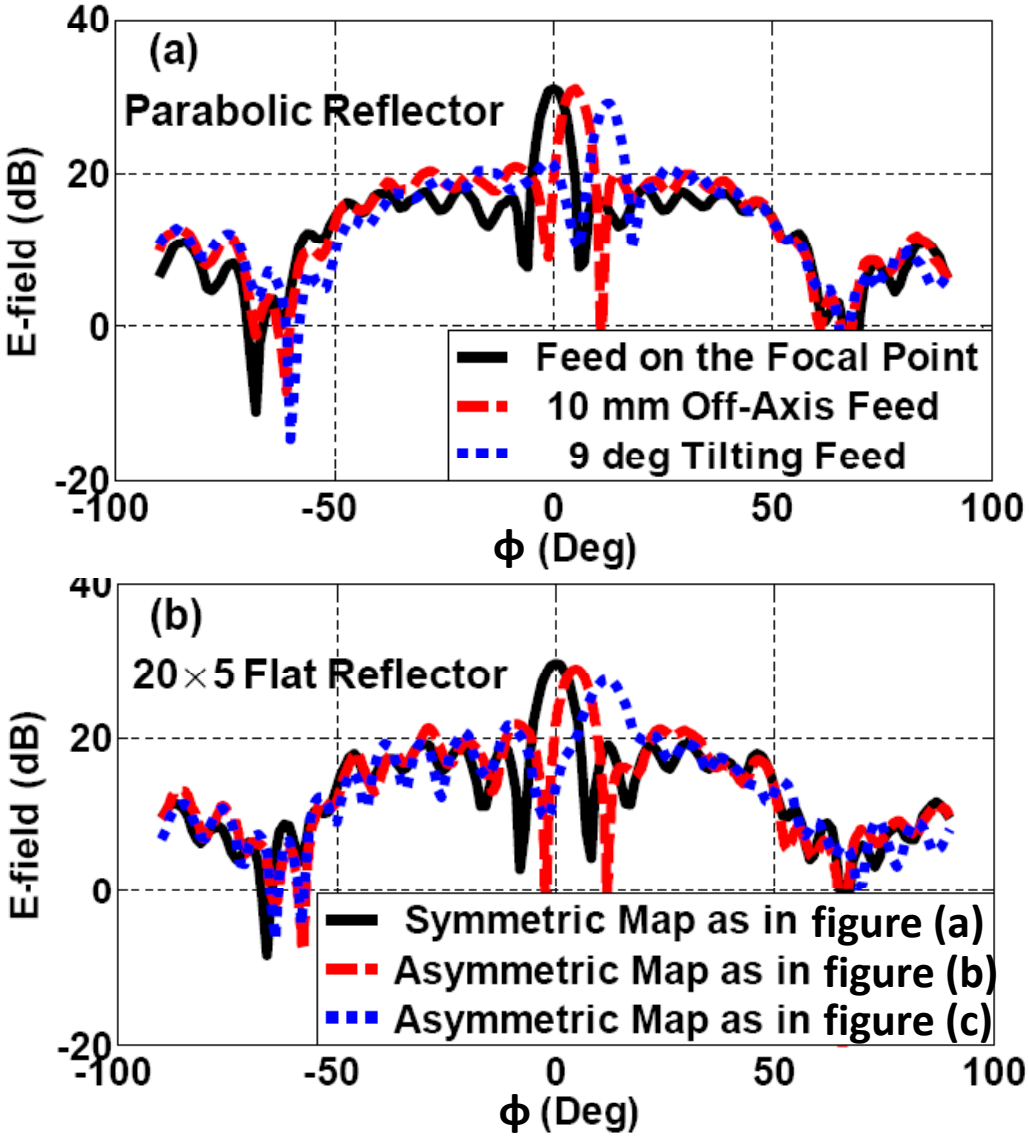

Figure 3.14: The radiation patterns of the parabolic reflector and the 20×5-block flat reflector. (a) Radiation patterns of the parabolic reflector with the feed on the focal point, 10 mm off-axis moved and 9^o tilted. (b) Radiation patterns of the transformation flat reflectors as shown in Fig. 3.13 (a)(b)(c) respectively.

feeding voltage, one can adjust the capacitance of each unit cell, and consequently control the equivalent permittivity within a block. This topic may be further investigated as future work.

3.4 Design of a Flat Lens

A convex lens is a common device in antenna systems, due to its function of transforming a spherical wave into a plane wave so as to increase the directivity. In this section, an all-dielectric flat lens is realised as the second application example of the DCT technique. FDTD based numerical simulation has validated the performances of the transformation lens, in terms of the directive property and the broadband performance.

3.4.1 Dimensions and parameters

A dielectric convex lens can be applied at different frequencies at various polarizations. Here, again, we design an all-dielectric flat lens at the C-band and the X-band given the precondition of E-polarization. It is noted that although a dielectric lens is designed in 2D circumstance, when rotated to the optical axis, it becomes a 3D device [26]. Performance of the 3D flat lens will be validated in Section 5.3.

The section view of a conventional convex lens is shown in Fig. 3.15(a). This lens transforms a cylindrical wave from a line source located at its focal point (or a spherical wave from a point source in a 3D problem) to a plane wave at the other side. The sample convex lens is supposed to be made of isotropic homogeneous dielectric with $\varepsilon_r = 3$. It has an aperture of 160 mm (4.3 λ_0 at 8 GHz), and the two surfaces are arcs on a circle with radius equals to 300 mm. The thickness of the lens varies from 45.6 mm to 23.8 mm, from the center ($x = 0$) to the two sides ($x = \pm$ 80 mm). To be noted, this convex lens has the same dimensions as the one in Section 2.3.2.2. When the convex lens is compressed to a flat one, the thickness reduces to about 50%, as thin as the compressed

lens which was presented in Section 2.3.2.2 through the ACT technique.

A similar process as before is applied to design the all-dielectric flat lens. The conventional convex lens in the virtual space has been completely compressed into the flat physical space with half a thickness. Contrary to the boundary condition of the flat reflector, here the top and bottom boundaries in the virtual space are curves. Since the boundaries are different before and after transformation, if we want to grant the transformation lens the same property as the conventional lens, we should add transformation media surrounding the flat profile (filling region II in Fig. 3.15(b)) in order to maintain the transformation space and to palliate the impedance mismatching [27]. Unfortunately, such filling materials commonly have some permittivity values less than the unity, which will result in narrow-band performance. In addition, if we fix the boundaries before and after transformation, the flat lens will lose the benefit of small volume.

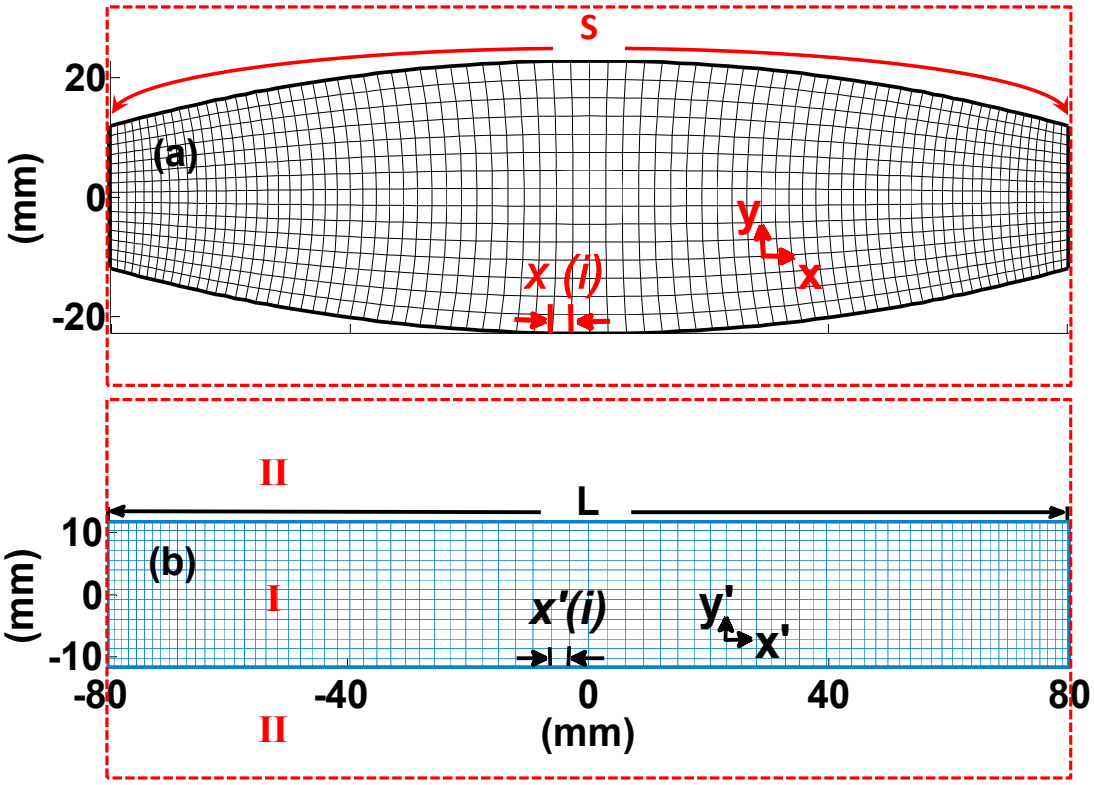

Figure 3.15: (a) The virtual space with distorted coordinates. A convex lens made of dielectric with $\varepsilon_r = 3$ is imbedded in the air. (b) The physical space with orthogonal coordinates. The transformation lens is inside region I.

It is obvious that both of the above two factors are of great importance in the broadband flat lens design. Therefore, we can assume that firstly a complete virtual space with air surrounding the convex lens (within the red box in Fig. 3.15(a)) is transformed to a physical space (within the red box in Fig. 3.15(b)), and then the materials with less-than-unity parameters in the physical space are replaced with the air. Therefore, the flat lens in the physical space can have a compact size and potentially broadband performance. As long as the reflection coefficient is acceptable, as will be proved, this approximation is valid in practice.

Similar procedures are carried out to generate a near-orthogonal grid in the distorted space. The convex lens is supposed to operate from 4 GHz to 12 GHz, and the wavelength inside the lens at 12 GHz is $\lambda_r = 14.4\ mm$. In the virtual space, the size of a cell on the left/right boundary is then chosen to be 1/9 λ_r, which is fine enough to discretise the space. To achieve a good orthogonality, the points are no longer averagely distributed on the top and bottom boundaries in Fig. 3.15(a). More points assemble at the four corners, resulting in smaller cells at the two sides and larger cells in the central area. In the physical space, the points on the top and bottom boundaries are determined in the same proportion as in the virtual space because x' is the projection of x. Note that since some cells in the physical space are not squares, the components of μ_{xx} and μ_{yy} have different values, implying the transformation media in the physical space become more anisotropic. Strictly speaking, the effective average refractive index has approximate values of $n'^2 \simeq \frac{1}{det(J)}$ in the central area and at the two sides. However, for a near-axis incidence, the isotropic approximation is acceptable, and the flat lens holds its performance, as will be demonstrated later.

The software of "GenGrid" is employed again to create the near-orthogonal grid following a similar procedure as before. The covariant metric g is calculated for each cell, in accordance with the scheme in Section 2.4. Fig. 3.16 shows the corresponding angle which determines the orthogonality of each cell. The FWHM index is 3.6°, indicating that local coordinate systems are fairly orthogonal and the proposed DCT technique

can be applied. The non-orthogonal cells which remain at the edges of the distribution in Fig. 3.16 are the ones located near the left/right boundary in the virtual space of Fig. 3.15(a). Within this approximation, we assume, as before, that $\partial x/\partial y$ and $\partial y/\partial x$ remain approximately close to zero.

In Fig. 3.17 the permittivity maps with different resolutions are presented, calculated by Eqs. (2.55) and (2.56). The high-resolution map in Fig. 3.17(a) is composed of 80 $\times$ 15 blocks, and each block is about 2 mm $\times$ 1.7 mm. Proper simplification is implemented to reduce the resolution using the same technique described in the previous section, and a low resolution permittivity map is exhibited in Fig. 3.17(b), consisting of 14 $\times$ 2 blocks sized 12.3 mm $\times$ 11.9 mm. This resolution has been investigated and validated, and the details will be presented in Chapter 5. The exact values of the relative permittivity map in Fig. 3.17(b) are reported in Table 3-B. Because the map is symmetric, only permittivity values in the right half of the map are provided. It is noted that the two rows of blocks have the same permittivity values, therefore the low-resolution map is in fact composed of 14 $\times$ 1 blocks.

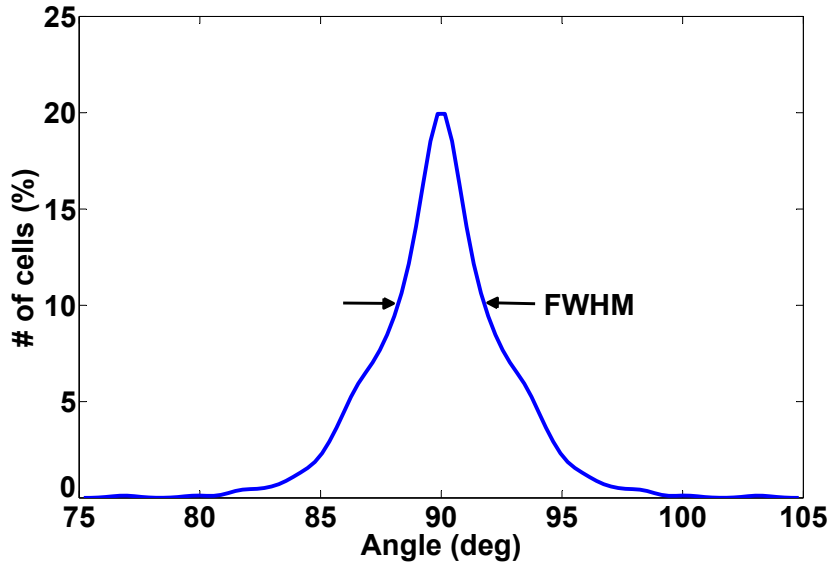

Figure 3.16: Distribution of the angle between two local coordinates in every cell of the virtual space. In this case the FWHM index is 3.6°, indicating that most of the local coordinates are near orthogonal.

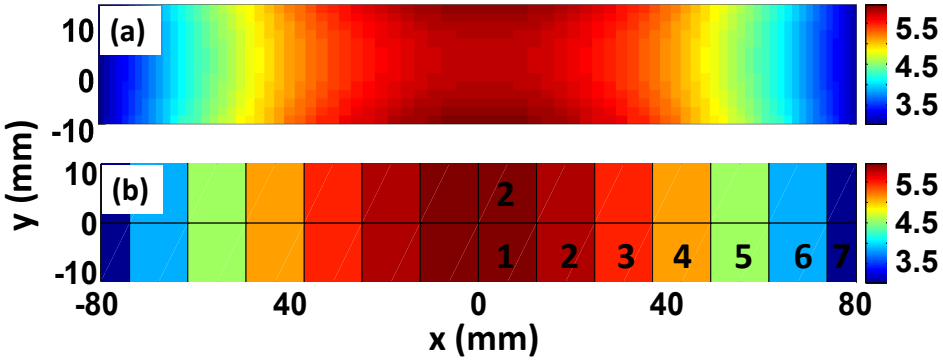

Figure 3.17: Permittivity maps of the flat lens. (a) The map consisting of 80 × 15 blocks, with each block sized 2 mm × 1.7 mm. (b) The map consisting of 14 × 2 blocks. The first and last columns have a width of 6.2 mm and the rest have a width of 12.3 mm.

Table 3-B: Relative permittivity values of the 14 × 2 dielectric blocks (right half)

		Column						
		1	2	3	4	5	6	7
Row	2	5.96	5.83	5.52	5.12	4.56	3.89	3.11
	1	5.96	5.83	5.52	5.12	4.56	3.89	3.11

3.4.2 Numerical verification

The FDTD method based simulations are employed to predict the performance of the designed flat lens. In Fig. 3.18 the real part of the electric field under different excitations are depicted. To test the focusing property of the 14×2-block low-resolution lens, we compare its field distribution (in Fig. 3.18(a)) with that of the conventional convex lens (in Fig. 3.18(b)), when a plane wave propagates along $+y$ direction to illuminate the devices. The focal length is measured from the center of the lens to the point with maximum amplitude. The flat lens has a focal length of 130 mm, whilst the conventional convex lens has a focal length of 131 mm. Apparently, the two lenses focus energy to almost the same position, even though their profiles are quite different. Next, line sources are placed on the focal points of the two lenses in order to generate plane waves on the other side. Two blocks of PEC are added to the left and right sides of the lens to prevent interference from leaky waves. Fig. 3.18(c) and 3.18(d) depict the real parts of the E_Z field when the low-resolution flat lens and the conventional lens are used, respectively.

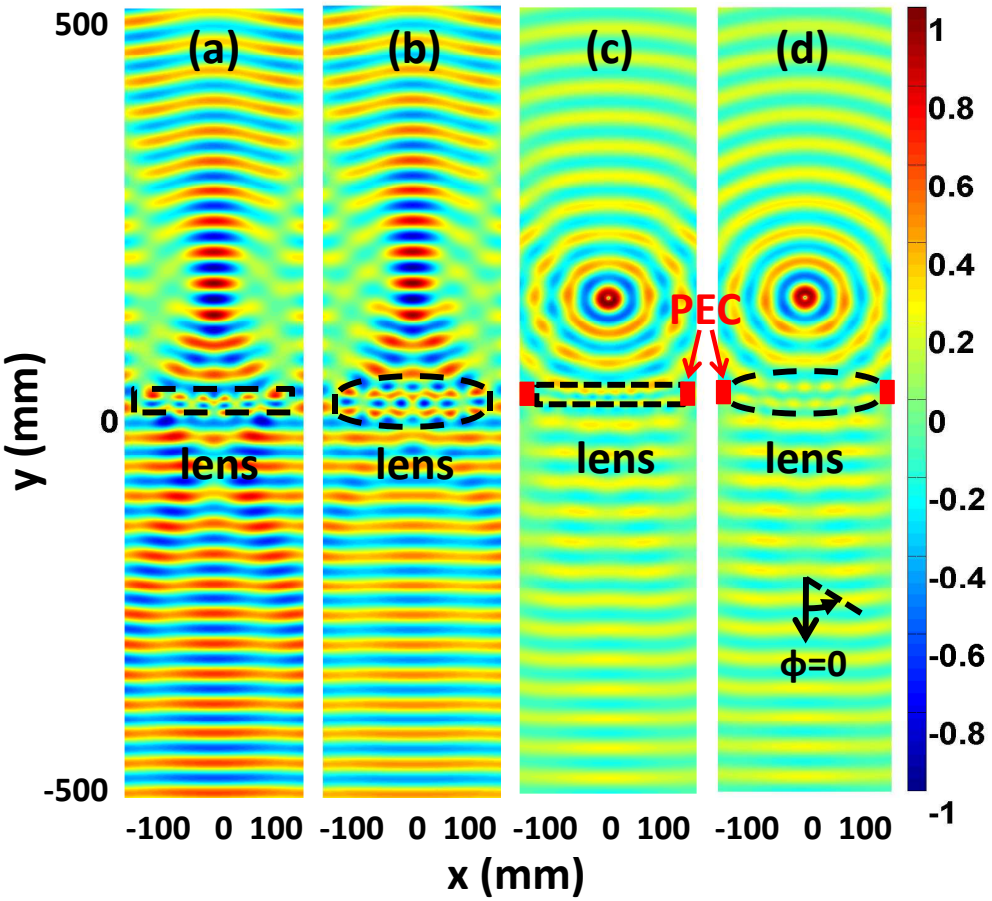

Figure 3.18: The real part of the E_z field at 8 GHz. (a) A plane wave illuminates the low-resolution flat lens from the bottom. The focal length is 130 mm. (b) The same plane wave illuminates the conventional lens from the bottom. The focal length is 131 mm. (c) A line source is located at the focal point to feed the low resolution flat lens. (d) A line source is located at the focal point to feed the conventional lens.

Indeed, plane waves are seen to emerge on the other side, which verifies the excellent performance of the simplified all-dielectric flat lens. Note also that the reflected waves are slightly stronger on the $y > 0$ side when the simplified flat lens is applied. This is because blocks with large permittivity values are located in the central area of the flat lens, causing a stronger impedance mismatching.

Fig. 3.19 depicts a comparison of the radiation patterns of the conventional lens and the two flat lenses with different resolutions. The flat lenses create highly directive beams around the radiating direction ($\phi = 0^o$ in Fig. 3.18(d)) similar as the convex lens does, but the energy in the direction of maximum radiation drops by about 20%. When the

resolution of the permittivity map decreases from 80 × 15 blocks to 14 × 2 blocks, the energy in the direction of $\phi = 0^o$ further drops to about 74% (-1.3 dB) of that of a convex lens, accompanied with slight increase of side lobes. The total radiating energy is also integrated from $\phi = -90^o$ to $\phi = 90^o$ and recorded in Table 3-C. When the convex lens is applied, the total radiating energy is 15.6501 arbitrary units. The two flat lenses have slightly lower radiating energy than the convex lens (85% and 92% respectively). The physical explanation is: the flat lenses have stronger impedance mismatching to the air because some dielectric blocks have higher permittivities than the convex lens.

Furthermore, radiation patterns of the flat lenses are tested at 4 GHz, 6 GHz, 10 GHz and 12 GHz to observe the influence of resolution on the operating bandwidth. Fig. 3.20 shows how the flat lenses with different resolutions have pretty similar radiation patterns when the operating frequency goes lower. When the operating frequency increases, the directive performance of the low-resolution lens begins to degrade slowly. The explanation for this deterioration can be found due to the fact that at a high frequency, the wavelength is smaller than the size of blocks in the low-resolution map, hence the flat lens no longer re-constructs the exact electromagnetic properties. However, the 14×2-block flat lens still obtains a decent performance over 4 GHz to 12 GHz. More study on the resolution will be presented in Chapter 5.

The reflection coefficient at the feed are also tested to measure the backscattering of the lenses. The devices are stimulated by wideband Gaussian pulses with a fixed bandwidth between 4 GHz to 12 GHz at the focal points and their reflections can be seen in Fig. 3.21. The reflection coefficient curves have similar shapes when the conventional convex lens, the 80×15-block, and the 14×2-block flat lenses are applied, but the flat lenses have higher reflections (about 5 dB increase) than the convex lens. This is also because at the central area of the flat lenses, permittivities are much higher than the value in the conventional lens, which causes an increased impedance mismatching to the air. However, the two flat lenses still have adequate performance in practice. When the resolution of the flat lens is reduced, the reflection keeps pretty similar over most of the

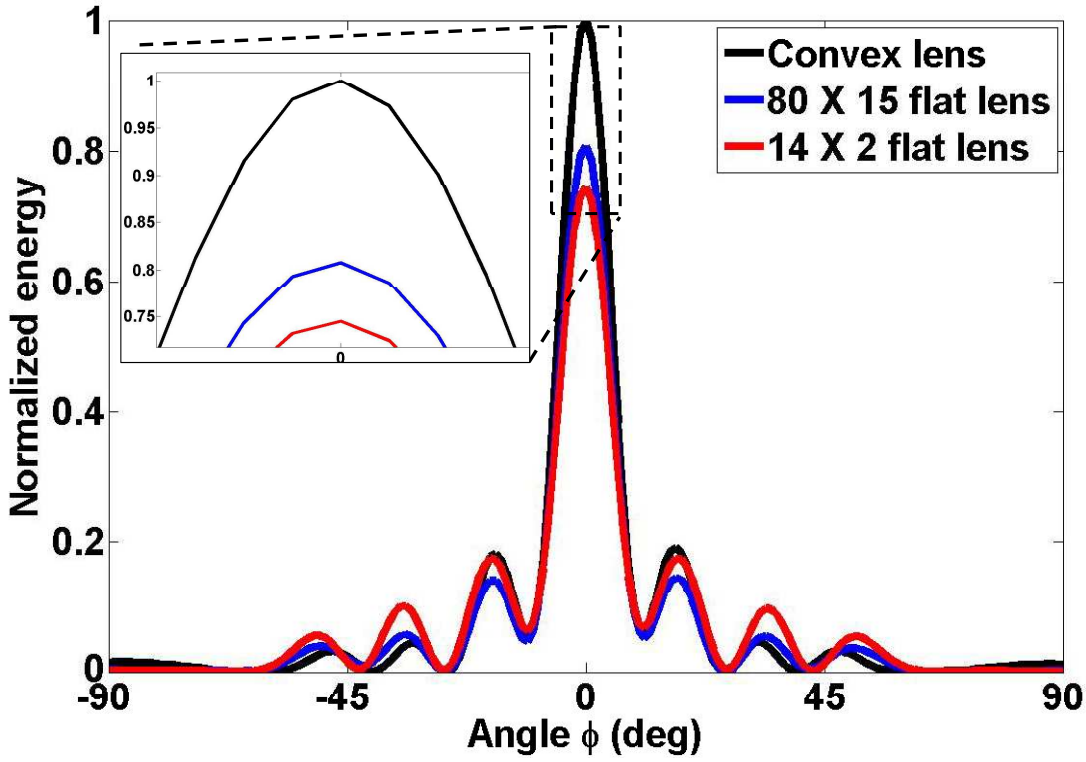

Figure 3.19: Comparison of the radiation patterns at 8 GHz. The definition of Φ is shown in Fig. 3.18(d).

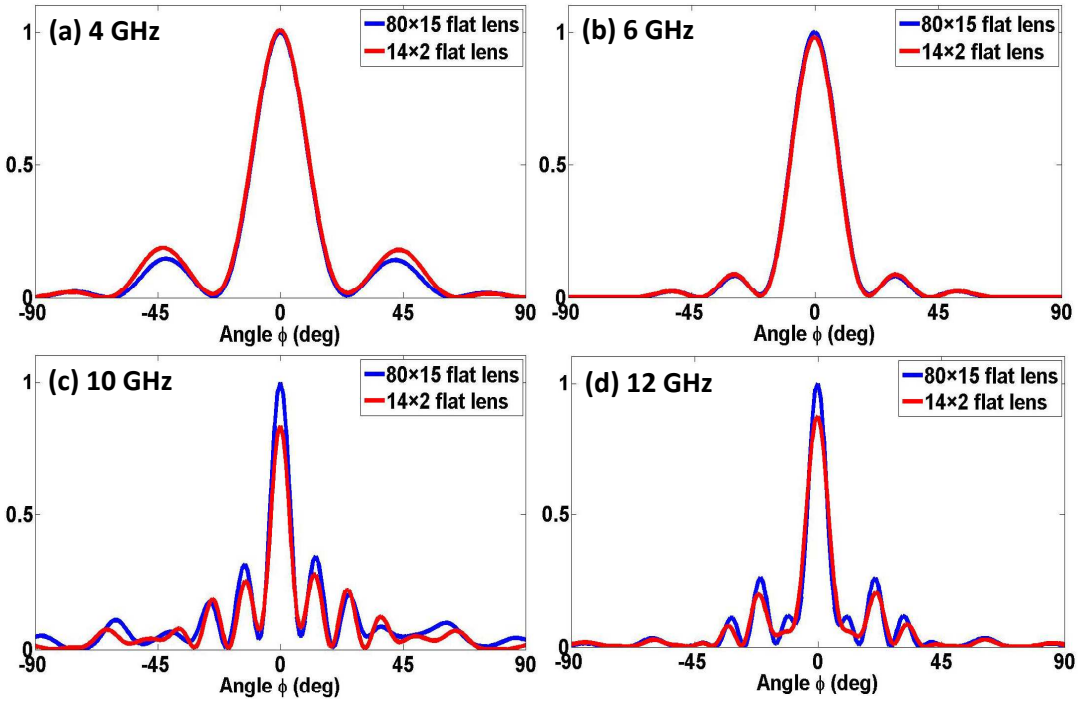

Figure 3.20: Comparison of the radiation patterns when the flat lenses are fed by a line source at the focal point. Two flat lenses with different resolutions (80×15-block and 14×2-block) are tested at 4 GHz, 6 GHz, 10 GHz and 12 GHz.

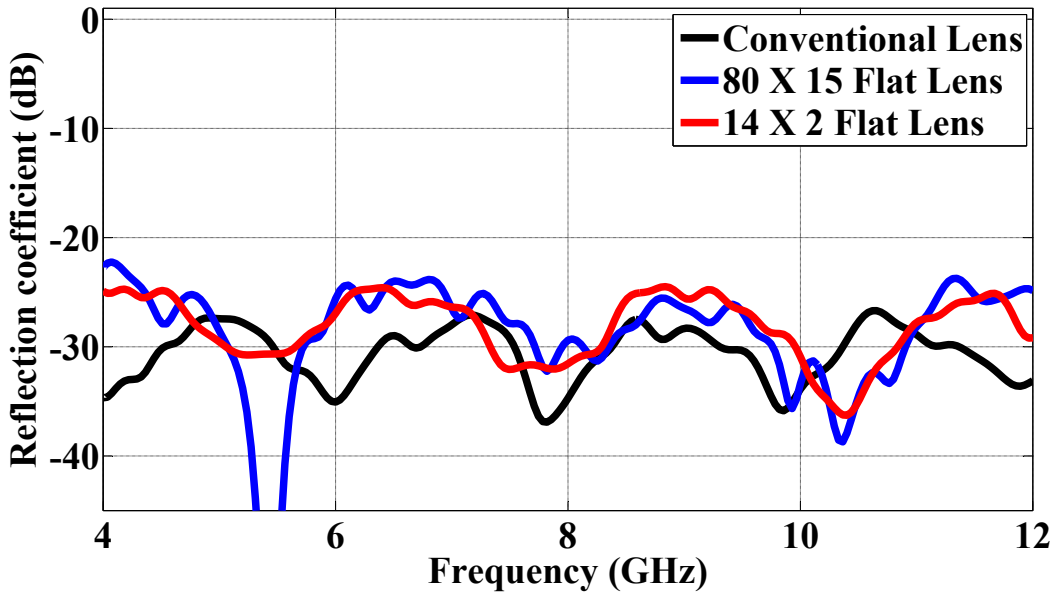

Figure 3.21: Comparison of the reflections between the conventional convex lens and the two flat lenses with different resolutions over 4-12 GHz. The lenses are stimulated by a wideband Gaussian pulse.

frequencies. Furthermore, some fluctuations are observed over the frequency band. This is because of the fact that when the distance between the source and the surface of the lens is even times of 1/4 λ_0, the reflected wave and the incident wave can cancel each other in the central area, leading to a low reflection coefficient. It is proved in Fig. 3.21 that the reflection of the conventional convex lens changes periodically in frequency, and the flat lenses retain this periodic property.

The numerical simulation results have proved that, although the 14×2-block flat lens has slightly worse performance than the high-resolution one, its directive property and operating bandwidth is considerably good. Furthermore, this flat lens requires only 7 different permittivity values due to its symmetric property, therefore is pretty apt to be constructed using dielectric blocks.

Table 3-C: Total radiating energy (normalised)

Case	Total energy (arb. units)
Convex lens	15.6501
80×15 flat lens	13.3063
14×2 flat lens	14.4214

3.5 Summary

In this chapter, the technique of discrete coordinate transformation was applied to create novel devices that are practically useful in antenna systems. The analytical coordinate transformation used for designing a cloak of invisibility requires the virtual space and the physical space to have the same boundary, and perform exact the same electromagnetic properties. We extended the concept from the coordinate transformation between two spaces to the coordinate transformation between two devices. Applying the DCT technique, two devices with different profiles can obtain the same electromagnetic performance. Therefore conventional antenna devices with curved surfaces can be replaced with flattened ones, which possess smaller volumes and can be easily manufactured.

A flat reflector and a flat lens were designed using this scheme as examples. Proper approximations were applied to remove the less-than-unity permittivities so as to achieve all-dielectric devices, under the condition that near-orthogonal transformation was achieved. Simplifications were also applied to reduce the resolution of the permittivity distribution, therefore the flat device became easily realisable. The FDTD method, combined with some extended configurations, were employed to numerically verify the predicted performance of the flat device. Simulation results have demonstrated very good agreement between transformation devices and the conventional ones. Besides, an alternative method to steer the radiation beam from the flat reflector was proposed, by changing the permittivity distribution inside the flat profile. In this way, no displacement or tilt between the feed and the reflector is required to control the radiation pattern, and therefore the system is shape-constant and position-fixed.

References

[1] U. Leonhardt, "Optical conformal mapping," *Science*, vol. 312, pp. 1777–1780, 2006.

[2] J. B. Pendry, D. Schurig, and D. R. Smith, "Controlling electromagnetic fields," *Science*, vol. 312, pp. 1780–1782, 2006.

[3] A. Taflove and S. C. Hagness, *Computational electrodynamics : the finite-difference time-domain method, 3rd Edition*. Artech House, 2005.

[4] Y. Hao and R. Mittra, *FDTD Modelling of Metamaterials: Theory and Applications*. Artech House, MA, 2009.

[5] Y. Zhao, C. Argyropoulos, and Y. Hao, "Full-wave finite-difference time-domain simulation of electromagnetic cloaking structures," *Opt. Express*, vol. 16, no. 9, pp. 6717–6730, 2008.

[6] C. Argyropoulos, Y. Zhao, and Y. Hao, "A radially-dependent dispersive finite-difference time-domain method for the evaluation of electromagnetic cloaks," *IEEE Trans. Ant. Propag.*, vol. 57, no. 5, pp. 1432–1441, 2009.

[7] CST, "3D EM Field Simulation-CST Computer Simulation Technology." http://www.cst.com.

[8] HFSS, "3D Full-wave Electromagnetic Field Simulation." http://www.ansoft.com/products/hf/hfss.

[9] COMSOL, "Multiphysics Modelling and Simulation." http://www.comsol.com.

[10] W. X. Jiang and T. J. Cui, "Optical transformation theory," in *Metamaterials: Theory, Design, and Applications*, T. J. Cui, R. P. Liu, and D. R. Smith, Eds. Springer, 2010, ch. 2, pp. 21–48.

[11] K. Yee, "Numerical solution of initial boundary value problems involving Maxwell's equations in isotropic media," *IEEE Trans. Ant. Propag.*, vol. 14, no. 3, pp. 302–307, 1966.

[12] J.-P. Bérenger, "A perfectly matched layer for the absorption of electromagnetic waves," *J. Comp. Phys.*, vol. 114, pp. 185–200, 1994.

[13] P. Harms, R. Mittra, and W. Ko, "Implementation of the periodic boundary condition in the finite-difference time-domain algorithm for fss structures," *Antennas and Propagation, IEEE Transactions on*, vol. 42, no. 9, pp. 1317–1324, 1994.

[14] G. Turner and C. Christodoulou, "Broadband periodic boundary condition for fdtd analysis of phased array antennas," in *Antennas and Propagation Society Interna-*

tional Symposium, 1998. IEEE, vol. 2. IEEE, 1998, pp. 1020–1023.

[15] P. Kildal, "Artificially soft and hard surfaces in electromagnetics," *IEEE Trans. Ant. Propag.*, vol. 38, no. 10, pp. 1537–1544, 1990.

[16] F. B. Hildebrad, "Introduction to Numerical Analysis," *NY: McGraw-Hill*, 1956.

[17] D. Pozar, *Microwave Engineering, 3rd.* John Wiley & Sons, Hoboken, NJ, USA, 2005.

[18] J. Kraus, *Antennas.* McGraw-Hill Education, 1988.

[19] D. Bao, K. Rajab, Y. Hao, E. Kallos, W. Tang, C. Argyropoulos, Y. Piao, and S. Yang, "All-dielectric invisibility cloaks made of batio3-loaded polyurethane foam," *New J. of Phys.*, vol. 13, p. 103023, 2011.

[20] H. Ma, W. Jiang, X. Yang, X. Zhou, and T. Cui, "Compact-sized and broadband carpet cloak and free-space cloak," *Opt. Express*, vol. 17, no. 22, pp. 19 947–19 959, 2009.

[21] W. Tang, C. Argyropoulos, E. Kallos, W. Song, and Y. Hao, "Discrete coordinate transformation for designing all-dielectric flat antennas," *IEEE Trans. Ant. Propag.*, vol. 58, no. 12, pp. 3795–3804, 2010.

[22] E. Kallos, C. Argyropoulos, and Y. Hao, "Ground-plane quasicloaking for free space," *Phys. Rev. A*, vol. 79, no. 6, p. 63825, 2009.

[23] C. Shannon, "Communication in the presence of noise," *Proc. IRE*, vol. 37, no. 1, pp. 10–21, 1949.

[24] S. Silver, *Microwave antenna theory and design.* Inspec/Iee, 1984, vol. 19.

[25] R. Yang, W. Tang, and Y. Hao, "Wideband beam-steerable flat reflectors via transformation optics," *Ant. Wireless Propag. Lett., IEEE*, vol. 10.

[26] ——, "A broadband zone plate lens from transformation optics," *Opt. Express*, vol. 19, no. 13, pp. 12 348–12 355, 2011.

[27] M. Yan, Z. Ruan, and M. Qiu, "Scattering characteristics of simplified cylindrical invisibility cloaks," *Opt. Express*, vol. 15, no. 26, pp. 17 772–17 782, 2007.

Chapter 4

Novel Functional Devices from the Control of Coordinate Transformation

4.1 Introduction

In Chapter 3, the technique of discrete coordinate transformation (DCT) was used to design flat devices from conventional ones which have curved surfaces. The principle behind these designs is to change the profile of a space but maintain its electromagnetic properties by engineering its background materials. Here, in this chapter, another approach to create new devices will be proposed and investigated. Instead of knowing an "existing" prototype of the device and modifying it into other forms, we will generate novel functional devices which are not found from conventional ones. This is achieved through controlled modification of the propagation path of the wave, and, consequently, through generation of a corresponding coordinate transformation to yield required material properties. The resulting design will lead to functional devices which have pre-specified electromagnetic performances.

In this chapter, two new devices will be proposed using the above approach. The first one is a combined system of a carpet cloak and a conducting cavity. Aside from concealing the cavity underneath, the carpet cloak itself works as a dielectric lens transforming the spherical waves generated from an antenna source inside the spherical cavity to quasi-plane waves. Therefore the hybrid structure operates as an undetectable antenna on the ground. Numerical simulations will be used to verify this design, and the approach towards physical construction will be discussed. The second application is an all-dielectric device for demonstrating extraordinarily enhanced transmission through a sub-wavelength slit. We will prove that by using this device, significantly increased transmission through a sub-wavelength aperture is achievable from 4 GHz to 8 GHz. A simplified device will be tested in an X-band waveguide, and the measured results will be used to validate the design and simulation results.

4.2 An Undetectable Combined Antenna Using a Carpet Cloak and a Cavity

In this section, we explore the new function of the carpet cloak as a new type of stealth radome to protect antennas. The carpet cloak has been introduced to conceal an object on the ground plane, as illustrated in Fig. 2.10 [1, 2]. A conducting bump under the carpet is undetectable to an outside observer because detecting incident waves cannot reach it. However, any radiation from beneath the carpet cloak cannot radiate outwards because it is reflected by the conducting surface of the bump on the bottom boundary of the carpet cloak. Aiming at this issue, we propose a technique called the "virtual boundary". Specifically, a spherical conducting cavity is located under the carpet cloak serving as a "virtual boundary", which can efficiently replace the conducting surface of the bump while reflecting the electromagnetic waves in the same wave as the bump does. Any external incidence on the carpet will see this configuration as a bare ground, and therefore, the combination of the carpet cloak and the conducting cavity is undetectable.

In a contrary manner, small probes inside the cavity can receive signals and sense the external incidence. Furthermore, the carpet cloak itself can be applied to operate as a beam-forming lens that converts spherical waves originated by the cavity into plane waves, and consequently generates directive beams even from a simple isotropic feed (e.g., a point source in three-dimensional (3D) circumstance or a line source in two-dimensional (2D) circumstance).

4.2.1 Method and design

4.2.1.1 Design of a carpet cloak

First of all, a carpet cloak is designed in the X-band to conceal a conducting bump with the shape of one quarter of a sphere. A 2D section view of the physical space that functions as a carpet cloak is shown in Fig. 4.1. The solid bold red line represents

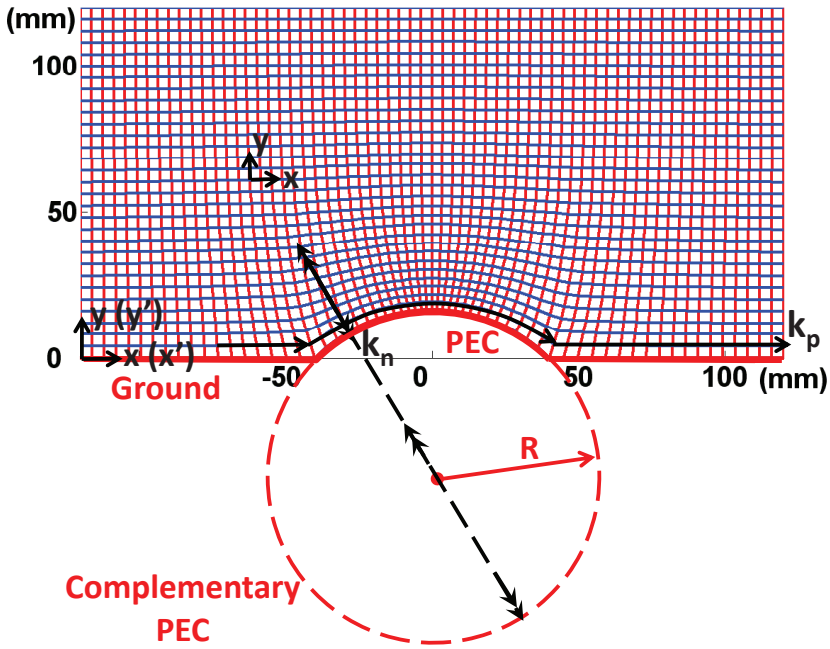

Figure 4.1: The 2D section view of the physical space that functions as a carpet cloak. The solid bold red line represents the perfect electric conductor (PEC) bump on the ground, with the shape of one quarter of a sphere. The dashed red line represents a spherical conducting cavity located underneath the carpet. The cavity is defined here as the "complementary PEC" to the PEC bump because they together complete a sphere. The radius of the sphere is 56.6 mm.

the bump, which can be viewed as a perfect electric conductor (PEC), and, sits on the bottom boundary of the carpet cloak. The size of the carpet cloak is 240 mm $\times$ 120 mm, and the radius of the sphere (marked as R in Fig. 4.1) is 56.6 mm.

According to the theory of discrete coordinate transformation, if the gird in Fig. 4.1 is carefully designed to be near-orthogonal, this distorted space can be realised by filling the background with spatially-dispersive dielectrics. The same procedure as that presented in Section 2.4 is carried out to generate a near-orthogonal grid. The orthogonality of the cell is again quantified by calculating the angle between two local coordinates in every cell. The distribution of the angle in degree is plotted in Fig. 4.2. It is observed that the full width at half maximum (FWHM) index of the distribution is only 2^o, indicating these local coordinate systems are indeed near-orthogonal. Thus, the orthogonal condition, which is vital to the performance of the carpet cloak, is approximately satisfied.

The relative permittivity map is obtained following a similar procedure as explained in Chapters 2 and 3. The map is given in Fig. 4.3. The coordinate transformation produces special regions at the bottom around $x = 40$ mm and $x = -40$ mm where the permittivity values are less than the unity. Two steps of simplification, as applied in Chapter 3, have been executed to render this carpet cloak more practical to realise. First, since most less-than-unity values are not very low, and the special regions are electrically small (no larger than $1/2$ λ_0 in the X-band), it is a safe approximation to set the values to ε_0. As we discussed before, this approximation may slightly damage the performance, but it guarantees a broad operating bandwidth. Second, a low-resolution map is generated in Fig. 4.3(b), which consists of 22×12 large blocks with dimensions less than $1/2$ λ_0 in the X-band. This resolution will be proved sufficient later through numerical simulations. It should be pointed out that in the rest of this section, demonstration of this design is primarily for 2D problems with an E-polarization (E_z, H_x, H_y). A 3D model is achievable by rotating the 2D model to the y axis (defined in Fig. 4.3). Since the rotated 3D device is symmetric and made of isotropic materials, it works for any polarization as long as the propagating direction is not parallel to the $x - z$ plane.

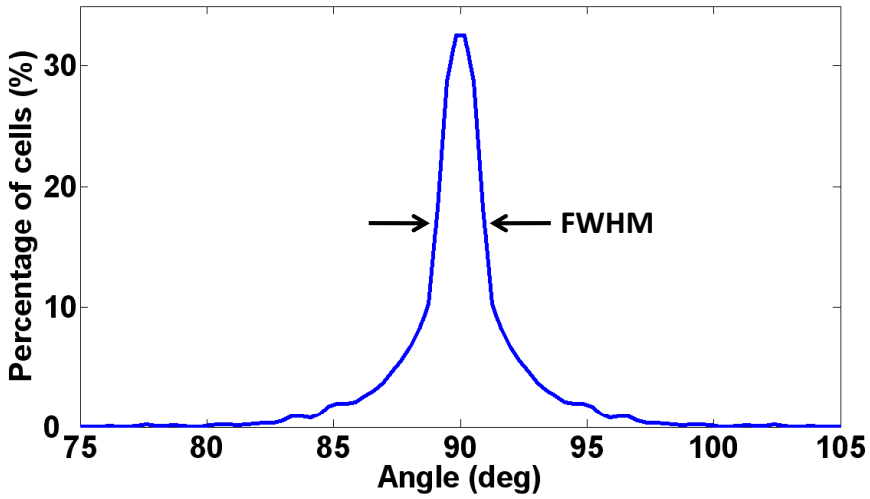

Figure 4.2: The distribution of the angle between two local coordinates of each cell. The FWHM index is only 2^{o}.

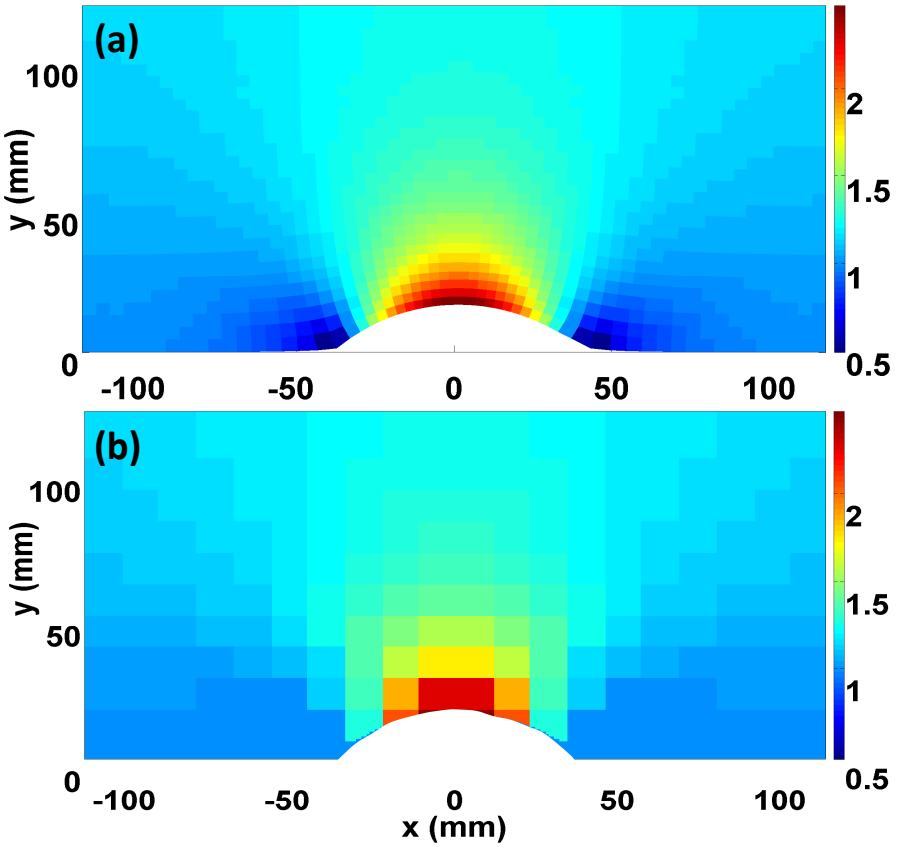

Figure 4.3: Relative permittivity maps of the carpet cloak. (a) High resolution map. (b) Simplified low-resolution map consisting of 22×12 dielectric blocks. The color bar shows the values of the relative permittivity.

4.2.1.2 The "virtual boundary" technique

Fig. 4.1 illustrates how a carpet cloak serves to conceal a PEC bump located on the ground. Inside the carpet cloak, travelling paths of an incident electromagnetic wave can be represented using the discrete coordinate system. The wave vector k, which indicates the direction of propagation, has two components along the two local coordinates in every cell: (i) the longitudinal coordinate (shown in red in Fig. 4.1), and (ii) the latitudinal coordinate (shown in blue). If the grid shown in Fig. 4.1 is strictly orthogonal, the longitudinal component of an incident wave would travel vertically downward, impinging normally on the bottom boundary of the carpet cloak and on the PEC bump. Also, it would be reflected back in the opposite direction, travelling back along the same path, as depicted by solid double-arrows in Fig. 4.1. Meanwhile, the latitudinal component would travel circumscribing the bump, following the lines tagged by single arrows. As a result, to an outside observer, the reflection from the carpet cloak would appear to be the same as that from an empty ground plane; and therefore, the bump on the ground is undetectable.

Although an object hidden under the PEC bump is undetectable, it cannot transmit or receive signals as an antenna. To handle this problem, we propose a concept called the "virtual boundary." In Fig. 4.1, the solid bold red line represents the PEC bump on the ground, with the shape of one quarter of a sphere. The dashed red line represents a spherical conducting cavity located under the ground. The cavity is defined here as the "complementary PEC" to the PEC bump because they together complete a sphere. If the PEC bump is replaced with the "complementary PEC," the longitudinal component of an incident wave can travel into the cavity and pass through the center of it. It is then reflected by the wall of the cavity and re-enter the carpet cloak perpendicularly from the bottom (as shown with the dashed black lines tagged by double arrows). Meanwhile, the latitudinal component of the incident wave travels along the latitudinal coordinate as before. With this arrangement, the "complementary PEC" can replace the PEC bump, working as a "virtual" conducting bottom boundary to the carpet cloak and reflecting

an incident wave in the same way as the PEC bump does. The space between the carpet cloak and the wall of the cavity is therefore concealed from external observers.

One possible problem with this scheme is the phase delay when the "complementary PEC" is employed. If the local coordinates are strictly orthogonal, at frequencies for which the cavity radius R is related to the wavelength λ_0 as follows:

$$4R = n\lambda_0 \quad (n = 1, 2, 3, ...), \tag{4.1}$$

the phase delay is eliminated and the "complementary PEC" works exactly as the PEC bump located at the bottom of the carpet cloak. At other frequencies, the phase delay will introduce scatterings because the phase front of reflected waves would no longer be uniform. The worst situation occurs when

$$4R = n\lambda_0 + 0.5\lambda_0 \quad (n = 1, 2, 3, ...). \tag{4.2}$$

Table 4-A lists the best frequency points which satisfy Eq. (4.1) and the worst frequency points which satisfy Eq. (4.2) within the X-band when the radius of cavity is 56.6 mm. Scattering caused by the phase delay can be viewed as though it is originating from a shallow pit in the ground, which is no deeper than $\lambda_0/4$ (eg., 7.5 mm at 10 GHz). In our design, the real depth of the cavity is 96.6 mm, so the equivalent depth is decreased by about 90%. Therefore, although the "virtual boundary" technique is not perfect over the entire operating frequency band, scattering from the deep cavity is effectively reduced. Furthermore, if the local coordinates are not perfectly orthogonal, an oblique incidence will be repeatedly reflected by the wall of the cavity. As a result, the theoretical prediction in Table 4-A may vary in practice.

Table 4-A: Frequencies of the best/worst concealing performance.

Best frequency point (GHz)	9.28	10.61	11.93
Worst frequency point (GHz)	8.62	9.94	11.27

4.2.1.3 Cylindrical-to-plane wave transformation

The conducting cavity can generate spherical waves when fed by a point source in the center. In the 2D circumstance as investigated in this section, a line source is applied and the transmitted cylindrical wave has a phase front parallel to the bottom profile of the carpet cloak. This means, when the cylindrical wave enters the carpet, the wave vector k only has the longitudinal component in the discrete coordinate system shown in Fig. 4.1. Within the carpet cloak, the cylindrical wave travels upwards along the longitudinal coordinates, with the latitudinal component of the wave vector remaining zero. When the wave finally leaves the carpet cloak from the top, the wave vector is in the manner of a plane wave, therefore the cylindrical wave is transformed into a plane wave. In this way, the carpet cloak itself works as a special beam-forming lens to create highly directive beams. In practice, a probe is located at the center as a line source. In the X-band, the diameter of a probe can be less than 1 mm, which is only about 1/30 of the wavelength; hence, this sub-wavelength conductor has almost no effect on the scattering patterns.

It is noted that the cavity has a periodic radiating performance over frequencies. At

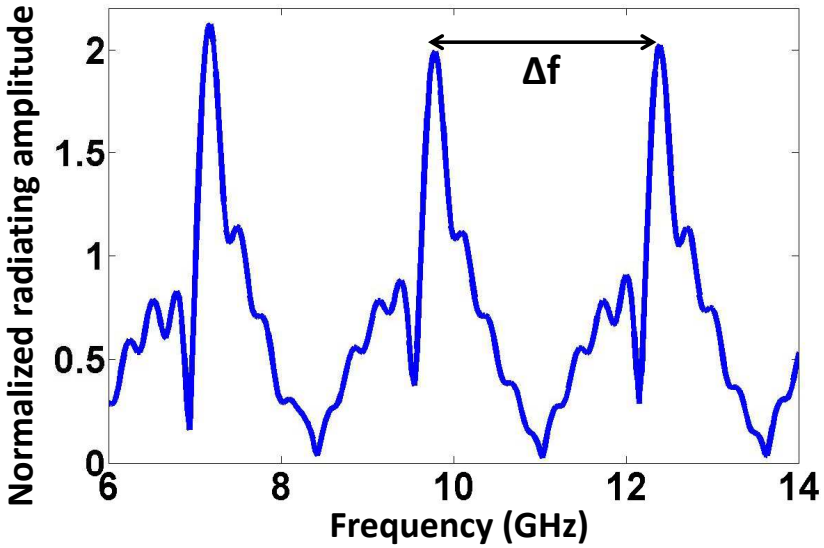

Figure 4.4: The radiating performance of the cylindrical cavity from 6 GHz to 14 GHz. Δf is about 2.65 GHz.

some frequencies, the cylindrical wave generated from the line source is eliminated by the waves reflected by the wall of the cavity, while at other frequencies it is enhanced by the reflected waves. The period Δf is expected to satisfy the equation

$$\Delta f \frac{2R}{c} 2\pi = 2\pi, \tag{4.3}$$

where R is the radius of the cavity which is 56.6 mm here, and c is the speed of light in vacuum. The Finite-Difference Time-Domain (FDTD) method presented in Chapter 3 has been employed to numerically test the radiating property of the cavity. A Gaussian pulse is generated at the center to stimulate the cavity, and the energy transmitted outside the cavity is recorded. Fig. 4.4 shows the radiating performance of the cavity from 6 GHz to 14 GHz. Obviously, the amplitude of the radiating field (E_z) varies between 0 to 2 and has a period of $\Delta f \approx 2.65$ GHz, which agrees well with Eq. (4.3). The fluctuation on the curve is because of the reflections at the edges of the cavity. This periodic radiating performance of the cavity will bring in some essential limitation of bandwidth to the hybrid antenna system, as will be studied in the next sub-section.

4.2.2 Numerical verification

4.2.2.1 The concealing performance

FDTD-based numerical simulations are employed in this sub-section to predict the performance of the design. We begin by evaluating the concealing performance of the carpet cloak and the efficacy of the "virtual boundary" technique. We choose one of the "best" frequency points in Table 4-A, namely 10.61 GHz, for the demonstration. The electric field distribution at 10.61 GHz is depicted in Fig. 4.5. In Fig. 4.5 (a), the carpet cloak shown in Fig. 4.3 (a) is located in the dashed black box on the ground above the cavity. All relative permittivity values less than one are approximated as one so as to avoid the use of resonant metamaterials in the design. A plane wave impinges from top left, with an incident angle of $\varphi = 135^o$ (φ defined in Fig. 4.5(a)). The incident wave is

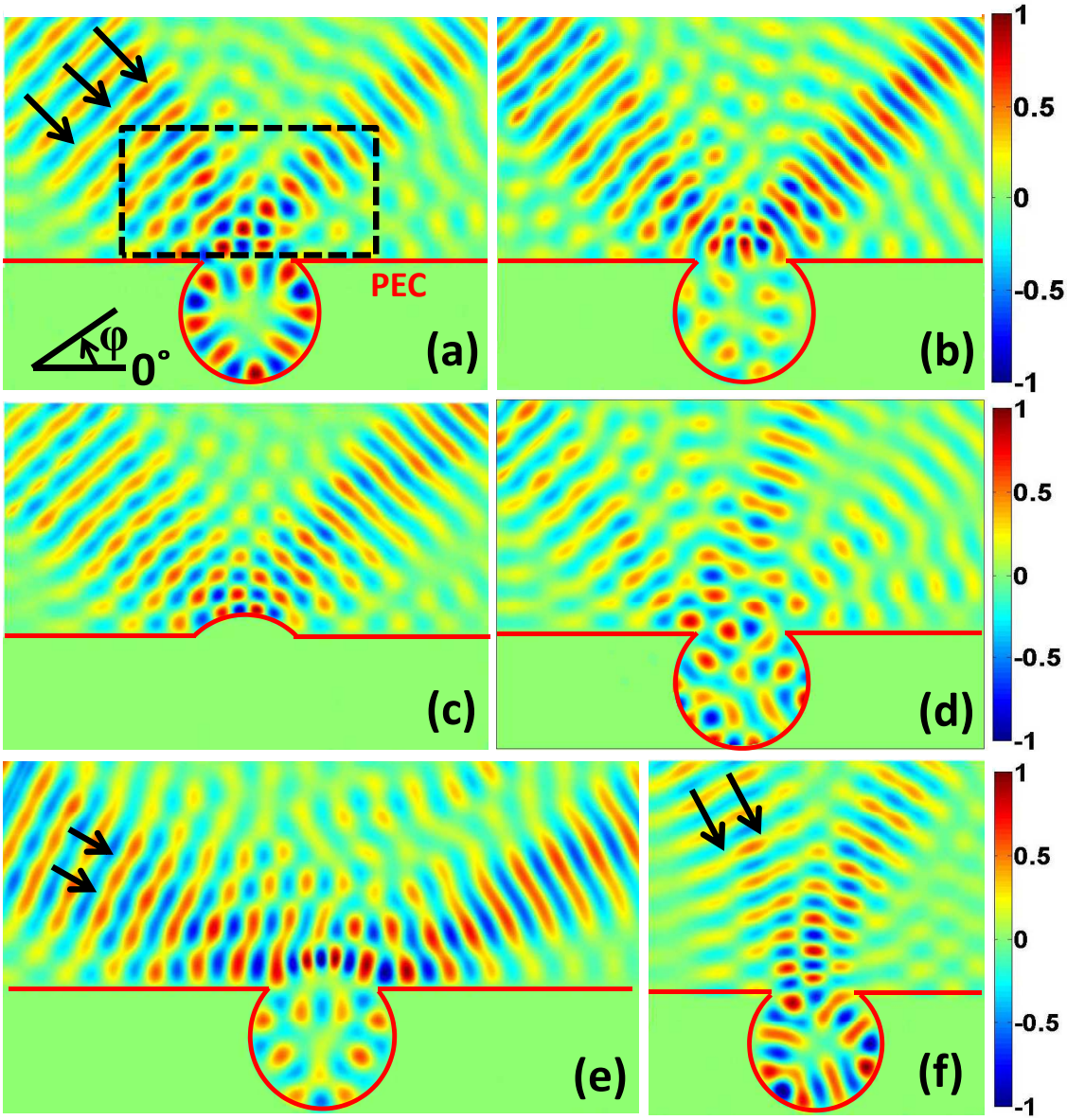

Figure 4.5: Electric field distributions with different configurations at 10.61 GHz. (a) A $\varphi = 135^o$ incidence impinges on the carpet cloak plus cavity combination. The permittivity map of the carpet is shown in Fig. 4.3(a), but all relative permittivity values less than one are approximated as one. (b) A 135^o incidence impinges on the carpet cloak plus cavity combination. The permittivity map is with low resolution, as shown in Fig. 4.3(b). (c) A 135^o incidence impinges on the carpet cloak plus PEC bump combination. (d) A 135^o incidence impinges on the bare cavity without the carpet cloak. (e) A 154^o incidence impinges on the carpet cloak plus cavity combination. (f) A 117^o incidence impinges on the carpet cloak plus cavity combination. The permittivity map in (e) and (f) are the same as in (b).

expected to be reflected exactly to $\varphi = 45^o$ as if it happens with a bare ground. Fig. 4.5 (a) shows that the reflection is concentrated around $\varphi = 45^o$, and includes some weak scatterings to other directions. When the simplified map in Fig. 4.3 (b) is applied above the cavity, the field distribution in Fig. 4.5 (b) shows slightly stronger scatterings to directions other than $\varphi = 45^o$. The scatterings are mainly attributed to the increase of refractions and reflections between neighbouring dielectric blocks when the permittivity map has a low resolution. Figures (a) and (b) have proved that the low-resolution map can almost maintain the performance of the carpet cloak as long as the dielectric blocks are smaller than half the wavelength. When the size of blocks increases, the scattering will increase and the concealing performance will be gradually destroyed. Fig. 4.5(c) presents the field distribution when the PEC bump, instead of the cavity, is located below the carpet cloak. Reflection to the direction of $\varphi = 45^o$ is indeed similar to those in (a) and (b), which proves the proposed "virtual boundary" technique is working as expected. Fig. 4.5(d) shows the case when the carpet cloak is removed and the cavity is exposed to the external incidence. Scatterings are enhanced significantly. Furthermore, in figures (e) and (f), incidences from $\varphi = 154^o$ and $\varphi = 117^o$ are also employed to test the design. More scatterings are observed in (e) when the incident direction moves towards the ground. This degraded concealing performance is due to the neglect of less-than-unity permittivities. With this incident direction, more of the incidence is focused on the neglected area; hence, the carpet cloak slightly loses its property. However, most of the incident energy is still reflected towards $\varphi = 26^o$. Fig. 4.5(f) also proves that the incident wave from $\varphi = 117^o$ is mostly reflected towards $\varphi = 63^o$.

To test the proposed broadband concealing performance, scattering patterns are plotted in Fig. 4.6 at random frequencies other than those listed in Table 4-A. The figure shows the angular distribution of the reflected waves (as recorded along a one-quarter circle 200 mm away from the origin point) when different incidences are launched at 8, 9, 10 and 12 GHz, respectively. The solid black curves represent the cases when the carpet cloak plus cavity combination is applied at an incidence of $\varphi = 135^o$, which is expected

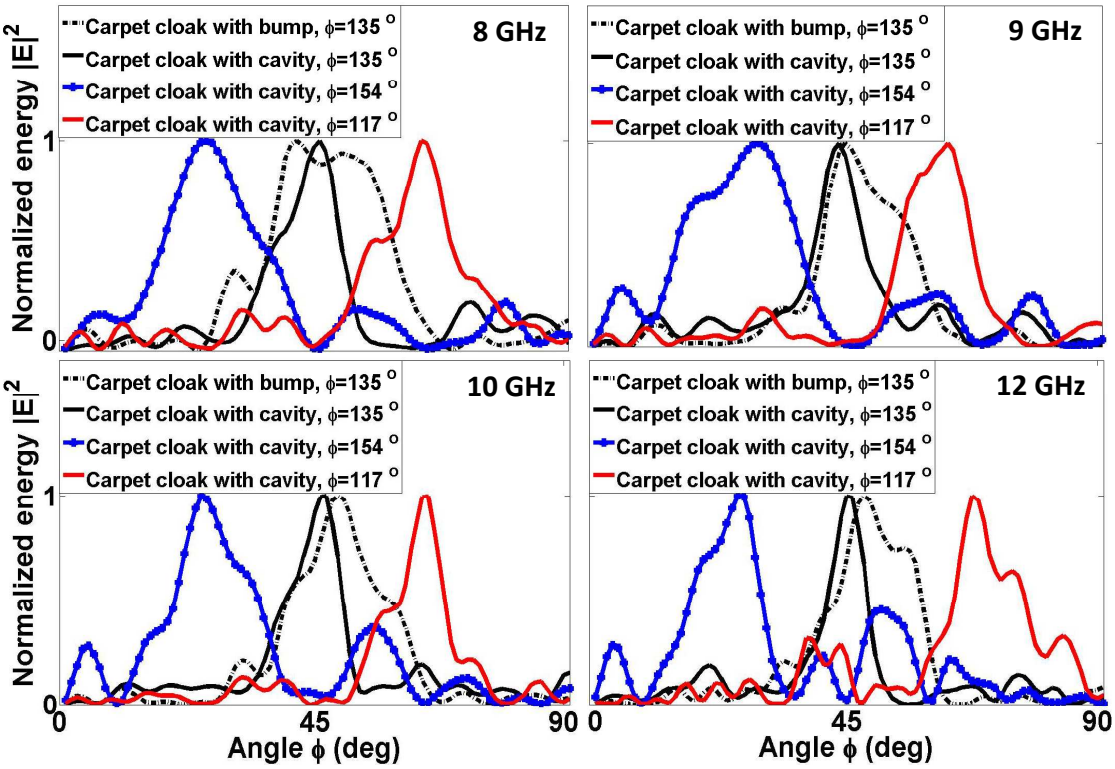

Figure 4.6: Angular distribution of the reflected field with different incidences over the X-band.

to be similar to the dashed black curves that represent the cases when the carpet cloak plus PEC bump combination is applied. Although the two curves look different, for both configurations, most incident waves are reflected to the direction around $\varphi = 45^o$ at all frequencies. Slightly higher side lobes are observed when the cavity is employed. Explanation to this degradation is when areas with less-than-unity permittivities are neglected, the longitudinal components of some incidences are no longer guided exactly normal to the bottom boundary of the carpet cloak. As a result, multiple reflection occurs in the cavity and part of the energy goes to other directions. The solid blue curves and solid red curves represent the cases when the incident direction is $\varphi = 154^o$ and $\varphi = 117^o$ respectively. According to the plot, the primary directions of reflection are $\varphi = 26^o$ and $\varphi = 63^o$, respectively. Some increased scatterings, especially when the incident direction is $\varphi = 154^o$, are found in other directions, which is also due to the simplification of the permittivity map.

4.2.2.2 The radiating performance

The radiating performance of the carpet cloak plus cavity combination is another important characteristic to be validated. We choose one random frequency, e.g. 10 GHz, to show how the carpet cloak serves as a beam-forming lens. Fig. 4.7(a) depicts the real part of electric field when a line source is located at the center of the cavity and the simplified carpet cloak in Fig. 4.3(b) is placed above the cavity. Clearly, the cylindrical wave emanating from the line source has been transformed into a quasi-plane wave by the carpet cloak, and most of the energy has been directed to the radiating direction of $\varphi = 90^o$. For comparison, Fig. 4.7(b) presents the field distribution when the carpet cloak is removed and the cavity radiates directly into the free space. Obviously, without the carpet cloak, the cavity cannot create highly directive beams.

Furthermore, the broadband performance of this design is tested from 8 GHz to 12 GHz. As shown in Fig. 4.4, the cavity itself is a band-pass radiator, transmitting signals in a periodic manner. As a result, although the concealing performance of the combination has been proved broadband, the radiating performance of this design is

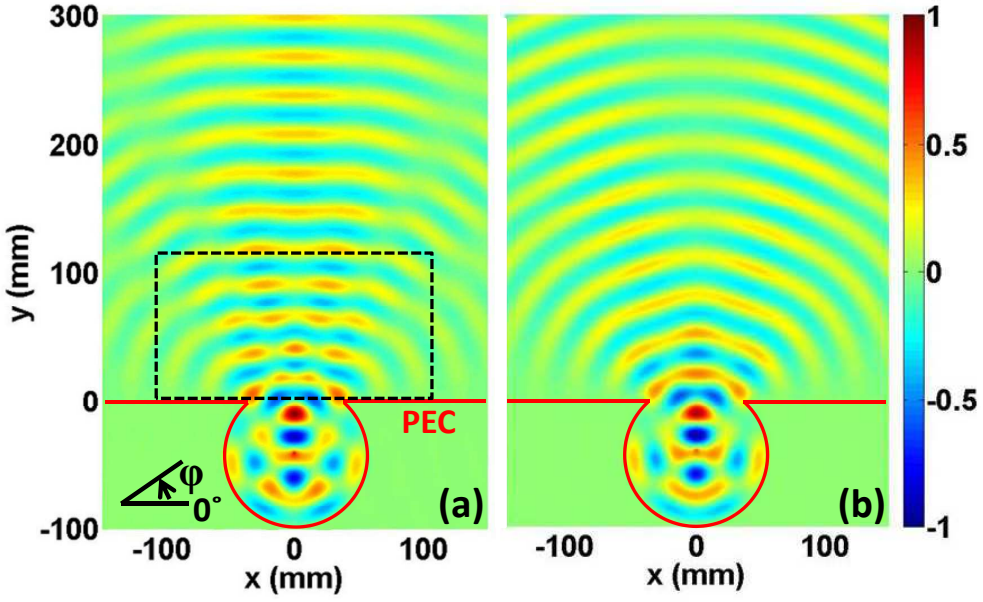

Figure 4.7: Electric field distributions at 10 GHz. (a) The carpet cloak plus cavity combination is stimulated by a line source located at the center of the cavity. The carpet cloak is placed inside the dashed black box. (b) The carpet cloak is removed and only the cavity is illuminated by the line source.

limited due to the essential property of the cavity. Fig. 4.8 shows the angular distribution of radiating energy before and after the carpet cloak is applied above the cavity. The energy is recorded along a semicircle 200 mm away from the origin point at frequencies of 8, 9, 10, 11 and 12 GHz. In Fig. 4.8(a), radiating ability of the cavity varies at different frequencies, with the maximum radiation occurring at 10 GHz and the minimum radiation occurring at 11 GHz, which agrees very well with Fig. 4.4. According to the radiation patterns in figure (a), the beam generated by the cavity is not directive all over the X-band. However, once the carpet cloak is added above the cavity, the beam becomes always directive, as shown in figure (b). Most of the radiating energy is concentrated to the radiating direction of $\varphi = 90^o$. Side lobes are mainly due to the simplifications. In

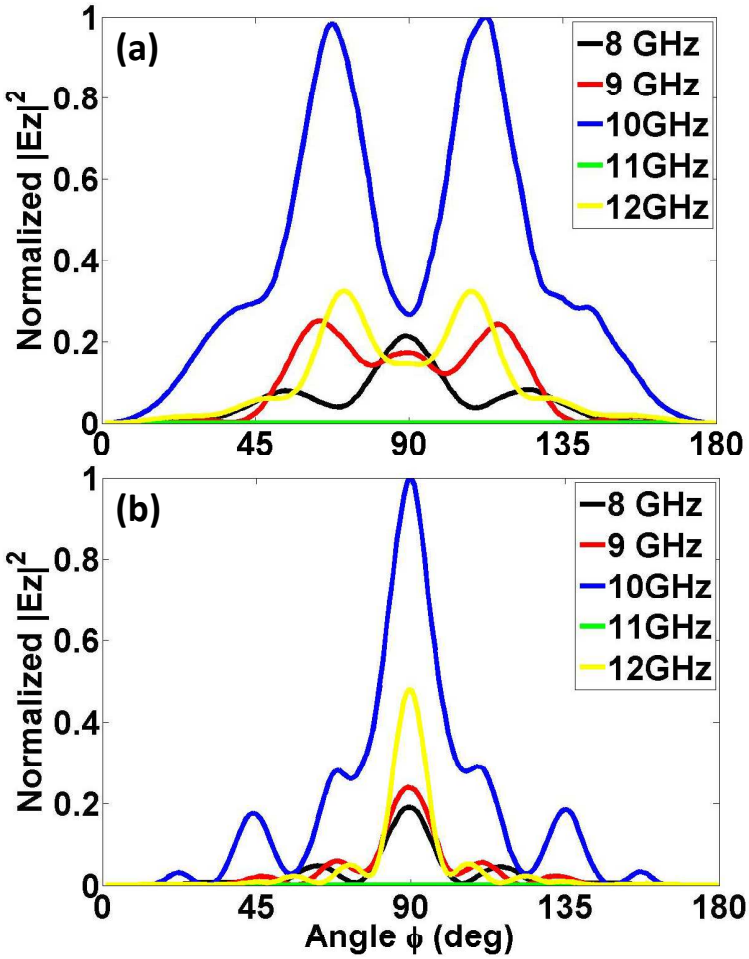

Figure 4.8: (a) Angular distribution of radiating energy from a cavity at 8, 9, 10, 11 and 12 GHz. (b) Angular distribution of radiating energy at 8, 9, 10, 11 and 12 GHz when the carpet is applied above the cavity.

conclusion, although the carpet cloak cannot increase the amplitude of radiation from the cavity, it serves to re-form a directive beam at all frequencies. In other words, the combination of the carpet cloak and cavity has a periodic bandwidth limitation, but the carpet cloak itself has been demonstrated to function as a beam-forming lens from 8 GHz to 12 GHz.

4.2.2.3 Comparison with an FSS radome

In the past, stealth radomes that use frequency selective surfaces (FSSs) have been developed to protect antennas from external detection [3]. An FSS is a bandpass filter, which is placed in front of a single antenna or an antenna array to reduce its radar cross section (RCS) [4]. The radome is transparent to electromagnetic waves within its pass-band; hence, the antenna behind it can freely receive, as well as transmit, signals within this band. In addition, it serves to ensure that the antenna/radome combination has a low RCS and therefore is difficult to detect. Alternatively, in the stop-band, the radome mimics a conducting surface and helps to isolate the antenna from external electromagnetic waves, which conceals the antenna. FSS-based stealth radomes have been successfully employed for many applications; however, they have two inherent disadvantages when used to protect antennas on the ground. First, the FSS is narrow-band, because it contains resonant elements. Second, the antenna/radome combination is unable to mimic an empty ground and to transmit/receive signals at the same time.

To further investigate the advantage and disadvantage of the proposed undetectable combination, a stealth radome is designed by using the FSS and tested for comparison. The dimensions of the FSS are given in the inset of Fig. 4.9 [4]. This surface is composed of circular ring elements pierced in a metallic sheet, which is embedded in a substrate with $\varepsilon_r = 2.2$. The commercial software Ansoft's HFSS is used to predict the performance of the FSS stealth radome. The transmission coefficient is plotted in Fig. 4.9. The pass-band of the FSS is located within the X-band, with the central operating frequency at 8.4 GHz, which is comparable to our design. For a normal incidence, for which the E

field is parallel to the FSS plane, the 3 dB pass-band spans from 6 GHz to 13.3 GHz. The transmission coefficient within this band decreases slightly when the incident angle is changed to 45^o. This bandwidth limitation can be attributed to the inherent resonant property of the elements. For comparison, the transmission coefficient of the carpet cloak is also plotted in Fig. 4.9. The carpet cloak is stimulated by a line source and the transmission coefficient is above -3 dB from 5 GHz to 15 GHz. According to the plot, the carpet cloak possesses a flatter transmission coefficient and a broader bandwidth than the FSS. In practice, an antenna placed behind the FSS can only operate within its pass-band from 6 GHz to 13.3 GHz. In contrast to this, the carpet cloak has much looser restrictions, either on the incident angle or on the operating bandwidth, as long as the resolution of the permittivity map is sufficient at the highest operating frequency. These advantages are granted by the isotropic and wideband property of the transformation media that required to construct the carpet cloak. In addition, it should be pointed out that the bandwidth and the angular performance of FSS radome can be further improved if the technique of multi-layered FSS is applied, as studied in [4]. The thickness and/or permittivity of substrate in each FSS layer is carefully designed to reduce the high sensitivity of single-layered FSS to the incident angle and the polarization, and consequently to improve the bandwidth. However, this improvement may result in an increased thickness of FSS and a slightly decreased transmission coefficient due to the dielectric loss. For comparison, bandwidth of the carpet cloak based radome is also able to be further improved if the resolution of the carpet cloak is increased. This is a common property of the DCT based devices, and will be demonstrated in Section 5.3.3.

Next, the concealing performance of the FSS radome and the proposed design are compared. The FSS radome and the carpet cloak are located above the same opening in the ground, where antenna elements can be hidden beneath, as illustrated in the inset in Fig. 4.10. An incident wave is launched from the top left to illuminate the ground, detecting any unusual structures. To make the antenna undetectable, we need to make the antenna/radome combination mimic a bare ground plane. In other words, most

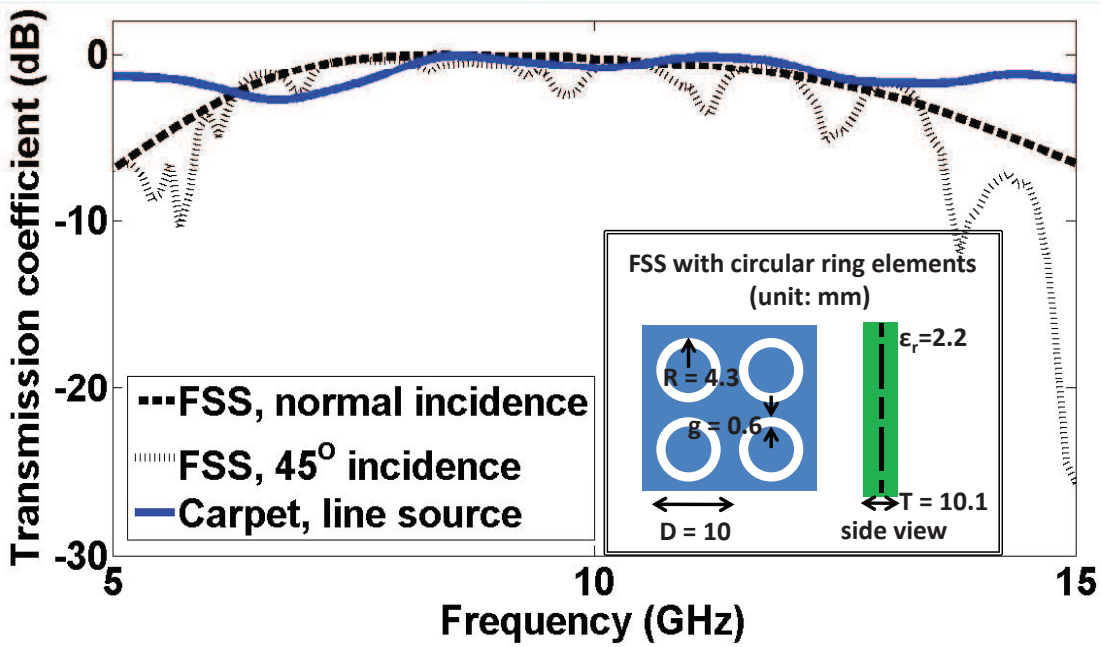

Figure 4.9: Transmission coefficient of the FSS radome and the carpet cloak. Dimensions of the FSS unit cell are defined in the inset.

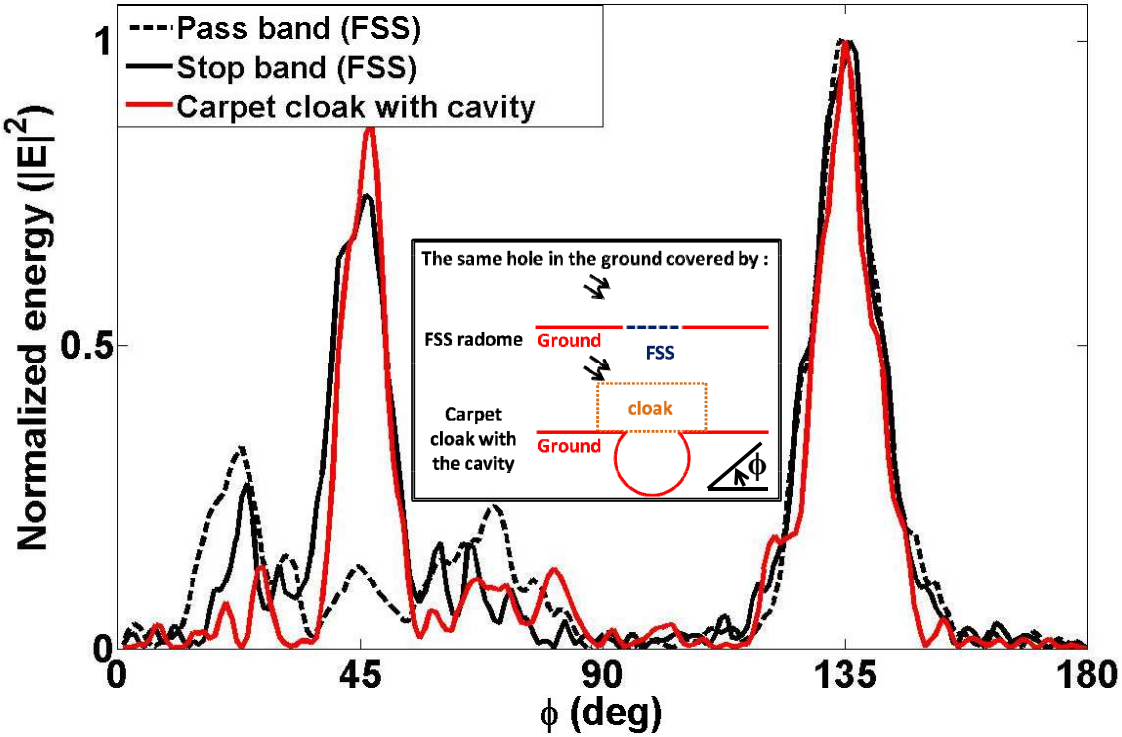

Figure 4.10: Field distribution when the FSS radome and the carpet cloak with the cavity are applied, respectively, to conceal the same opening in the ground plane.

incident energy should be reflected along the specular direction, i.e., along $\varphi = 45^o$. Fig. 4.10 plots the angular distribution of the energy of electric field when the incident angle is $\varphi = 135^o$. When an FSS radome is placed above the opening, within its pass-band, most incident energy penetrates through and the scattered fields are distributed from $\varphi = 0^o$ to $\varphi = 90^o$. This behavior is totally different from the performance of a bare ground plane. In the stop-band, most incident energy is reflected to $\varphi = 45^o$, with relatively low scatterings to other directions. These scattering patterns indicate that the FSS radome protects the underground antenna only in its stop-band, when the antenna cannot receive or transmit signals. The field distribution of the carpet cloak plus cavity combination at 10.61 GHz is also plotted for comparison. Obviously, the carpet cloak is better able to mimic a ground plane and to conceal the antenna element hidden below at the same time.

It can be concluded from above comparison that the new carpet cloak based radome has an advantage of protecting an underground antenna from an external detector without isolating the radiation of the antenna. However, the FSS based radome can be easily applied to many antennas and antenna arrays, whilst this new radome is only able to conceal specific antennas.

4.2.3 Discussion of realisation methods

A number of methods can be adopted for realising the required permittivity map of designed transformation devices. One of them is to use sub-wavelength resonator arrays, which have already been known as metamaterials [5–9].

For our design, according to the permittivity map in Fig. 4.3(b), the device is composed of 22×12 blocks with their dimensions less than $1/2\ \lambda_0$ in the X-band. Their relative permittivity values vary from 1 to 2.5. This permittivity variation is not large, so non-resonant metamaterials, which offer a relatively wideband response, is a good choice for fabricating a sample device. One kind of the matematerial units, the I-shaped

electric resonator in Fig. 4.11, is one of possible approaches as it is efficient to produce required permittivity values. Fig. 4.11(a) shows one sample resonator, and (b) illustrates the typical distribution of its effective permittivity. The real part of permittivity (blue curve) follows the Lorentz model, goes extremely large around the resonance frequency (f_r), and changes rapidly. This property indicates an essential disadvantage of resonant metamaterials: its narrow-band performance. However, in some cases when required relative permittivities are not much larger or much less than unity, such as this carpet cloak design, the resonant metamaterials can operate very well off the resonance. For example, in Fig. 4.11(b) the I-shaped resonator has a relatively constant distribution of permittivity values over frequencies much lower than the resonance frequency. In addition, it should be pointed out that anisotropic property of metamaterials have not been properly characterised. Most of resonant metamaterials produce anisotropic

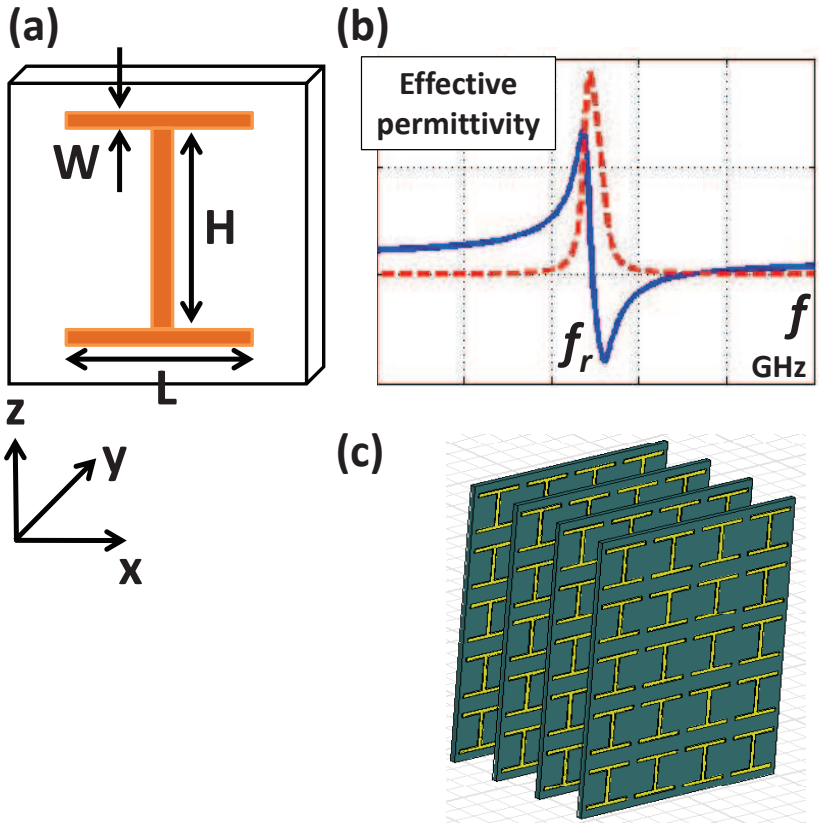

Figure 4.11: The I-shaped electric resonator. (a) Dimensions of a unit cell. (b) The effective permittivity of I-shaped resonator arrays. Blue curve: the real part. Dashed red curve: the imaginary part. (c) A group of I-shaped resonators to mimic a homogeneous block in the permittivity map.

permittivities or permeabilities.

The procedure of designing the carpet cloak presented in this section is discussed below. The permittivity map in Fig. 4.3(b) is divided into 10 mm × 10.9 mm sized blocks, and in the z direction, the height is chosen to be 15 mm, the same as the height of our measurement platform (as described in [10]). For the purpose of mimicking a homogeneous dielectric block, all unit elements should be of sub-wavelength in the X-band, hence we chose the dimension of each unit cell to be $2.5 \times 2.725 \times 3\ mm^3$. One sample block is shown in Fig. 4.11(c). Because the required relative permittivity ranges from 1 to 2.5, the relative permittivity of the substrate is chosen to be 2.65 and its thickness is 0.25 mm. The carpet cloak has already been fabricated using metamaterial units in [2] and [11]. A similar procedure can be carried out to design a large array of I-shaped resonators for our device. The dimension H is key to obtain the effective permittivity, and, hence, a parametric study is conducted to understand the relationship between the value of H and the effective permittivity. A retrieval process [12] is applied to obtain the effective permittivity value from S parameters simulated in Ansoft's HFSS. For simplicity, here we assume $W = 0.2$ mm and $L = H + 2W$. Consequently, the relative effective permittivity is plotted as a function of the dimension H, as shown in Fig. 4.12. By using this curve, we can find out the required dimensions of the I-shaped resonator

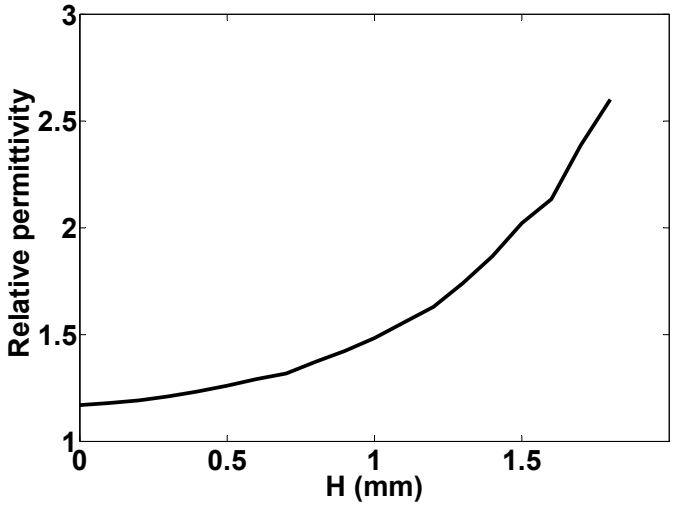

Figure 4.12: The relative effective permittivity versus the dimension of H.

in order to achieve specific permittivity values from 1.17 to 2.6. The value less than 1.17 can be approximated as 1.1 and obtained by printing a small patch on a substrate with low permittivity.

An advantage of using resonant metamaterials based on printed circuit board (PCB) approaches is its low cost and readiness for mass-production. The main drawback is that strong spatial and spectral dispersions may occur and therefore limit the bandwidth of devices.

Another straightforward way is to use artificial composites with extremely low loss and nearly constant permittivities over operating frequencies. This method has been applied in the work reported in [10], where a simplified carpet cloak was constructed of six blocks of polyurethane foam loaded with $BiTiO_3$. Another example is described in the following section of this chapter, when a proposed new device for sub-wavelength transmission enhancement is realised by using several blocks of dielectric materials [13, 14]. One possible disadvantage of this method is that special fabricating processes may be demanded to fulfill all required permittivities, therefore the manufacture process can be expensive and time consuming.

4.3 Broadband Extraordinary Transmission in a Sub-wavelength Aperture

In this section, the discrete coordinate transformation is applied to design an all-dielectric device for extraordinary transmission (ET) through a single sub-wavelength slit. The proposed scheme has a broadband feature and can be applied from microwave to optical frequencies. Numerical simulations are used to verify the performance of the device, demonstrating that significantly increased transmission is achieved through the sub-wavelength aperture from 4 GHz to 8 GHz. A simplified device is tested in an X-band waveguide, and the experimental results confirm that the device can provide increased

transmission with a -3 dB bandwidth of more than 1 GHz, in a region which would otherwise be a stop band caused by the sub-wavelength aperture in the waveguide.

4.3.1 The scheme to enhance the transmission

The extraordinary (optical) transmission (EOT) of electromagnetic waves through periodic arrays of subwavelength holes [15] or slits [16] made in opaque — mostly metallic — screens has been extensively studied over the last decade. Comprehensive review papers reporting on the basic physics behind the phenomenon are available nowadays [17–19]. The research of periodic structures has also stimulated the study of the transmission properties through single holes or slits. Sometimes the physics of EOT through periodic structures is closely related with the physics of enhanced transmission through single apertures, as it is the case of slits or holes around which the conducting surface is periodically structured [20–22]. The periodically perforated screen or the periodically structured surface (a metal surface with corrugations, for instance) support surface waves (the so-called *spoof plasmons* [23]) which are strongly excited around certain critical frequencies. However, any other mechanism provoking field enhancement at the aperture level would automatically induce enhanced transmission. Thus, it seems almost obvious that high quality factor resonators placed close to or inside the holes will produce resonant enhancement of the fields and, consequently, enhanced transmission [24, 25]. Other methods have been proposed to enhance transmission of electromagnetic waves through electrically small slits or holes [26, 27].

A common feature to all the methods mentioned above is their intrinsic narrow band behavior. Narrow bandwidth is associated with its resonant nature of the underlying design principle. However, here we demonstrate how a non-resonant technique can be applied through the DCT to enhance the transmission.

The main idea is to build a distorted space which can smoothly induce much more energy from an electrically large aperture into a smaller one. Fig. 4.13(a) shows a space

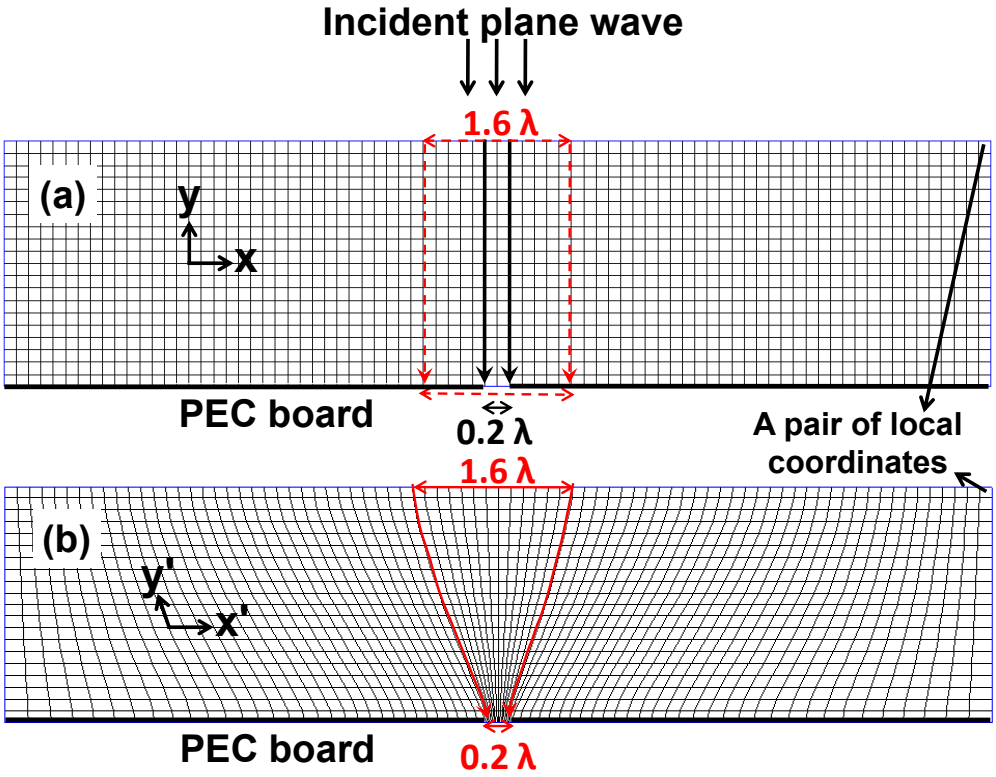

Figure 4.13: (a) The space with Cartesian coordinates. (b) The distorted space where waves travel according to the curved coordinates.

in the Cartesian coordinates. When a plane wave travels into the space from the top, the wave vector k is in the direction towards the bottom along the local coordinates, as illustrated with black arrows, and so is the Poynting vector S, which represents the flowing of energy. For a perfect electric conductor (PEC) with a 0.2 λ_0 (λ_0 the wavelength of free space at operating frequency) wide slit, most incident energy is reflected and little energy could pass through the slit. When the aperture of the slit is enlarged to, for instance, 1.6 λ_0, the transmitted energy increases significantly. A distorted space is designed in Fig. 4.13(b), where the wave vector k is bent towards the slit along the local coordinates. In this way, the energy received from a virtual electrically-large aperture (1.6 λ_0 in Fig. 4.13) can efficiently pass through an electrically-small slit (0.2 λ_0 here), hence the transmission through a sub-wavelength slit could be enhanced dramatically in the distorted space.

The DCT technique is used to design the transformation media for the distorted

space. 2D circumstance with H_x, H_y and E_z components is again applied to simplify the problem. This polarization is applicable to the environment inside a waveguide because its dominant mode is TE_{10} mode. Experimental results in an X-band waveguide will be presented later in this section. A practical way to realise the distorted space is to use all-dielectric background materials. It have been proved that a near-orthogonal grid in the distorted space is key to the all-dielectric transformation media. However, in this scenario, it is difficult to generate a grid with excellent orthogonality in the distorted space which links the sub-wavelength slit with an electrically large aperture. Instead, fine mesh is carefully generated in the same way as before using the software of "GenGrid" to ensure most cells are nearly orthogonal, especially in the central region above the slit. Although such an engineering approximation may not represent a mathematically strict transformation, and, hence, the proposed device is sensitive to the incident angle, the pre-designed performance of extraordinary transmission is still evident over a broad band of frequencies, as will be demonstrated in the following part.

The relative permittivity map shown in Fig. 4.14 is calculated using the same scheme

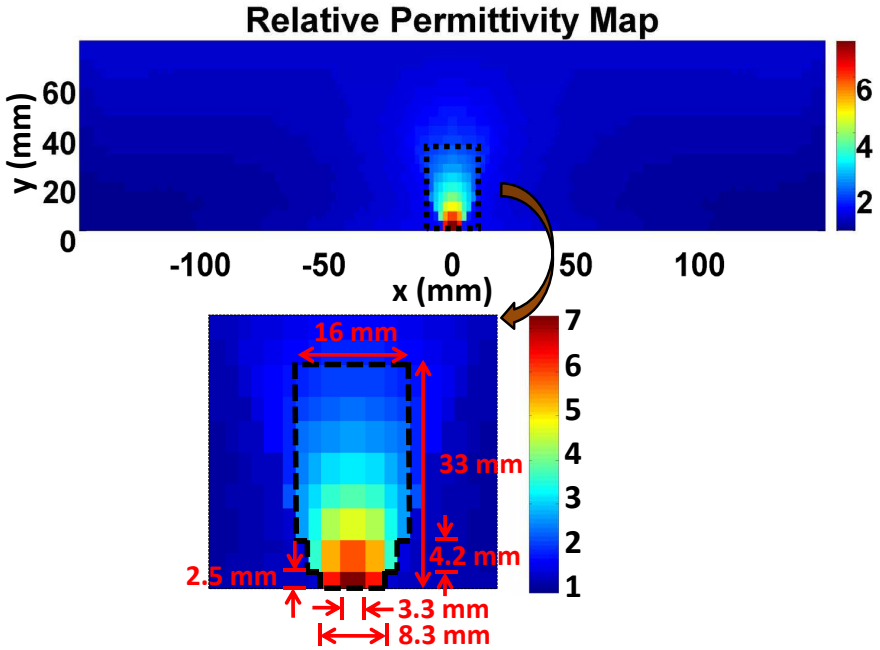

Figure 4.14: The relative permittivity map of the distorted space. The dashed black line outlines the profile of the enhancement device.

explained in Section 2.4. Relative permittivity is very close to unity in most parts of the distorted space, which means most of the transformation media could be considered as the air, and dielectrics with varying ε_r are mainly required in the central area surrounding the slit. The dashed black line in Fig. 4.14 outlines the profile of such a device and the detailed permittivity map. The device has a size of 0.43 λ_0 $\times$ 0.88 λ_0 at 8 GHz.

4.3.2 Numerical simulation results

4.3.2.1 Enhanced performance at a single frequency

FDTD based numerical simulations are used to test the performance of the designed device without loss of generality. The operating frequency is set to 8 GHz, the wavelength in free space (λ_0) being 37.5 mm accordingly. The sub-wavelength slit on the PEC plate is 0.2 λ_0 (7.5 mm) wide and 0.067 λ_0 (2.5 mm) thick. The simulation domain is shown in Fig. 4.15(a). Periodic boundary conditions (PBC) are applied to realise an infinite plane wave incidence with E-polarization impinging from the top. The amplitude of the electric field is plotted to present the distribution of energy. In Fig. 4.15(a), the incident plane wave irradiates on the PEC plate which has the sub-wavelength slit. Extremely low field intensity is observed on the other side of the plate. Fig. 4.15(b) shows the field distribution when the slit is enlarged to 1.6 λ_0 (60 mm) wide. Much energy passes through the slit and propagates further, as expected. When the proposed enhancement device, shown in Fig. 4.14, is located over the 0.2 λ_0 wide slit (inside the region defined by the black box illustrated in Fig. 4.15(c)), a significant enhancement of the field is observed on the other side of the PEC plate. Ideally, from the point of view of coordinate transformation, the transmitted energy should be the same in (b) and (c) if all energy received by the 1.6 λ_0 slit on the top is guided to the 0.2 λ_0 slit on the bottom. However, the device includes only the central part of the distorted space and the orthogonality in the distorted space is not guaranteed everywhere. The anisotropic property needs to be included to ensure the maximum transmission. Nevertheless, the proposed device still

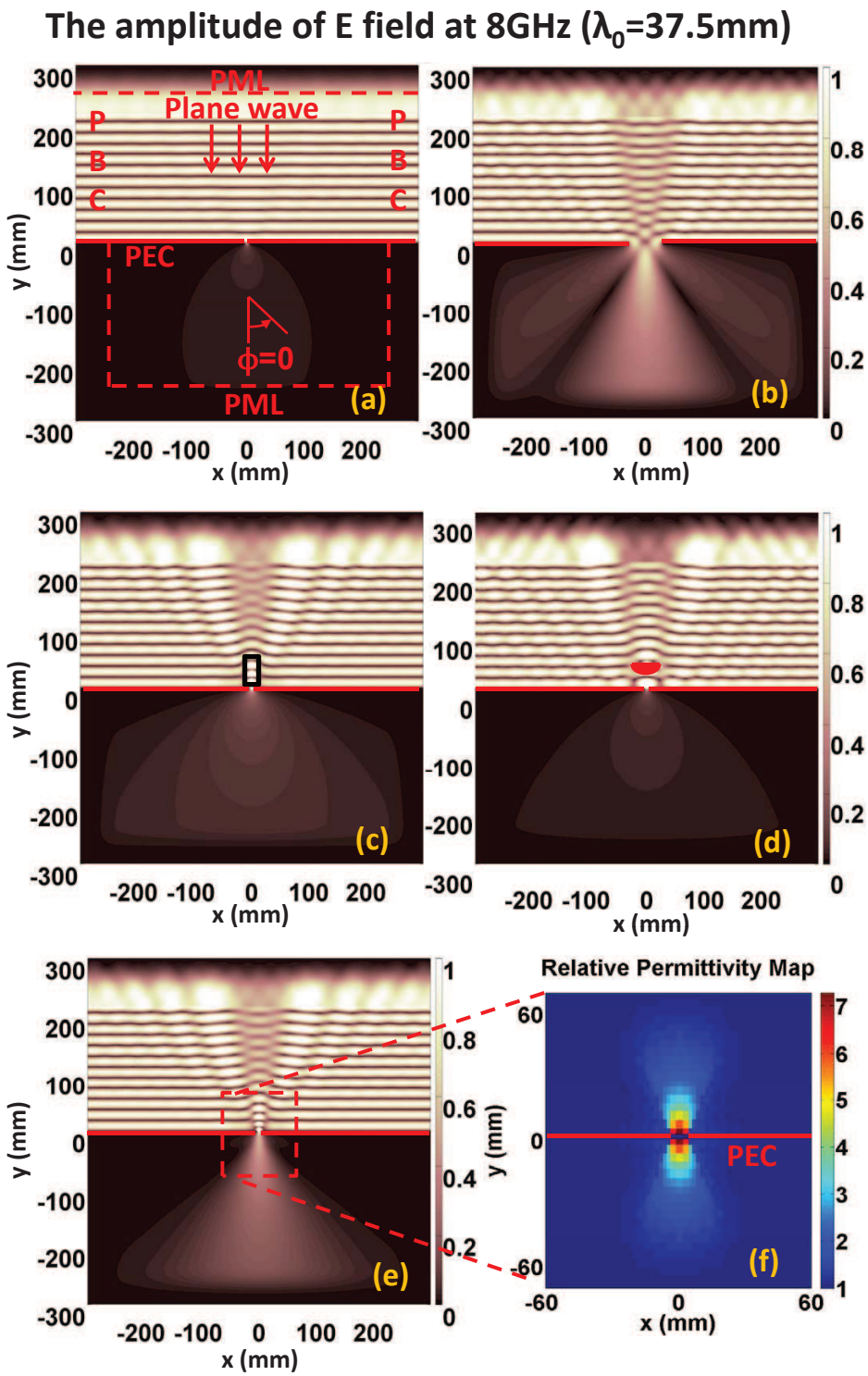

Figure 4.15: Amplitude of the electric field in different cases. (a) The incident plane wave illuminates a PEC plate with a 0.2 λ_0 wide slit. (b) The incident plane wave illuminates a PEC plate with a 1.6 λ_0 wide slit. (c) The incident plane wave illuminates the above mentioned sub-wavelength slit when the proposed enhancement device is applied in the black box. (d) The incident plane wave illuminates the sub-wavelength slit after crossing a focusing lens with its focal point located on the slit. (e) The incident plane wave illuminates a PEC plate with a pair of enhancement devices at both sides of the sub-wavelength slit. (f) The permittivity map around the slit in case (e). The map is symmetric.

produces strong field enhancement, when comparing Fig. 4.15(a) and (c). A conventional focusing lens is also applied and the result is presented in Fig. 4.15(d) as a reference. The lens has an aperture of 1.6 λ_0 and its focal point is set to be at the center of the 0.2 λ_0 wide slit, in order to focus more energy directly inside the slit. In this case, the transmission through the 0.2 λ_0 wide slit only increases slightly. Thus the proposed device outperforms the conventional dielectric lens for field enhancement. Furthermore, the device can be mirrored to the other side of the PEC plate as shown in Fig. 4.15(f). The transmitted electromagnetic wave travels through a second distorted space and leads to much more enhanced field distribution. Fig. 4.15(e) shows that behind the PEC plate the transmitted wave is constrained in a bundle and a directive beam is achieved.

Radiation patterns are depicted to further compare the field enhancement performance. In Fig. 4.16(a), the amplitude of E_z is recorded on a semicircle 3 λ_0 away from the center of the slit. The x axis is the value of ϕ defined in Fig. 4.15(a). The amplitude of the transmitted E_z field is low when there is only a 0.2 λ_0 wide slit on the PEC plate. Once the lens is added, the field increases slightly. However, a significant field enhancement is observed when the proposed device is put above the slit. The amplification at $\phi = 0^o$ is about 3.25 for amplitude and 10.56 for power. When the mirrored device is added on the other side, the amplification increases remarkably. Around the angle of $\phi = 0^o$, the E field is not much weaker than that when there is a 1.6 λ_0 wide slit on the PEC plate. Note that when the slit is 1.6 λ_0 wide, the two side lobes come from the reflection of the PEC plate, which is already observed in Fig. 4.15(b). Fig. 4.16(b) shows the radiation pattern at a semicircle 6 λ_0 away from the center of the slit (far field). The patterns in (b) are similar to those in (a). The amplifications are observed as before while the amplitudes around $\phi = 0^o$ decrease when the waves travel to the far field.

Fig. 4.17 also shows the energy distribution along the propagating path. The energy is recorded at the direction of $\phi = 0^o$, from the center of the slit towards the bottom in Fig. 4.15. When the transmitted wave travels to the far field, the enhancement of energy

is preserved once the designed device is applied. A pair of devices produce much more transmitted energy than a single one all along the propagating path. Note that the blue curve, which represents the energy when a pair of devices are used, is not smooth from 0.25 λ_0 to 0.8 λ_0. This area is inside the mirrored device and the reflection between

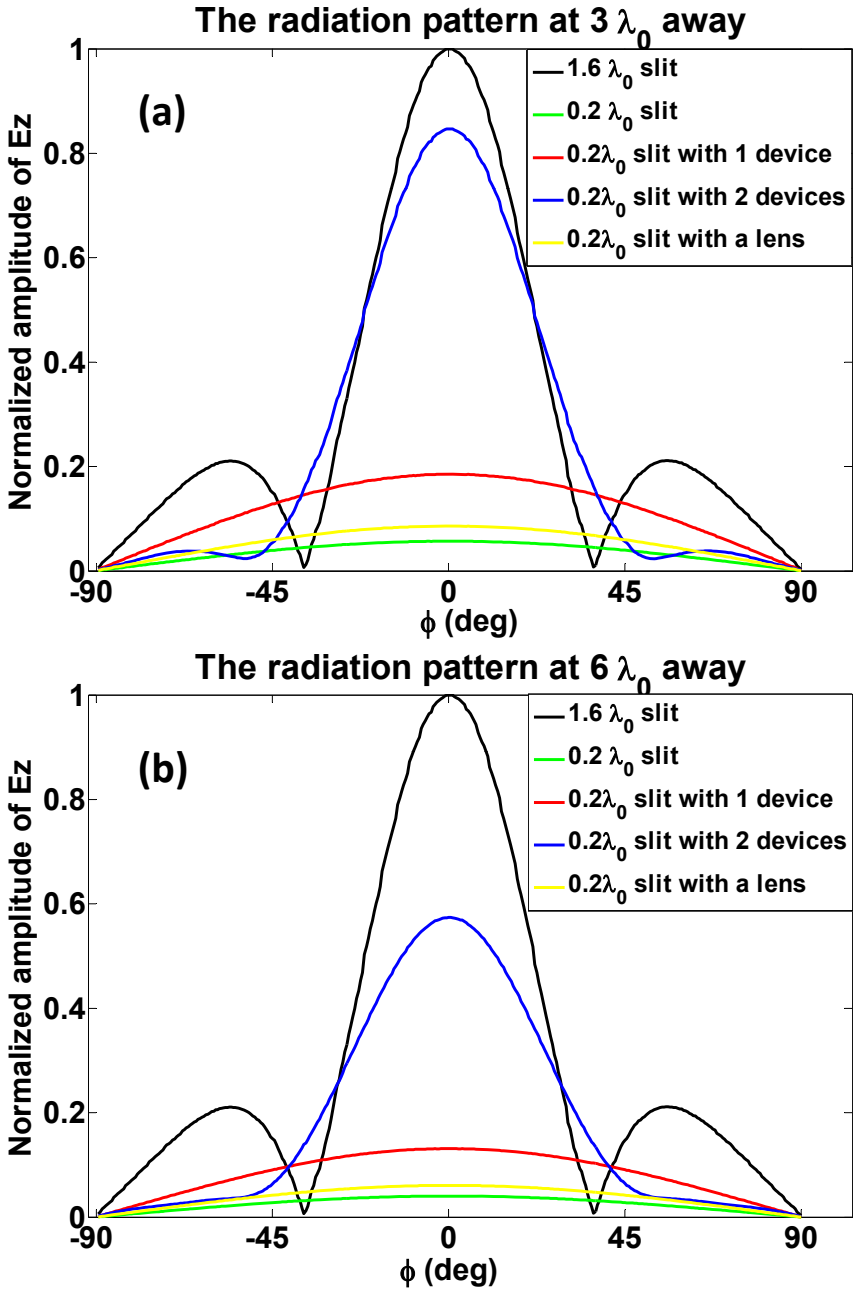

Figure 4.16: (a) The radiation pattern recorded at a semicircle 3 λ_0 away from the center of the slit. (b) The radiation pattern recorded at a semicircle 6 λ_0 away from the center of the slit. The operating frequency is 8 GHz.

different dielectric blocks is considerable.

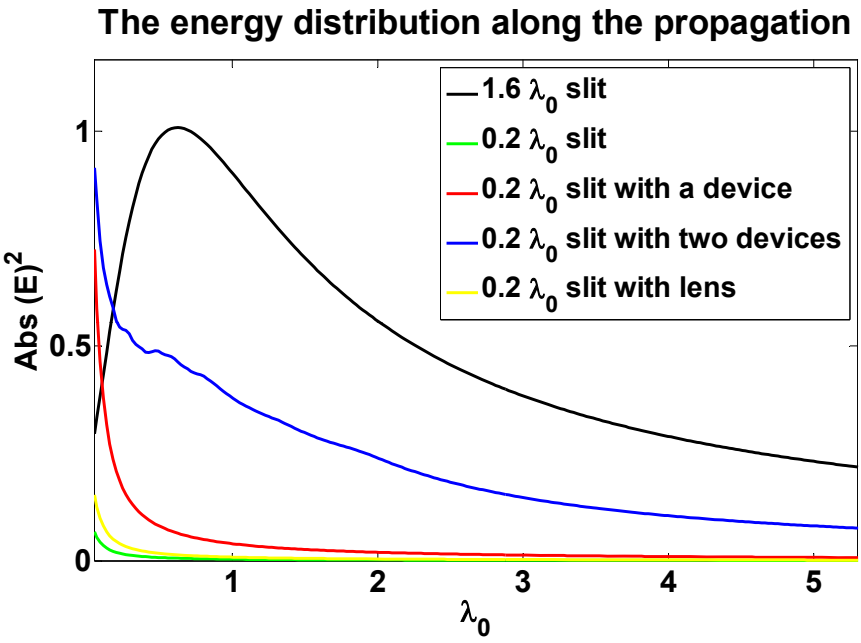

Figure 4.17: The transmitted energy distribution along the propagating direction. The propagating distance is recorded in term of the wavelength away from the slit center.

4.3.2.2 The transmitted energy

To quantify the transmitted energy, a broadband Gaussian pulse is applied to excite the slit. Its behaviour in the frequency domain is depicted as the sub-figure in Fig. 4.19(a) by using the Fourier transformation. The Poynting vector over the slit represents the energy passing through. By integrating the Poynting vector at the lower surface of the

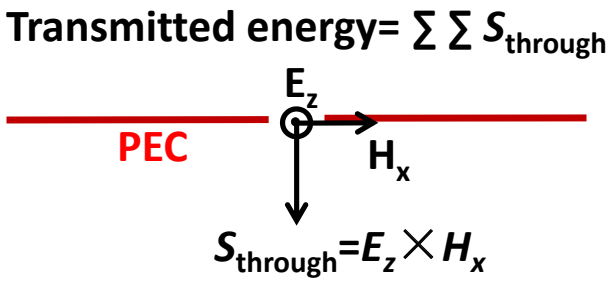

Figure 4.18: Integrate the Poynting vector at the lower surface of the PEC plate over time to get the transmitted energy.

PEC plate (as shown in Fig. 4.18), the total energy transmitted over time is available. Note that at the lower surface of the PEC plate, only perpendicular electric field and parallel magnetic field exist. So, the transmitted energy could be calculated as shown in Fig. 4.18. Table 4-B gives the values of the transmitted energy in different cases. It is obvious that extremely poor transmission is obtained for the 7.5 mm slit if compared with the energy crossing the 60 mm slit. When a focusing lens is applied, the enhancement is very limited. But once the new enhancement device is located above the 7.5 mm wide slit, the transmission increases dramatically (it is about 12 times more energy transmitted than those without the device). When applying the mirrored device, the transmission is further increased (about 15 times more than those without the device). With the implementation of two devices, the transmitted energy increases to about $1/4 \sim 1/3$ of the value when the slit is enlarged to 60 mm. The discrepancy between case 1 and cases 4 and 5 is mainly due to the simplification of ignoring anisotropic properties.

Table 4-B: Values of the transmitted energy in different cases.

Case No.	The PEC plate with:	Transmitted energy (arb. units)
1	a 60 mm wide slit	965
2	a 7.5 mm wide slit	19
3	a 7.5 mm wide slit and a lens	28
4	a 7.5 mm wide slit and a device	248
5	a 7.5 mm wide slit and a pair of devices	300

4.3.2.3 The broadband performance

To investigate the broadband performance of the proposed device, an incident pulse spanning from 4 GHz to 8 GHz is applied and the average amplitude of transmitted E_z field at the locations of 0.1 λ_0 and 3 λ_0 (at 6 GHz) away behind the PEC plate is recorded during every time step. The frequency domain responses are calculated and plotted in Fig. 4.19. Slight enhancement is observed at some frequencies, when the conventional lens is used. Once the proposed devices are applied, the transmitted electric field is considerably higher than the values without any devices over the whole

frequency domain. When the transmitted waves travel from the very near field of 0.1 λ_0 (Fig. 4.19(a)) to the far field of 3 λ_0 (Fig. 4.19(b)), the significant enhancement is still held. Note that in Fig. 4.19(a), since the observation line is inside the mirrored device, the case with a pair of devices is not plotted.

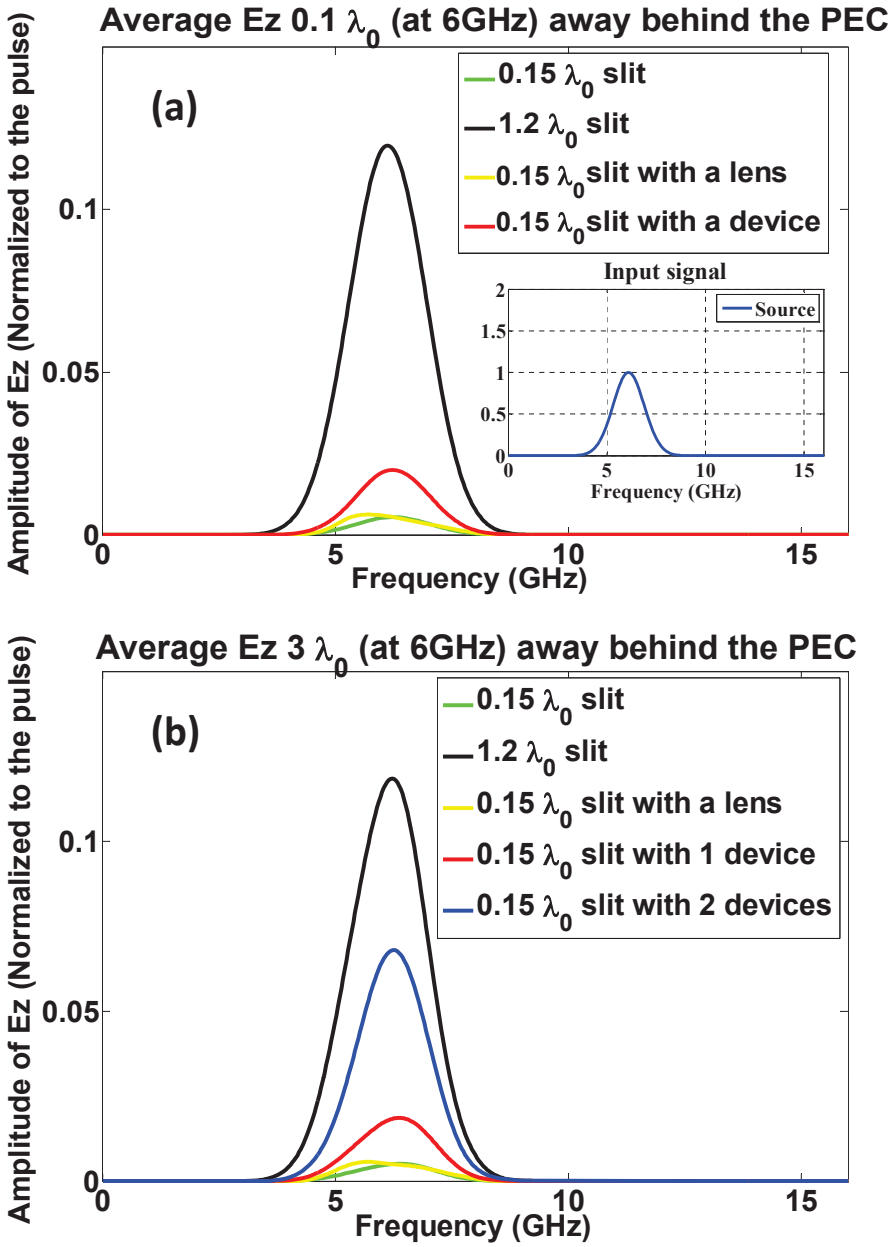

Figure 4.19: (a) The average amplitude of Ez field recorded on the line 0.1 λ_0 (at 6 GHz) away behind the PEC plate. (b) The average amplitude of Ez field recorded on the line 3 λ_0 (at 6 GHz) away behind the PEC plate.

The transmission enhancement produced by the transformation devices and the lens are also calculated and plotted in Fig. 4.20. The amplitude of electric field shown in Fig. 4.19 is normalised at each frequency point by the value of the green curve, which represents the transmitted field through the sub-wavelength slit without any devices.

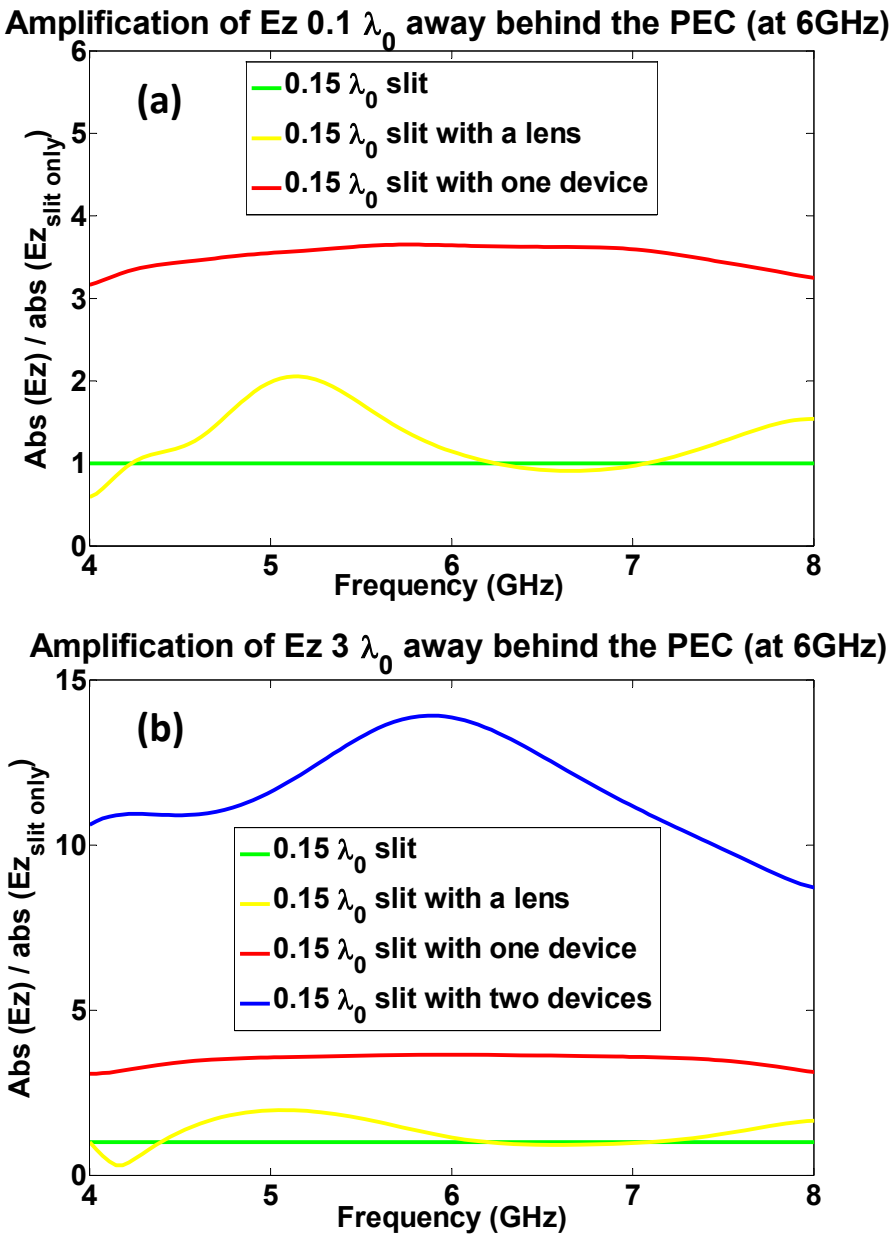

Figure 4.20: (a) Amplifications at the line 0.1 λ_0 (at 6 GHz) away behind the PEC plate over the frequency spectrum. (b) Amplifications at the line 3 λ_0 (at 6 GHz) away behind the PEC plate over the frequency spectrum. The amplitude of electric field is normalised at each frequency point to the value of the green curve (which represents the transmitted field through the sub-wavelength slit) to represent the amplification factor.

The results give the detailed information of the amplification, and demonstrate that the designed device can significantly enhance the transmission over a wide frequency range.

4.3.3 Experimental verification

This designed device is manufactured and tested in experiment in collaboration with my colleague Di Bao *et al* [14]. According to the permittivity map shown in Fig. 4.14 (the same as in Fig. 4.21(a)), the device is composed of many small blocks with the size of around 3×3 mm^2, with the relative permittivity varying from 1 to about 7. Considering those small blocks presented in Fig. 4.21(a) are of sub-wavelength size at the central frequency of 8 GHz ($\lambda_0 = 37.5$ mm), the permittivity map can be simplified into only very few blocks, as shown in Fig. 4.21(b). The dimensions of the four blocks are $[\, 20\times 15,\ 15\times 8,\ 10\times 8,\ 8\times 7\,]$ mm^2 from top to bottom, and their relative permittivities are $[\ 2.1,\ 3,\ 4.5,\ 6\ ]$. Since the size of the biggest block is comparable to a half of the wavelength at 8 GHz, the simplification is feasible, as discussed in Chapter 3.

A number of methods have been suggested for the attainment of the required parameter. One of them is to use the I-shaped metamaterials as discussed in the previous section. However, an undergoing problem is that, in order to obtain materials with the relative permittivity higher than 7, it is necessary for the I-shaped material to operate

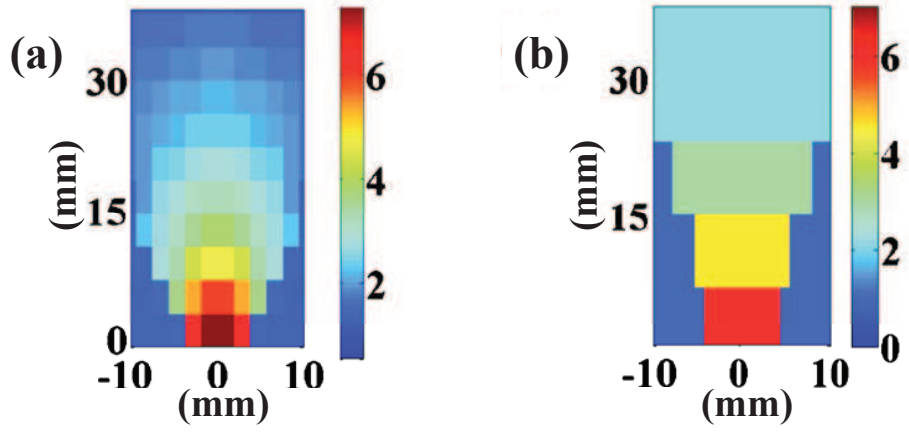

Figure 4.21: (a) The relative permittivity map of the high-resolution device. (b) The relative permittivity map of the simplified device.

near the resonance, which inevitably leads to high dispersion and narrow bandwidth. On the other hand, there exist commercially available ceramics and other dielectric materials with extremely low loss and nearly constant permittivities over a broadband of frequencies. A pair of mirrored devices are fabricated from these dielectric materials as shown in Fig. 4.22(a). They are made from Teflon and have been tested of possessing the required permittivity values.

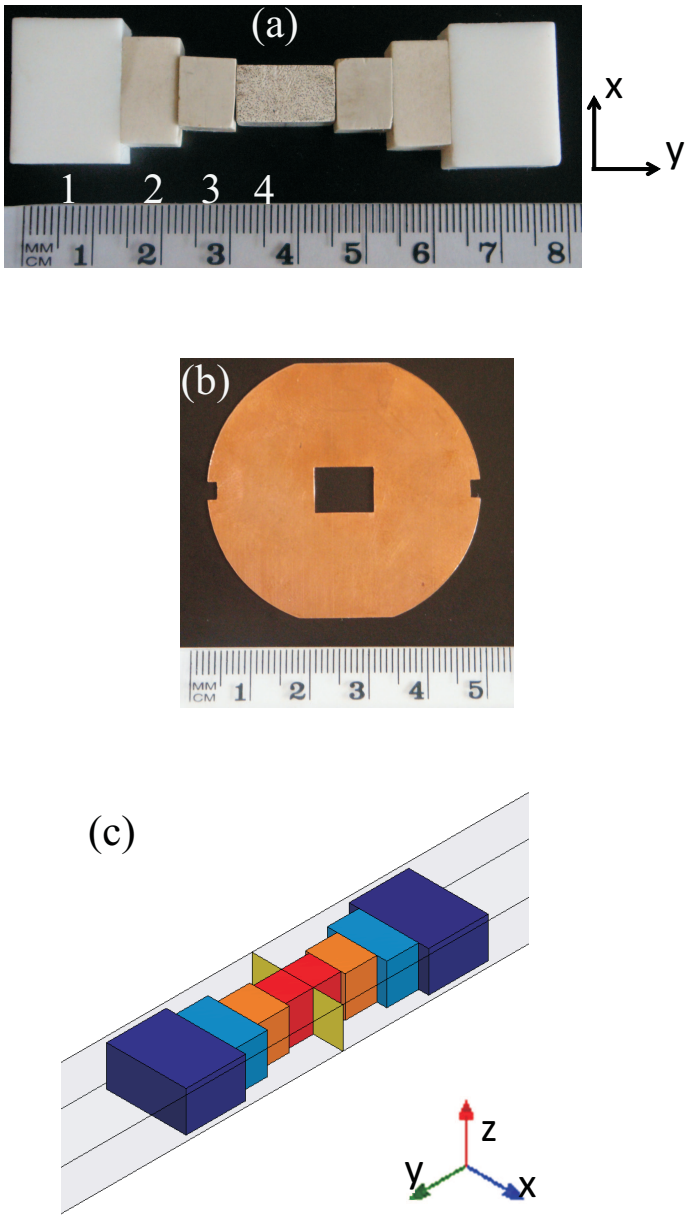

Figure 4.22: (a) A photograph of the device sample. (b) Metallic plate with a sub-wavelength aperture used in the experiment. (c) The configuration of the device and its arrangement in the waveguide.

The experiment is then carried out in an X-band waveguide with a cross section of $22.86 \times 10.16\ mm^2$ (see Fig. 4.22(c)). Practically, each half of the device is filled into one section of waveguide, and then contacted face to face. A piece of copper plate with an aperture of $10.16 \times 8 \times 0.25\ mm^2$ is introduced between the two sections to make a small aperture, as shown in Fig. 4.22(b).

The transmission coefficients are measured and plotted in Fig. 4.23, and compared with simulation results from Ansoft's HFSS. Fig. 4.23 shows that when there is only an aperture of width $8\ mm$, the transmission is lower than $-10\ dB$. With the device placed by the two sides of the aperture, the transmission is enhanced by about $10\ dB$ with the $-3\ dB$ bandwidth from 7.7 to 8.8 GHz in the experiment. From another point of view, this device effectively obtains a performance of impedance matching. In addition, simulation result suggests that the device with a high resolution in Fig. 4.21(a) has $-3\ dB$ passband over the whole X-band beyond 7.7 GHz, as shown in Fig. 4.23. The

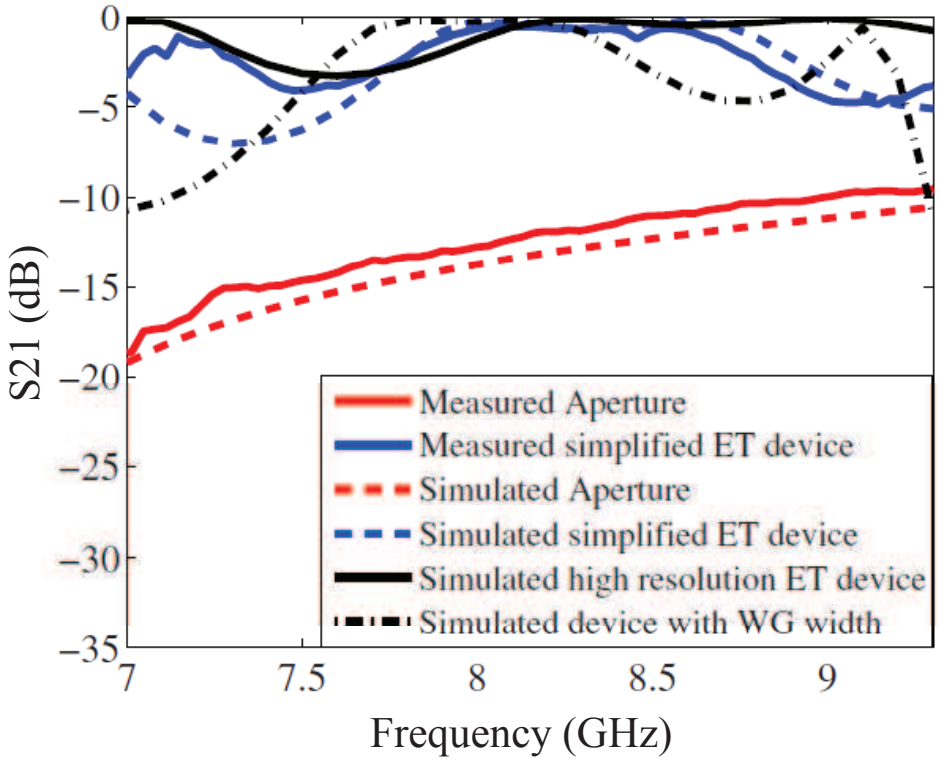

Figure 4.23: The measured and simulated results of the enhancement device.

bandwidth reduction of the simplified device is due to the fact that at higher frequencies the wavelength gets smaller and becomes comparable to the dimensions of the big blocks, hence the low resolution of dielectric map is no longer sufficient. Better performance and enlarged bandwidth can be expected by increasing the resolution.

4.4 Summary

In this chapter, practical applications of the DCT technique was extended to create new devices with novel functions. These devices do not rely on any prototype reference but are constructed via the manipulation of electromagnetic wave propagation. Local coordinates are generated according to the propagating path of waves, and under the near-orthogonal condition, the manipulated wave propagation can be realised using an array of isotropic dielectric blocks with spatially varying permittivities. Reasonable simplifications and approximations can help to alleviate the complication during practical realisation of electromagnetic devices based on the discrete coordinate transformation.

Two devices were proposed and investigated as examples. The first one was a combined antenna structure consisting of a carpet cloak and a conducting cavity. This device becomes "invisible" in virtue of the carpet cloak, but can still radiate as an antenna under the carpet via using a technique called the "virtual boundary". The Finite-Difference Time-Domain method was used to numerically verify the device at the X-band. Simulation results demonstrated that external incidences cannot clearly distinguish the combined antenna from an empty ground plane. The highly directive radiation was also presented. Realisation methods were discussed and a metamaterial sample consisting of I-shaped resonators was investigated. The second example was a device for the transmission enhancement through a sub-wavelength aperture. This device mimics a distorted space in which energy received from a large aperture is guided efficiently into a sub-wavelength aperture. Extraordinary transmission through a 7.5 mm slit was achieved over a wide band from 4 GHz to 8 GHz when the device was applied. FDTD

based simulations, and experimental measurement have verified the design.

References

[1] J. Li and J. Pendry, "Hiding under the carpet: A new strategy for cloaking," *Phys. Rev. Lett.*, vol. 101, no. 20, p. 203901, 2008.

[2] R. Liu, C. Ji, J. J. Mock, J. Y. Chin, T. J. Cui, and D. R. Smith, "Broadband ground-plane cloak," *Science*, vol. 323, no. 5912, pp. 366–369, 2009.

[3] B. A. Munk, *Frequency Selective Surfaces Theory and Design.* John Wiley & Sons, Inc., 2000.

[4] J. D. Kraus and R. J. Marhefka, *Antennas: For All Applications.* McGraw-Hill, New York, 3rd edition, 2003.

[5] J. B. Pendry, A. J. Holden, W. J. Stewart, and I. Youngs, "Extremely low frequency plasmons in metallic mesostructures," *Phys. Rev. Lett.*, vol. 76, no. 25, pp. 4773–4776, 1996.

[6] J. Pendry, A. Holden, D. Robbins, and W. Stewart, "Magnetism from conductors and enhanced nonlinear phenomena," *IEEE Trans. Micr. Theory Techn.*, vol. 47, no. 11, pp. 2075–2084, 1999.

[7] D. Schurig, J. Mock, and D. Smith, "Electric-field-coupled resonators for negative permittivity metamaterials," *Appl. Phys. Lett.*, vol. 88, p. 041109, 2006.

[8] J. Huangfu, L. Ran, H. Chen, X. Zhang, K. Chen, T. Grzegorczyk, and J. Kong, "Experimental confirmation of negative refractive index of a metamaterial composed of Ω-like metallic patterns," *Appl. Phys. Lett.*, vol. 84, p. 1537, 2004.

[9] W. X. Tang, H. Zhao, X. Zhou, J. Y. Chin, and T. J. Cui, "Negative index material composed of meander line and SRRs," *Prog. Electromagn Res. B*, vol. 8, pp. 103–114, 2008.

[10] D. Bao, K. Rajab, Y. Hao, E. Kallos, W. Tang, C. Argyropoulos, Y. Piao, and S. Yang, "All-dielectric invisibility cloaks made of batio3-loaded polyurethane foam," *New J. of Phys.*, vol. 13, p. 103023, 2011.

[11] H. Ma, W. Jiang, X. Yang, X. Zhou, and T. Cui, "Compact-sized and broadband carpet cloak and free-space cloak," *Opt. Express*, vol. 17, no. 22, pp. 19 947–19 959, 2009.

[12] D. Smith, S. Schultz, P. Markoš, and C. Soukoulis, "Determination of effective permittivity and permeability of metamaterials from reflection and transmission coefficients," *Phys. Rev. B*, vol. 65, no. 19, p. 195104, 2002.

[13] W. Tang, Y. Hao, and F. Medina, "Broadband extraordinary transmission in a single sub-wavelength aperture," *Opt. Express*, vol. 18, no. 16, pp. 16 946–16 954, 2010.

[14] D. Bao, K. Rajab, W. Tang, and Y. Hao, "Experimental demonstration of broadband transmission through subwavelength aperture," *Appl. Phys. Lett.*, vol. 97, p. 134105, 2010.

[15] T. W. Ebbesen, H. J. Lezec, H. F. Ghaemi, T. Thio, and P. A. Wolff, "Extraordinary optical transmission through sub-wavelength hole arrays," *Nature*, vol. 391, pp. 667–669, 1998.

[16] J. A. Porto and F. J. Garc, "Transmission resonances on metallic gratings with very narrow slits," *Phys. Rev. Lett.*, vol. 83, no. 14, pp. 2845–2848, 1999.

[17] C. Genet and T. W. Ebbesen, "Light in tiny holes," *Nature*, vol. 445, pp. 39–46, 2007.

[18] F. J. García-de Abajo, "Colloquium: Light scattering by particle and hole arrays," *Rev. Mod. Phys.*, vol. 79, pp. 1267–1290, 2007.

[19] F. J. Garcí a Vidal, L. Martí n Moreno, T. W. Ebbesen, and L. Kuipers, "Light passing through subwavelength apertures," *Rev. Mod. Phys.*, vol. 82, pp. 729–787, 2010.

[20] H. J. Lezec, A. Degiron, E. Devaux, R. A. Linke, L. Martí n Moreno, F. J. Garcí a Vidal, and T. W. Ebbesen, "Beaming light from a subwavelength aperture," *Science*, vol. 297, no. 5582, pp. 820–822, 2002.

[21] F. J. Garcí a Vidal, H. J. Lezec, T. W. Ebbesen, and L. Martí n Moreno, "Multiple paths to enhance optical transmission through a single subwavelength slit," *Phys. Rev. Lett.*, vol. 90, p. 213901, 2003.

[22] L. A. Dunbar, M. Guillaumée, F. de León-Pérez, C. Santschi, E. Grenet, R. Eckert, F. López-Tejeira, F. J. Garcí a Vidal, L. Martin-Moreno, and R. P. Stanley, "Enhanced transmission from a single subwavelength slit aperture surrounded by grooves on a standard detector," *App. Phys. Lett.*, vol. 95, p. 011113, 2009.

[23] J. B. Pendry, L. Martí n Moreno, and F. J. Garcí a Vidal, "Mimicking surface plasmons with structured surfaces," *Science*, vol. 305, pp. 847–848, 2004.

[24] K. Aydin, A. O. Cakmak, L. Sahin, B. Bilotti, L. Vegni, and E. Ozbay, "Split-ring-resonator-coupled enhanced transmission through a single subwavelength aperture," *Phys. Rev. Lett.*, vol. 102, p. 013904, 2009.

[25] A. O. Cakmak, K. Aydin, E. Colak, Z. Li, F. Bilotti, L. Vegni, and E. Ozbay, "Enhanced transmission through a subwavelength aperture using metamaterials," *App. Phys. Lett.*, vol. 95, p. 052103, 2009.

[26] F. Bilotti, L. Scorrano, E. Ozbay, and L. Vegni, "Enhanced transmission through a sub-wavelength aperture: resonant approaches employing metamaterials," *J. Opt. A: Pure Appl. Opt.*, vol. 11, p. 114029, 2009.

[27] F. J. Valdivia-Valero and M. Nieto-Vesperinas, "Resonance excitation and light concentration in sets of dielectric nanocylinders in front of a subwavelength aperture. Effects on extraordinary transmission," *Opt. Express*, vol. 18, no. 7, pp. 6740–6754, 2010.

Chapter 5

Performance Analysis of DCT Based Devices

5.1 Introduction

In this chapter, we shall analyse the pros and cons of the discrete coordinate transformation (DCT), and investigate in detail the performance of the DCT based devices in comparison with those from the analytical coordinate transformation (ACT).

The first question of designing a DCT based device may be: how to decide the transformation region for the physical space and the virtual space? A general answer is, the transformation region should be much larger than the disturbed area (e.g., the area of a conducting bump under a carpet cloak). There is no theoretical definition of a "large-enough" region; however, from an engineering point of view, one can decide the transformation region by balancing the volume of the transformation device and its performance (e.g., the bandwidth or the radiation pattern of an antenna). In Section 5.2, we shall explain how to define the transformation region, and demonstrate the relationship between the size of the region and the accuracy of applying the DCT technique.

Another issue is about the resolution of the transformation media. In designs presented in Chapters 3 and 4, simplification of the permittivity map played an important role in producing practical devices with easy fabrication. However, a map with low resolution inevitably degrades the performance, whilst a map with high resolution increases the complexity of fabrication. In Section 5.3, we will propose a method to quantify the trade-off between the resolution of permittivity map and the device performance. Designs with different resolutions will also be compared in terms of the radiation pattern and the bandwidth.

In addition to the DCT technique, the analytical coordinate transformation (ACT) technique was studied in Chapter 2 and some devices were designed as examples. The ACT is a more general way, when compared with the DCT, to design transformation devices. In Section 5.4, the advantages and disadvantages of the DCT will be investigated by comparing three-dimensional (3D) flat lenses created by the ACT and the DCT respectively.

At the end of this chapter, we will discuss the applicability of the DCT technique. It was proved in Chapter 2 that to employ the DCT technique, a near-orthogonal local coordinate grid is necessary. Accordingly, the curvature included in the transformation region may affect the orthogonality of a grid in the mesh generation, and consequently control the property of resulting devices. The limitation of the DCT technique will be investigated in Section 5.5.

5.2 Define the Transformation Region

According to the theory of coordinate transformation, the boundary condition before and after transformation should remain exactly the same [1]. Only under this condition, the physical space is able to perfectly mimic the virtual space, and holds the same electromagnetic property. However, when we manipulate a curved device to a flattened one, some part of the boundary condition may be changed if we ignore the complementary

space at the curved boundary. For example, in Fig. 5.1, a parabolic reflector made of perfect electric conductor (PEC) is located on the South boundary of the transformation region. After applying DCT, the East, West and North boundaries are held as before but the South boundary will be flattened. As a result, discontinuity of the refractive index (or the permittivity in dielectrics) may happen at the interface between the air and the dielectrics, causing additional reflections or refractions. Therefore, the transformation region should be carefully defined to minimise the discontinuity on the boundary.

Here we use the design of a flat reflector as an example to show the importance and the limitation of transformation region. According to the theory of DCT, the permittivity of dielectrics in the physical space is relative to the area in each grid cell, proved in Section 2.4 as

$$n'^2 \simeq \varepsilon'_z/\varepsilon_0 \simeq \frac{\Delta x \Delta y}{\Delta x' \Delta y'}. \tag{5.1}$$

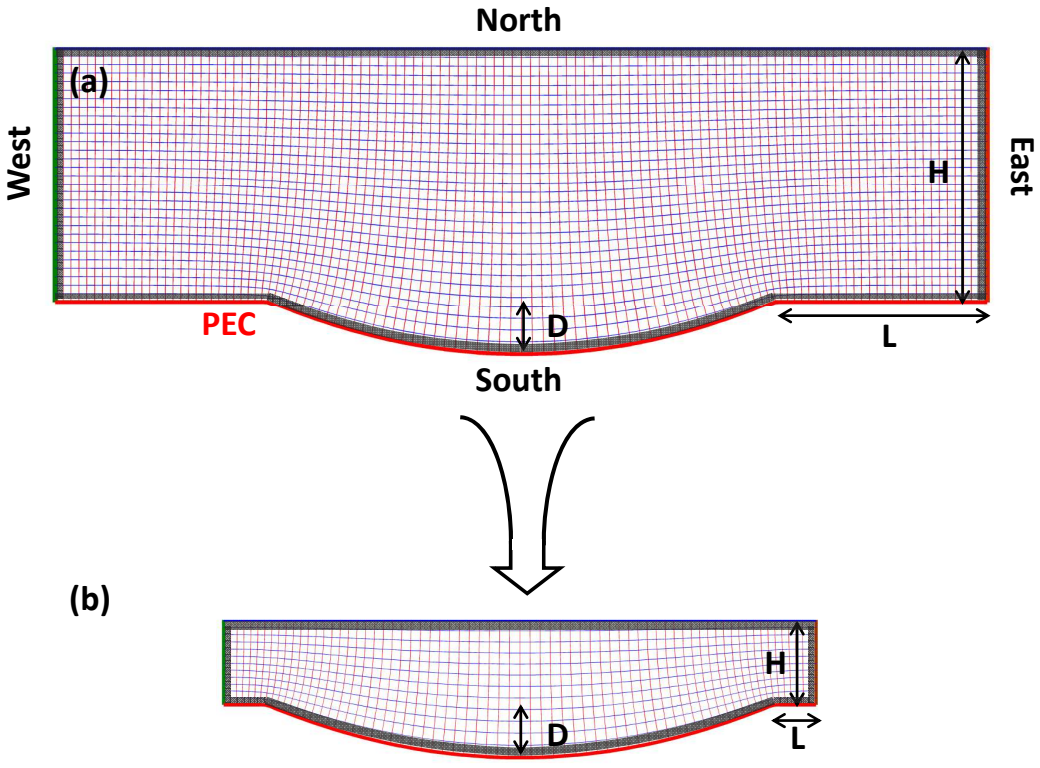

Figure 5.1: Transformation region with different size. (a) 330 mm × 90 mm. (b) 210 mm × 30 mm.

Parameters in Eq. (5.1) are the same as those marked in Fig. 2.11. According to Eq. (5.1), if the area of a cell in the virtual space doubles the area of its peer cell in the physical space, then the permittivity in the physical cell should double the value in the virtual cell. Since both spaces are surrounded by the air, we use the top left cell in both spaces as a reference and set the permittivity in this cell to be ε_0. For example, in Fig. 5.1, if all cells on the boundary (shown as the grey ones) have the same area as the top left one, the permittivity on the boundary is always ε_0 in both the virtual space and the physical space. As a result, the flat reflector causes no impedance mismatching to the air.

To achieve the above target, a straightforward solution is that if the dimension H in Fig. 5.1 is much larger than the depth of the parabolic curvature (D), saying 10 times or even more, then the disturbance of the curvature is less importance. In other words, if the transformation region is big enough, we can easily achieve uniform cells on the West, East and North boundaries, and on most part of the South boundary. Unfortunately, a large transformation region usually results in a big transformation device, which is inefficient in practice. Therefore, a practical way is to find a trade-off between the size of the transformation region and the performance of resulting devices.

To quantify this problem, an index is defined to represent the reflection on the boundary of a transformation device. According to the Fresnel equations [2], the reflection coefficient and the transmission coefficient between the air and a dielectric of ε_r can be written respectively as

$$R = \frac{\cos\theta - \sqrt{\frac{\varepsilon_r}{\varepsilon_0} - \sin^2\theta}}{\cos\theta + \sqrt{\frac{\varepsilon_r}{\varepsilon_0} - \sin^2\theta}}, \tag{5.2}$$

and

$$T = \frac{2\cos\theta}{\cos\theta + \sqrt{\frac{\varepsilon_r}{\varepsilon_0} - \sin^2\theta}}. \tag{5.3}$$

θ is the incident angle. For any $\varepsilon_r > \varepsilon_0$, the reflection coefficient always has a negative symbol. It should be pointed out that Eqs. (5.2) and (5.3) are applicable for vertical polarization, which agrees with the two-dimensional (2D) E-polarization we use throughout this thesis. A general and simple way to calculate the reflection is to assume the incident angle is $\theta = 0^{\text{o}}$ when it is impossible to predict an arbitrary incidence. So Eq. (5.2) is re-written as

$$R = \frac{1 - \sqrt{\varepsilon_r}}{1 + \sqrt{\varepsilon_r}}. \tag{5.4}$$

The average reflection coefficient on the boundary is therefore defined as

$$R_{ave} = \frac{1}{N} \sum_{i=1}^{N} \frac{1 - \sqrt{\varepsilon_i}}{1 + \sqrt{\varepsilon_i}}, \tag{5.5}$$

where N is the total number of cells on the boundary (e.g., those grey cells in Fig. 5.1), and ε_i is the relative permittivity in each cell.

In the reflector design, the focal length of the parabolic reflector is 108.6 mm and the depth D in Fig. 5.1 is 18.6 mm. Accordingly, the height of the transformation region H is gradually changed from 90(=108.6-18.6) mm to 30 mm (which is one wavelength at 10 GHz), with a spacing of 15 mm. Also the extra length on the two sides (L) is changed from 75 mm to 15 mm. Table 5-A lists the average reflection coefficient (R_{ave}) with different values of H and L. It should be pointed out that the average reflection coefficient is specifically used to quantify the reflection between the device and the air, and, therefore, cells on the South boundary in Fig. 5.1 are not included in Eq. (5.5) because a PEC reflector is located there. The PEC surface can be viewed as a mirror to duplicate the transformation region, and as a result, in this design, cells on the West, East and North boundaries are calculated twice in Eq. (5.5).

According to the data shown in Table 5-A, we can conclude the relation between the transformation region and the reflection on the boundary. First, as the height H and the extra length L of the region decrease, the average reflection coefficient increases

accordingly. Second, with a fixed H, the value of L does not significantly affect the performance. This is the reason why we could approximately neglect the two sides in Fig. 3.13. Third, once H is larger than 75 mm, R_{ave} changes slower as the value of H further increases. Therefore, $H = 75$ mm is considered as a practical limit for performance and size trade-off.

The discontinuity to the air brings in the increase of return loss, and the potential degradation of radiation pattern. However, as listed in Table 5-A, the average reflection coefficient is only 4.76% when $H = 75$ mm and $L = 60$ mm (which is the dimension we used in Section 3.3). This reflection is indeed minimal. In Section 3.3, numerical simulations have demonstrated the expected function of transformation reflectors, with slightly increased return loss and side-lobes. If a better performance is required, H and L should be amended. For any DCT based device design, one can use this kind of table to roughly predict and control the properties.

Table 5-A: The average reflection coefficient (R_{ave}) with different values of H and L.

	H (mm)					
		90	75	60	45	30
L (mm)	75	0.0356	0.0458	0.0604	0.0804	0.1186
	60	0.0378	0.0476	0.0632	0.0902	0.1318
	45	0.0394	0.0494	0.0678	0.0990	0.1434
	30	0.0428	0.0532	0.0718	0.1000	0.1608
	15	0.0488	0.0576	0.0744	0.1056	0.1686

5.3 Limitation of the Resolution

Transformation devices created by the DCT technique can have very detailed permittivity maps if the space is discretised with a fine grid. Although all required permittivity values can be realised using dielectrics, it is rather complicated to fabricate many dielectric blocks and distribute them into the assigned profile. A post processing is to simplify the permittivity map, as used in Chapters 3 and 4. In this section, we investigate the limitation of resolution for transformation devices. It is proved that transformation devices

with a low-resolution map retain similar performance as those with high-resolution ones within a limited bandwidth of operation, while accompanied by predictable degradations of the radiation pattern above the "cut-off" frequency.

5.3.1 The sampling theorem

The fundamental limitation is based on the Nyquist-Shannon sampling theorem [3]. Sampling is the process of converting a signal (for example, a function of continuous time or space) into a numeric sequence (a function of discrete time or space) [4]. Shannon's version of the theorem states: "*If a function f(t) contains no frequencies higher than W cps, it is completely determined by giving its ordinates at a series of points spaced 1/2W seconds apart.*" Fig. 5.2 interprets this theorem in the spatial domain. When propagating in the physical space, at a fixed time, the electromagnetic wave is a function of continuous space. Transformation media with a high resolution discretise the space using a high sampling rate while low-resolution ones discretise the space using a low sampling rate. If the electromagnetic wave operates in a frequency band from f_L to f_H, to accurately reconstruct information of the wave, the sampling rate f_s should satisfy

$$f_s > 2f_H. \tag{5.6}$$

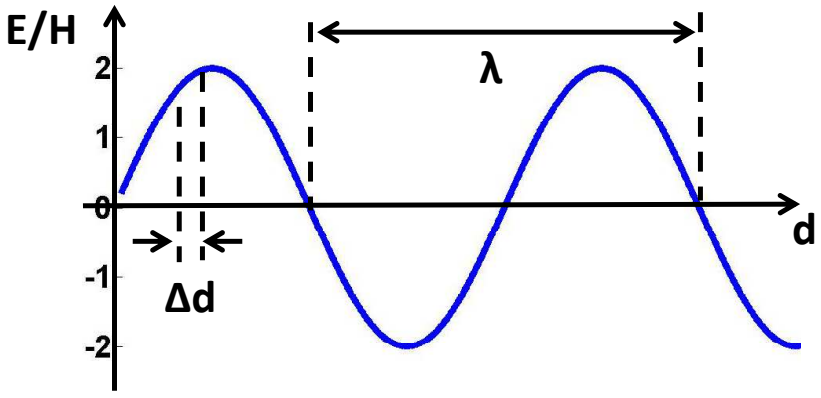

Figure 5.2: An electromagnetic wave propagates in the spatial domain at a fixed time.

Because

$$f_s = \frac{1}{\triangle d},\ f = \frac{1}{\lambda}, \tag{5.7}$$

the resolution of the discrete space should satisfy

$$\triangle d < \frac{1}{2}\lambda_H. \tag{5.8}$$

$\triangle d$ is the dimension of blocks in the permittivity map of a transformation device, and λ_H is the minimum wavelength within the frequency band. According to Eq. (5.8), as long as dielectric blocks are smaller than half a wavelength at operating frequencies, the simplified device can maintain the property of a high-resolution one. When the operating frequency goes higher, the resolution of dielectric map should increase accordingly.

5.3.2 Comparison between 2D flat lenses with different resolutions

Next, we will compare a series of transformation lenses with different resolutions for the radiating performance. In Section 3.4, a flat lens has been created from a conventional convex lens, and two maps with different resolutions (80×15-block and 14×1-block) are provided (see Fig. 5.3). Here, two additional permittivity maps with 40 × 8 blocks and 20 × 4 blocks are also generated to test how the reduction of resolution influences the performance in terms of the radiation pattern and the bandwidth.

The flat lenses are expected to operate from 4 GHz to 12 GHz, so the minimum wavelength is calculated at 12 GHz. In the transformation media, the average relative permittivity is about 5, therefore half the minimum wavelength is about 5.6 mm. Dimensions of blocks in different maps are given in Table 5-B. Apparently, blocks in the the 80×15-block map and in the 40×8-block map are smaller than half the wavelength, which means both the two resolutions are fine enough. Blocks in the the 20×4 map is slightly bigger than half the wavelength. This reduced resolution may slightly harm the

Table 5-B: Dimensions of blocks in permittivity maps with difference resolutions.

Resolution	Dimension of blocks (mm)
80×15	2×1.59
40×8	4×2.98
20×4	8×5.95
14×1	12.3×23.8

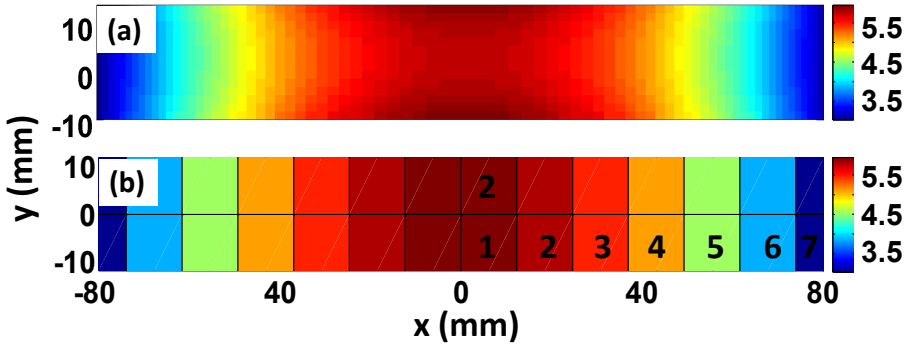

Figure 5.3: Permittivity maps of the flat lens. (a) The map consisting of 80×15 blocks. (b) The map consisting of 14×1 blocks.

performance, but not significantly. The 14×1-block map has an unqualified resolution, which will result in obvious degradation to the performance, according to the sampling theorem.

To prove the above presumption, the radiation patterns of the conventional lens and the four flat lenses with different resolutions are depicted in Fig. 5.4. Configuration of the simulation is the same as in Fig. 3.16. When the permittivity map decreases from 80×15 blocks to 40×8 blocks and then to 20×4 blocks, the performance remains almost unchanged at 8 GHz. In the radiating direction of $\phi = 0^o$, the three curves are exactly the same. The 20×4-block map has slightly increased side lobes when compared with the other two. However, it can be considered as the threshold resolution. A visible degradation is observed when the map reduces to 14×1 blocks. The energy validated in the direction of $\phi = 0^o$ drops to about 75% (-1.25 dB) of that of a convex lens, accompanied with an obvious increase of side lobes. Although its performance is acceptable for many applications in practice, from a theoretical point of view, properties of a propagating wave is not accurately re-constructed under this resolution.

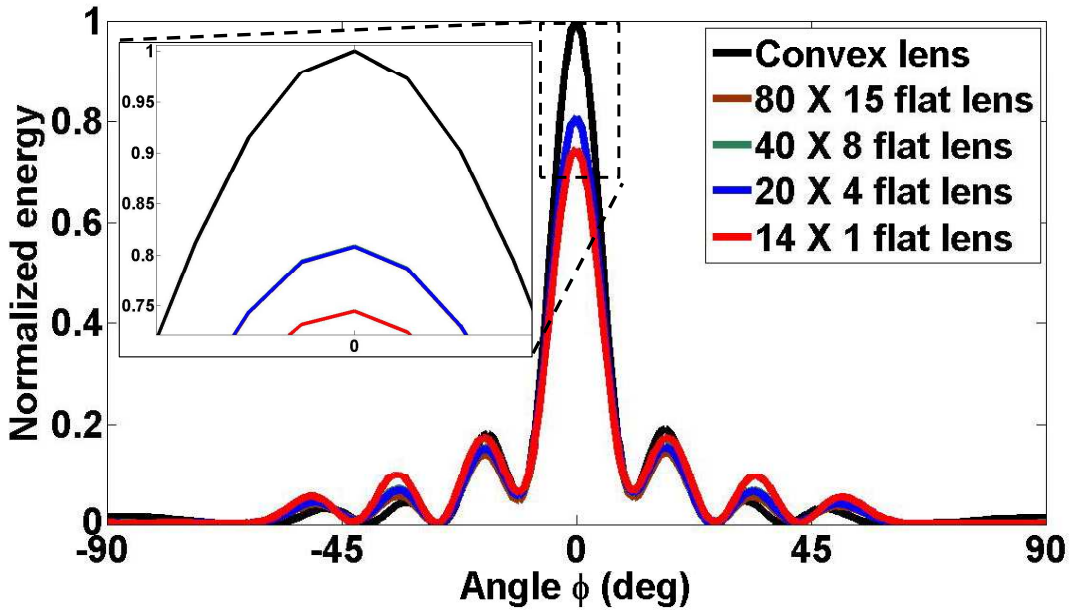

Figure 5.4: Comparison of the radiation patterns at 8 GHz. The definition of Φ is shown in Fig.3.16(d).

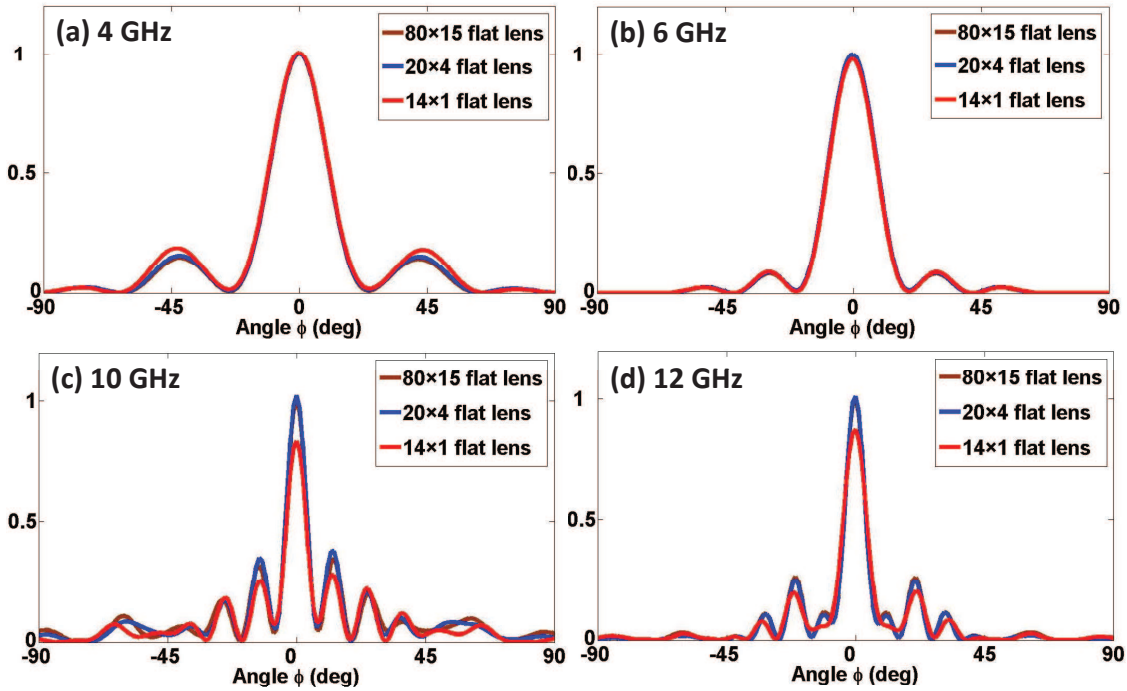

Figure 5.5: Comparison of the radiation patterns when the flat lenses are fed by a line source at the focal point. Three lenses with different resolutions (80×15 blocks, 20×4 blocks and 14×1-blocks) are tested at 4 GHz, 6 GHz, 10 GHz and 12 GHz respectively.

In Fig. 5.5, the radiation patterns are also tested at 4 GHz, 6 GHz, 10 GHz and 12 GHz, respectively. Again, the 20×4-block map is proved to have almost the same performance as the 80×15-block map, indicating the resolution is adequate. As the operating frequency increases, the 14×1-block map brings in lower radiation around $\phi = 0^o$ and different side lobes. This, again, demonstrates the presumption according to the sampling theorem.

5.3.3 Comparison between 3D flat lenses with different resolutions

In previous chapters, we simulated the DCT based devices only in the 2D circumstance with E-polarization. Since the created devices are made of isotropic dielectrics, a 3D model is straightforwardly accomplished by extending a 2D model to the third dimension. For example, when rotated to its optical axis, the above 2D flat lens becomes a 3D one, as illustrated in Fig. 5.6. In this subsection, 3D flat lenses with different resolutions are tested. On the one hand, we want to demonstrate that the rotated 3D lens does serve as a beam-forming lens. On the other hand, the directivity is calculated to define the bandwidth of a lens.

It has been demonstrated in the 2D circumstance that the 20×4-block map is a considerable threshold with a qualified resolution, whilst the 14×1-block map is with an unqualified resolution. Now we test their 3D models to further prove the limitation of device performance with low dielectric resolutions. The Ansoft's HFSS is applied as another tool for numerical simulation. An electric dipole is located at the focal point to generate an incident Hertzian-Dipole Wave, and the directivity of the two flat lenses and the convex lens are compared.

Fig. 5.7 (a) to (c) present the directivity patterns of the three lenses in both the E-plane and the H-plane at 4 GHz, 8 GHz and 12 GHz, respectively. At 4 GHz, when the resolution of the 14×1-block lens is similar to half the wavelength, the 14×1-block lens has almost the same directivity as the 20×4-block one. When the frequency increases to

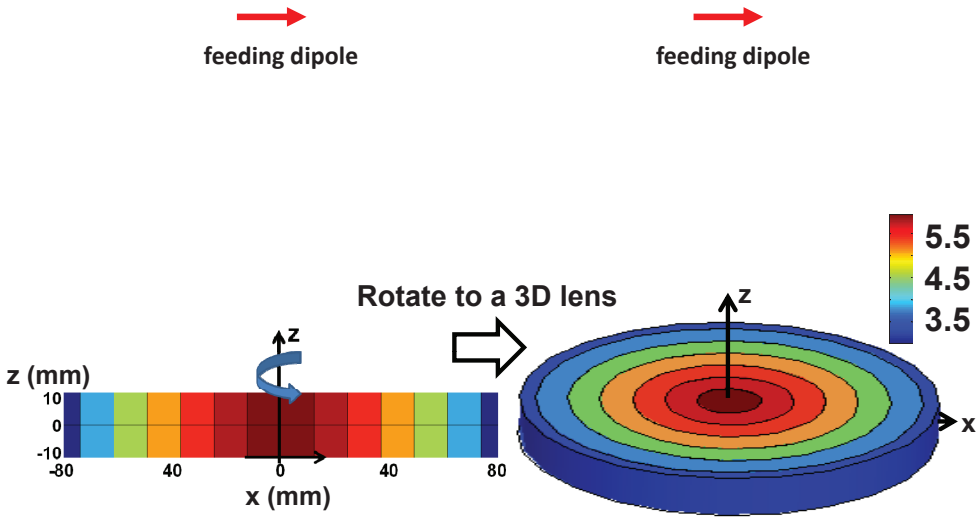

Figure 5.6: A 3D flat lens is created by rotating the 2D permittivity map to its optical axis. The 3D lens is made of annular dielectric blocks. Colour bar shows the relative permittivity values.

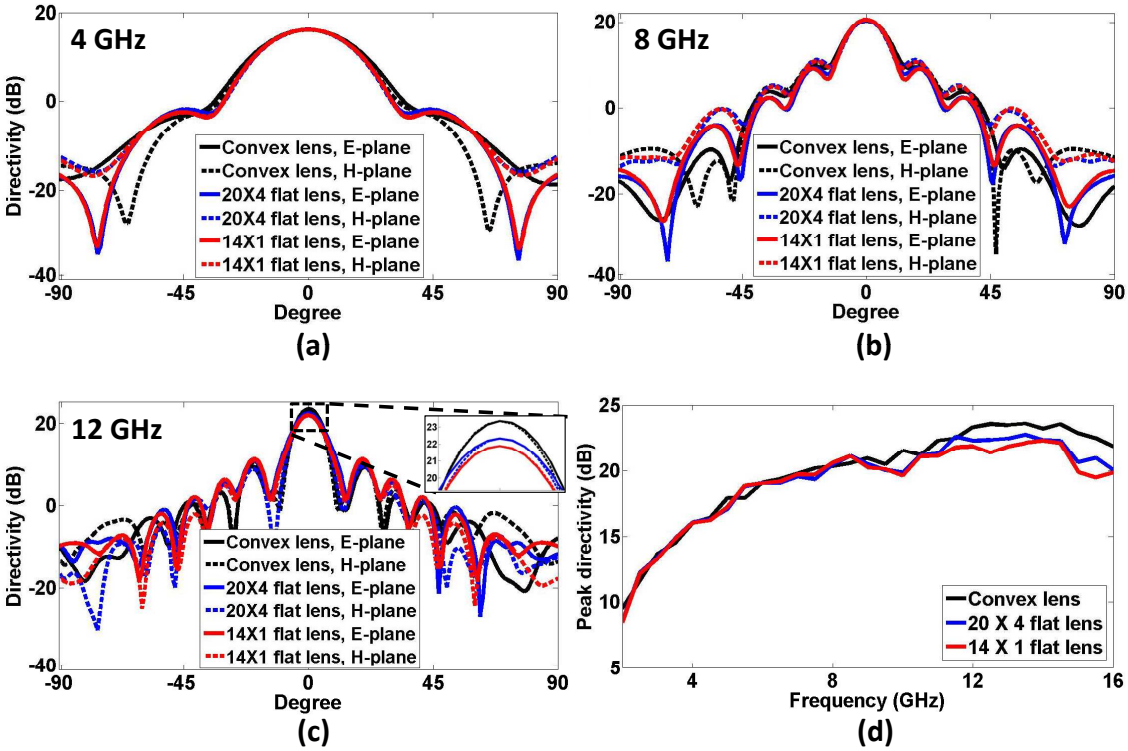

Figure 5.7: Comparison of the directivity of the convex lens, the 20×4-block lens and the 14×1-block lens. The directivity patterns are drawn in the E-plane and the H-plane at (a) 4 GHz, (b) 8 GHz and (c) 12 GHz. In (d), the peak directivity of the three lenses are plotted from 2 GHz to 16 GHz.

8 GHz, the two lenses still have very similar directivity patterns. The lower-resolution one has slightly lower peak directivity (the maximum directivity over all the directions, as defined by HFSS), and a bit increased side lobes. As the operating frequency further increases to 12 GHz, the difference between the two lenses enlarges. The peak directivity of the low-resolution lens decreases further and the side lobes increase as well. However, the low-resolution lens still holds an acceptable directivity pattern, which agrees well with the results in the 2D simulation. Besides, the convex lens always has the best directivity in terms of the highest peak directivity and the lowest side lobes.

Fig. 5.7 (d) plots the peak directivity of the three lenses from 2 GHz to 16 GHz, so as to compare their operating bandwidth [5]. The convex lens has a -3 dB bandwidth from about 8.5 GHz to about 16.7 GHz (8.2 GHz span), the 20×4-block lens has a bandwidth from about 7.7 GHz to about 16 GHz (8.3 GHz span), and the 14×1-block lens has a bandwidth from about 6.6 GHz to about 15.5 GHz (8.9 GHz span). Overall, in the entire frequency band, the peak directivity decreases as the convex lens, the 20×4-block lens and the 14×1-block lens is applied respectively. Differences between the three lenses increases as the frequency goes higher. It is also noticed that at lower frequencies, all three lenses have low directivity. The underlying physics is that when the aperture size of a lens is comparable to the wavelength, it cannot efficiently focus energy to the focal point, or reform the phase front of the wave.

5.4 Comparison with the ACT Based Design

5.4.1 The composing material

The analytical coordinate transformation (ACT) has been studied and employed for creating novel functional devices along recent years. This technique provides a general method to design transformation media, as long as one can define the Jacobian matrix between the coordinate systems in the virtual space and the physical space. The

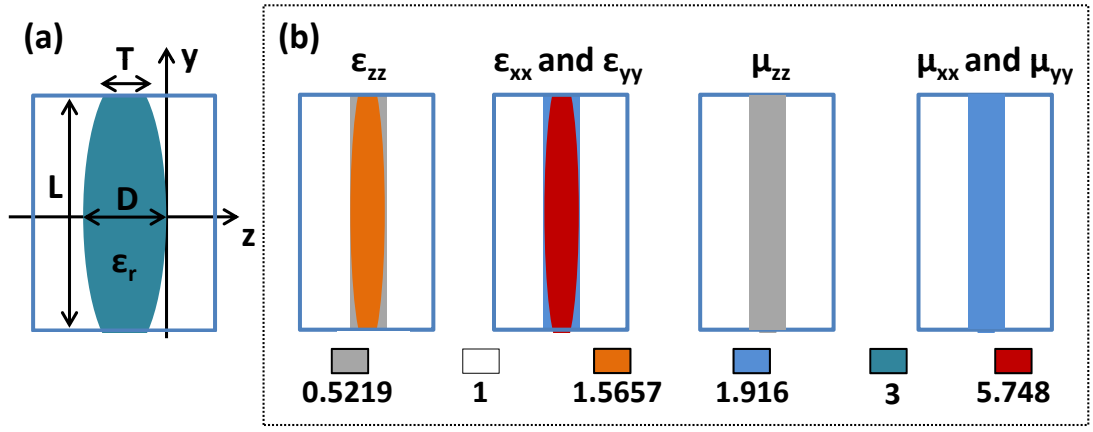

Figure 5.8: (a) The original convex lens. (b) The relative permittivity and relative permeability maps of the ACT based lens. The colored blocks represent relative permittivity/permeability values.

obtained transformation media are usually anisotropic in both permittivity and permeability. Example designs in Section 2.3 indeed displayed this property. Furthermore, if the transformation region includes singular points, permittivity or permeability values can approach the infinity. This kind of parameters are impossible to realise in practice.

The DCT was therefore proposed and developed as a more practical way of using the coordinate transformation (CT) technique. Although the DCT is not applicable when one boundary of the transformation region goes to infinite, for example the inner boundary of a cylindrical cloak can shrink to an axis in the virtual space, this technique is a functional tool to generate devices in practice. In Chapters 2 and 3, we have designed flat lenses from the same convex lens by using the ACT and the DCT respectively. Here, we use them as examples to compare the two techniques.

Fig. 5.8 illustrates the permittivity and permeability values of the transformation lens by using the ACT technique. To be noted, the coordinate system here is different from that in Fig. 2.6. Composing materials of this ACT based lens have two features. First, it's anisotropic in permittivity and permeability. Although it is possible to manufacture materials with required anisotropic permittivity, or even with anisotropic permeability, the manufacturing procedure is very complicated and expensive. Second, less-than-unity permittivity and permeability are required. This kind of parameters are rarely found in

nature, as a result, metamaterials are commonly employed as the solution.

Here we design a prototype of the ACT based lens using metamaterials. There are two anisotropic materials required in Fig. 5.8(b): in the outer part of the compressed region, the permittivity tensor is (1.916,1.916,0.5219)ε_0 and the permeability tensor is (1.916,1.916,0.5219)μ_0; in the inner part, the permittivity tensor is (5.748, 5.748, 1.5657)ε_0 and the permeability tensor is (1.916,1.916,0.5219)μ_0. To obtain the required electromagnetic parameters, metamaterials are constructed from resonant unit cells. Fig. 5.9(a) shows the arrangement of two neighbouring unit cells. The cubic block represents an artificial material possessing the permittivity tensor of (1.916, 1.916,5)ε_0 and the permeability tensor of (1.916,1.916,1.916)μ_0, which is possibly made available with some limitations. However, in order to achieve less-than-unity permittivity and permeability in the z direction, resonant structures are necessary. We have studied the I-shaped resonator in Section 4.2.3. Here, in addition, a magnetic resonator termed as the split-ring resonator (SRR) [6], is also adopted to provide less-than-unity permeability in the z direction. Artificial materials are constituted of the unit cells which are extended to three directions, as shown in Fig. 5.9(a). It should be pointed out that in order to obtain a homogeneous metamaterial, each unit cell should be of sub-wavelength and oriented in all three dimensions. In this case, since the central operating frequency is 8 GHz, the size of a unit cell is set to be 3.97 mm. This size is one sixth of the thickness of the compressed lens (as is marked as T in Fig. 5.8(a)), in other words, the compressed lens has six layers in the z direction.

Fig. 5.9(b) and (c) plot the relative effective permittivity and permeability of the metamaterial [7]. From 4 GHz to 15 GHz, the real parts of ε_{xx} and ε_{yy} increase slowly from the required value of 1.916ε_0 to around 5ε_0. This means, in the x and y directions, the frequency dispersion is relatively weak. However, strong frequency dispersion is observed in the z direction, due to the resonant nature of the I-shaped structure. On the one hand, the resonance serves to create less-than-unity permittivity between 9 GHz to 12.5 GHz. On the other hand, it causes fast change of permittivity, and consequently

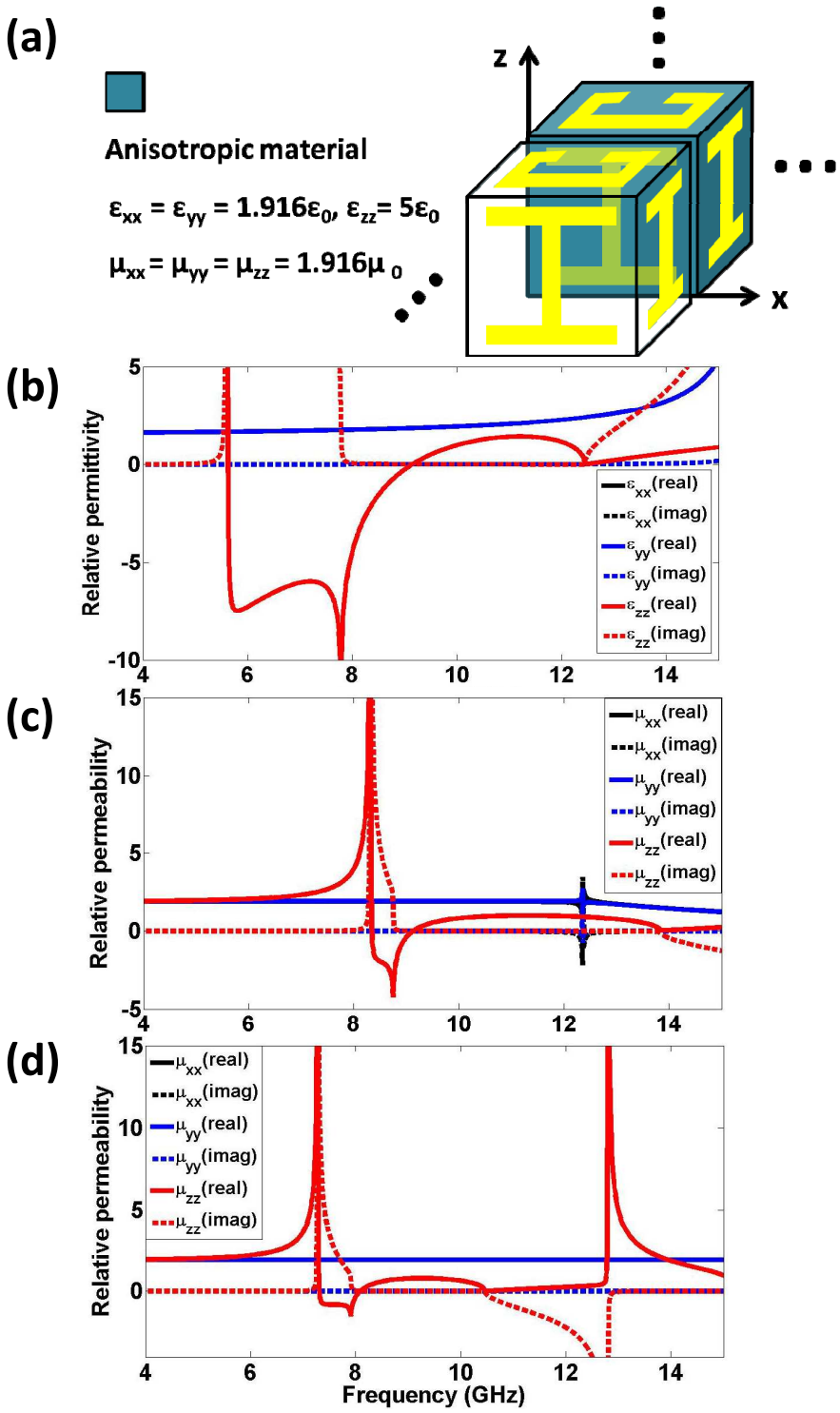

Figure 5.9: Realise the less-than-unity permittivity and permeability values by using metamaterials. (a) The unit cells to construct the metamaterial filling the outer part of the compressed region in Fig. 5.8(b). (b) The relative permittivity of the metamaterial that fills the outer part of the compressed region. (c) The relative permeability of the metamaterial that fills the outer part of the compressed region. (d) The relative permeability of the metamaterial that fills the inner part of the compressed region.

brings in a narrow-band property. In Fig. 5.9(b), the permittivity of 0.5219 is only found around 9.5 GHz, 12.4 GHz and 13.9 GHz, while changes very fast against the frequency. It should be noted that the narrow band property of the I-shaped resonators did not present in Section 4.2.3 when we constructed a carpet cloak. This is because the permittivity values required for that carpet cloak were larger than unity, so frequencies with required permittivities were far away from the resonance frequency of the I-shaped resonator. Fig. 5.9(c) shows that μ_{xx} and μ_{yy} have a constant value of 1.916, as required. In the z direction, μ_{zz} is frequency-dispersive, also due to the magnetic resonance of the SRR. The required relative permeability of 0.5219 is found between 9.5 GHz to 13.5 GHz. Figures in (b) and (c) indicate that by using resonant metamaterials, the less-than-unity permittivity and permeability can be created in a narrow band. A different unit cell is found to construct metamaterial that fills the inner part of the compressed region in Fig. 5.8 (b). The new cubic block has a permittivity tensor of (5.748,5.748,1.5657)ε_0 and a permeability tensor of (1.916,1.916,1.916)μ_0. Since the less-than-unity permittivity is no longer required, the I-shaped structures are not included in the unit cells. Fig. 5.9(d) plots the relative effective permeability of the metamaterials in the inner part of the compressed region. The required permeability of 0.5219 happens between 8.4 GHz to 10.2 GHz, indicating the metamaterial is also narrow-band.

In contrast with the ACT based lens, the DCT based flat lens has much simpler parameters. First of all, only the permittivity distribution is required, as shown in Fig. 5.3. The permeability is constant as that of the air. Second, the constructing materials are isotropic, and their permittivity values are usually larger than unity. According to these properties, the lens is achievable from conventional dielectric blocks. These dielectrics can be easily found or fabricated [8, 9], and are not expensive. It is noted that, some DCT based devices, such as the flat reflector in Section 3.3, include neglectable areas with less-than-unity permittivities. In addition, it will be challenging to manufacture the DCT based lens at high frequencies, because the permittivity map should have very fine resolution as the wavelength goes shorter, as we discussed in the previous sec-

tion. However, in general, the DCT based lens has an advantage over the ACT based lens because its constructing materials are easily realisable.

5.4.2 The bandwidth

Next, we are going to evaluate the bandwidth of the ACT based compressed lens. A 3D lens is formed by rotating the parameter maps in Fig. 5.8(b) to the z axis, and then is simulated in the Ansoft's HFSS. To start with, we test the ideal model which is only composed of homogeneous materials. These ideal materials possess the required anisotropic permittivity and permeability as defined in Fig. 5.8(b). The lens is simulated at different frequencies. By plotting the peak directivity at each frequency point, the ACT based lens is compare with the convex lens and the DCT based lenses in Fig. 5.10 from 4 GHz to 16 GHz. At high frequencies from 13 GHz to 16 GHz, the ACT based lens has the most similar peak directivity as the convex lens, and is more directive than the DCT based lenses. At frequencies lower than 9.5 GHz, peak directivity of the ACT based lens is obviously lower than the other three lenses. Physical explanation of this property is that because the ACT lens includes less-than-unity refractive index in the outer part, the relative wavelengths at low frequencies are much larger than the thickness

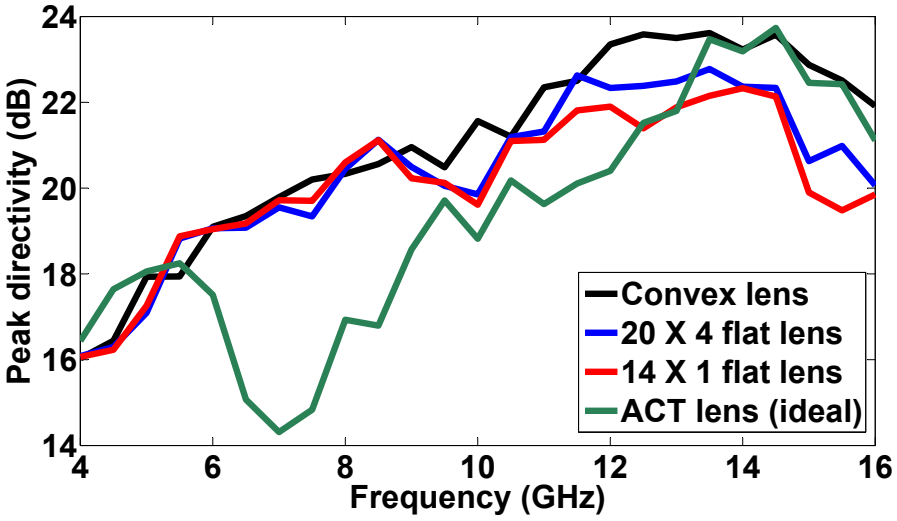

Figure 5.10: Comparison of the convex lens, the ACT based lens and the DCT based lenses with different resolutions.

of the lens. As a result, the focusing property of the lens no longer holds and the focal point is not correct any more. Beyond 7 GHz, the thickness of the outer part becomes comparable to the relative wavelength, so the directivity begins to increase. Fig. 5.10 has demonstrated that the ACT based lens is not as functional as the DCT based lens at low frequencies, and consequently possesses a much narrower operating bandwidth.

Furthermore, the adoption of resonant metamaterials will bring in more dispersion to the ACT based lens. Fig. 5.9(b)-(d) have presented the dispersive feature of metamaterials which are possible solutions to manufacture the ACT based lens. Table 5-C lists detailed permittivity and permeability values provided by the metamaterials from 4 GHz to 15 GHz. The required anisotropic permittivity and permeability only exist around 10 GHz. When the parameters change from the ideal values in Fig. 5.8(b) to the realised values in Table 5-C, the performance of the lens will degrade. For example, at 12 GHz, the ideal lens has a peak directivity of 20.4 dB, but the realised lens has a peak directivity of 16.86 dB. This fact indicates that the ACT based lens is sensitive to the parameters. As a result, the bandwidth of a manufactured lens is even narrower than that shown in Fig. 5.10. In conclusion, the DCT based lens has another advantage over the ACT based lens that its operating bandwidth is much broader.

Table 5-C: Relative effective permittivity and permeability of the metamaterials designed in Fig. 5.9.

	Outer part				Inner part			
f (GHz)	$\varepsilon_{xx}/\varepsilon_{yy}$	ε_{zz}	μ_{xx}/μ_{yy}	μ_{zz}	$\varepsilon_{xx}/\varepsilon_{yy}$	ε_{zz}	μ_{xx}/μ_{yy}	μ_{zz}
4	1.628	12.71	1.91	1.919	5.748	1.566	1.91	1.925
5	1.651	19.91	1.91	1.965	5.748	1.566	1.91	1.992
6	1.683	-7.289	1.91	2.061	5.748	1.566	1.91	2.19
7	1.722	-6.04	1.91	2.321	5.748	1.566	1.91	3.616
8	1.775	-4.468	1.91	3.995	5.748	1.566	1.91	-0.337
9	1.845	-0.2575	1.91	-0.397	5.748	1.566	1.91	0.771
10	1.941	1.006	1.91	0.822	5.748	1.566	1.91	0.635
11	2.078	1.412	1.91	0.989	5.748	1.566	1.91	0.095
12	2.28	1.142	1.918	0.961	5.748	1.566	1.91	0.252
13	2.608	0.214	1.708	0.770	5.748	1.566	1.91	4.943
14	3.272	0.567	1.465	0.062	5.748	1.566	1.91	1.846
15	5.344	0.877	1.228	0.242	5.748	1.566	1.91	0.962

5.5 Limitation of the Curvature

The DCT technique has been proved to beat the ACT technique in terms of easy realisation methods and broad operating bandwith. However, it cannot be straightforwardly applied to all problems as the ACT does. One exception is, as mentioned previously, that the DCT is not applicable when one boundary of the transformation region goes to infinite, for example the inner boundary of a cylindrical cloak can shrink to an axis in the virtual space. Even if the boundary is finite, the DCT technique requires "smooth" curvature on the boundary. The term of "smooth" is roughly defined as "non-sudden bend by a large angle". However, this definition is vague. In order to state this problem clearly, here we are going to study the limitation of curvature in the DCT technique.

Fig. 5.11 presents the flat reflector design for instance. Φ is the bending angle as marked in figure (a). When the bending angle increases, more points on the bottom boundary assemble around the bend in order to keep local coordinates near-orthogonal. This arrangement brings in big cells around the central area and small cells around the

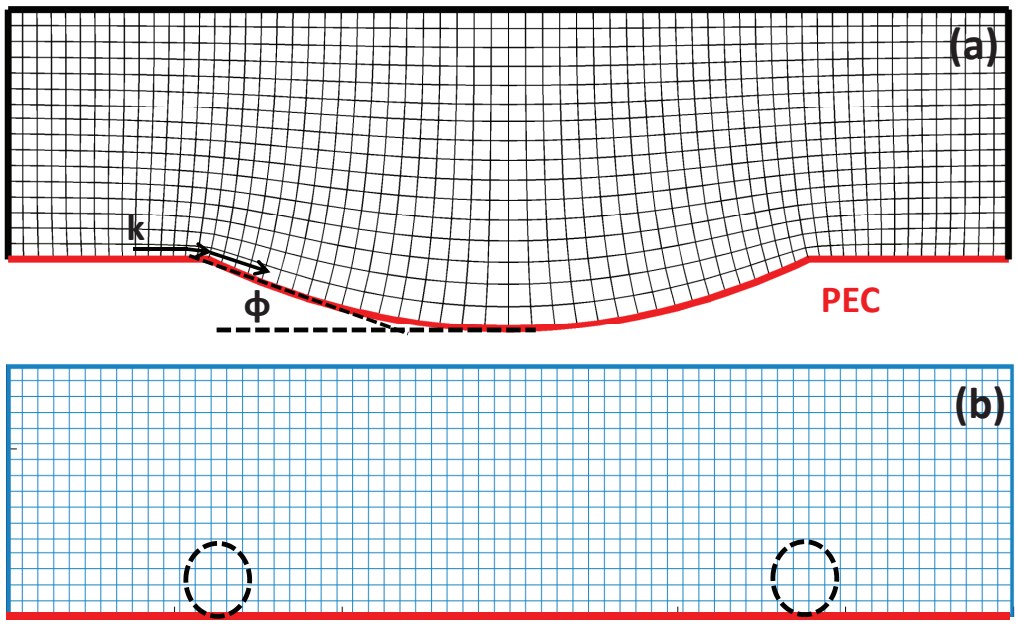

Figure 5.11: (a) Grid in the virtual space with a bending angle of Φ. (b) Uniform grid in the physical space.

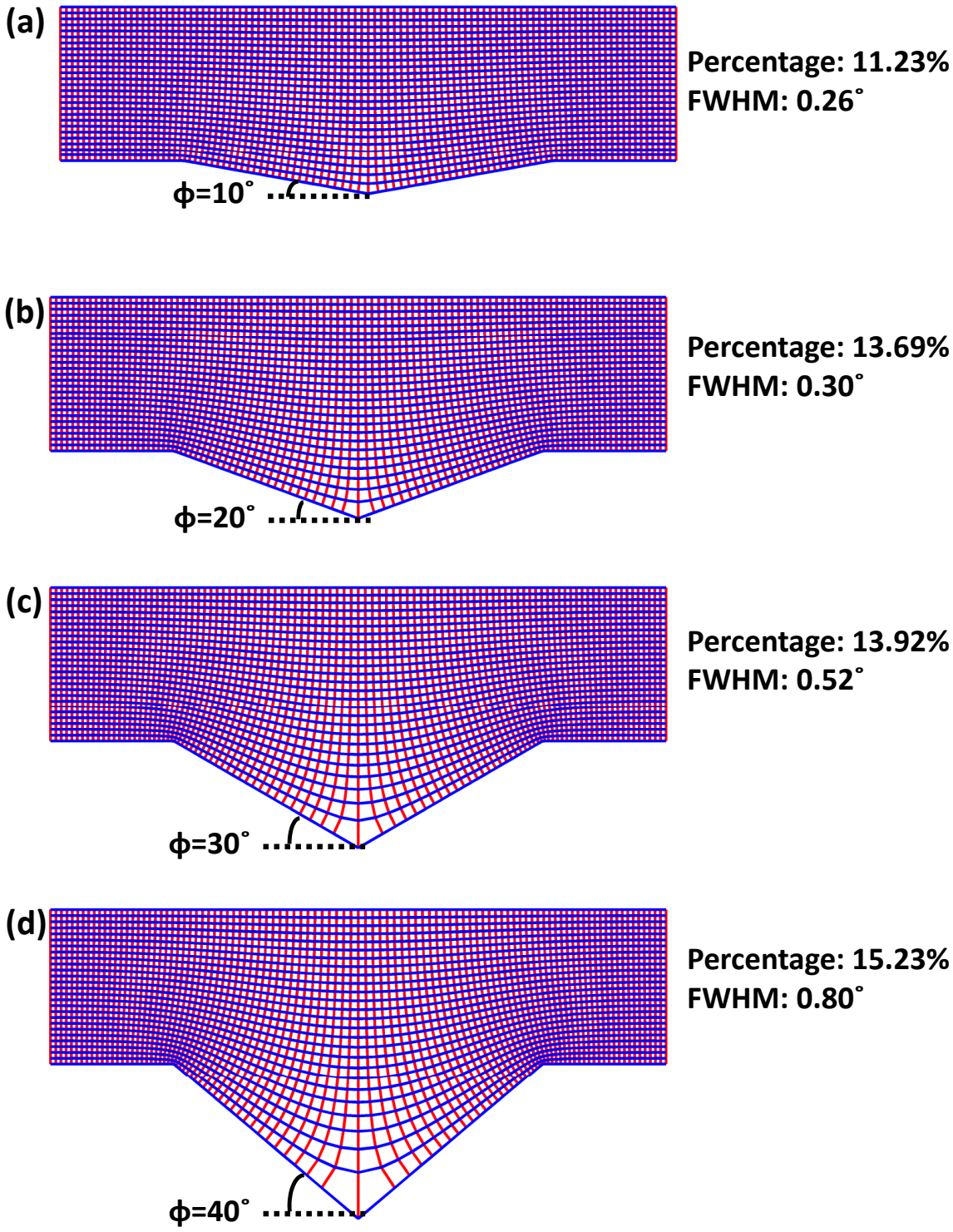

Figure 5.12: (a)-(d) The distorted spaces with different bending angles from 10° to 40°. The percentage of less-than-unity cells, and the full width at half maximum (FWHM) index are noted for each case.

bend. According to Eq. (5.1), cells bigger than the one on the top left corner result in permittivity values larger than unity, whilst cells smaller than the top left one result in permittivity values less than unity. Therefore, blocks with the highest permittivities are found in the central area of the flat reflector, close to the PEC surface shown in Fig. 5.11(b). Meanwhile, the less-than-unity values happen inside the two dashed circles. It is also predictable that curvature with a larger angle of Φ will result in more less-than-unity cells around the bend.

To simplify the problem, the measure of curvature is represented by the bending angle Φ on the bottom boundary in Fig. 5.12. Four distorted meshes with different bending angles are compared in Fig. 5.12. From (a) to (d), the transformation region remains the same, while the angle of Φ increases from 10^{o} to 40^{o}. Two indices are employed to measure the property of the distorted grid. The first one is the percentage of less-than-unity cells. If this index is high, the less-than-unity permittivities cannot be neglected, and hence, a DCT based device is no longer achievable by using conventional dielectrics. The second one is the full width at half maximum (FWHM) index which was studied in Chapters 2 to 4. This index represents the orthogonality of a grid. An ideally orthogonal grid has a FWHM index of 0^{o}. If this index is high, electromagnetic parameters of a DCT based device become anisotropic. Conclusions are drawn according to Fig. 5.12 that as the bending angle increases, the area with less-than-unity permittivities enlarges, and the orthogonality of the grid degrades. As a result, the all-dielectric devices designed using the DCT technique lose performance. In other words, the DCT technique gradually becomes invalid.

5.6 Summary

Some vital properties of the DCT technique were investigated in this chapter. This technique provides us with a more practical way to create transformation devices, when compared to the ACT technique. The composing materials in a DCT based device are

conventional dielectrics, which are easily obtainable from the nature or in laboratories. Thanks to the low frequency dispersion of dielectrics, the DCT based devices obtain broadband performance. On the contrast, the ACT based devices commonly require anisotropic materials with less-than-unity permittivities and permeabilities. These complicated materials are difficult to fabricate, and are usually highly dispersive of frequency. As a result, the ACT based devices have much narrower bandwidth than the DCT based ones. Two flat lenses, created by the ACT and the DCT respectively, were compared in this chapter in terms of the directivity and the operating bandwidth. Simulation results confirmed the above statement.

According to the study in this chapter, a general procedure of designing a DCT based device is concluded here. First, the transformation region is decided according to the curvature on boundaries. A large transformation region results in better property of the near-orthogonal grid, and consequently better performance of the transformation device. However, a trade-off should be chosen considering both the performance and the volume of device. Second, Eq. (5.1) is applied to calculate the permittivity map, as we did in Chapters 3 and 4. After that, simplifications are carried out to reduce the resolution of the map, in order to achieve an easily realisable device. To maintain the performance, the lowest resolution should be no less than half the wavelength at the highest operating frequency. At the end, the designed device is manufactured using dielectrics or non-resonant metamaterials.

In some cases when singularities exist on the boundary, the DCT technique is invalid, whilst the ACT technique can still work. This is because if the boundary is infinite, a near-orthogonal grid cannot be generated. Besides, when the transformation region includes large curvature on the boundary, the near-orthogonal property in local coordinates cannot hold, and less-than-unity permittivities cannot be ignored. For these cases, the DCT technique becomes invalid. In order to solve this problem, an extension of the DCT technique, the multiple DCT technique, will be proposed and demonstrated in the next chapter.

References

[1] J. B. Pendry, D. Schurig, and D. R. Smith, "Controlling electromagnetic fields," *Science*, vol. 312, pp. 1780–1782, 2006.

[2] E. Hecht, *Optics, 1987*.

[3] C. Shannon, "Communication in the presence of noise," *Proc. IRE*, vol. 37, no. 1, pp. 10–21, 1949.

[4] "Nyquist-cshannon sampling theorem," http://en.wikipedia.org/wiki/Nyquist-Shannon_sampling_theorem.

[5] R. Yang, W. Tang, and Y. Hao, "A broadband zone plate lens from transformation optics," *Opt. Express*, vol. 19, no. 13, pp. 12 348–12 355, 2011.

[6] J. Pendry, A. Holden, D. Robbins, and W. Stewart, "Magnetism from conductors and enhanced nonlinear phenomena," *IEEE Trans. Micr. Theory Techn.*, vol. 47, no. 11, pp. 2075–2084, 1999.

[7] D. Smith, S. Schultz, P. Markoš, and C. Soukoulis, "Determination of effective permittivity and permeability of metamaterials from reflection and transmission coefficients," *Phys. Rev. B*, vol. 65, no. 19, p. 195104, 2002.

[8] D. Bao, K. Rajab, W. Tang, and Y. Hao, "Experimental demonstration of broadband transmission through subwavelength aperture," *Appl. Phys. Lett.*, vol. 97, p. 134105, 2010.

[9] D. Bao, K. Rajab, Y. Hao, E. Kallos, W. Tang, C. Argyropoulos, Y. Piao, and S. Yang, "All-dielectric invisibility cloaks made of batio3-loaded polyurethane foam," *New J. of Phys.*, vol. 13, p. 103023, 2011.

Chapter 6

Multiple Discrete Coordinate Transformation and Its Applications

6.1 Introduction

The coordinate transformation, as a unique technique to control the electromagnetic waves, has been presented in Chapter 2 accompanied with its applications from the "cloaks of invisibility" to microwave devices. However, practically implementing most of the transformation devices is still challenging because the media required to construct them are usually very complicated and cannot be found directly in the nature. One reliable solution to circumvent this limitation, as proved in this thesis, is the practical implementation of this technique: the discrete coordinate transformation (DCT). Due to the discretisation of the transformation space, local coordinate systems before and after transformation become near-orthogonal. As a result, singularity and anisotropy that exist during the analytical coordinate transformation (ACT) are minimised, and therefore, an all-dielectric solution of a transformation device is achieved.

However, there are restrictions of applying the DCT technique, as we discussed in Section 5.5. If the transformation space (either the virtual space or the physical space) has an infinite boundary, generating near-orthogonal local coordinate systems becomes impossible. As a result, the DCT technique is no longer applicable. Furthermore, even all boundaries are finite, they should not include strongly-bent curvature, because that will degrade the accuracy of the all-dielectric solution. For these reasons, the DCT technique has remained invalid to a variety of applications.

To extend the applicability of this technique, in this chapter, we will propose the multiple discrete coordinate transformation. A transit space will be introduced between the virtual space and the physical space, in order to implement new boundaries which contain no singularities but only "smooth" curvature. First, we will explain from the theory that this design method can efficiently reduce the inaccuracy which happens in one-step transformation. Second, an all-dielectric absorber will be created by compressing a pyramidal absorber. Applying the multiple DCT technique, the thickness of the pyramidal absorber can be reduced by 2/3. The transformation absorber requires only lossy dielectrics, hence is much easier to fabricate compared with the one we designed in Section 2.3.2.3 using the ACT technique. The Finite-Difference Time-Domain (FDTD) method based numerical simulations will demonstrate the performance of the transformation absorber.

6.2 Multiple Discrete Coordinate Transformation

We use an example to explain the multiple discrete coordinate transformation. Fig. 6.1 shows a space where a metal plate is located horizontally. An incident wave propagates from the South (S) to the North (N), parallel to the East (E) and the West (W) boundaries, as marked by arrowed black lines in Fig. 6.1(a) and (b). Normally, the wave impinging on the metal plate will be reflected. However, the technique of coordinate transformation makes it possible to circumvent the metal plate by steering the wave.

We have discussed the limitation of applying the DCT technique in Section 5.5, that if the bending angle (e.g., ϕ in Fig. 6.1(b)) is large, the orthogonality in local coordinate systems will be broken. In this circumstance, the transformation media are anisotropic in both permittivity and permeability, and must include less-than-unity values. In contrast, if it does not require a sharp bend of the wave, (e.g., as portrayed by the arrowed blue lines in Fig. 6.1(b)), an all-dielectric design is competent to steer the wave. This is similar to the wave control in the carpet cloak [1], or in the extraordinary transmission device we designed in Section 4.3 [2].

This limitation of the discrete coordinate transformation can be interpreted from another point of view. A carper cloak is considered as a two-dimensional (2D) cloaking device because an object is transformed to an infinite conducting surface rather than an infinite point as a spherical cloak does (which is a real three-dimensional cloak). In order to create a 3D cloak, a second step of coordinate transformation is needed, which transforms the surface to a point. Fig. 6.1(c) plots the section view of the second transformation. The conducting surface, shown by the red line, is located on the boundary of the physical space. If this line is mapped to an infinite point (shown as the black dot in the right figure), the DCT technique is not applicable because a grid connecting a point and a line can never be near-orthogonal. In contrast, the red line can be possibly transformed to a shorter line (shown as the blue curve in the right figure of Fig. 6.1(c)) using a near-orthogonal grid. As a result, a DCT based carpet cloak, or an isotropic all-dielectric cloaking device, is not able to serve as a 3D cloak. However, it can efficiently reduce the radar cross section (RCS) [3] of an object in all directions.

Fig. 6.2 illustrates an extreme situation when the bending angle is exactly 90^{o}. Fig. 6.2(a) is the virtual space without the metal plate, where all local coordinate systems are perfectly orthogonal. Fig. 6.2(b) is the physical space with the metal plate. In this space, local coordinates are generated according to the propagating paths of a wave. It is shown that the North boundary (represented by blue lines) shrinks while the East boundary (represented by brown lines) expands. Some un-structured [4] cells are found

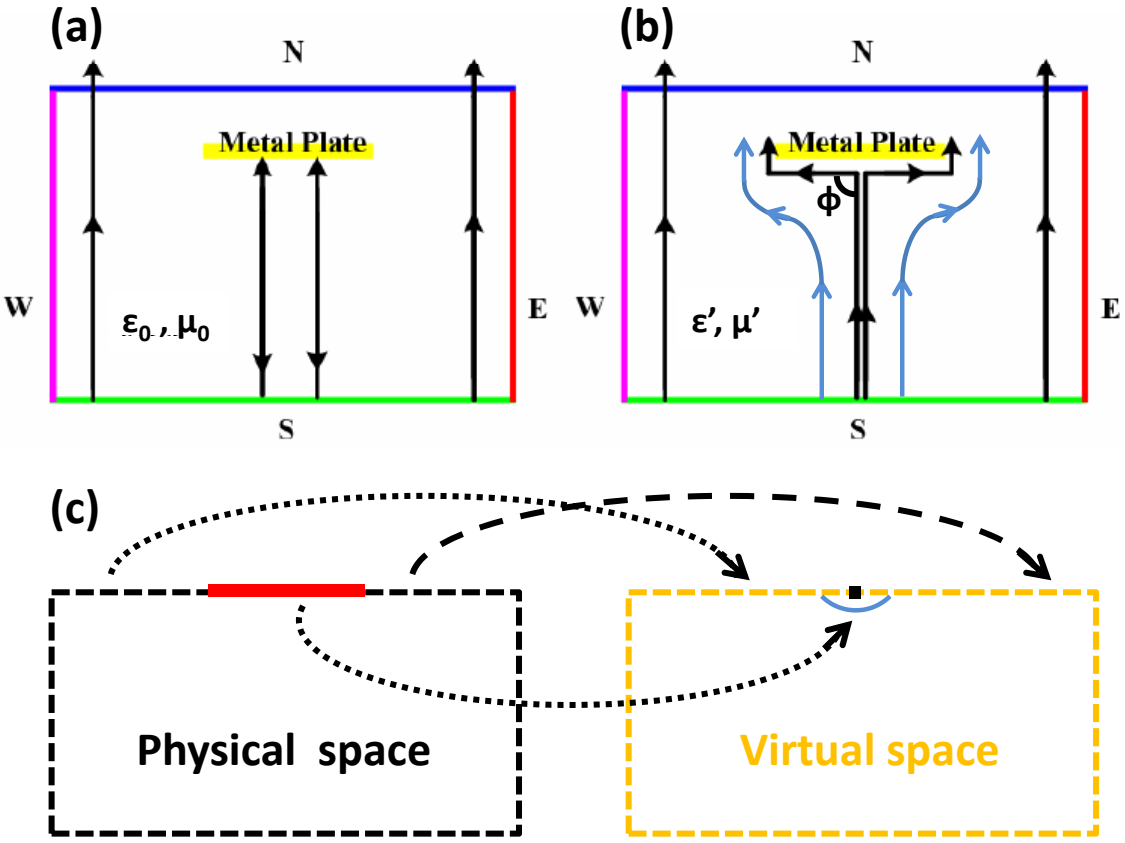

Figure 6.1: (a) The propagating wave is blocked by a metal plate. (b) The propagating wave is guided to avoid the metal plate using transformation media. (c) Mapping between the physical space with a conducting surface and the virtual space with an infinite conducting point (the black dot) or a smaller conducting surface (the blue curve).

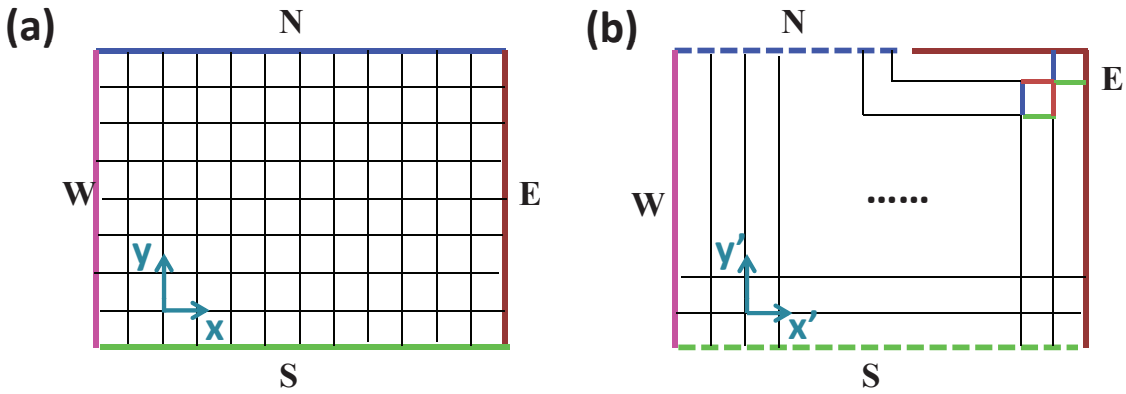

Figure 6.2: Local coordinate systems in the (a) virtual space and (b) the physical space when the discrete coordinate transformation is applied directly.

in the physical space. For example, the two cells on the top right. They have only North (shown in blue), South (shown in green) and East (shown in brown) boundaries. As a result, they cannot be described using the (x', y') local coordinate system, and therefore, the DCT technique is not applicable. In other cases when the bending angle is slightly less than 90^o, the West boundary exists but the isotropy and orthogonality of these cells are very poor.

Now, we are going to propose a solution, the multiple DCT technique, to efficiently release the limitation of bending angle, so as to achieve a sudden bend of the propagating wave right before the metal plate. Instead of executing the DCT directly from the virtual space to the physical space, a transit space is introduced between them. Fig. 6.3 gives the schematic showing of the multiple transformation process. Between the original virtual space in Fig. 6.3(a) and the transit physical space in Fig. 6.3(b), we can perform the discrete coordinate transformation and achieve all dielectric transformation media, because the grid in Fig. 6.3(b) is only slightly distorted. For example, if the bending angle ϕ in Fig. 6.3(b) is 40^o, according to the investigation in Section 5.5, the orthogonality of the grid is quite acceptable, and less-than-unity values play a minor part in the permittivity map. Fig. 6.3(b) also shows that the incident wave has been split into two parts but only through a smooth bend. To complete the design, we alter part of the boundary by changing West (W1) and East (E1) into North (N3 and N4), as shown in Fig. 6.3(c). This re-arrangement brings in a new near-orthogonal grid in Fig. 6.3(c). It should be pointed out that the filling media in Fig. 6.3(b) and Fig. 6.3(c) are exactly the same, but the space in Fig. 6.3(c) is termed the "transit virtual space" because it is the corresponding virtual space to the target physical space in Fig. 6.3(d). A second round of the discrete coordinate transformation thus can be carried out between Fig. 6.3(c) and (d). Finally we achieve the target physical space in Fig. 6.3(d), which can be realised using only dielectrics. The incident wave in the target physical space follows a sharply bent path as tagged with the black arrows.

The physics behind the multiple discrete coordinate transformation is not difficult

to understand. Assuming the original virtual space in Fig. 6.3(a) is the empty space with (ε_0, μ_0). According to Eq. (2.32), the permittivity and permeability in the target physical space in Fig. 6.3(d) can be written as

$$\bar{\bar{\varepsilon}}_2 = \frac{J_{21'}\frac{J_{10}\bar{\bar{\varepsilon}}_0 J_{10}^T}{det(J_{10})}J_{21'}^T}{det(J_{21'})},\ \bar{\bar{\mu}}_2 = \frac{J_{21'}\frac{J_{10}\bar{\bar{\mu}}_0 J_{10}^T}{det(J_{10})}J_{21'}^T}{det(J_{21'})}, \tag{6.1}$$

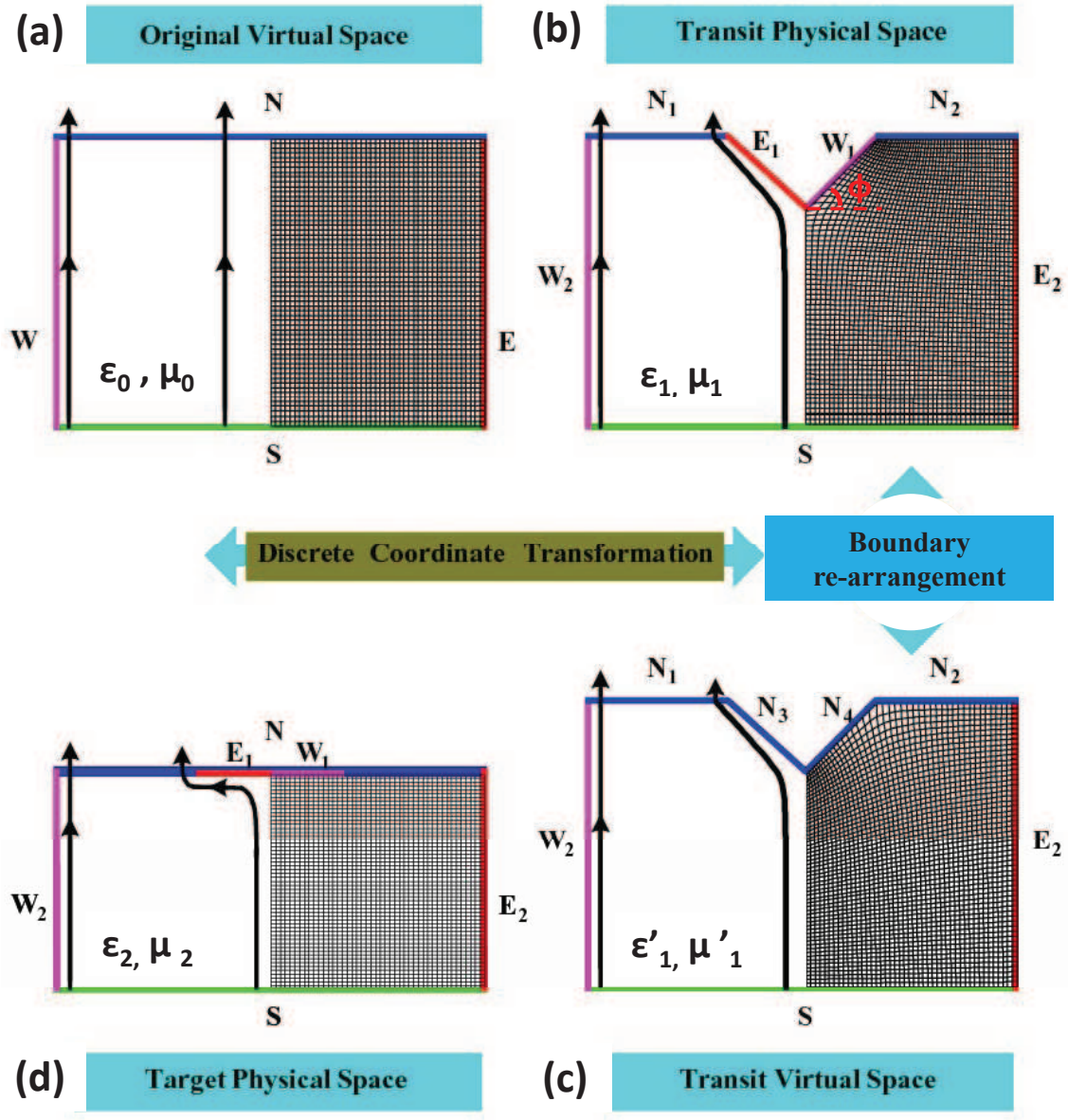

Figure 6.3: Schematic showing of the multiple transformation. (a) The original virtual space. (b) The transit physical space. (c) The transit virtual space. (d) The target physical space. Boundary re-assignment happens between the two transit spaces.

where J_{10} and $J_{21'}$ are the Jacobian transformation matrices between the original virtual space and the transit physical space, and between the transit virtual space and the target physical space, respectively. To be noted, different subscripts 1 and $1'$ are used to distinguish the coordinate systems in the transit physical space and the transit virtual space. Imaging a small dot at a random position in the original virtual space. The electromagnetic parameters at the dot is $(\varepsilon_0,\ \mu_0)$. After the first round of the discrete coordinate transformation, in a two-dimensional (2D) circumstance with E-polarization as we discussed in Section 2.4, the parameters at the dot in the transit physical space becomes

$$\varepsilon_{1z} \simeq \varepsilon_0 \frac{\Delta x_0 \Delta y_0}{\Delta x_1 \Delta y_1},\ \mu_{1x} = \mu_{1y} = \mu_0. \tag{6.2}$$

The permittivity and the permeability maps are duplicated to the transit virtual space, hence $\varepsilon_{1'} = \varepsilon_1,\ \mu_{1'} = \mu_1$. After the second round of the discrete coordinate transformation, the permittivity and permeability at the dot in the target physical space are re-written as

$$\varepsilon_{2z} \simeq \varepsilon_0 \frac{\Delta x_0 \Delta y_0}{\Delta x_1 \Delta y_1} \frac{\Delta x_{1'} \Delta y_{1'}}{\Delta x_2 \Delta y_2},\ \mu_{2x} = \mu_{2y} = \mu_0. \tag{6.3}$$

Obviously, as long as the grid in all spaces are near-orthogonal, both the two steps of discrete coordinate transformation are valid, and consequently the target physical space can be realised with dielectrics designed by Eq. (6.3). Note that $\Delta x_{1'} \neq \Delta x_1$ and $\Delta y_{1'} \neq \Delta y_1$ in Eq. (6.3) because the local coordinate systems are different in the transit physical space and the transit virtual space.

To sum up, the multiple DCT technique serves to release the limitation in a one-step DCT technique. It offers an all-dielectric way to create a physical space which can strongly distort the propagation of incident waves. From the point of view of geometry, the multiple DCT can change the profile of a device more flexibly than the one-step DCT does. Furthermore, more transit spaces can be inserted between the original virtual space

and the target physical space, in order to reduce the bending angle in each step, and consequently improve the properties of the all-dielectric design.

6.3 An Application: Compression of a Pyramidal Absorber

In this section, one example application of the multiple DCT technique is presented. A pyramidal absorber which is electrically thick will be compressed by about 67%. Such compression is a baffling problem to the one-step DCT because the pyramidal profile is usually very sharp. As a result, orthogonality and isotropy of local coordinate systems are seriously destroyed and the all-dielectric solution becomes invalid. However, the multiple DCT technique can guarantee the isotropic and dielectric properties of the transformation media, by inserting several transit spaces. The target physical space, a much thinner absorber, is proved functional through numerical simulations.

6.3.1 Pyramidal absorbers

Indoor measurements can seriously be corrupted by wall scattering errors. For this reason, electromagnetic anechoic chambers are in widespread use throughout the world in making precise measurements [5]. In order to mimic the free space environment, in anechoic chambers, absorber structures are normally mounted on the walls to attenuate reflections from chamber confinement.

The principle of absorbers is easy to understand. An absorber should achieve impedance matching from the free space at its front surface to the medium at its back surface (e.g., the conducting wall of a chamber). When propagating inside the absorber, the wave losses most energy to the lossy materials. As a result, back wall reflections are efficiently eliminated. The first investigation on practical absorbers arose in the 1940s. Resonant absorbers like the $\lambda/4$ Salisbury screen [6] and the "Jaumann Sandwich" [5] were discussed at the beginning of absorber development [7]. These resonant absorbers are

essentially narrow-band because the operating frequency is decided by their locations. Research on broadband absorbers began in the late 1940s when people experimented to construct absorbers with gradually tapered lossy materials [8]. One kind of the broadband absorbers, the urethane pyramidal absorber, has been popularly used in anechoic chambers since the 1960s.

The excellent absorption of the pyramidal absorbers is due to the multiple reflections between neighbouring pyramids. When an incident wave enters the pyramid array, it is reflected by many individual sides of the pyramids. Experiencing many times of reflections and re-reflections, the wave reaches the conducting backwall after a long propagating path. Because the absorber material is lossy, most energy of the incident wave is absorbed before it arrives the wall, and therefore, the reflection from the wall is indeed weak. Furthermore, the reflected wave experiences again the multiple reflections, until it finally travels outside the pyramid array from the tips with very low energy. In this way, the pyramidal absorbers can guarantee excellent performance over a broad frequency band.

An important property of the pyramidal absorber is, to achieve great absorption, the tip-to-base thickness should be no less than one-quarter wavelength [8]. Obviously, it is impractical to construct a chamber at low frequencies because the pyramidal absorber can be very thick and heavy. Due to this problem, absorber providers have been facing demand for a compact broad-band absorber since late 1970s. Several kinds of thin absorbers, such as the ferrite tiles [9], have been proposed and successfully applied. However, most of them require complex permeability to determine the reflection and attenuation characteristics. In contrast, we are going to propose an all-dielectric approach to a compact broad-band absorber by using the multiple DCT technique in the next sub-section.

6.3.2 Design of the transformation absorber

In Section 2.3.2.3, we compressed a pyramidal absorber to 1/3 the thickness by using the technique of analytical coordinate transformation (ACT). Electromagnetic parameters of the transformation absorber were given in Eq. (2.30). That design required anisotropic complex permittivities and permeabilities simultaneously, hence is challenging to fabricate. Furthermore, the ACT based absorber could be practically narrow-band if the less-than-unity parameters are realised using resonant metamaterials. As a result, the ACT based absorber is not efficient in practice.

Now we propose an all-dielectric way to compress the same pyramidal absorber by using the multiple DCT technique. Fig. 2.7(a) is re-drawn in Fig. 6.4 for convenience. This microwave absorber is fabricated by the TDK Corporation [10], and has been tested to provide lower than -20 dB reflectivity from 1 GHz to 100 GHz. This product is mainly made from urethane, and we assume it has a normal permittivity of 2.9 ε_0 and a loss tangent of 0.5. This kind of material usually has no magnetic response, so we assume the permeability is μ_0.

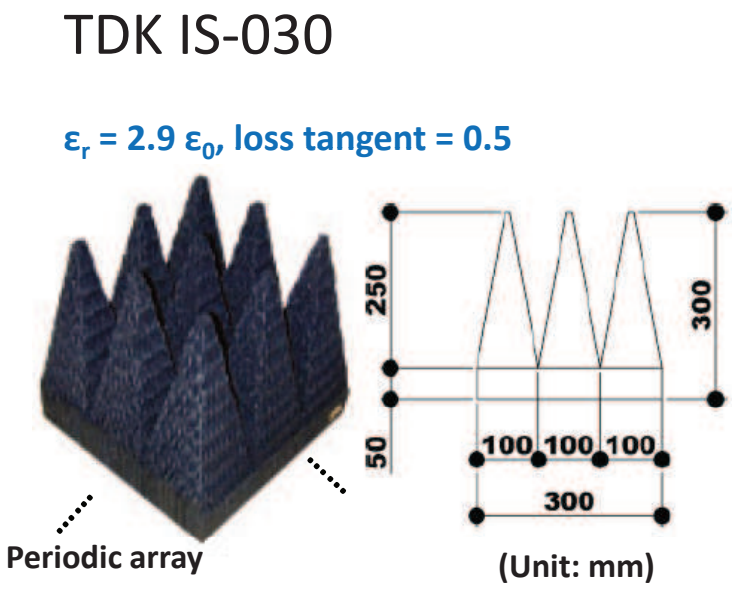

Figure 6.4: Geometry of a 3 × 3 microwave pyramidal absorber unit from the TDK corporation (left), and its dimensions (right).

Obviously, because the base of the absorber is much thinner (50 mm) than the pyramids (250 mm), plus the pyramids have very sharp tips, the one-step DCT technique is invalid in this case. Fig. 6.5 explains the main idea of applying the technique of multiple DCT. Each peaky pyramid is discretised into 10 layers, as marked in Fig. 6.5 from Layer 0 to Layer 9. Each layer has a thickness of 25 mm, half the value of the thickness in base. First of all, Layer 0, combined with the base, is compressed from 75 mm thick to 55 mm thick. Second, Layer 1 is added to the previously achieved transformation media, and the whole combination is compressed from 80 mm thick to 60 mm thick. The same procedure carries on until all ten layers have been compressed. Finally, the target map is 100 mm in width and 100 mm in thickness, as shown in the right figure in Fig. 6.5. The total thickness is therefore reduced by 2/3.

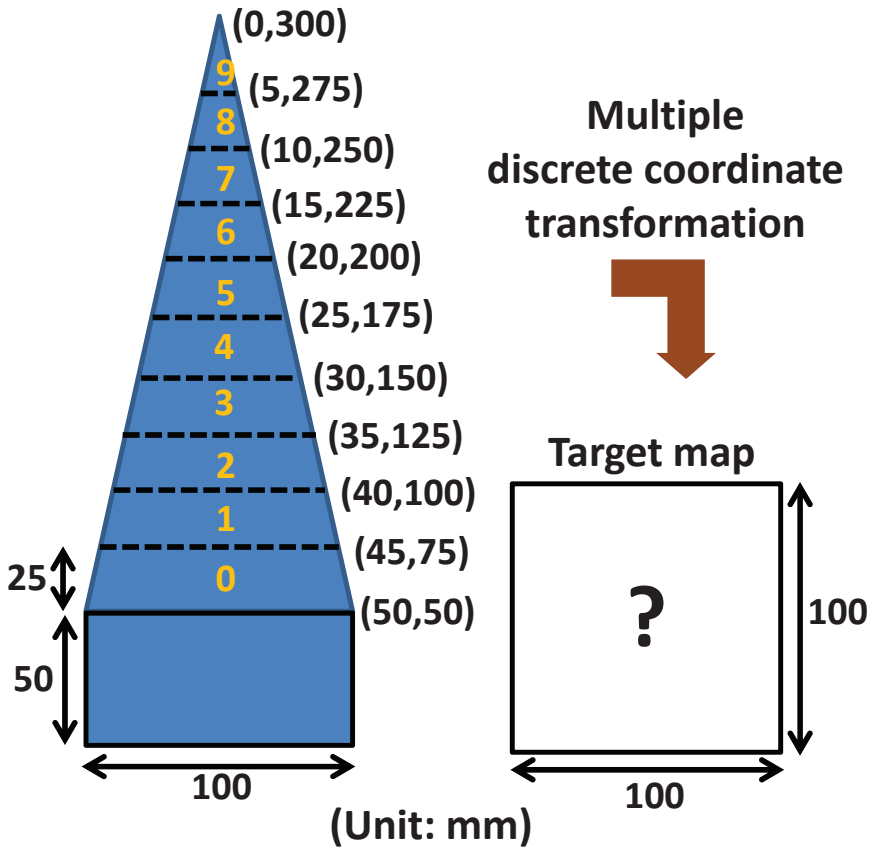

Figure 6.5: (Section view.) The pyramid in Fig. 6.4 is discretised into 10 layers, and the multiple DCT technique is applied to compress the absorber. Positions of the top right points in each layer are noted in the figure.

Fig. 6.6 explains the first round of the discrete coordinate transformation in detail as an example. At the beginning, it should be pointed out that, there are two principles during the design. First, in all steps from (a) to (g) in Fig. 6.6, materials on all boundaries except the perfect electric conductor (PEC) boundary should be the same. This is key to maintain the same reflectivity before and after transformation. In other words, only the PEC boundary is compressed because change of reflection on this boundary only contributes slightly to the total reflection of the transformation absorber. Second, since the pyramids are periodically extended, it is reasonable to flip two halves of the transformation region, like what we do from Fig. 6.6(c) to Fig. 6.6(d), and from Fig. 6.6(f) to Fig. 6.6(g).

To start with, the base and the first layer (Layer 0 in Fig. 6.5) are located into the transformation region portrayed by the dashed black box in Fig. 6.6 (a). Notice that the top left and top right corners are occupied with the air. Then, the transformation region is compressed from the PEC boundary, as shown in Fig. 6.6(b). The height of the bump is

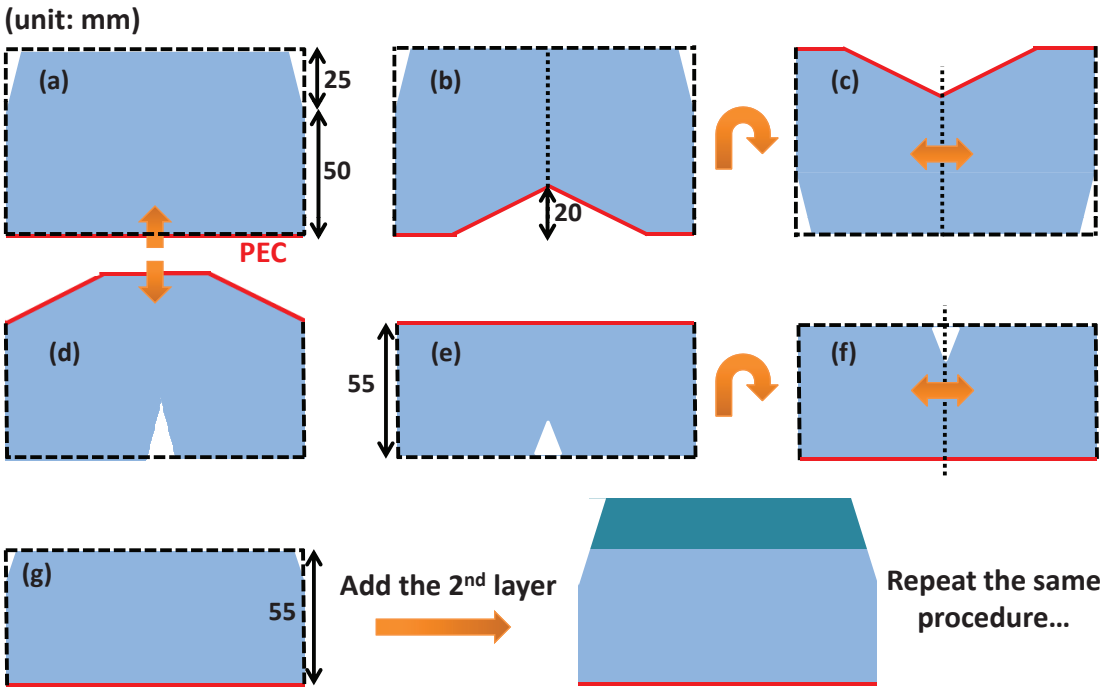

Figure 6.6: The first round of the discrete coordinate transformation.

chosen to be 20 mm, much less than the thickness of the transformation region (75 mm). It should be clarified that from Fig. 6.6(b) afterwards, transformation regions inside the dashed boxes are filled with spatially dispersive media. In Fig. 6.6(c), the transformation region is rotated by 180^o, whilst the left half and the right half are exchanged. After this re-arrangement, another round of discrete coordinate transformation is executed in Fig. 6.6(d), compressing the transformation region from the top and consequently reducing the total thickness to 55 mm. Since the bending angle in Fig. 6.6(b) and (d) is not large, both steps of discrete coordinate transformation can result in isotropic all-dielectric transformation media. In Fig. 6.6(f) and (g), the transformation region is rotated and flipped again to its original arrangement, but the thickness is 20 mm lower than the original value in Fig. 6.6(a). At the end, the second layer of the pyramid is located above the transformation media that achieved in Fig. 6.6(g), and the same procedure from Fig. 6.6(a) to (g) will be repeated.

After all the ten layers in Fig. 6.5 have been compressed, an isotropic all-dielectric transformation absorber is finally achieved. The relative permittivity map, including both the real part and the imaginary part, is presented in Fig. 6.7. The size of one unit pyramid has been reduced from 100 mm $\times$ 100 mm $\times$ 300 mm to 100 mm $\times$ 100 mm $\times$ 100 mm. The staircase in Fig. 6.7 has a resolution of 0.5 mm, which is also the resolution of the FDTD grid during the simulations in the following sub-section. The permittivity value in each 0.5mm-size block ranges from ε_0 to about 22 ε_0, and the high values only exist in a few blocks close to the bottom boundary. Less-than-unity permittivities are required in very small area, therefore can be ignored. In conclusion, the transformation absorber in Fig. 6.7 can be constructed using common dielectrics. Note that the thickness of the transformation absorber can be further reduced if the height of the bump in Fig. 6.6(b) is larger than 20 mm. However, a thinner absorber will be accompanied by higher permittivity values.

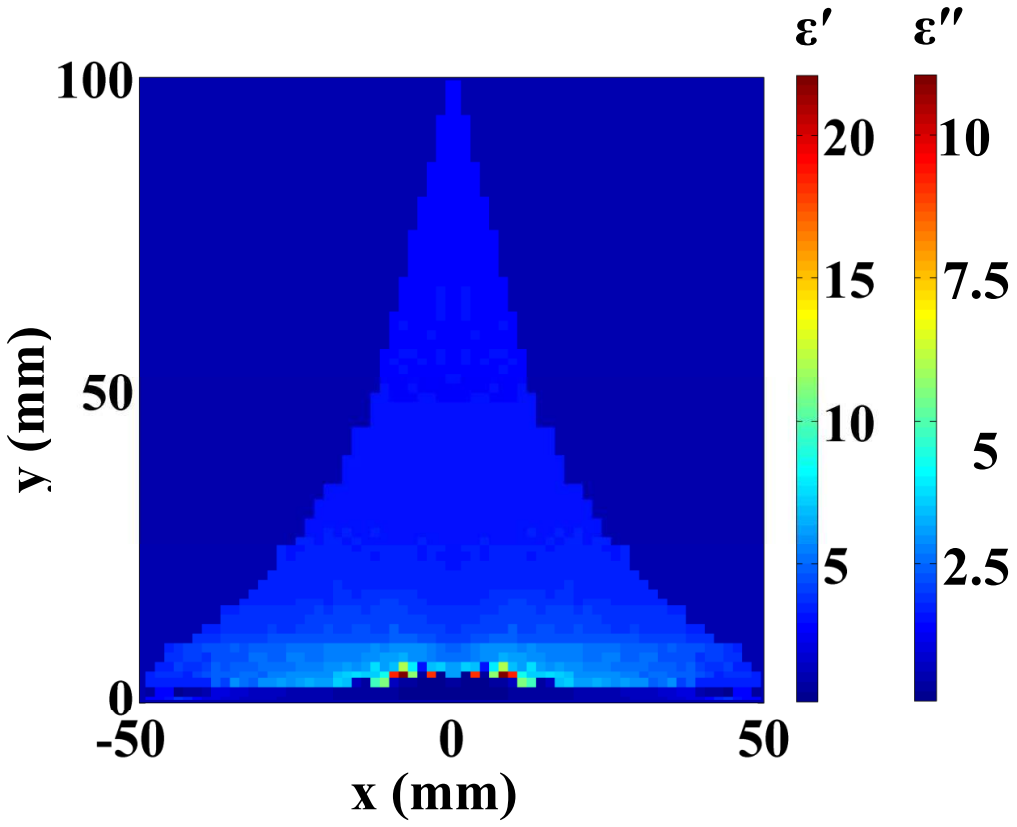

Figure 6.7: The relative permittivity map of the transformation absorber. Colour bars present the real part (ε') and the imaginary part (ε'') respectively.

6.3.3 Numerical verification

A common way to examine the performance of an absorber is shown in Fig. 6.8. An absorber array is mounted on the conducting wall (shown as the PEC), while incident waves from different directions are launched towards the wall in order to test the scattering and absorbing properties of the absorber [11]. In the measurement, the location of an transmitter is steered gradually from $\phi = 0^o$ to $\phi = 90^o$ (ϕ defined in Fig. 6.8), and a receiver is located at the coherent position to measure the reflection. For example, if the transmitter is placed at $\phi = 45^o$, then the receiver should be placed at $\phi = 135^o$ accordingly.

However, before fabricating a prototype, we use numerical simulations to predict the

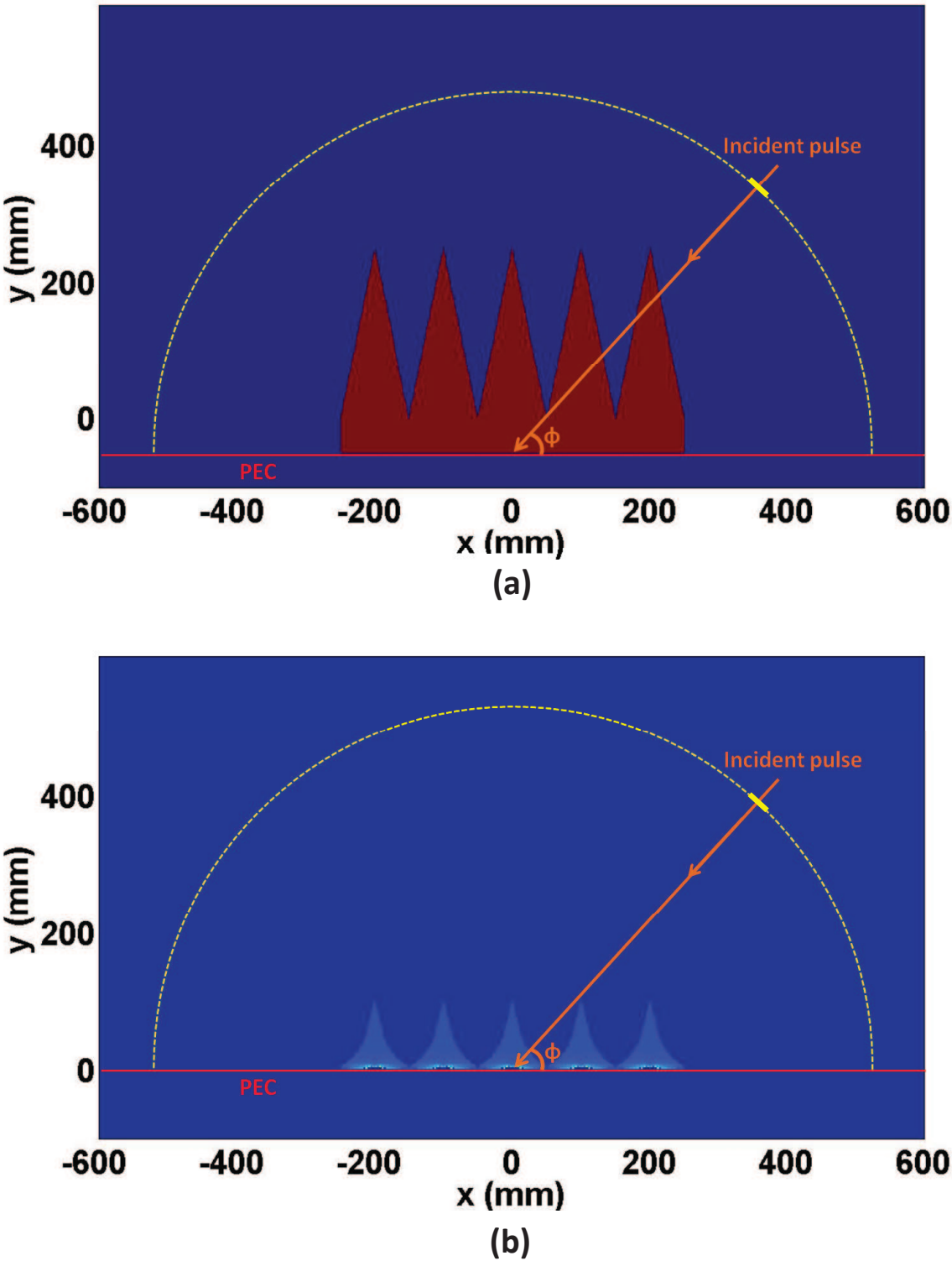

Figure 6.8: Simulation setup to test (a) the pyramidal absorber and (b) the transformation absorber.

performance of our design. In this case, the FDTD method based simulation is again employed. The simulation is in a 2D circumstance, including H_x, H_y and E_z components. The setup of simulation is plotted in Fig. 6.8. Noted that in the measurement, the transmitter and the receiver are always located in the far field; but in the simulation, to save computing memory, a short source (30 mm long) is originated 500 mm away (which is the radius of the yellow semi-circle in Fig. 6.8) from the center of the absorber array. This distance is only a few wavelengths below 3 GHz, and hence, the transmitter is not always in the far field. In other words, scattering may happen at all directions from $\phi = 0^o$ to $\phi = 180^o$. According to this concern, we use a wide-band Gaussian pulse as the source, integrate the electric field along the whole semi-circle at each time step, isolate the reflected signal from the incident signal, and calculate the reflection coefficient in frequency domain by comparing the reflected signal with the incident one. The source has a Gaussian distribution from 2 GHz to 20 GHz in the frequency domain, hence is able to provide broad-band information.

Fig. 6.9 plots the reflection coefficient when the pyramidal absorber and the transformation absorber are mounted on the conducting wall respectively. The incident pulse is located at $\phi = 90^o$ (see Fig. 6.9(a)), $\phi = 45^o$ (see Fig. 6.9(b)) and $\phi = 27^o$ (see Fig. 6.9(c)) for testing (ϕ defined in Fig. 6.8). At the normal incidence when $\phi = 90^o$, the red curve has a similar shape as the black one, indicating that the transformation absorber obtains some performance of the pyramidal one, and is able to reduce the reflection from 2 GHz to 20 GHz. However, the reflection coefficient on the red curve is about 10 dB higher than that on the black curve, which means the transformation absorber is not as efficient as the original pyramidal one at a normal incidence. When the incidence is from $\phi = 45^o$, the red curve possesses a more similar shape as the black one in Fig. 6.9(b), and the difference between the two curves becomes smaller. When the incidence is from $\phi = 27^o$, the transformation absorber produces very similar reflection coefficient as the pyramidal absorber in the entire frequency band from 2 GHz to 20 GHz. These results have demonstrated that the backwall reflection under an arbitrary

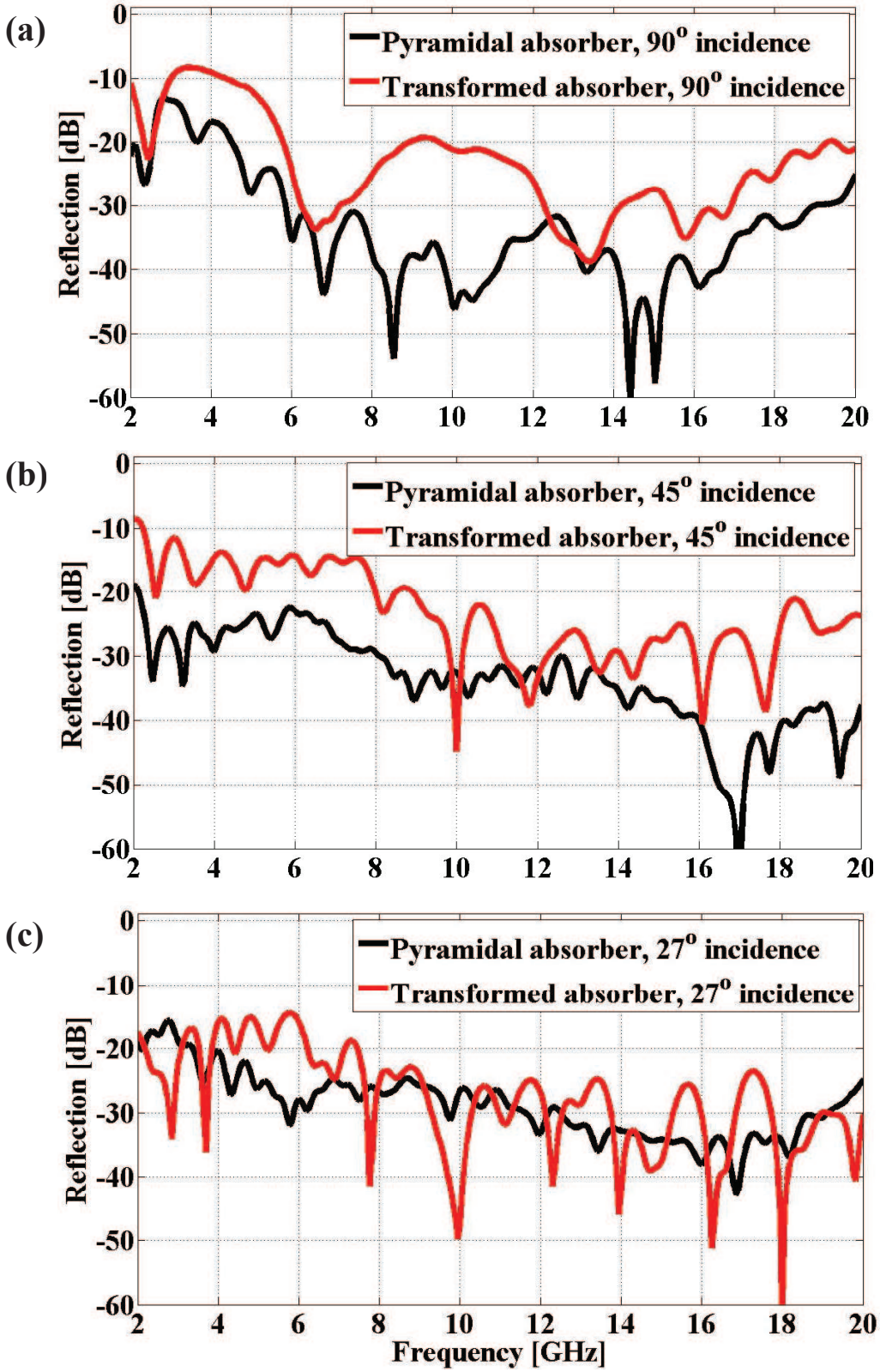

Figure 6.9: Reflection from the conducting wall when the pyramidal absorber and the transformation absorber are applied respectively. The incidence is from (a) $\phi = 90^{\circ}$, (b) $\phi = 45^{\circ}$ and (c) $\phi = 27^{\circ}$.

incidence can be effectively reduced by the transformation absorber within a broad frequency band. The degradation of absorbing performance under a near-normal incidence is mainly due to the absence of an adequate base in the transformation absorber. Therefore, a better transformation absorber is potentially achievable if we increase the base in the pyramidal absorber. Nevertheless, the transformation absorber shown in Fig. 6.7 already obtains an acceptable broadband performance, and possesses a much smaller thickness when compared with the original pyramidal absorber.

6.4 Summary

In this chapter, the technique of multiple discrete coordinate transformation was proposed as an extension to the one-step discrete coordinate transformation. We explained why the one-step DCT technique cannot deal with transformations between an infinite area and a finite area, and therefore is not able to strongly distort the propagation of an electromagnetic wave. The multiple DCT technique was then presented as a solution to this issue. It was analysed from the theory that the multiple transformation can fiercely manipulate the propagation of an wave without bringing in anisotropic or magnetic materials. An pioneering application of the multiple DCT technique was reported, that the thickness of a large pyramidal absorber can be reduced by 2/3. The achieved transformation absorber only contained lossy dielectrics, which can be easily found or fabricated. Numerical simulation results demonstrated that the transformation absorber can functionally reduce the backwall reflection from 2 GHz to 20 GHz.

There are many potential applications of the multiple discrete coordinate transformation. For example, by inserting transit spaces between the virtual space and the physical space, one can improve the performance of the transformation device because better orthogonal and isotropic grids are guaranteed during the design procedure. Therefore, all devices we have designed using the one-step discrete coordinate transformation can be further modified.

References

[1] J. Li and J. Pendry, "Hiding under the carpet: A new strategy for cloaking," *Phys. Rev. Lett.*, vol. 101, no. 20, p. 203901, 2008.

[2] W. Tang, Y. Hao, and F. Medina, "Broadband extraordinary transmission in a single sub-wavelength aperture," *Opt. Express*, vol. 18, no. 16, pp. 16 946–16 954, 2010.

[3] J. Kraus, *Antennas*. McGraw-Hill Education, 1988.

[4] J. Thompson, B. Soni, and N. Weatherill, *Handbook of grid generation*. CRC, 1999.

[5] W. Emerson, "Electromagnetic wave absorbers and anechoic chambers through the years," *IEEE Trans. Ant. Propag.*, vol. 21, pp. 484–490, 1973.

[6] W. Salisbury, "Absorbent body for electromagnetic waves," June 10 1952, US Patent 2,599,944.

[7] F. Trautnitz, "Emc absorbers through the years with respect to the new site vswr validation procedure in the frequency range from 1 to 18 ghz-a practical approach," in *Electromagnetic Compatibility, 2007. EMC 2007. IEEE International Symposium on*. IEEE, 2007, pp. 1–6.

[8] C. Holloway, R. DeLyser, R. German, P. McKenna, and M. Kanda, "Comparison of electromagnetic absorber used in anechoic and semi-anechoic chambers for emissions and immunity testing of digital devices," *IEEE Trans. Electromagn. Compat.*, vol. 39, no. 1, pp. 33–47, 1997.

[9] S. Kim, S. Jo, K. Gueon, K. Choi, J. Kim, and K. Churn, "Complex permeability and permittivity and microwave absorption of ferrite-rubber composite at x-band frequencies," *IEEE Trans. Magnetics*, vol. 27, no. 6, pp. 5462–5464, 1991.

[10] "TDK corporation," http://www.tdk.com/.

[11] B. Dewitt and W. Burnside, "Electromagnetic scattering by pyramidal and wedge absorber," *IEEE Trans. Ant. Propag.*, vol. 36, no. 7, pp. 971–984, 1988.

Chapter 7

Conclusions and Future Work

7.1 Summary

This thesis has mainly focused on the application of the discrete coordinate transformation in antenna and microwave engineering. This work is a useful exploration to the recently proposed research area of coordinate transformation, and a practical implementation of the transformation device design. The theory of the coordinate transformation was developed in its discretised form, aiming to provide an all-dielectric approach to create new devices with controllable shapes and novel properties. The designing method developed in this thesis can help the engineering community to better understand the new research field of coordinate transformation, and to easily conceive and design novel functional devices in practice.

Specifically, in Chapter 2, the fundamentals of the coordinate transformation theory were studied, in order to clearly explain the physics behind it. The scheme of designing transformation based devices was presented, and several example devices, including the "cloaks of invisibility", were designed as applications of the analytical coordinate transformation (ACT) technique. Limitations and challenges in the ACT based devices were discussed, and then the discrete coordinate transformation (DCT) was developed

as a more practical case of the coordinate transformation theory. The theory of the discrete coordinate transformation was developed in detail, and limitations and conditions of applying this technique were discussed. The orthogonality and distortion in local coordinate systems decide the permittivity and permeability distributions in the physical space, hence are the key to an all-dielectric device. Finally, towards the end of this chapter, potential applications of the DCT technique were discussed.

Chapter 3 focused on designing flattened devices using the technique of discrete coordinate transformation. Applying this technique, accompanied with some reasonable simplifications, a conventional device with curved surfaces can be replaced with a flat transformation device which is composed of only isotropic dielectrics. Two example devices, a flat reflector and a flat lens were proposed and tested in this chapter. The flat reflector was created from a parabolic reflector. It maintained the function of transforming a spherical wave originated from a small horn antenna to a plane wave, and therefore was able to create highly directive beams, as well as the parabolic one. An extension of the reflector design, a beam steering scheme was also proposed and discussed. The second example, the flat lens, was created from a dielectric convex lens. The transformation lens was only half the thickness of the convex lens, and possessed a flat profile. It also maintained the property of focusing an incident plane wave to a point, as well as transforming a spherical wave from the focal point to an plane wave. The Finite-Difference Time-Domain (FDTD) method based numerical modelling was the primary tool used to verify these designs. Several specific configurations were employed to the basic FDTD method in order to simulate the transformation devices accurately and efficiently.

Chapter 4 presented another way of applying the technique of discrete coordinate transformation. Instead of creating a flat device from an existing one, we projected the propagating paths of electromagnetic waves, and generated a corresponding device with predicted electromagnetic properties. Two examples were also proposed and verified. The first one was an undetectable antenna combined with a carpet cloak and a conducting cavity. A so-called "virtual boundary" was employed to remove the conducting bump

at the bottom of the carpet cloak. With this arrangement, a probe under the carpet cloak was able to freely transmit and receive signals. Meanwhile, the whole combination remains undetectable due to the shelter of the carpet cloak. Furthermore, the carpet cloak itself worked as a specific dielectric lens which transformed a spherical wave from the probe to a plane wave, and consequently generated highly directive beams. The realisation method of this design was discussed. The second example was a dielectric device which can extraordinarily enhance the transmission through a sub-wavelength aperture. This device served to introduce the incident energy from an electrically large aperture into a sub-wavelength aperture with minimised reflections. FDTD based simulation results demonstrated both of the designs. At the end of this chapter, a prototype of the extraordinary transmission device was manufactured and measured in an X-band waveguide, and the measured results agreed very well with the simulated results.

Chapter 5 reviewed the performance of the above designed DCT based devices, and studied the limitation of applying the DCT technique. First, the principle of deciding the transformation region was investigated, and the way to find a trade-off between the volume and the performance of a transformation device was presented. After that, the resolution in a transformation device was studied. Sampling of the permittivity map of the device is very important because it significantly reduces the complexity of fabrication. However, it inevitably results in degradation of performance. It was confirmed that half the wavelength is a reliable threshold of the qualified resolution. And then, the analytical coordinate transformation and the discrete coordinate transformation were compared. An ACT based lens and a DCT based lens, created from the same convex lens, were tested for demonstration. The DCT based designs showed advantages of easy composing materials and broad operating band. At the end of this chapter, it was proved that large curvature on the boundary of the transformation region brings in inaccuracy to the all-dielectric design. As a result, the one-step discrete coordinate transformation cannot fiercely manipulate the propagation of an electromagnetic wave.

In Chapter 6, an extension of the one-step discrete coordinate transformation, the

multiple discrete coordinate transformation was proposed. By inserting transit spaces, a sudden bend of the wave can be achieved by several smooth bends, or a device with large curvature can be gradually flattened without the necessity of anisotropic or magnetic materials. An isotropic all-dielectric absorber was transformed from a pyramidal absorber as an initial example of the multiple transformation. FDTD based numerical simulations demonstrated that although the thickness was reduced by 2/3, the transformation absorber obtained good absorbing properties from the pyramidal one within a broad frequency band.

7.2 Future Work

Arising from the research carried out during this thesis, areas of potential further research on the coordinate transformation could include the following;

1. Improve the performance of the transformation absorber

In Chapter 6, we initially designed a transformation absorber based on a pyramidal one. Although this design has proved good absorption and broad operating bandwidth, it does not work as well as the pyramidal one when the incidence was near-normal to the conducting wall. This is mainly due to the lack of a base in the transformation absorber. Therefore, further investigation aiming to improve the performance is interesting. For example, another prototype of the transformation absorber can be created based on another pyramidal absorber with a thicker base, or through more steps of discrete coordinate transformation.

2. Three-dimensional (3D) carpet cloaks

We explained that the one-step discrete coordinate transformation cannot project an infinite boundary to a finite boundary. Due to this problem, the existing carpet cloak is actually a two-dimensional cloaking device. However, by applying the multiple discrete coordinate transformation, we can gradually approach an infinitely small point,

and approximately achieve a 3D all-dielectric carpet cloak. Fig. 7.1 briefly explains the scheme. The arrowed black (solid and dashed) lines represent the two components of an incidence. If filled with the first permittivity map (noted in the top left figure), the physical space can mimic a virtual space where a conducting surface is vertically located. And if filled with the second permittivity map (noted in the bottom left figure), the physical space can mimic a virtual space where a conducting surface is horizontally located. Therefore, combining the two steps of coordinate transformation, it is possible to conceal the diamond-shaped region from an arbitrary incidence. To be noted, even though the 3D carpet cloak may not be perfect because of approximations throughout the design, it is able to efficiently reduce the radar cross section (RCS) of the cloaked region.

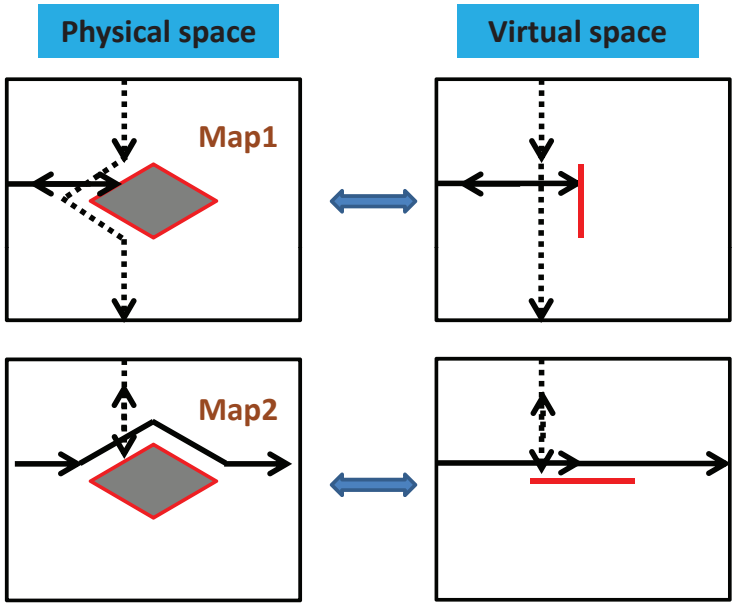

Figure 7.1: Section view of the multiple coordinate transformation for a 3D carpet cloak design.

3. Coordinate transformation in multi-reflector or multi-lens systems

Transformation devices created from a single reflector or a single lens have been validated in this thesis. In practice, there exist many devices containing more than one element structure, for example, a Cassegrain reflector, or a triplet lens. They have better performance than single devices, but sometimes are inefficient due to the increased

volume. Therefore, it is very useful to apply the discrete coordinate transformation to create a compact reflector or lens which maintains the good performance of the multi-reflector or multi-lens system, meanwhile possesses a much smaller volume. It is even better if the designed devices can be realised by conventional dielectrics alone.

4. Discrete coordinate transformation using un-structured grid

During the discrete coordinate transformation in this thesis, structured grids are always used to describe the local coordinate systems. However, sometimes staircases are not sufficient to portray the geometry. For example, when the transformation space has less than four boundaries as shown in Fig. 7.2, or when it has a strongly-bent boundary. In these cases, an un-structured grid can be more efficient and accurate to discretise the space. Fig. 7.2 shows three examples where an un-structured grid is more flexible and suitable than a structure one. It is also interesting to find the expression of the discrete coordinate transformation in non-Cartesian local coordinate systems in the un-structured grids.

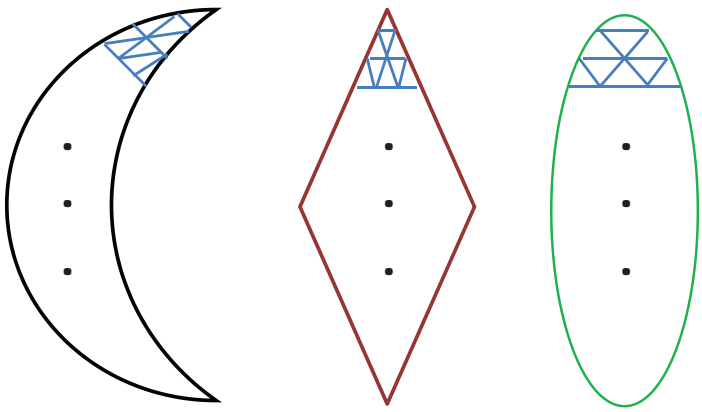

Figure 7.2: Non-Cartesian local coordinate systems in un-structured grids.

5. Time-variant coordinate transformation

Until now, the coordinate transformation involves only the space dimensions. If the desired device moves or changes shape with speeds comparable to that of light, the dimension of time should also be introduced into the coordinate transformation.

Media that facilitate space-time transformations have been discussed in [1, 2], based on Einstein's general relativity. It is very interesting to explore novel phenomenons and properties in the four-dimensional coordinate transformation.

References

[1] U. Leonhardt and T. Philbin, "General relativity in electrical engineering," *New J. of Phys.*, vol. 8, p. 247, 2006.

[2] ——, "Transformation optics and the geometry of light," *Progress in Optics*, vol. 53, pp. 69–152, 2009.

Appendix A

Form Invariance in Maxwell's Equations

Propagation of light, or electromagnetic wave in general, in complex structures is more complicated than that in uniform background material. It requires to solve the Maxwell's equations

$$\bigtriangledown \times \mathbf{E} = -\mu\mu_0 \partial \mathbf{H}/\partial t, \quad \bigtriangledown \times \mathbf{H} = +\varepsilon\varepsilon_0 \partial \mathbf{E}/\partial t, \tag{A.1}$$

where the electric field $\mathbf{E}$ and the magnetic field $\mathbf{H}$ are functions of the coordinate system, and the permittivity ε and the permeability μ may also depend on position.

The Maxwell's equations in a general coordinate system has been carefully studied in [1]. The space can be described by a random coordinate system of

$$q_1(x, y, z), q_2(x, y, z), q_3(x, y, z), \tag{A.2}$$

where (x, y, z) is Cartesian coordinate system and (q_1, q_2, q_3) don't need to be orthogonal. If we define a set of points by equal increments along the q_1, q_2, q_3 axes, the mesh will appear distorted in the original (x, y, z) system, as shown in Fig. A.1. Maxwell's

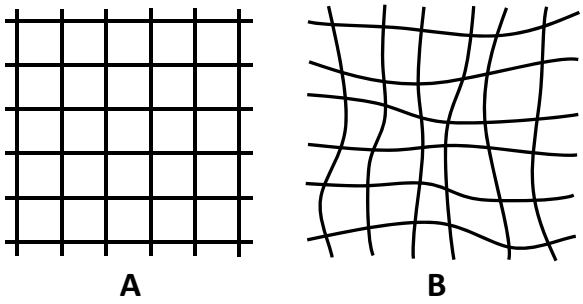

Figure A.1: A: A space described in (x, y, z) coordinate system. B: The same space described in (q_1, q_2, q_3) coordinate system. The grid in B is distorted.

equations in Eq. (A.1) are written in the original (x, y, z) system, and when applied in a new coordinate system they become

$$\bigtriangledown_q \times \hat{\mathbf{E}} = -\mu_0 \hat{\mu} \partial \hat{\mathbf{H}} / \partial t, \quad \bigtriangledown_q \times \hat{\mathbf{H}} = +\varepsilon_0 \hat{\varepsilon} \partial \hat{\mathbf{E}} / \partial t, \tag{A.3}$$

where $\hat{\varepsilon}$, $\hat{\mu}$ are tensors, and $\hat{E}$, $\hat{H}$ are electric and magnetic fields re-normalised in the new coordinates. Eq. (A.3) indicates that even under different coordinate systems, we are still solving the Maxwell's equations, but simply change the definition of $\hat{\varepsilon}$ and $\hat{\mu}$.

Next we will find out the relations between ε and $\hat{\varepsilon}$, μ and $\hat{\mu}$, $\mathbf{E}$ and $\hat{\mathbf{E}}$, $\mathbf{H}$ and $\hat{\mathbf{H}}$. Define three units vectors (u_1, u_2, u_3) along the generalised (q_1, q_2, q_3) axes. Considering the geometry relationship between the two systems are:

$$dx = \frac{\partial x}{\partial q_1} dq_1 + \frac{\partial x}{\partial q_2} dq_2 + \frac{\partial x}{\partial q_3} dq_3, \quad etc. \tag{A.4}$$

The length of a line element in (x, y, z) system can be written as

$$\begin{aligned} ds^2 = dx^2 + dy^2 + dz^2 = Q_{11} dq_1^2 + Q_{22} dq_2^2 + Q_{33} dq_3^2 \\ + 2Q_{12} dq_1 dq_2 + 2Q_{13} dq_1 dq_3 + 2Q_{23} dq_2 dq_3, \end{aligned} \tag{A.5}$$

where,

$$Q_{ij} = \frac{\partial x}{\partial q_i} \frac{\partial x}{\partial q_j} + \frac{\partial y}{\partial q_i} \frac{\partial y}{\partial q_j} + \frac{\partial z}{\partial q_i} \frac{\partial z}{\partial q_j}. \tag{A.6}$$

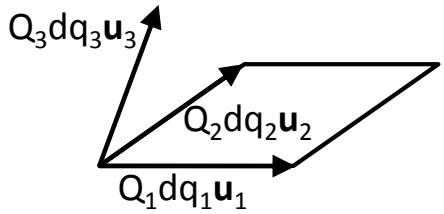

Figure A.2: Small element represented in (q_1, q_2, q_3) system.

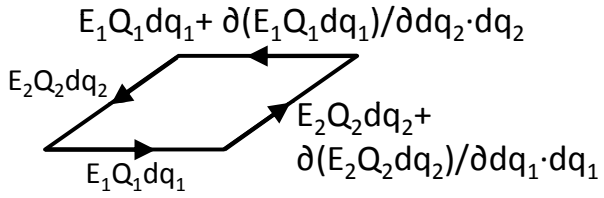

Figure A.3: The integration path to calculate $\nabla \times \mathbf{E}$.

So, the length of a line element directed along one of the three axes is written as

$$ds_i = Q_i dq_i, \quad (Q_i^2 = Q_{ii}). \tag{A.7}$$

To calculate the left-handed side of the Maxwell's equations (eg. $\nabla \times \mathbf{E}$), consider a small element as shown in Fig. A.2. The projection of $\nabla \times \mathbf{E}$ on the $u_1 - u_2$ plane can be calculated using the Stokes' theorem:

$$\int_s \nabla \times \mathbf{E} \cdot dS = \oint_{\partial S} \mathbf{E} \cdot dr. \tag{A.8}$$

The integration path on the right-handed side of Eq. (A.8) is illustrated in Fig. A.3, with the definition of

$$E_1 = \mathbf{E} \cdot \mathbf{u}_1, \; E_2 = \mathbf{E} \cdot \mathbf{u}_2, \; E_3 = \mathbf{E} \cdot \mathbf{u}_3 \tag{A.9}$$

So Eq. (A.8) becomes

$$\nabla \times \mathbf{E} \cdot (Q_1 dq_1 \mathbf{u}_1 \times Q_2 dq_2 \mathbf{u}_2) = dq_1 \frac{\partial}{\partial q_1}(E_2 dq_2 Q_2) - dq_2 \frac{\partial}{\partial q_2}(E_1 dq_1 Q_1) \tag{A.10}$$

or

$$(\nabla \times \mathbf{E}) \cdot (\mathbf{u}_1 \times \mathbf{u}_2) Q_1 Q_2 = \frac{\partial \hat{E}_2}{\partial q_1} - \frac{\partial \hat{E}_1}{\partial q_2} = (\nabla_q \times \hat{\mathbf{E}})^3, \tag{A.11}$$

where

$$\hat{E}_1 = Q_1 E_1, \ \hat{E}_2 = Q_2 E_2, \ \hat{E}_3 = Q_3 E_3 \tag{A.12}$$

are the relations between the electric components in different coordinate systems. It is noted that in Eq. (A.11) the superscript of the last item represents the contravariant components of a vector. So '3' means 'component 3' of curl evaluated in the new system.

Insert $(\mathbf{u}_1 \times \mathbf{u}_2) Q_1 Q_2$ into Maxwell's equations in Eq. (A.1), we have

$$\bigtriangledown \times \mathbf{E} \cdot (\mathbf{u}_1 \times \mathbf{u}_2) Q_1 Q_2 = -\mu\mu_0 \partial \mathbf{H} / \partial t \cdot (\mathbf{u}_1 \times \mathbf{u}_2) Q_1 Q_2. \tag{A.13}$$

The magnetic field $\mathbf{H}$ can be written in terms of the contravariant components as

$$\mathbf{H} = H^1 \mathbf{u}_1 + H^2 \mathbf{u}_2 + H^3 \mathbf{u}_3 \tag{A.14}$$

and also expressed in terms of the covariant components as

$$\mathbf{g}^{-1} \begin{pmatrix} H^1 \\ H^2 \\ H^3 \end{pmatrix} = \begin{pmatrix} \mathbf{u}_1 \cdot \mathbf{u}_1 & \mathbf{u}_1 \cdot \mathbf{u}_2 & \mathbf{u}_1 \cdot \mathbf{u}_3 \\ \mathbf{u}_2 \cdot \mathbf{u}_1 & \mathbf{u}_2 \cdot \mathbf{u}_2 & \mathbf{u}_2 \cdot \mathbf{u}_3 \\ \mathbf{u}_3 \cdot \mathbf{u}_1 & \mathbf{u}_3 \cdot \mathbf{u}_2 & \mathbf{u}_3 \cdot \mathbf{u}_3 \end{pmatrix} \begin{pmatrix} H^1 \\ H^2 \\ H^3 \end{pmatrix} = \begin{pmatrix} H_1 \\ H_2 \\ H_3 \end{pmatrix}, \tag{A.15}$$

where $\mathbf{g}$ is the matric tensor, and

$$H_1 = \mathbf{H} \cdot \mathbf{u}_1, \ H_2 = \mathbf{H} \cdot \mathbf{u}_2, \ H_3 = \mathbf{H} \cdot \mathbf{u}_3. \tag{A.16}$$

By inverting the matric tensor,

$$H^i = \sum_{j=1}^{3} g^{ij} H_j. \tag{A.17}$$

Substituting Eqs. (A.17) and (A.14) into Eq. (A.13), we have

$$\begin{aligned} \bigtriangledown \times \mathbf{E} \cdot (\mathbf{u}_1 \times \mathbf{u}_2) Q_1 Q_2 = -\mu\mu_0 \sum_{j=1}^{3} g^{3j} \frac{\partial H_j}{\partial t} \mathbf{u}_3 \cdot (\mathbf{u}_1 \times \mathbf{u}_2) Q_1 Q_2, \\ (\mathbf{u}_1 \cdot (\mathbf{u}_1 \times \mathbf{u}_2) = 0,\ \mathbf{u}_2 \cdot (\mathbf{u}_1 \times \mathbf{u}_2) = 0). \end{aligned} \tag{A.18}$$

To locate the link of parameters between two coordinate systems, we define the permeability in the (q_1, q_2, q_3) system as

$$\hat{\mu}^{ij} = \mu g^{ij} |\mathbf{u}_1 \cdot (\mathbf{u}_2 \times \mathbf{u}_3)| Q_1 Q_2 Q_3 (Q_i Q_j)^{-1}. \tag{A.19}$$

Note that

$$|\mathbf{u}_1 \cdot (\mathbf{u}_2 \times \mathbf{u}_3)| = |\mathbf{u}_3 \cdot (\mathbf{u}_1 \times \mathbf{u}_2)| = |\mathbf{u}_2 \cdot (\mathbf{u}_3 \times \mathbf{u}_1)| \tag{A.20}$$

is the volume of the element parallelepiped. Similar to Eq. (A.12), we can also define the relationship between magnetic fields in two systems as

$$\hat{H}_1 = Q_1 H_1,\ \hat{H}_2 = Q_2 H_2,\ \hat{H}_3 = Q_3 H_3. \tag{A.21}$$

Substituting Eqs. (A.19) and (A.21) into Eq. (A.18), we have

$$\bigtriangledown \times \mathbf{E} \cdot (\mathbf{u}_1 \times \mathbf{u}_2) Q_1 Q_2 = -\mu_0 \sum_{j=1}^{3} \hat{\mu}^{3j} \frac{\partial \hat{H}_j}{\partial t}. \tag{A.22}$$

On the left-handed side, the electric field and the permeability are described in the (x, y, z) system, and on the right-handed side, the magnetic field and the permeability are described in the (q_1, q_2, q_3) system. The link between two systems is therefore built

up. Substituting Eq. (A.11) into Eq. (A.22), we have the Maxwell's equation in the new system as

$$(\bigtriangledown_q \times \hat{\mathbf{E}})^i = -\mu_0 \sum_{j=1}^{3} (\hat{\mu}^{ij} \frac{\partial \hat{H}_j}{\partial t}). \tag{A.23}$$

The superscript on the left-handed side represents the contravariant components of the **E** vector. Eq. (A.23) shows clearly that the Maxwell's equations are form-invariant in the new system. Furthermore, by symmetry between E and H fields, we have

$$(\bigtriangledown_q \times \hat{\mathbf{H}})^i = +\varepsilon_0 \sum_{j=1}^{3} (\hat{\varepsilon}^{ij} \frac{\partial \hat{E}_j}{\partial t}), \tag{A.24}$$

where

$$\hat{\varepsilon}^{ij} = \varepsilon g^{ij} |\mathbf{u}_1 \cdot (\mathbf{u}_2 \times \mathbf{u}_3)| Q_1 Q_2 Q_3 (Q_i Q_j)^{-1}. \tag{A.25}$$

References

[1] A. J. Ward and J. B. Pendry, "Refraction and geometry in Maxwell's equations," *J. Mod. Opt*, vol. 43, no. 4, pp. 773–793, 1996.

Appendix B

Foundation of the Finite-Difference Time-Domain Method

The Finite-Difference Time-Domain (FDTD) Method [1, 2] is a direct solution to the Maxwell's equations and is simple and straightforward to solve problems with complex structures. As a time domain solution, it is also convenient in dealing with the wideband characteristics of metamaterial based devices.

The foundation of FDTD is laid down by Yee in 1966 [1]. Yee chose a geometric relation for his spatial sampling of the vector components of the electric and magnetic fields that robustly represent both the differential and integral forms of Maxwell's equations. The original Yee's FDTD algorithm is second-order accurate in both time and space. Numerical dispersion can be kept small by using a cell size that is sufficiently small in comparison to the wavelength, say on the order of $\lambda/20$ or $\lambda/30$. Both electric and magnetic fields are calculated in time and space using the coupled Maxwell's curl equations.

Consider a region of space that has no electric or magnetic current sources, but may have materials that absorb electric or magnetic field energy. The time-dependent Maxwell's equations are given in differential and integral form by:

$$\begin{aligned} \frac{\partial \overrightarrow{B}}{\partial t} &= -\nabla \times \overrightarrow{E} - \sigma^* \overrightarrow{H} \\ \frac{\partial \overrightarrow{D}}{\partial t} &= \nabla \times \overrightarrow{H} - \sigma \overrightarrow{E} \\ \nabla \cdot \overrightarrow{D} &= 0 \\ \nabla \cdot \overrightarrow{B} &= 0 \end{aligned} \tag{B.1}$$

and

$$\begin{aligned} \frac{\partial}{\partial t} \int\int_A \overrightarrow{B} \cdot d\vec{A} &= -\oint_l \overrightarrow{E} \cdot dl - \int\int_A \sigma^* \overrightarrow{H} \cdot d\vec{A} \\ \frac{\partial}{\partial t} \int\int_A \overrightarrow{D} \cdot d\vec{A} &= \oint_l \overrightarrow{H} \cdot dl - \int\int_A \sigma \overrightarrow{E} \cdot d\vec{A} \\ \oiint_A \overrightarrow{D} \cdot d\vec{A} &= 0 \\ \oiint_A \overrightarrow{B} \cdot d\vec{A} &= 0, \end{aligned} \tag{B.2}$$

where

σ^*: equivalent magnetic loss ($ohms/metre$)

σ: electric conductivity ($siemens/metre$)

$\overrightarrow{E}$: electric field, also called the electric flux density ($volt/metre$)

$\overrightarrow{H}$: magnetic field strength ($ampere/metre$)

$\overrightarrow{D}$: electric displacement field ($coulomb/metre^2$)

$\overrightarrow{B}$: magnetic field, also called the magnetic flux density ($tesla, or\ volt-seconds/metre^2$)

A: surface area ($metre^2$)

In linear, isotropic, non-dispersive materials, $\overrightarrow{D}$ and $\overrightarrow{B}$ are related to $\overrightarrow{E}$ and $\overrightarrow{H}$ as:

$$\overrightarrow{D} = \varepsilon \overrightarrow{E} = \varepsilon_0 \varepsilon_r \overrightarrow{E}, \ \overrightarrow{B} = \mu \overrightarrow{H} = \mu_0 \mu_r \overrightarrow{H}. \tag{B.3}$$

Substituting Eq. (B.3) into Eq. (B.1) yields Maxwell's curl equations in linear, isotropic, non-dispersive materials:

$$\begin{aligned} \frac{\partial \overrightarrow{H}}{\partial t} &= -\frac{1}{\mu} \nabla \times \overrightarrow{E} - \frac{1}{\mu} \sigma^* \overrightarrow{H} \\ \frac{\partial \overrightarrow{E}}{\partial t} &= \frac{1}{\varepsilon} \nabla \times \overrightarrow{H} - \frac{1}{\varepsilon} \sigma \overrightarrow{E}. \end{aligned} \tag{B.4}$$

Writing out the vector components of the curl operators of Eq. (B.4) yields the following system of six coupled scalar equations under Cartesian coordinate:

$$\begin{aligned} \frac{\partial H_x}{\partial t} &= -\frac{1}{\mu} [\frac{\partial E_z}{\partial y} - \frac{\partial E_y}{\partial z}] - \frac{1}{\mu} \sigma^* H_x \\ \frac{\partial H_y}{\partial t} &= -\frac{1}{\mu} [\frac{\partial E_x}{\partial z} - \frac{\partial E_z}{\partial x}] - \frac{1}{\mu} \sigma^* H_y \\ \frac{\partial H_z}{\partial t} &= -\frac{1}{\mu} [\frac{\partial E_y}{\partial x} - \frac{\partial E_x}{\partial y}] - \frac{1}{\mu} \sigma^* H_z, \end{aligned} \tag{B.5}$$

$$\begin{aligned} \frac{\partial E_x}{\partial t} &= \frac{1}{\varepsilon} [\frac{\partial H_z}{\partial y} - \frac{\partial H_y}{\partial z}] - \frac{1}{\varepsilon} \sigma E_x \\ \frac{\partial E_y}{\partial t} &= \frac{1}{\varepsilon} [\frac{\partial H_x}{\partial z} - \frac{\partial H_z}{\partial x}] - \frac{1}{\varepsilon} \sigma E_y \\ \frac{\partial E_z}{\partial t} &= \frac{1}{\varepsilon} [\frac{\partial H_y}{\partial x} - \frac{\partial H_x}{\partial y}] - \frac{1}{\varepsilon} \sigma E_z. \end{aligned} \tag{B.6}$$

The system of six coupled partial differential equations in Eq. (B.5) and Eq. (B.6) forms the basis of the FDTD numerical algorithm for the electromagnetic waves interacting with general three-dimensional objects.

Yee's FDTD scheme discretises Maxwell's curl equations by approximating the time and space first-order partial derivatives with centered differences using mesh and the

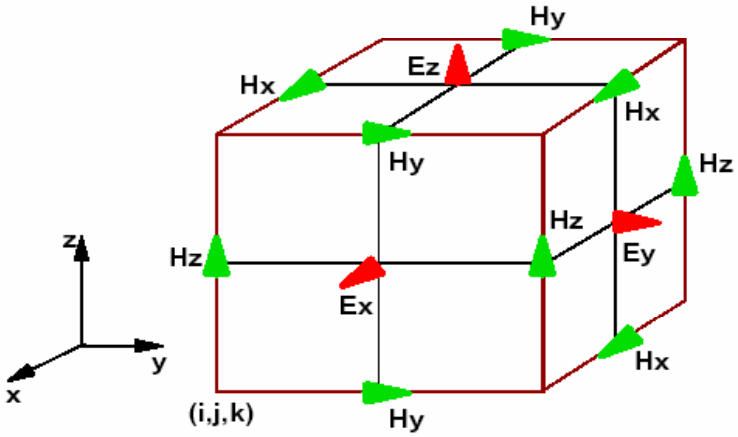

Figure B.1: Yee's spatial grid. [3]

leapfrog scheme. This algorithm centers its $\overrightarrow{E}$ and $\overrightarrow{H}$ components in a three-dimensional space, as shown in Fig. B.1, so that every $\overrightarrow{E}$ component is surrounded by four $\overrightarrow{H}$ components, and every $\overrightarrow{H}$ component is surrounded by four $\overrightarrow{E}$ components. This provides a beautiful simple picture of three-dimensional space being filled by an interlinked array of Faraday's Law and Ampere's Law contours. It is possible to identify $\overrightarrow{E}$ components associated with displacement current flux linking with $\overrightarrow{H}$ loops, as well as $\overrightarrow{H}$ components associated with magnetic flux linking with $\overrightarrow{E}$ loops.

Utilizing Yee's spatial gridding scheme, the spatial partial derivatives in Eq. (B.5) and Eq. (B.6) can be approximated by central differential operators:

$$\frac{\partial E_y}{\partial z} \mid_{(i+\frac{1}{2},j,k)} \approx \frac{E_y(i+\frac{1}{2},j,k+\frac{1}{2}) - E_y(i+\frac{1}{2},j,k-\frac{1}{2})}{\triangle z}, etc. \tag{B.7}$$

Consequently the first line of Eq. (B.5) becomes

$$\frac{\partial H_x(i+\frac{1}{2},j,k)}{\partial t} + \frac{1}{\mu(i+\frac{1}{2},j,k)} \cdot \sigma^*(i+\frac{1}{2},j,k) H_x(i+\frac{1}{2},j,k) = -\frac{1}{\mu(i+\frac{1}{2},j,k)} \cdot [\frac{E_z(i+\frac{1}{2},j+\frac{1}{2},k) - E_z(i+\frac{1}{2},j-\frac{1}{2},k)}{\triangle y} - \frac{E_y(i+\frac{1}{2},j,k+\frac{1}{2}) - E_y(i+\frac{1}{2},j,k-\frac{1}{2})}{\triangle z}]. \tag{B.8}$$

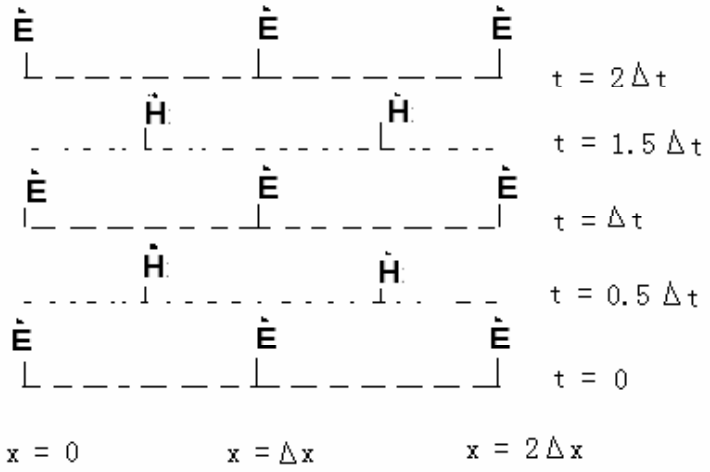

Figure B.2: Leapfrog scheme-the temporal scheme of the FDTD method. [3]

Yee's algorithm also centers its $\overrightarrow{E}$ and $\overrightarrow{H}$ components in time. It is in term of a leapfrog arrangement (see Fig. B.2). All of the $\overrightarrow{E}$ components in the modelled space are completed and stored in memory using the previous $\overrightarrow{E}$ and the newly updated $\overrightarrow{H}$ data. Then $\overrightarrow{H}$ is recomputed based on the previous $\overrightarrow{H}$ and the newly updated $\overrightarrow{E}$. This process continues until time-stepping is concluded. A central differential approximation is applied to Eq. (B.8):

$$\frac{\partial H_x}{\partial t} \mid^{(n\triangle t)} \approx \frac{H_x^{(n\triangle t+\frac{1}{2}\triangle t)} - H_x^{(n\triangle t-\frac{1}{2}\triangle t)}}{\triangle t}, \tag{B.9}$$

with approximation of

$$H_x^{(n\triangle t)} \approx \frac{H_x^{(n\triangle t+\frac{1}{2}\triangle t)} + H_x^{(n\triangle t-\frac{1}{2}\triangle t)}}{2}. \tag{B.10}$$

Eq. (B.8) becomes a discretised equation which can be solved easily using computer

program as:

$$H_x(i+\frac{1}{2},j,k)^{(n\triangle t+\frac{1}{2}\triangle t)} = \frac{\frac{1}{\triangle t}-\frac{\sigma^*}{2\mu}}{\frac{1}{\triangle t}+\frac{\sigma^*}{2\mu}} H_x(i+\frac{1}{2},j,k)^{(n\triangle t-\frac{1}{2}\triangle t)}$$
$$-\frac{1}{(\frac{1}{\triangle t}+\frac{\sigma^*}{2\mu})\cdot\mu\triangle y}[E_z(i+\frac{1}{2},j+\frac{1}{2},k)^{(n\triangle t)} - E_z(i+\frac{1}{2},j-\frac{1}{2},k)^{(n\triangle t)}]$$
$$+\frac{1}{(\frac{1}{\triangle t}+\frac{\sigma^*}{2\mu})\cdot\mu\triangle z}[E_y(i+\frac{1}{2},j,k+\frac{1}{2})^{(n\triangle t)} - E_y(i+\frac{1}{2},j,k-\frac{1}{2})^{(n\triangle t)}]. \quad \text{(B.11)}$$

Numerical stability of the Yee algorithm requires a bounding of the time-step ($\triangle t$) according to the space increment ($\triangle x$, $\triangle y$ and $\triangle z$). This is Courant-Friedrich-Levy (CFL) stability condition, given in three dimensions by

$$\triangle t \leq \triangle t_{max} = \frac{1}{c\sqrt{\frac{1}{\triangle x^2}+\frac{1}{\triangle y^2}+\frac{1}{\triangle z^2}}}. \quad \text{(B.12)}$$

In a cubic grid (where $\triangle x = \triangle y = \triangle z = \triangle$), Eq. (B.12) can be expressed as

$$\triangle t \leq \triangle t_{max} = \frac{\triangle}{c\sqrt{3}}. \quad \text{(B.13)}$$

This limit on $\triangle t$ has allowed the successful application of the FDTD method to a wide variety of electromagnetic-wave-modelling problems for moderate electrical size.

A brief introduction is given above on the foundation of the FDTD method. Further discussion on transformation device modelling is given in detail in Chapter 3.

References

[1] K. Yee, "Numerical solution of initial boundary value problems involving Maxwell's equations in isotropic media," *IEEE Trans. Ant. Propag.*, vol. 14, no. 3, pp. 302–307, 1966.

[2] A. Taflove and S. C. Hagness, *Computational electrodynamics : the finite-difference time-domain method, 3rd Edition.* Artech House, 2005.

[3] Y. Hao and R. Mittra, *FDTD Modeling of Metamaterials: Theory and Applications*. Artech House, 2009.